ESCUELA TÉCNICA SUPERIOR DE INGENIERÍA DE TELECOMUNICACIÓN

UNIVERSIDAD POLITÉCNICA DE CARTAGENA

PROYECTO FIN DE CARRERA

Band-pass waveguide filters and multiplexers design by the structure segmentation technique

Alumno: David Martínez Martínez

Director: Alejandro Álvarez Melcón

Co-director: Mónica Martínez Mendoza

Fecha: July 31, 2014

Universidad Politécnica de Cartagena

Author	David Martínez Martínez
Author's email	mtnez.david@gmail.com
Director	Alejandro Álvarez Melcón
Director's email	alejandro.alvarez@upct.es
Co-director	Mónica Martínez Mendoza
Co-director's email	shanaz00@hotmail.com
Title	Band-pass waveguide filters and multiplexers design by the structure segmentation technique.
Spanish title	Diseño de filtros pasobanda y multiplexores utilizando la técnica de diseño basada en la segmentación de la estructura.

Summary

This work presents a technique for the efficient design of bandpass waveguide microwave filters using a segmentation technique. The segmentation technique was originally developed for in-line filters, and the main contribution of this work is in the combination of this technique with the coupling matrix formalism. In this way we have used this useful design technique for complex coupling topologies, beyond the in-line configuration. As an example some dual mode filters are designed using the new coupling matrix formalism, validating the theory presented.

In addition, this technique has been used in the design of diplexers and triplexers with the previously designed filters.

Furthermore, a novel dual-mode filter topology that can be implemented through this technique is proposed. Finally, in order to validate these contributions, a dual-mode filter has been designed with the introduced topology for a real application in the space sector in collaboration with the *European Space Agency*.

Degree	Ingeniería de Telecomunicación
Department	Tecnologías de la Información y las Comunicaciones
Submission date	July 31, 2014

Keywords

Filter design, microwave, waveguide, coupling matrix, in-line, dual-mode, triple-mode, resonant cavity, wideband filters, all-inductive, multiplexers design, star multiplexers, diplexers, triplexers, spurious, spurious suppression, Chebyshev, chained functions, self-equalized, transmission zeros.

To my couple Verónica.

Acknowledgements

Firstly, I wish to thank especially my project supervisor and co-supervisor namely Dr. Alejandro Álvarez Melcón and Dr. Mónica Martínez Mendoza for all the support and inspiration that I have been given during the accomplishment of this work. In addition, they have provided me with much of the software and tools as well as the knowledge needed to successfully complete this project.

I would also like to thank the European Space Agency, in particular Dr. Marco Guglielmi and Petronilo Martin Iglesias for their confidence and for giving me the opportunity to work in a real application for the space sector. Furthermore, I would like to express my gratitude for considering the filters designed throughout this work and for including it in ongoing projects at ESTEC.

Secondly I would like to show my appreciation to Jose Manuel Pérez Escudero, Dr. Jose Antonio Lorente Acosta, María Teresa Sancho Ruiz de Castañeda and others who have helped me and given me new ideas for finding the solution to problems faced along the work as well as new future research lines.

Finally I would like to express my genuine gratitude to my family, my couple Verónica and all those who have been with me and have supported both me and the work I have been doing.

Contents

Acknowledgements ix

Contents xi

List of Figures xv

List of Tables xxi

1 Introduction 1
- 1.1 State of the art . . . 1
- 1.2 Objectives and motivation of this work . . . 2
- 1.3 Original contributions . . . 2
- 1.4 Description and organization of the report . . . 3

2 Coupling matrix theory 5
- 2.1 Introduction . . . 5
- 2.2 Coupling matrix elements meaning . . . 5
- 2.3 Bandpass to lowpass transformation . . . 6
  - 2.3.1 Bandpass to lowpass frequency scaling . . . 6
  - 2.3.2 Bandpass to lowpass filter scaling . . . 6
- 2.4 Analysis of the network . . . 7
  - 2.4.1 Impedance matrix computation . . . 7
  - 2.4.2 Transmission and reflection coefficients . . . 8
- 2.5 Step by step analysis and coupling matrix segmentation . . . 9
  - 2.5.1 Lowpass prototype with impedance inverters . . . 9
  - 2.5.2 Step by step design technique . . . 13
  - 2.5.3 Coupling matrix scaling . . . 14
  - 2.5.4 Computing the inductances of the bandpass prototype . . . 15
- 2.6 Conclusions . . . 17

3 Inductive in-line filters design 19
- 3.1 Introduction . . . 19
- 3.2 Coupling matrix topology for in-line filters . . . 19
- 3.3 Filter design . . . 20
  - 3.3.1 Design of odd order (N) filters . . . 20
  - 3.3.2 Design of even order (N) filters . . . 28
- 3.4 Wideband in-line filters design . . . 31
  - 3.4.1 Wideband filters design procedure . . . 31
  - 3.4.2 Design of a sixth-order in-line filter with 500 MHz bandwidth . . . 32
  - 3.4.3 Design of an eighth-order in-line filter with 1GHz bandwidth . . . 35
  - 3.4.4 Eleventh-order in-line filter with 2.5GHz bandwidth . . . 37
- 3.5 Conclusions . . . 38

4 Dual-mode filters design **41**
4.1 Introduction . . . 41
4.2 All inductive dual-mode resonators . . . 43
4.2.1 Technology with modes TE_{301} and TE_{102}. . . . 45
4.2.2 Technology with modes TE_{201} and TE_{102}. . . . 45
4.3 Coupling matrix topology for inductive dual-mode filters . . . 45
4.4 Generalization of the design procedure . . . 48
4.4.1 Coupling matrix scaling . . . 49
4.4.2 Computation of the lumped elements values . . . 50
4.4.3 Example for waveguide technology . . . 50
4.5 Inductive dual-mode filters design procedure . . . 52
4.6 Third-order dual-mode filter without offsets in the irises . . . 53
4.6.1 Filter specifications and coupling matrix scaling . . . 53
4.6.2 Forward design . . . 55
4.6.3 Backward design . . . 57
4.6.4 Results . . . 58
4.7 Third-order dual-mode filter with offsets in the irises . . . 58
4.7.1 Filter specification and coupling matrix . . . 59
4.7.2 Forward design . . . 60
4.7.3 Backward design . . . 63
4.7.4 Results . . . 63
4.8 Fourth-order dual-mode filter with two dual-mode cavities and offset technology . . . 64
4.8.1 Filter specifications and coupling matrix . . . 64
4.8.2 Forward design . . . 66
4.8.3 Backward design . . . 68
4.8.4 Results . . . 68
4.9 Sixth-order dual-mode filter with two dual-mode cavities and offset technology . . . 70
4.9.1 Filter specifications and coupling matrix . . . 70
4.9.2 First segment . . . 71
4.9.3 Second segment . . . 71
4.9.4 Result . . . 73
4.10 Conclusions . . . 76

5 Multiplexers design **77**
5.1 Introduction . . . 77
5.1.1 Hybrid coupled multiplexers . . . 77
5.1.2 Circulator-coupled multiplexers . . . 78
5.1.3 Directional filters multiplexers . . . 79
5.1.4 Manifold-coupled multiplexers . . . 79
5.1.5 Star junction multiplexers . . . 80
5.2 Diplexer with in-line filters . . . 80
5.2.1 In-line filters . . . 81
5.2.2 H-plane diplexer . . . 82
5.2.3 E-plane diplexer . . . 83
5.2.4 E-plane triplexer . . . 85
5.3 Diplexer with dual-mode filters . . . 90
5.3.1 E-plane diplexer with TE_{102} and TE_{301} modes . . . 90
5.3.2 H-plane diplexer with TE_{102} and TE_{201} modes . . . 92
5.3.3 Isolated fourth-order filters . . . 97
5.3.4 H-plane diplexer with fourth-order dual mode filters . . . 99
5.4 Conclusions . . . 99

6 Dual-mode filter with input-output single-mode cavities **103**
6.1 Introduction . . . 103
6.2 Adding input and output single-mode cavities . . . 103
6.2.1 Coupling matrix for this topology . . . 105
6.3 Design example . . . 107
6.3.1 Structure view . . . 107
6.3.2 Design procedure . . . 108
6.3.3 First segment . . . 109

6.3.4 Second segment . . . 109
6.3.5 Third segment . . . 111
6.3.6 Results . . . 112
6.4 Designed filters . . . 115
6.4.1 Filter 1 (5-1-0) . . . 117
6.4.2 Filter 2 (5-2-0) . . . 117
6.4.3 Filter 3 (6-2-0) . . . 118
6.4.4 Filter 4 (8-2-0) . . . 118
6.4.5 Filter 5 (8-3-0) . . . 118
6.4.6 Filter 6 (10-2-0) . . . 120
6.4.7 Filter 7 (10-4-0) . . . 120
6.5 Design for manufacturing . . . 125
6.5.1 Thickness of the coupling windows . . . 125
6.5.2 Rounded edges . . . 126
6.5.3 Tuning screws . . . 126
6.5.4 Structure for manufacturing . . . 127
6.6 Conclusions . . . 127

7 Conclusions 129

8 Future work 131
8.1 Introduction . . . 131
8.2 Corrections of the coupling matrix scaling for wideband filters . . . 131
8.3 Spurious suppression in in-line filters by using dual-mode cavities . . . 132
8.4 Dual-mode filter design with elements that favor the coupling to the TE_{201} mode and lower the coupling to the TE_{102} mode. . . . 134
8.5 Self-equalized dual-mode filters with complex transmission zeros . . . 135
8.6 Dual-mode filters with input and output single-mode cavities and extracted poles. . . . 138
8.7 Adapting the designed dual-mode filters with input and output single-mode cavities to manifold multiplexers . . . 138
8.8 Dual-mode filters with input and output dual-mode cavities that implements "Chained responses" . . . 140
8.9 Transversal waveguide filters with triple-mode cavities . . . 144
8.9.1 Triple-mode filter with input/output single-mode cavities . . . 146

Appendix 151

A Synthesis of the Chebyshev filter function 153
A.1 Determination of P(s) . . . 153
A.2 Determination of F(s) . . . 154
A.3 Determination of the constants ϵ and ϵ_R . . . 156
A.4 Determination of E(s) . . . 157
A.5 Examples . . . 157

B Electromagnetic simulation software 163
B.1 Optimization with the electromagnetic analysis software FEST3D . . . 164

C Convergence study 167

D Simulation and optimization of several resonant modes simultaneously with the electromagnetic software FEST3D 169

E Matlab designed GUI 171

Bibliography 173

List of Figures

2.1 Bandpass prototype network of bandpass filter. . . . 5
2.2 Couplig matrix for generic filter topology. . . . 6
2.3 Lowpass prototype network of bandpass filter. . . . 7
2.4 Standalone network used to analyze the coupling matrix. . . . 7
2.5 Filter prototype with parameters g_ks. . . . 10
2.6 Lowpass prototype with inductive elements and impedance inverters. . . . 10
2.7 Ideal impedance inverter. . . . 10
2.8 Impedance seen looking from inductances g_N and L_N. . . . 11
2.9 Impedance seen looking from inductances g_{N-1} and L_{N-1}. . . . 12
2.10 Impedance seen looking from inductances g_k and L_k. . . . 12
2.11 Input impedance of LPP with g_k values and LPP with inductances and impedance inverters. . . . 13
2.12 Redefinition of the LPP with coupling elements. . . . 14
2.13 Equivalent series circuit to the waveguide resonator. . . . 16
2.14 Comparison between the input impedance of both circuits in Figure 2.13 with different fractional bandwidths (Δ). . . . 16

3.1 Coupling matrix topology for in-line filters. . . . 19
3.2 In-line filters structure with the parameters definition used in this chapter. . . . 20
3.3 Coupling matrix which gives the desired fifth-order response. . . . 20
3.4 Scaled coupling matrix of the designed fifth-order filter. . . . 21
3.5 First segment of the filter structure. It is composed of only the first iris. . . . 21
3.6 First segment of the fifth-order scaled coupling matrix. . . . 21
3.7 Comparison between the response given by the coupling matrix and by the filter segment in the step 1 of a fifth-order filter. . . . 22
3.8 Second segment of the fifth-order filter scaled coupling matrix. . . . 22
3.9 Second segment of the filter structure. . . . 23
3.11 Third segment of scaled coupling matrix. . . . 23
3.12 Third segment of the fifth-order filter structure. . . . 23
3.13 Given response in step 3 for the fifth-order filter segment. . . . 24
3.14 Fourth segment of the fifth-order filter scaled coupling matrix. . . . 24
3.15 Fourth segment of the filter structure. . . . 25
3.16 Given response in the step 4 by the fifth-order filter segment. . . . 25
3.17 Fifth segment of the filter structure. . . . 25
3.18 Fifth segment of the fifth-order filter scaled coupling matrix. . . . 25
3.19 Given response in step 5 by the fifth-order filter segment. . . . 26
3.20 Complete filter structure (sixth segment) of a fifth-order filter. . . . 26
3.21 Complete scaled fifth-order filter coupling matrix (sixth segment). . . . 27
3.22 Total filter response obtained in step 6 by the designed fifth-order filter. . . . 27
3.23 Coupling matrix which given the desired eighth-order response. . . . 28
3.24 Scaled eighth-order filter coupling matrix. . . . 28
3.25 Structure and parameters of the designed eighth-order filter. . . . 29

3.26 Partial responses en each step of the eighth-order filter. . . . 30
3.27 Coupling matrix which given the desired sixth-order response. . . . 33
3.28 Scaled sixth-order filter coupling matrix. . . . 33
3.29 Partial responses in each step of the sixth-order filter. . . . 34
3.30 Coupling matrix which given the desired eighth-order response. . . . 35
3.31 Scaled eighth-order filter coupling matrix. . . . 35
3.32 Partial responses in each step of the eighth-order filter. . . . 36
3.33 Structure of the designed eleventh-order filter. . . . 37
3.34 Final response of the eleventh-order filter. . . . 38
3.35 Real partial response in each step after segmenting the final eleventh-order filter. . . . 39

4.1 Coupling-routing diagram of in-line and transversal topologies. . . . 41
4.2 Dual mode filter with two cylindrical resonators. . . . 42
4.3 Coupling diagram of the dual-mode filter with two cylindrical resonators. . . . 42
4.4 Dual-mode resonant cavity with the modes TE_{301} and TE_{201}. . . . 43
4.5 Dual-mode resonant cavity with the modes TE_{201} and TE_{201}. . . . 44
4.6 Coupling-routing diagram of a second-order inductive dual-mode filter. . . . 44
4.7 Electrical response of a single dual-mode cavity. . . . 45
4.8 Field patterns of a dual-mode cavity with the modes TE_{301} and TE_{102}. . . . 46
4.9 Field patterns of dual-mode cavity with the modes TE_{201} and TE_{102}. . . . 46
4.10 Coupling-routing diagram of a fourth-order inductive dual-mode filter with two dual-mode cavities. . . . 47
4.11 Dual mode fourth-order filter with two dual-mode cavities and parameters of its structure. 47
4.12 Generalized coupling-routing diagram for an inductive dual-mode filter with only dual-mode cavities. . . . 48
4.13 Coupling matrix of a dual-mode filter with only dual-mode cavities. . . . 48
4.14 Lumped-elements prototypes. . . . 49
4.15 Equivalent circuits to the waveguide resonator. . . . 50
4.16 Desired filter structure and parameters to be optimized for the third-order dual-mode filter with non-offset irises (scaled drawing). . . . 53
4.17 Coupling-routing diagram of a third-order dual-mode filter. . . . 53
4.18 Coupling matrix of the third-order dual-mode filter with a transmission zero above the passband. . . . 54
4.19 Coupling to the first mode (TE_{102}) and to the second one (either TE_{301} or TE_{301}) in a dual-mode cavity. . . . 55
4.20 Filter segments in the forward design of the third-order non offset filter. . . . 56
4.21 First segment of the coupling matrix for each resonant mode. . . . 56
4.22 Real and theoretical response in each forward step of the third-order non-offset dual-mode filter. . . . 56
4.23 Scaled matrix in the forward step 2 of the third-order dual-mode filter without offset. 57
4.24 Filter segments in the backward design of the third-order non offset filter. . . . 57
4.25 Scaled matrix in the backward step 1 of the third-order dual-mode filter without offset. 57
4.26 Second matrix segment of the third-order dual-mode filter in the backward step 2. . . . 58
4.27 Final response of the third-order non-offset filter. . . . 59
4.28 Filter structure of the third order dual mode filter with offset (scaled drawing). . . . 59
4.29 Coupling matrix of the third-order dual-mode filter with with a more distant from the passband transmission zero from the passband. . . . 60
4.30 Ideal filter responses of the two last investigated filters.. . . . 60
4.31 Filter segments in the forward design of the third-order filter with offset in the irises. . 62
4.32 Real and theoretical response in each forward step of the third-order dual-mode filter with offset. . . . 62
4.33 Filter segments in the backward design of the third-order filter with offset. . . . 63
4.34 Final response of the third-order dual-mode filter with offset. . . . 64
4.35 Filter structure of the fourth-order filter with two transmission zeros (scaled drawing). 65
4.36 Coupling matrix of the fourth-order dual-mode filter with two transmission zeros. . . . 65
4.37 Filter segments in the forward design of the fourth-order filter whit two transmission zeros. . . . 67
4.38 Real and theoretical response in each step of the fourth-order dual-mode filter with two transmission zeros. . . . 67

4.39 Filter segments in the backward design of the fourth-order filter with two transmission zeros. . . . 68
4.40 Final response of the fourth-order filter with two transmission zeros. . . . 69
4.41 Filter structure of the designed sixth-order filter with offset (scaled drawing). . . . 70
4.42 Coupling-routing diagram for an inductive dual-mode filter with three dual-mode cavities. 70
4.43 Coupling matrix of a sixth-order dual-mode filter with three transmission zeros. . . . 71
4.44 Structure in the step 1 of the sixth-order dual-mode filter with three transmission zeros. 71
4.45 Real and theoretical response in the step 1 of the sixth-order dual-mode filter with three transmission zeros. . . . 72
4.46 Structure in the step 2 of the sixth-order dual-mode filter with three transmission zeros. 72
4.47 Real and theoretical response in the step 2 of the sixth-order dual-mode filter with three transmission zeros. . . . 73
4.48 Structure view and parameters in step 3 of the sixth-order filter with three transmission zeros. . . . 74
4.49 Real and theoretical response in the step 3 of the sixth-order dual-mode filter with three transmission zeros. . . . 74
4.50 Final response of the sixth-order filter with three transmission zeros. . . . 75

5.1 Simplified satellite payloads diagram. . . . 78
5.2 Hybrid coupled multiplexer. . . . 78
5.3 Circulator coupled multiplexer. . . . 79
5.4 Multiplexer with directional filters. . . . 79
5.5 Manifold multiplexer. . . . 80
5.6 Star multiplexer. . . . 80
5.7 Coupling matrix used for all in-line filters in diplexers design. . . . 81
5.8 In-line filters for each channel. . . . 81
5.9 H-plane diplexer. . . . 82
5.10 Response in each step of the H-plane in-line diplexer. . . . 84
5.11 E-plane diplexer. . . . 85
5.12 Response in each step of the E-plane in-line diplexer. . . . 86
5.13 E-plane triplexer. . . . 87
5.14 Response in each step of the E-plane in-line triplexer. . . . 89
5.15 E-plane diplexer with the TE_{102} and TE_{301} modes. . . . 91
5.16 Response in each step of the third-order diplexer with the TE_{301} mode. . . . 93
5.17 H-plane diplexer with the TE_{102} and TE_{201} modes. . . . 94
5.18 Response in each step of third-order diplexer with TE_{201} mode. . . . 96
5.19 Isolated fourth-order filters with two transmission zeros. . . . 98
5.20 H-plane diplexer with fourth-order dual mode filters and two transmission zeros in each channel. . . . 100
5.21 Final response of the diplexer with fourth-order filters and two transmission zeros in each channel. . . . 102

6.1 Input couplings to the first dual-mode cavity in both topologies. Both topologies A and B are shown in Figure 6.2. . . . 104
6.2 Generalized coupling-routing diagram for both topologies of all-inductive dual mode filters. . . . 105
6.3 Relation between the coupling to the second mode (TE_{201}) and to the first mode (TE_{102}) in the dual-mode cavity. Both topologies A and B are shown in Figure 6.2. . . . 106
6.4 Coupling matrix of a dual mode filter with dual-mode cavities and single-mode cavities in the filter input and output. . . . 106
6.5 Coupling matrix which provides the sixth-order response. . . . 107
6.6 Ideal response of the sixth-order filter with input and output single-mode cavities. . . . 107
6.7 Matching of each resonance in the sixth-order filter with each value of the coupling matrix. . . . 108
6.8 Designed sixth-order filter with 2 TZ by adding dual-mode cavities to the filter input and output. . . . 108
6.9 Structure in the first step of the sixth-order dual mode filter. . . . 109
6.10 Real and theoretical response in step 1 of the sixth-order dual mode filter. . . . 110
6.11 Structure in the second step of the sixth-order dual mode filter. . . . 110
6.12 Real and theoretical response in step 2 of the sixth-order dual mode filter. . . . 110

6.13 Structure in the third step of the sixth-order dual mode filter. . . . 111
6.14 Real and theoretical response in step 3 performing firstly the forward design and then the backward design. . . . 113
6.15 Real and theoretical response in step 3 performing the backward design before the forward one. . . . 113
6.16 Final filter response with each one of the results listed in Table 6.6. . . . 113
6.17 Final filter response after performing a global optimization. . . . 114
6.18 Final filter structure. . . . 114
6.19 Reflection and rejection levels required. . . . 115
6.20 Coupling matrix of filter 1 (5-1-0). . . . 117
6.21 Response of filter 1 (5-1-0). . . . 117
6.22 Coupling matrix of filter 2 (5-2-0). . . . 117
6.23 Response of filter 2 (5-2-0). . . . 118
6.24 Coupling matrix of filter 3 (6-2-0). . . . 118
6.25 Response of filter 3 (6-2-0). . . . 119
6.26 Coupling matrix of filter 4 (8-2-0). . . . 119
6.27 Response of filter 4 (8-2-0). . . . 119
6.28 Coupling matrix of filter 5 (8-3-0). . . . 119
6.29 Response of filter 5 (8-3-0). . . . 120
6.30 Coupling matrix of filter 6 (10-2-0). . . . 120
6.31 Response of filter 6 (10-2-0). . . . 121
6.32 Coupling matrix of filter 7 (10-4-0). . . . 121
6.33 Response of filter 7 (10-4-0). . . . 121
6.34 Structure and parameters of each filter. . . . 122
6.34 Structure and parameters of each filter (continuation). . . . 123
6.35 Filter structure with thicker irises and tuning screws in the resonators.. . . . 125
6.36 Details of the rounded edges close to a coupling window. . . . 126
6.37 Tuning screws modeled as squared screws of 1.6 mm side. . . . 127
6.38 Final filter structure ready for manufacturing. . . . 128
6.39 Filter response of the structure ready for manufacturing. . . . 128

8.1 Comparison between input impedance of both circuits in Figure 2.13 with different fractional bandwidth (Δ). . . . 131
8.2 In-line filter with spurious suppression. . . . 133
8.3 In-line filter with wider second and fourth cavities. . . . 133
8.4 In-line filter with wider first and last cavities. . . . 134
8.5 Dual-mode cavity with vacuum and with a dielectric strip. . . . 135
8.6 Dual-mode cavity with double iris configuration. . . . 135
8.7 Fifth order self-equalized filter with two transmission zeros in the real axis ($s = \pm\sigma + j \cdot 0$) and another two in the complex axis ($s = j\omega$). . . . 136
8.8 Sixth order self-equalized filter with two transmission zeros in the real axis ($s = \pm\sigma + j \cdot 0$) and another two in the complex axis ($s = j\omega$). . . . 136
8.9 Eight order self-equalized filter with two transmission zeros in the real axis ($s = \pm\sigma + j \cdot 0$) and another ones in the complex axis ($s = j\omega$). . . . 136
8.10 Eight order self equalized filter with two transmission zeros in the real axis ($s = \pm\sigma + j \cdot 0$) and three in the complex axis ($s = j\omega$). . . . 137
8.11 Tenth order self-equalized filter with two transmission zeros in the real axis ($s = \pm\sigma + j \cdot 0$) and another two in the complex axis ($s = j\omega$). . . . 137
8.12 Tenth order self-equalized filter with two transmission zeros in the real axis ($s = \pm\sigma + j \cdot 0$) and four in the complex axis ($s = j\omega$). . . . 137
8.13 Topology with input/output single-mode cavities and extracted poles. . . . 138
8.14 Manifold multiplexer with the presented dual-mode filters with input/output single-mode cavities. . . . 139
8.15 Final response of the manifold multiplexer presented in Figure 8.14. . . . 139
8.16 Comparison between a chained (2+2) function without transmission zeros and with two transmission zeros provided by the first seed. . . . 141
8.17 Comparison between (6-2-0) chained functions and a (5-2-0) Chebyshev function. . . . 142
8.18 Comparison between (6-2-0) chained functions and a (4-2-0) Chebyshev function. . . . 143
8.19 Coupling-routing diagram of a third order fully transversal filter. . . . 144
8.20 Transversal matrix with a reflection level of -12.5 dB. . . . 144

8.21 Field pattern of each resonant mode in the triple-mode cavity. 145
8.22 Transversal matrix that provides the target response for the triple-mode filter. 146
8.23 Response of the designed triple mode filter. 146
8.24 Structure of the triple mode filter. 147
8.25 Coupling-routing diagram of a fifth order triple-mode filter with input/output single-mode cavities. 147
8.26 Triple mode matrix with the topology shown in Figure 8.25. 147
8.27 Response of a triple-mode filter with input/output single-mode cavities. 148
8.28 Structure of the triple mode filter with input/output single-mode cavities. 148
8.29 Response of a triple-mode filter with 100 MHz bandwidth. 149
8.30 Structure of the triple mode filter with 100 MHz bandwidth. 150

A.1 Chebyshev function with 3 transmission zeros at $s = j\infty$. 154
A.2 Chebyshev function with 4 transmission zeros at $s = j\infty$, $s = -j\infty$, $s = 2$ and $s = -2$. 155
A.3 LPP fourth-orden response without transmission zeros. 159
A.4 LPP fourth-orden response with a transmission zero at $s = 1.5j$. 160
A.5 LPP fourth-orden self-equalized response with two transmission zeros at $s = \pm 2$. . . . 161
A.6 LPP fourth-orden response with two transmission zero at $s = \pm 0.5 + 1.5j$. 162

B.1 Interface of FEST3D software used in this work. 163
B.2 Optimization window of fest3d. 165
B.3 Constraint in the optimization windows of fest3d. 165

C.1 General specifications window. 168
C.2 Comparison between a convergent and a not convergent result by checking the “All-Inductive” box. 168

D.1 Dual structure used to optimize the coupling to two resonant modes simultaneously. . 169

E.1 Matlab designed GUI. 172

List of Tables

3.1 Result of the optimized fifth-order filter parameters in step 1. . . . 22
3.2 Obtained dimensions of the fifth-order filter parameters in step 2. . . . 23
3.3 Relevant geometrical parameters for the fifth-order filter in step 3. . . . 23
3.4 Result of the fifth-order filter parameters in the step 4. . . . 24
3.5 Result of the fifth-order filter parameters in step 5. . . . 25
3.6 Result of the fifth-order filter parameters in step 6. . . . 27
3.7 Result of optimized parameters in each step of the eighth-order filter. . . . 29
3.8 Result of the wideband sixth-order filter parameters in each step. . . . 33
3.9 Result of the wideband eighth-order filter parameters in each step. . . . 36
3.10 Final parameters values of the designed eleventh-order filter. . . . 37

4.1 Result of the optimized third-order non-offset filter parameters in each step. . . . 58
4.2 Parameters value of filter structure in Figure 4.16. . . . 58
4.3 Dimensions of the optimized third-order filter with iris offset in each step. . . . 63
4.4 Parameters value of the filter structure in Figure 4.28. . . . 64
4.5 Theoretical dimensions of the dual-mode cavities. . . . 66
4.6 Dimensions of the optimized fourth-order filter with two transmission zeros in each step. 69
4.7 Final dimensions of the fourth-order filter with two transmission zeros. . . . 69
4.8 Theoretical dimensions of the dual-mode cavities in the sixth-order filter with three transmission zeros. . . . 71
4.9 Dimensions in the step 1 of the sixth-order dual-mode filter with three transmission zeros. . . . 72
4.10 Dimensions in the step 2 of the sixth-order dual-mode filter with three transmission zeros. . . . 73
4.11 Dimensions in the forward step 3 of the sixth-order dual-mode filter with three transmission zeros. . . . 74
4.12 Parameters value of filter structure in Figure 4.35. . . . 75

5.1 Parameters value in each step of the H-plane in-line diplexer. . . . 83
5.2 Parameters value in each step of the E-plane in-line diplexer. . . . 86
5.3 Parameters value in each step of the E-plane in-line triplexer. . . . 88
5.4 Parameters value in each step of the third-order diplexer with the TE_{301} mode. . . . 92
5.5 Parameters value in each step of the third-order diplexer with TE_{201} mode. . . . 95
5.6 Parameters of the first-channel isolated filter with two transmission zeros. . . . 97
5.7 Parameters of the second-channel isolated filter with two transmission zeros. . . . 98
5.8 Parameters value in each step of the diplexers with fourth-order filters and two transmission zeros in each channel. . . . 101

6.1 Initial dimensions of the dual mode cavities. . . . 109
6.2 Dimensions in step 1 of the sixth-order dual mode filter. . . . 109
6.3 Dimensions in step 2 of the sixth-order dual mode filter. . . . 110
6.4 Dimensions in step 3 performing firstly the forward design and then the backward design. 111

6.5 Parameters in step 3 performing the backward design before the forward one. 112
6.6 Comparison of the central iris dimensions obtained in both forward and backward design. 112
6.7 Parameters value of the filter structure in Figure 6.18. 114
6.8 Rejection required in each frequency range. 115
6.9 Specifications of all filters designed in this section. 116
6.10 Physical dimensions of all filters designed in this section. 123
6.10 Physical dimensions of all filters designed in this section (continuation). 124

8.1 Different possibilities to implement a 6th-order response by a chained function. 141
8.2 Dimensions of the triple-mode filter. 146
8.3 Dimensions of the triple-mode filter with input/output single-mode cavities. 149
8.4 Dimensions of the triple-mode filter with 100 MHz bandwidth. 150

B.1 Usage of FEST3D algorithms throughout this work. 164

1 INTRODUCTION

In the early 70s, after the first telecommunication satellite was launched and operating, the general interest on microwave systems for communications began to grow all around the world enormously and unexpectedly. Lately, with the development of terrestrial microwave communication, it took place the expansion of the civil communications systems that saturated the available electromagnetic spectrum with numerous services of any nature: telecommunication, broadcasting, safety, etc. The overcrowding of the useful frequencies spectrum leaded to a crucial importance in the microwave systems design field. Particularly, the design of filters with a higher order filtering functions and improved frequency specifications to accommodate a larger number of channels within reduced frequency range. As a result, a race began to achieve filters with the lowest insertion loss within the passband and the highest rejection in the stopband [Cameron et al., 2007].

Furthermore, due to the development of the space sector and the growing interest of extremely high frequencies to overcome the saturation of the electromagnetic spectrum, the mass and volume of the filtering structures have become critical aspects. The modern microwave filter for the space sector must operate at higher frequencies and achieve a compact-size and reduced mass to afford the launching process.

1.1 State of the art

Presently, the design of waveguide microwave filters remains a very important activity for the development of various communication technologies, such as those used in mobile and satellite systems. The design of such components is often difficult due to the high sensitivity of the responses to the different elements of the structure (resonators and coupling elements). This high sensitivity makes optimization techniques not reliable, and often find difficulties in the convergence to the final desired response.

By using traditional design techniques, the different coupling elements and cavities will be dimensioned separately. However, when all the elements are assembled in the final filter, interactions and undesired couplings between them appear. Due to this, in general it is required new optimizations to correct the overall response. Moreover, these interactions are larger when the filter bandwidth increases.

Some authors have developed advanced filters equivalents and corrections of the filter prototypes [Vanin et al., 2004], others perform the filter design by optimizing the filter prototype in continuous iterations in order to obtain the same behavior as the one provided by the real filter structure [Soto et al., 2010]. However, these novel methods are developed for in-line filters and it comes into a major matter when the aim is the efficient dimensioning of filters with more complex topologies.

With regard to the optimization of the filter structure, it is not possible when the complexity of the structure increases due to the high number of variables and local minima which may cause the optimization to not converge or to get stuck in a local minimum. Thus, in order to achieve the desired structure, having an appropriate initial point and applying an intelligent procedure are necessary.

In this context, in [Guglielmi and Melcon, 1993, Guglielmi, 1994] an alternative design technique based on the segmentation of the structure in several steps ("step-by-step" technique) was presented. The advantage of this method is that different parts of the structure are adjusted by adding in a step-by-step fashion the different elements (coupling elements, resonators) that will exist when the final

filter is assembled. Therefore each optimization step takes into account the presence and interactions between adjacent elements. Moreover, at each step, the number of parameters to be optimized is small. Thus each step in the optimization is relatively simple.

Nevertheless, the technique described was also developed for in-line waveguide filters. Although this type of filters is widely used in practice, it is also desirable to implement filters with alternative coupling topologies. For instance, in many applications it is needed to introduce couplings between non-adjacent resonators to implement transmission zeros in the insertion loss response of bandpass filters. This issue can be done by using dual-mode cavities. These cavities support two resonant modes within them. Thus each dual-mode cavity provides two electrical resonances and a transmission zero by the interaction between both modes within the cavity.

In spite of the fact that dual-mode cavities with circular waveguide technology [Cameron et al., 2007] are widely known and implemented [Cogollos et al., 2010], this kind of cavities lead to a too bulky and difficult to integrate structures. Furthermore the design of circular dual-mode cavities is rather difficult and both tuning and coupling screws are necessary to excite and control the resonant modes within the cavity.

Alternatively, in [Guglielmi et al., 2001] a new topology of dual-mode cavities was presented. This topology is used to implement the dual-mode cavities by rectangular cavities and with all-inductive technology. Moreover no coupling screws are needed since both resonant modes are excited through a one single coupling window with inductive technology. As a result, more compact-size filters are obtained with a considerable reduction in terms of footprint, mass or volume meanwhile the all-inductive technology allows the efficient design and the low-cost manufacturing of these filter. However, this filters lack of an efficient and accurate design procedure since the filters structure of the dual-mode cavities must be micrometricaly dimensioned in order to provide the right coupling to each resonant mode and to properly adjust its resonant frequency.

Finally, as far as applications are concerned, in the space sector, the principal application of microwave filters is as part of the channel multiplexers. Channel multiplexers are essential part of satellite payloads since they allow to separate a wideband signal into a group of narrowband channels that can be amplified through high power amplifiers (HPAs). They also allow to combine these amplified channels into a wideband signal for transmission trough a single antenna [Cameron et al., 2007]. These multiplexers are essentially composed of a large number of microwave filters. Thus they have benefited from the improvements in the framework of microwave filters such as the higher selectivity of dual-mode filters due to the presence of transmission zeros. This fact allows to increase the number of allocated channels and even to implement adjacent channels with a higher rejection between them [Macchiarella and Tamiazzo, 2010, Macchiarella, 2011, Hu et al., 2013].

1.2 Objectives and motivation of this work

The objective and significance of this work is to adapt the design technique, introduced for the first time by Guglielmi [Guglielmi and Melcon, 1993] for in-line filters, to the context established by the coupling matrix [Cameron et al., 2007]. In this way we open for the first time, the possibility to use the step-by-step segmentation technique for the design of more complex coupling topologies.

Moreover, in order to validate the generalized procedure, it is intended to use it for the efficient design of the all-inductive dual-mode filters proposed by Guglielmi [Guglielmi et al., 2001]. Another objective will be to use the new design procedure to generalize the proposed topology with the said all-inductive dual-mode cavities through the advantages of the presented procedure.

Finally, in order to provide more practical applications, some diplexers and triplexers will be built with the all-inductive dual-mode filters using the proposed segmentation technique.

1.3 Original contributions

In this work we first present the theory that generalize the step-by-step segmentation technique in the coupling matrix context. Then, we present several examples of dual-mode filters with transmission zeros using the all-inductive waveguide technology proposed in [Guglielmi et al., 2001]. These examples consist on a extension of the dual-mode filter designed by Guglielmi and demonstrate that

the use of the proposed design technique is very effective for the dimensioning of waveguide filters that implement alternative coupling topologies.

Next we perform a study on new dual-mode topologies that can improve the overall behavior of the dual-mode filters with only dual-mode cavities. In this field, we introduce a novel topology by adding single-mode cavities to the filter input and output. With this topology, it is possible to overcome the limitations of the dual-mode filter proposed by Guglielmi in terms of bandwidth, insertion losses and how far the transmission zeros can be placed with respect to the passband. In addition, by adding single-mode cavities, a higher freedom for the irises thickness and offset is achieved and this even leads to a more compact size when the filter order increases.

Furthermore, in collaboration with the European Space Agency, a set of filters with this novel topology and different specifications have been designed by using the proposed segmentation technique in order to fulfill the requirement of a real application for the space sector. In view of the given advantages, one of the designed filters has been selected for manufacturing as an alternative to the widely know in-line filters with extracted poles [Rhodes and Cameron, 1980, Montejo-Garai et al., 2005b, Mohottige et al., 2013] and it is currently in process of manufacturing a breadboard at the European Space Agency.

Finally, this work opens numerous lines of research and further extension of the presented topologies and applications.

1.4 Description and organization of the report

The present work is composed of a group of seven chapters in which the theory and application of the proposed design technique is discussed. In addition, in an eighth chapter, a large number of new research lines and future work are suggested in order to further develop the content of each chapter. Following is a brief summary of each chapter.

1. The current chapter provides a piece of history and the state of the art of microwave filters. Moreover, the initial motivation for the project and its objectives, as well as a brief summary of the other chapters are introduced.

2. In the second chapter the theory of the coupling matrix is reviewed and the segmentation technique presented in [Guglielmi and Melcon, 1993, Guglielmi, 1994] is adapted to the context of the coupling matrix for the design of in-line topologies.

3. In the third chapter, some in-line filters are designed by segmenting the filter structure and the coupling matrix to validate the theory given in the previous chapter [Martínez et al., 2013]. Moreover this procedure is applied for the first time to the design of wideband filters with in-line topology.

4. The fourth chapter provides the theory that generalizes the step-by-step design procedure for the design of any filter structure whose coupling topology can be represented by the coupling matrix. In addition, through using the novel design technique, we present some examples of the dual-mode filters proposed in [Guglielmi et al., 2001] as well as another one by generalizing the mentioned topology.

5. In the fifth chapter some diplexers and triplexers with star configuration are designed by the segmentation technique and by using the dual-mode filters designed in the previous chapter.

6. In the sixth chapter a new dual-mode filter topology is introduced by adding single-mode cavities to the filter input and output. With this topology, a substantial group of filters is designed in collaboration with the European Space Agency to fulfill the specifications of a given application for the space sector.

7. The seventh chapter contains an overview of all the work and the general conclusions drawn from the work done.

8. Finally, the eight chapter offers a list of future work lines intended to extend the theory and practice developed in each chapter. With these lines of future work we open the possibility to improve both the accuracy and the efficiency of the discussed design approach.

2 COUPLING MATRIX THEORY

2.1 Introduction

The coupling matrix allows us to know the response of a microwave filter which can be represented by a bandpass prototype (BPP) network. Each element of the coupling matrix corresponds to the coupling value between each filter resonator and any other resonator in the filter. This form of representation is particularly useful because operations such as inversion or partitioning can be applied and in this way, for instance, it is easier to obtain the partial responses given by segments of a microwave filter [Cameron et al., 2007].

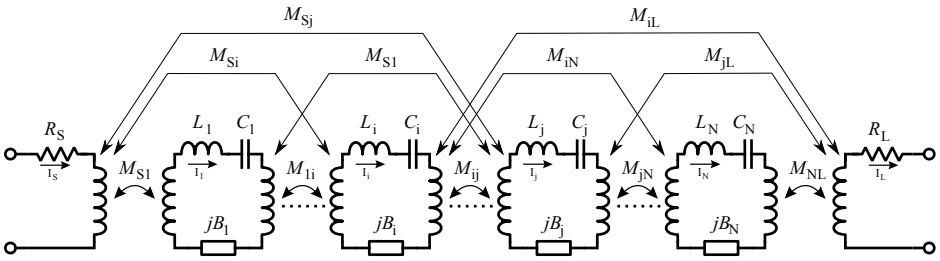

Figure 2.1: Bandpass prototype network of bandpass filter.

In order to understand the coupling matrix formalism it is necessary to review the bandpass and lowpass prototype (BPP and LPP) networks of a bandpass microwave filter [Cameron et al., 2007]. The BPP network is shown in Figure 2.1, where FIR (Frequency Invariant Reactance) elements have been considered in order to model the resonant frequency shifting in asynchronous filters. This circuit consists of cascade-connected series resonators coupled by transformers. Moreover, each i-th resonator is coupled with any j-th resonator by the coupling value given by the elements"M_{ij}" in Figure 2.2.

2.2 Coupling matrix elements meaning

Figure 2.2 shows the most complete coupling matrix topology for a generalized Nth-order filter network. Different coupling elements can be distinguished [Cameron et al., 2007].

1. Coupling elements from M_{S1} to M_{SN} and from M_{1S} to M_{NS} indicate the coupling between the source and each resonator in the network. In a waveguide-implemented filter, these elements refer to the coupling value between the input waveguide and the filter resonators 1 to N.

2. Coupling element from M_{1L} to M_{NL} and from M_{L1} to M_{L1} indicate the coupling between each resonator and the load or between each resonator and the output waveguide in the designed filter.

3. Element in the main diagonal from M_{11} to M_{NN} are not referred to any coupling value but they indicate a change in the resonant frequency of the correspondent resonator. These elements list the values of the FIR elements shown in Figure 2.1 or 2.3 and they are non-zero only in asynchronous filters where at least one resonator have a frequency shift with respect to the center frequency of the filter.

$$M = \begin{bmatrix} M_{SS} & M_{S1} & M_{S2} & \cdots & M_{Si} & \cdots & M_{Sj} & \cdots & M_{SN} & M_{SL} \\ M_{1S} & M_{11} & M_{12} & \cdots & M_{1i} & \cdots & M_{1j} & \cdots & M_{1N} & M_{1L} \\ M_{2S} & M_{21} & M_{22} & \cdots & M_{2i} & \cdots & M_{2j} & \cdots & M_{2N} & M_{2L} \\ \vdots & \vdots & \vdots & \ddots & \vdots & \ddots & \vdots & \ddots & \vdots & \vdots \\ M_{iS} & M_{i1} & M_{i2} & \cdots & M_{ii} & \cdots & M_{ij} & \cdots & M_{iN} & M_{iL} \\ \vdots & \vdots & \vdots & \ddots & \vdots & \ddots & \vdots & \ddots & \vdots & \vdots \\ M_{jS} & M_{j1} & M_{j2} & \cdots & M_{ji} & \cdots & M_{jj} & \cdots & M_{jN} & M_{jL} \\ \vdots & \vdots & \vdots & \ddots & \vdots & \ddots & \vdots & \ddots & \vdots & \vdots \\ M_{NS} & M_{N1} & M_{N2} & \cdots & M_{Ni} & \cdots & M_{Nj} & \cdots & M_{NN} & M_{NL} \\ M_{LS} & M_{L1} & M_{L2} & \cdots & M_{Li} & \cdots & M_{Lj} & \cdots & M_{LN} & M_{LL} \end{bmatrix}$$

Figure 2.2: Couplig matrix for generic filter topology.

4. Elements M_{SL} and M_{LS} are related to the direct input-output coupling.

5. Finally, elements M_{SS} and M_{LL} are always zero because they are related to the source and load in the filter which are non-resonating elements.

2.3 Bandpass to lowpass transformation

The coupling matrix is defined for the lowpass filter prototype (LPP), and its elements are valid only when the LPP is being analyzing. Thus, in order to obtain a bandpass filter response from a coupling matrix it is necessary to map the bandpass frequencies and the bandpass prototype (BPP) to a lowpass domain. Then, the obtained response can be represented in the desired frequency range.

2.3.1 Bandpass to lowpass frequency scaling

The frequency range in the lowpass domain is defined both positive and negative. Then it is necessary to ensure that both positive and negative frequencies defined in the lowpass domain map the right frequencies on the BPP response, in the bandpass domain. The expression for the bandpass-to-lowpass transformation can be written as (2.1) in order to archive the above mentioned requirements [Cameron et al., 2007].

$$\omega_{LP} = \frac{\omega_0}{\omega_2 - \omega_1}\left[\frac{\omega_{BP}}{\omega_0} - \frac{\omega_0}{\omega_{BP}}\right] \tag{2.1}$$

2.3.2 Bandpass to lowpass filter scaling

The coupling element of a coupling matrix are frequency-invariant, then a scaling of the bandpass resonators to lowpass resonators is necessary in order to have a lowpass response. The series resonator of the BPP can be transformed into the lowpass domain in order to obtain the LPP shown in Figure 2.3 by the following steps [Cameron et al., 2007]:

1. Replace all the mutual inductive couplings, provided by transformers, with inverters with the same value as the mutual couplings of the transformers. The inverters then provides the same amount of coupling energy between the resonator nodes as the transformers, and with the same 90° phase change.

2. Transform the bandpass network BPP to a lowpass prototype LPP network with the band edges at $\omega = \pm 1$ by letting the value of the series capacitance go to infinity (zero series impedance) and by scaling the value of the series inductance using the expression of the bandpass resonators slope-parameters X:

$$X_i = \omega_0 L r_i = \frac{1}{\omega_0 C r_i} = \frac{\omega_1'}{\Delta} L_i \qquad k \in \{1, N\} \tag{2.2}$$

where Lr_i and Cr_i are the bandpass resonators elements, L_i the lowpass ones, ω_1' is the -3dB bandwidth of the LPP (usually set $\omega_1' = 1$) and Δ is the filter fractional bandwidth.

$$\Delta = \frac{\omega_2 - \omega_1}{\omega_0} \tag{2.3}$$

Thus, keeping invariant the slope-parameter, the proper value of the LPP inductances can be obtained by

$$L_i = \omega_0 \frac{\Delta}{\omega_1'} Lr_i \qquad k \in \{1, N\} \tag{2.4}$$

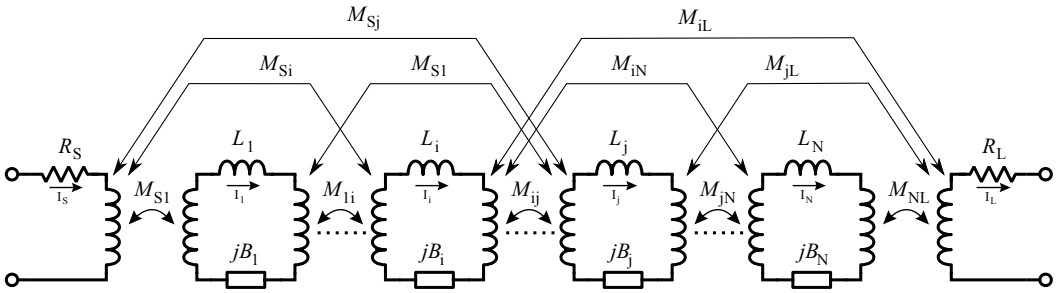

Figure 2.3: Lowpass prototype network of bandpass filter.

Since the coupling elements are frequency-invariant it is possible to think that the analysis in lowpass or bandpass domains yield the response with the same insertion loss and rejection amplitudes independently of the lowpass lumped elements, however, this is only true when the complete filter is being analyzed. This is not valid when analyzing a filter segment as internal inductances may operate as a load. Thus when we are trying to analyze a filter segment, a lumped element scaling is also necessary. This scaling will be reviewed in the next chapter [Martínez et al., 2013].

2.4 Analysis of the network

There are several ways to get the filter response from the coupling matrix [Cameron et al., 2007]. On the one hand, by representing each resonator with its ABCD matrix and on the other hand, the way that is used in this work, considering the filter as a standalone network such the one shown in Figure 2.4. In this Figure it is possible to see the filter network represented by its open-circuit impedance or its short-circuit admitance matrices and also the generator e_g with its internal impedance R_S and the output impedance R_L loading the network.

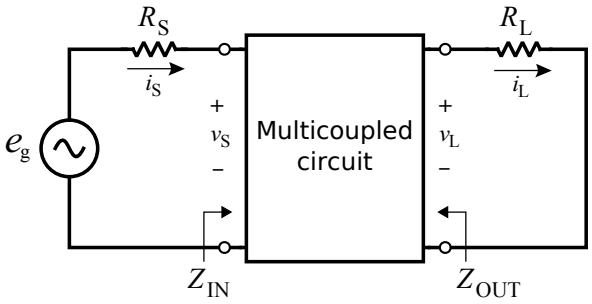

Figure 2.4: Standalone network used to analyze the coupling matrix.

2.4.1 Impedance matrix computation

Considering the LPP in Figure 2.3, the equation (2.5) is obtained by a Kirchoff analysis in the source mesh.

$$e_g = i_S \cdot R_S + i_1 \cdot jM_{S1} + i_2 \cdot jM_{S2} + \cdots + i_L \cdot jM_{SL} \tag{2.5}$$

In any element "k" other than the source or load, a similar expression (2.6) without excitation term is obtained. It should be noted that the kth mesh contains a s-dependent term[1].

$$0 = i_S \cdot jM_{kS} + i_1 \cdot jM_{k1} + i_2 \cdot jM_{k2} + \cdots + i_k \cdot (sL_k + jM_{kk}) + \cdots + 1_L \cdot jM_{iL} \tag{2.6}$$

where the FIR element M_{kk} has been considered in the k-resonator. Finally, the equation (2.7) is obtained for the load mesh.

$$0 = i_S \cdot jM_{LS} + i_1 \cdot jM_{L1} + i_2 \cdot jM_{L2} + \cdots + i_L \cdot R_L \tag{2.7}$$

By rewriting the above equations in matrix form for all resonators, it is obtained the generic analysis expression shown in equation (2.8).

$$\begin{bmatrix} e_g \\ 0 \\ 0 \\ \vdots \\ 0 \\ \vdots \\ 0 \\ 0 \end{bmatrix} = \begin{bmatrix} R_S & jM_{S1} & jM_{S2} & \cdots & jM_{Sk} & \cdots & jM_{SN} & jM_{SL} \\ jM_{1S} & sL_1 + jM_{11} & jM_{12} & \cdots & jM_{1k} & \cdots & jM_{1N} & jM_{1L} \\ jM_{2S} & jM_{21} & sL_2 + jM_{22} & \cdots & jM_{2k} & \cdots & jM_{2N} & jM_{2L} \\ \vdots & \vdots & \vdots & \ddots & \vdots & \ddots & \vdots & \vdots \\ jM_{kS} & jM_{k1} & jM_{k2} & \cdots & sL_k + jM_{kk} & \cdots & jM_{kN} & jM_{kL} \\ \vdots & \vdots & \vdots & \ddots & \vdots & \ddots & \vdots & \vdots \\ jM_{NS} & jM_{N1} & jM_{N2} & \cdots & jM_{Nk} & \cdots & sL_N + jM_{NN} & jM_{NL} \\ jM_{LS} & jM_{L1} & jM_{L2} & \cdots & jM_{Lk} & \cdots & jM_{LN} & R_L \end{bmatrix} \cdot \begin{bmatrix} i_S \\ i_1 \\ i_2 \\ \vdots \\ i_k \\ \vdots \\ i_N \\ i_L \end{bmatrix} \tag{2.8}$$

and by comparing this expression with the equation (2.9) for Figure 2.4 it is possible to obtain general expression (2.11) for matrix $[Z]$.

$$[e_g] = [Z] \cdot [i] \tag{2.9}$$

$$[i] = [Z]^{-1} \cdot [e_g] = [Y] \cdot [e_g] \tag{2.10}$$

$$[Z] = \begin{bmatrix} R_S & 0 & 0 & \cdots & 0 & 0 \\ 0 & sL_1 & 0 & \cdots & 0 & 0 \\ 0 & 0 & sL_2 & \cdots & 0 & 0 \\ \vdots & \vdots & \vdots & \ddots & \vdots & \vdots \\ 0 & 0 & 0 & \cdots & sL_N & 0 \\ 0 & 0 & 0 & \cdots & 0 & R_L \end{bmatrix} + \begin{bmatrix} 0 & jM_{S1} & jM_{S2} & \cdots & jM_{SN} & jM_{SL} \\ jM_{1S} & jM_{11} & jM_{12} & \cdots & jM_{1N} & jM_{1L} \\ jM_{2S} & jM_{21} & jM_{22} & \cdots & jM_{2N} & jM_{2L} \\ \vdots & \vdots & \vdots & \ddots & \vdots & \vdots \\ jM_{NS} & jM_{N1} & jM_{N2} & \cdots & jM_{NN} & jM_{NL} \\ jM_{LS} & jM_{L1} & jM_{L2} & \cdots & jM_{LN} & 0 \end{bmatrix} \tag{2.11}$$

2.4.2 Transmission and reflection coefficients

Firstly, it is necessary to consider the admitance parameters matrix $[Y']$ as well as the impedance parameters matrix $[Z']$. These parameters relate the source mesh with the load mesh as it is shown in the equations (2.12) to (2.13) [Cameron et al., 2007].

$$\begin{bmatrix} i_S \\ i_L \end{bmatrix} = [Y'] \cdot \begin{bmatrix} e_g \\ 0 \end{bmatrix} \tag{2.12}$$

$$\begin{bmatrix} e_g \\ 0 \end{bmatrix} = [Z'] \cdot \begin{bmatrix} i_S \\ i_L \end{bmatrix} \tag{2.13}$$

From Figure 2.4 and given the above relations for the $[Z]$ and $[Y]$ matrix it is quite easy to obtain admitance parameters $[Y']$ and the impedance parameters matrix $[Z']$ [Cameron et al., 2007]. Indeed the admitance and impedance parameters can be defined as:

$$[Y'] = \begin{bmatrix} Y'_{11} & Y'_{12} \\ Y'_{21} & Y'_{22} \end{bmatrix} = \begin{bmatrix} Y_{SS} & Y_{SL} \\ Y_{LS} & Y_{LL} \end{bmatrix} \tag{2.14}$$

$$[Z'] = \begin{bmatrix} Z'_{11} & Z'_{12} \\ Z'_{21} & Z'_{22} \end{bmatrix} = \frac{1}{[Y']} \tag{2.15}$$

Now, it is possible to compute the scattering parameters matrix in a passive network by considering the following expressions:

$$S_{11} = \frac{Z_{IN} - R_S}{Z_{IN} + R_S} \tag{2.16}$$

$$S_{22} = \frac{Z_{OUT} - R_L}{Z_{OUT} + R_L} \tag{2.17}$$

$$S_{21} = S_{12} = 2\sqrt{\frac{R_S}{R_L}} \cdot \frac{v_N}{e_g} \tag{2.18}$$

[1] In this work, the variable s refers to the Laplace complex variable: $s = \sigma + j\omega$ where ω is the real frequency in rad/s. Moreover, in this chapter only the real frequency axis is considered, thus we will assume that $\sigma = 0$.

where Z_{IN} corresponds to the input impedance of the filter network meanwhile Z_{OUT} refers to the output impedance. Then, by relating v_N to i_N from (2.12):

$$i_L = Y'_{21} \cdot e_g = \frac{v_N}{R_L} \tag{2.19}$$

and substituting in (2.18), the expression for the S_{21} coefficient is obtained.

$$S_{21} = 2\sqrt{\frac{R_S}{R_L}} \cdot \frac{v_N}{e_g} = 2\sqrt{\frac{R_S}{R_L}} \cdot R_L Y'_{21} = 2\sqrt{R_S R_L} \cdot Y'_{21} \tag{2.20}$$

Regarding the reflection coefficients S_{11} and S_{22}, the first one can easily be obtained from the input and source impedances. Considering the expression for the filter input impedance Z_{IN}:

$$Z_{IN} = \frac{v_S}{i_S} = \frac{e_g Z_{IN}}{Z_{IN} + R_S} \cdot \frac{1}{e_g Y'_{11}} \tag{2.21}$$

Thus

$$Y'_{11} = \frac{1}{Z_{IN} + R_S} \tag{2.22}$$

where v_S is the voltage in the voltage divider between Z_{IN} and R_S and i_S is obtained from (2.12). Finally, by introducing the expression (2.22) in (2.23), the reflection coefficient at the input port is obtained.

$$S_{11} = \frac{Z_{IN} - R_S}{Z_{IN} + R_S} = \frac{Z_{IN} + R_S - 2R_S}{Z_{IN} + R_S} = 1 - \frac{2R_S}{Z_{IN} + R_S} \tag{2.23}$$

$$S_{11} = 1 - 2R_S Y'_{11} \tag{2.24}$$

Similarly, the reflection coefficient S_{22} is obtained for the output port:

$$S_{22} = 1 - 2R_L Y'_{22} \tag{2.25}$$

2.5 Step by step analysis and coupling matrix segmentation

Step by step design has been presented in [Guglielmi et al., 1991, Guglielmi, 1994] and it involves the filter design process by segmenting the filter structure, what systematically leads to the final design of the complete filter geometry. The advantages of this procedure are both the number of parameters involved in each stage that is quite lower than the number of parameters in the complete filter structure, as well as the fact that the interactions between adjacent elements are considered in each iteration.

2.5.1 Lowpass prototype with impedance inverters

In this section the filter prototypes shown in Figure 2.5 are considered where the meaning of each g-parameters is:

- $g_k|_{k=(1:n)}$ = Inductance of a series coil or the capacitance of a shunt capacitor.
- g_0 = Generator resistance R'_0 if $g_1 = C'_1$ or generator conductance G'_0 if $g_1 = L'_1$.
- g_{n+1} = Load resistance R'_{n+1} if $g_n = C'_n$ or load conductance G'_{n+1} if $g_n = L'_n$.

These filter prototypes give a lowpass response with a bandwidth of ω'_1. Usually, the values of lowpass prototype are normalized to set $g_0 = 1$ and $\omega'_1 = 1$. If it it is desired to get any other bandwidth or impedance level the circuit transformation shown in equations (2.26) to (2.28) can be applied.

$$R = \left(\frac{R_0}{R'_0}\right) R' \quad or \quad G = \left(\frac{G_0}{G'_0}\right) G \tag{2.26}$$

$$L_k = \left(\frac{R_0}{R'_0}\right)\left(\frac{\omega'_1}{\omega_1}\right) L'_k = \left(\frac{G'_0}{G_0}\right)\left(\frac{\omega'_1}{\omega_1}\right) L'_k \tag{2.27}$$

$$C_k = \left(\frac{R'_0}{R_0}\right)\left(\frac{\omega'_1}{\omega_1}\right) C'_k = \left(\frac{G_0}{G'_0}\right)\left(\frac{\omega'_1}{\omega_1}\right) C'_k \tag{2.28}$$

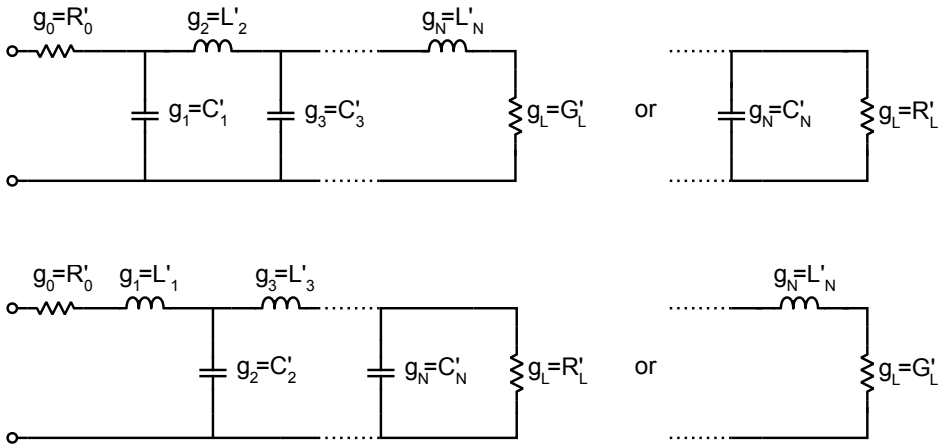

Figure 2.5: Filter prototype with parameters g_ks.

where R'_0, R', G'_0, G', L'_k, C'_k, ω'_1 are the normalized parameters; R, G, L_k, C_k, the scaled ones and R_0, G_0, ω_1 the desired values of impedance and bandwidth.

However since in this work the designed filter will have a bandpass response, the lowpass-to-bandpass transformation will be used in order to obtain the filter response in the desired bandpass domain. These filter prototypes and as well as how to calculate the prototypes parameters can be reviewed in [Matthaei and Yones, 1980].

2.5.1.1 Conversion of filter prototypes to use impedance inverters and inductive elements

In order to perform a step by step analysis it is desirable to convert the LPP shown in Figure 2.5 to its equivalent form which uses only inductive elements and ideal impedance inverters as shown in Figure 2.6. In this way it is possible to obtain the value of the impedance inverters from the coupling matrix. Thus the waveguide filter is better represented and operations such as partitioning can be applied.

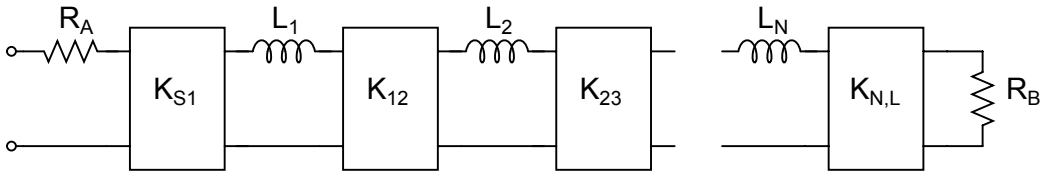

Figure 2.6: Lowpass prototype with inductive elements and impedance inverters.

These ideal impedance inverters (Figure 2.7) operate like a quarte-wavelength line of characteristic impedance K at all frequencies[2]. Thus if it is terminated in a impedance Z_b in one end, the module of input impedance Z_a seen looking in at the other end [Matthaei and Yones, 1980] is expressed as shown in equation (2.29) and the phase suffers a 90 degrees shifting. Equation (2.30).

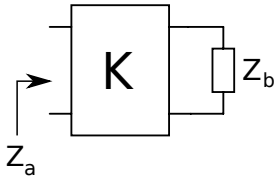

Figure 2.7: Ideal impedance inverter.

$$|Z_a| = \frac{K^2}{|Z_b|} \tag{2.29}$$

[2]This fact will be a drawback in the design of wideband waveguide filters since coupling windows of the waveguide are frequency-dependent. Thus the behavior of the waveguide structure will only be represented accurately in a narrow bandwidth.

$$phase(Z_a) = phase(Z_b) - 90^o \tag{2.30}$$

Then a series inductance in one side of the impedance inverter is seen as a shunt capacitance in the other side and vice versa. Thus by setting the right values of the K inverter it is possible to obtain the same response with the LPPs shown in Figures 2.5 and 2.6 regardless of the values of elements R_A, L_k and R_B [Matthaei and Yones, 1980].

First of all, it is obvious that both circuits in Figure 2.5 are equivalent. Then, by equating the equivalent impedance before each inductance L_k in the corresponding circuit in Figure 2.5 with the impedance seen at the input of L_k inductance in Figure 2.6 the right values of the impedance inverters are obtained.

For the inductance $L'_N = g_N$ (Figure 2.8) [3] the input impedance is

$$Z_{in}(g_n) = sg_N + \frac{1}{g_L} \tag{2.31}$$

and the input impedance for L_N in Figure 2.8 is

$$Z_{in}(L_N) = sL_N + \frac{K^2_{N,L}}{R_B} \tag{2.32}$$

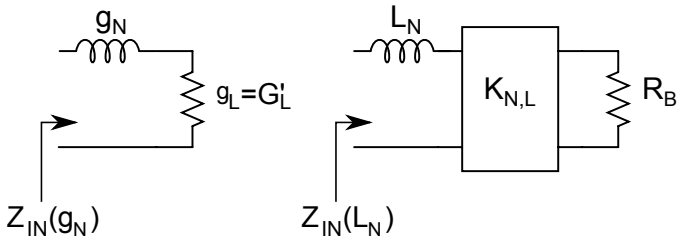

Figure 2.8: Impedance seen looking from inductances g_N and L_N.

It is easy to realize that there is an impedance scale factor between inductances $L'_N = g_N$ and L_N. Considering this scale factor the expression (2.33) is obtained.

$$Z_{in}(L_N) = \frac{L_N}{g_N} Z_{in}(g_n) \tag{2.33}$$

Equating the equations (2.33) and (2.32) and solving for $K_{N,L}$:

$$Z_{in}(L_N) = \frac{L_N}{g_N} Z_{in}(g_n) = sL_N + \frac{L_N}{g_N}\frac{1}{g_L} = sL_N + \frac{K^2_{N,L}}{R_B} \tag{2.34}$$

$$K_{N,L} = \sqrt{\frac{L_N R_B}{g_N g_L}} \tag{2.35}$$

Repeating the analysis for the input impedance of the inductance $L'_{N-1} = g_{N-1}$ in Figure 2.9 the expression (2.36) is obtained meanwhile, the expression (2.37) shows the input impedance for L_{N-1} in Figure 2.9.

$$Z_{in}(g_{N-1}) = sg_{N-1} + \frac{1}{Z_{in}(g_N)} \tag{2.36}$$

$$Z_{in}(L_{N-1}) = sL_{N-1} + \frac{K^2_{N-1,N}}{Z_{in}(L_N)} \tag{2.37}$$

Considering the scale factor shown in (2.33) the expression (2.38) is obtained.

$$Z_{in}(L_N - 1) = \frac{L_{N-1}}{g_{N-1}} Z_{in}(g_{N-1}) \tag{2.38}$$

[3] Inductances in Figure 2.5, 2.8, 2.9, 2.10 or 2.11 has been named with the formalism g_k in order to distinguish it from the inductances in Figure 2.6

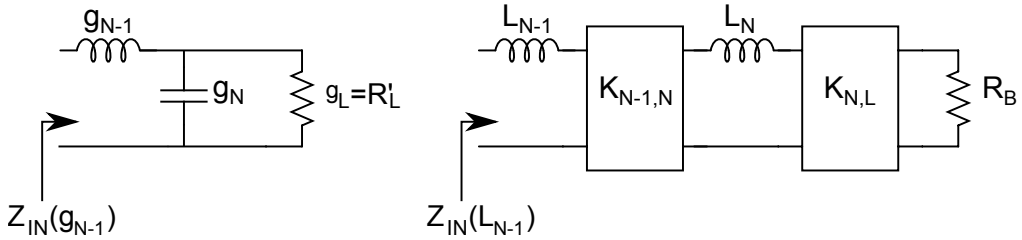

Figure 2.9: Impedance seen looking from inductances g_{N-1} and L_{N-1}.

and by equating the equations (2.38) and (2.37), the following relation between $Z_{in}(L_{N-1})$ and $Z_{in}(g_{N-1})$ is achieved.

$$Z_{in}(L_{N-1}) = \frac{L_{N-1}}{g_{N-1}} Z_{in}(g_{N-1}) = sL_{N-1} + \frac{L_{N-1}}{g_{N-1}} \frac{1}{Z_{in}(g_N)} = sL_N + \frac{K^2_{N-1,N}}{Z_{in}(L_N)} \tag{2.39}$$

Thus the desired expression for the impedance inverter is obtained by solving for $K_{N-1,N}$ and by using (2.33).

$$K_{N-1,N} = \sqrt{\frac{L_{N-1}}{g_{N-1}} \cdot \frac{Z_{in}(L_N)}{Z_{in}(g_N)}} = \sqrt{\frac{L_{N-1}L_N}{g_{N-1}g_N}} \tag{2.40}$$

For the generic $L'_k = g_k$ and L_k input impedance shown in Figure 2.10 it is necessary to perform a similar process.

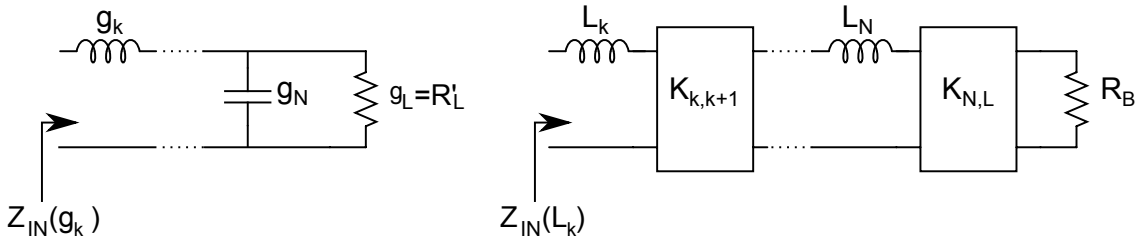

Figure 2.10: Impedance seen looking from inductances g_k and L_k.

$$Z_{in}(g_k) = sg_k + \frac{1}{Z_{in}(g_{k+1})} \tag{2.41}$$

$$Z_{in}(L_k) = sL_k + \frac{K^2_{k,k+1}}{Z_{in}(L_{k+1})} \tag{2.42}$$

Here, the scale factor is:

$$Z_{in}(L_k) = \frac{L_k}{g_k} Z_{in}(g_k) = sL_k + \frac{L_k}{g_k} \frac{1}{Z_{in}(g_{k+1})} = sL_k + \frac{K^2_{k,k+1}}{Z_{in}(L_{k+1})} \tag{2.43}$$

$$Z_{in}(L_{k+1}) = \frac{L_{k+1}}{g_{k+1}} Z_{in}(g_{k+1}) \tag{2.44}$$

Thus solving for $K_{k,k+1}$ using (2.33):

$$K_{k,k+1} = \sqrt{\frac{L_k}{g_k} \cdot \frac{Z_{in}(L_{k+1})}{Z_{in}(g_{k+1})}} = \sqrt{\frac{L_k L_{k+1}}{g_k g_{k+1}}} \tag{2.45}$$

Finally, the input impedance for the complete LPP in (Figure 2.11) is:

$$Z_{in}(g_0) = sg_0 + \frac{1}{Z_{in}(g_1)} \tag{2.46}$$

$$Z_{in}(R_A) = sR_A + \frac{K^2_{k,k+1}}{Z_{in}(L_1)} \tag{2.47}$$

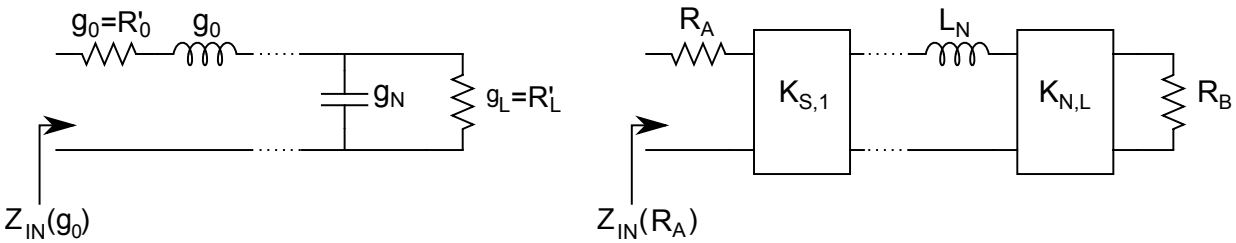

Figure 2.11: Input impedance of LPP with g_k values and LPP with inductances and impedance inverters.

Both input impedances will be the same except for a possible impedance scale factor namely:

$$Z_{in}(R_A) = \frac{R_A}{g_0} Z_{in}(g_0) \tag{2.48}$$

Equating (2.48) and (2.47) and solving for $K_{S,1}$ the final expression for the input impedance inverter is obtained as shown in (2.51).

$$Z_{in}(R_A) = R_A + \frac{R_A}{g_0} \frac{1}{Z_{in}(g_1)} = R_A + \frac{K_{S,1}^2}{Z_{in}(L_1)} \tag{2.49}$$

$$Z_{in}(L_1) = \frac{L_1}{g_1} Z_{in}(g_1) \tag{2.50}$$

$$K_{S,1} = \sqrt{\frac{R_A L_1}{g_0 g_1}} \tag{2.51}$$

In summary, by equating the input impedance in each segment of the filter prototypes in Figures 2.5 and 2.6 the following expressions for the impedance inverters are achieved in order to obtain the same response with both filter prototypes [Matthaei and Yones, 1980].

$$K_{S,1} = \sqrt{\frac{R_A L_1}{g_0 g_1}} \tag{2.52}$$

$$K_{k,k+1} = \sqrt{\frac{L_k L_{k+1}}{g_k g_{k+1}}} \quad k \in [1, N-1] \tag{2.53}$$

$$K_{N,L} = \sqrt{\frac{L_N R_B}{g_N g_L}} \tag{2.54}$$

2.5.2 Step by step design technique

Once the LPP with impedance inverters and inductances has been obtained the step-by-step analysis [Guglielmi and Melcon, 1993, Guglielmi, 1994] can be performed. This design technique consists in the filter design by segmenting the filter structure in a step-by-step fashion. In each step only one filter segment is added to the filter structure and then it is optimized. In this way there is a small number of parameters to optimize. Performing systematically each design step the final filter geometry is achieved.

Moreover in the classical waveguide filter design, the coupling windows and resonators are designed separately and when they are put together, interactions between adjacent elements appear that modify the total filter response and readjusting the filter dimensions may be required. The main advantage of of the step by step design procedure is that in each step the interactions between adjacent elements are considered, thus a better and more accuracy result is obtained. Moreover since there are only a few parameters to optimize in each step the optimization is quite fast and the final result is accomplished in a simple way.

2.5.2.1 Design procedure

The first design step is to get a right transfer function (S_{21} parameter) which fulfills the desired electrical specifications in order to use it as a goal to perform the adjustment of the filter parameters. In the mentioned step-by-step design, the key tasks are:

1. Getting the theoretical partial responses of the first filter segment by computing the S_{21} parameter after the first impedance inverter in Figure 2.6.

2. Using a full wave simulator, the first coupling windows of the desired filter in a doubly terminated configuration is optimized to fit the S_{21} parameter obtained in the previous task. In this optimization it is only necessary to adjust the first coupling window.

3. Once the dimensions of the first coupling window are obtained, the first filter cavity and second window are added to the structure. Then this cavity and window are optimized in order to get the S_{21} parameter given by the LPP in Figure 2.6 after the second impedance inverter. In this step, only the parameters of the filter segment which have been added are adjusted. However since the load of the previous segment has been changed it may be necessary a small adjustment of the previous segment. This adjustment is quite fast as the dimensions of previous segment obtained in the previous step are quite close to the final values.

4. Next, the following filter segment is added and the previous task is repeated until the dimensions of the complete filter are extracted.

2.5.3 Coupling matrix scaling

The above design procedure has been developed in [Guglielmi and Melcon, 1993, Guglielmi, 1994] for in-line filters. In this work, the step-by-step design technique has been adapted to the coupling matrix formalism. The aim is to be able to obtain the partial filter responses by segmenting the filter coupling matrix and by analyzing each matrix segment as if it was a complete coupling matrix. In that way it is possible to use this technique for the design of more complex microwave filters whose topology are represented by the coupling matrix. For instance, if it is desired to design a filter with transmission zeros, the in-line topology can not be used because coupling between non-adjacent elements will be required.

However, when it comes to get the partial responses from the coupling matrix a difficulty appears. It is known that coupling matrix gives the total response of a given filter with source and load impedances scaled to unity, but if a coupling matrix segment is needed, the response obtained directly from the coupling matrix will be incorrect because internal matrix coupling elements can not be analyze as a load coupling elements. In this case, a coupling matrix scaling is necessary in order to be able to segment the coupling matrix and to obtain the right partial responses.

For that, it is necessary to notice that the coupling matrix elements can be written as :

$$M_{i,j} = \frac{1}{\sqrt{g_i g_j}} \tag{2.55}$$

where $g_k s$ are the filter prototype parameters shows in Figure 2.5 [Matthaei and Yones, 1980].

With this definition of the coupling elements, the LPP from Figure 2.6 is quite similar to the LPP used to get coupling matrix response which is redefined in Figure 2.12.

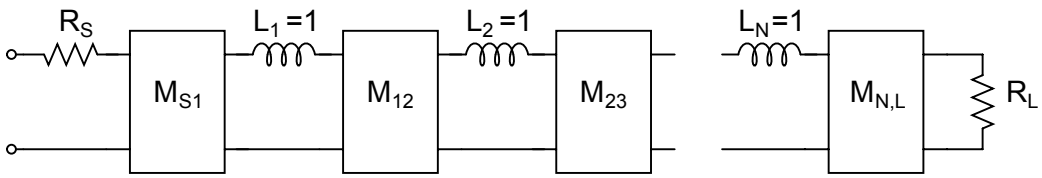

Figure 2.12: Redefinition of the LPP with coupling elements.

It can be proven that the use of impedance inverters values or coupling values is equivalent when all lumped component of LPP have unit values. However if the inductances values L_i are scaled, it is necessary to scale the impedance inverters K_{ij} as well. Then the same response is obtained. The issue is that since the scaling of the lumped elements is arbitrary when the complete matrix is analyzed, the total response can be obtained with all elements scaled to unity. As a result the impedance inverters K_{ij} become the coupling elements M_{ij}.

Nevertheless, in order to obtain the partial filter responses, it is no longer possible to apply any scaling, but the actual scaling with the technology that will be used to design the filter. Thus, it

is necessary to use the real inductance value according to the physical filter structure in which the filter will be implemented and also, the coupling matrix must be scaled in order to obtain the same behavior as with the LPP with impedance inverters in the low-pass domain.

Given the expressions (2.35), (2.40) and (2.51) for the band-pass impedance inverters and the expression (2.55) for the low-pass normalized coupling elements, a scaled coupling matrix can be defined as follow:

$$M'^2_{Sj} = R_S L_j M^2_{S,j} \qquad j \in \{1, N\} \tag{2.56}$$

$$M'^2_{i,i+1} = L_i L_{i+1} M^2_{i,i+1} \qquad i, j \in \{1, N\} \tag{2.57}$$

$$M'^2_{i,L} = L_i R_L M^2_{i,L} \qquad i \in \{1, N\} \tag{2.58}$$

In order to perform this scaling, the lumped elements of the LPP can not be obtained from the real filter structure as it implements a band-pass filter. Thus it is necessary to calculate the lumped elements of the BPP from the filter structure first and use the "band-pass to low-pass" transformation to obtain the required lumped elements in the lowpass domain. Introducing the expression (2.4) in the above expressions:

$$M'^2_{Sj} = R_S L_j M^2_{S,j} = \omega_0 \Delta R_S L r_j M^2_{S,j} \qquad j \in \{1, N\} \tag{2.59}$$

$$M'^2_{i,i+1} = L_i L_{i+1} M^2_{i,i+1} = (\omega_0 \Delta)^2 L r_i L r_{i+1} M^2_{i,i+1} \qquad i, j \in \{1, N\} \tag{2.60}$$

$$M'^2_{i,L} = L_i R_L M^2_{i,L} = \omega_0 \Delta L r_i R_S M^2_{i,L} \qquad i \in \{1, N\} \tag{2.61}$$

where R_S and R_L are the filter input and output impedance, the LPP bandwidth ω'_1 is been set to 1 as usual and the inductances of the BPP Lr_i are obtained from the equivalent inductance of a real resonator. In our case, these inductances will be computed by using rectangular waveguide resonators operating in the TE_{10} mode, as we will use waveguide technology to implement the filters.

2.5.4 Computing the inductances of the bandpass prototype

In order to get right partial responses from the coupling matrix, it has to be scaled with the physical inductances of the band-pass filter in the technology in which it will be implemented. Figure 2.13 shows a real waveguide resonator modeled as a half wavelength transmission line and its equivalent LC circuit where Lr_i and Cr_i are the inductances and capacitances of the i-resonator equivalent circuit. In addition Z_{IN_i} is the input impedance of the i-th resonator of the BPP[4] and $Z_{IN_{i_{eq}}}$ the input impedance for the equivalent circuit [Martínez et al., 2013].

The aim is to get the values of the lumped elements in Figure 2.13 that provide the same slope parameter and resonant frequency as the transmission line in Figure 2.13. Since both circuits resonate at the same frequency, by equating the input impedances Z_{IN_i} and $Z_{IN_{i_{eq}}}$ at other frequency, for instance the upper cut-off frequency it is possible to get the expression for the inductances in equation 2.64 that represent a good approximation. Consequently, the expression to extract the proper inductances of the BPP is obtained by imposing two conditions:

1. Both circuit resonate at the same frequency.
2. The input impedances are equated at a second frequency point. Then both circuits will provide the same slope parameter in a given frequency range.

Input impedances from Figure 2.13 are

$$Z_{IN_i} = j \frac{\omega \mu_0}{\beta} tan\,(\beta l) \tag{2.62}$$

$$Z_{IN_{I_{eq}}} = j \frac{1}{\omega_0 C r_i} \left(\frac{\omega}{\omega_0} - \frac{\omega_0}{\omega} \right) = j \omega_0 L r_i \left(\frac{\omega}{\omega_0} - \frac{\omega_0}{\omega} \right) \tag{2.63}$$

Equating both expressions and solving, the inductance of the lumped resonators Lr_i is obtained.

$$Lr_i = \frac{\omega_{C_2} \mu_0}{\beta_i} tan \left(\beta_i \frac{\lambda_g}{2} \right) \frac{1}{\omega_0 \left(\frac{\omega_{C_2}}{\omega_0} - \frac{\omega_0}{\omega_{C_2}} \right)} \tag{2.64}$$

[4] To obtain Z_{IN_i} it is necessary to consider the impedance of the desired TE mode which is propagating through the waveguide. For dual mode resonators computing the input impedance for each resonating mode will be necessary in order to get the coupling value or transmission value for each desired mode.

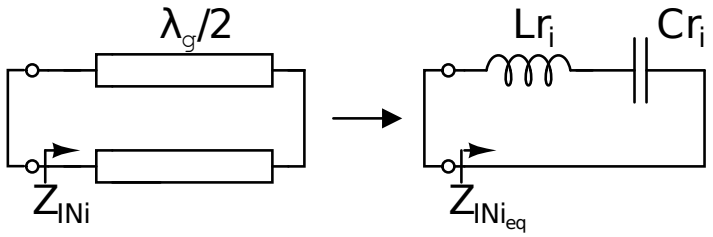

Figure 2.13: Equivalent series circuit to the waveguide resonator.

The above calculation has been performed for the upper cut-off frequency ω_{C_2} because at this frequency waveguide resonator and LC have an inductive behavior. Similarly, the capacitive element Cr_i of the series resonator could be obtained by using other frequency below the center frequency such as the lower cut-off frequency ω_{C_1}.

Since the transmission line resonator in Figure 2.13 has a dispersive behavior, both slope parameters can not be fitted perfectly. However equating the input impedance of both resonators at two frequencies, namely f_0 and the upper cut-off frequency fc_2, it is possible to get a quite small error within the whole filter bandpass as long as the filter bandwidth is small enough as shown in Figure 2.14a. Moreover, when considering wideband filters, this scaling is still useful, in spite of the poorer matching between the input impedance of the transmission line resonator and the input impedance of the resonator with lumped elements (Figure 2.14b).

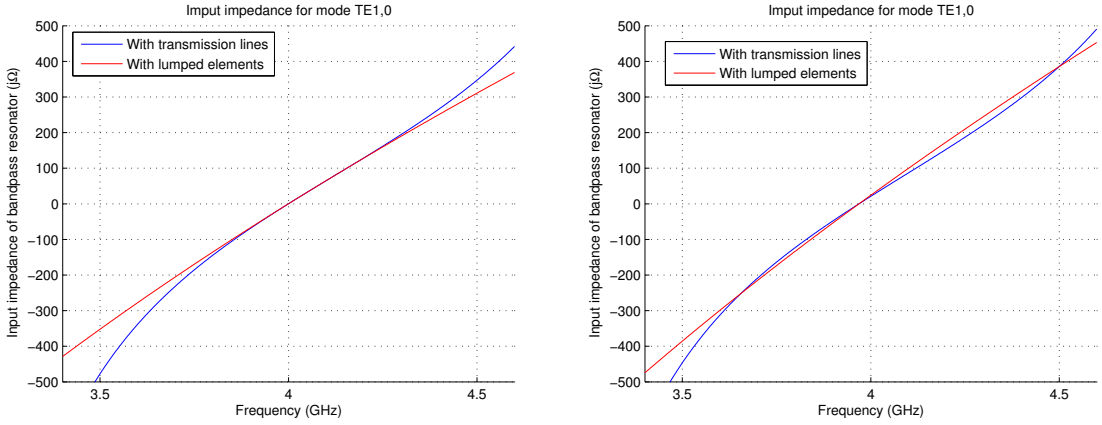

(a) Bandwidth of 100 MHz ($\Delta = 2.5\%$).

(b) Bandwidth of 1 GHz ($\Delta = 25\%$).

Figure 2.14: Comparison between the input impedance of both circuits in Figure 2.13 with different fractional bandwidths (Δ).

It should be noted that the slope parameter of each circuit shown in Figure 2.13 can also be obtained by differentiating the expression (2.65) of the input impedance of the resonator [Matthaei and Yones, 1980]. However if we would use, instead, the expression for the slope parameter shown in equation (2.65) , it could be possible to fit perfectly the slope parameter at $f = f_0$, however the dispersive behavior would be more noticeable at the edges of the passband and the result would be worse for larger bandwidths.

$$X = \frac{\partial Z_{IN}}{\partial \omega} \tag{2.65}$$

Thus, having two resonators that resonate at f_0 and by equating the input impedances at the upper cut-off frequency fc_2, it is possible to get the values of the lumped elements of the BPP that provide the right slope parameters. Finally the values of the inductances of the LPP are obtained by applying the bandpass-to-lowpass transformation.

2.6 Conclusions

In this chapter the coupling matrix theory has been reviewed as well as the low-pass and band-pass prototypes and the transformations lowpass-to-bandpass and bandpass-to-lowpass between them.

Moreover, it has been done for the first time a scaling of the coupling matrix, in the context of the step-by-step design technique, by scaling the lumped element of the LPP. Thus, each resonator of the scaled LPP provides the same slope parameter as the desired waveguide resonator in a given bandwidth. In this way, if the coupling matrix is segmented, each segment will provide the same response as the corresponding segment of the filter structure.

3 INDUCTIVE IN-LINE FILTERS DESIGN

3.1 Introduction

The step-by step design technique is based on the filter design by segmenting the filter structure in a step-by-step fashion. This technique was proposed in [Guglielmi and Melcon, 1993, Guglielmi, 1994] for in-line filters in which there is coupling only between adjacent resonators. This kind of filters are quite easy to optimize by an step-by-step procedure since in each step only one resonator is optimized and there is only one resonant mode in it. Moreover the number of parameters to be optimized in each step is very small and and their final values are too similar to the values obtained in the previous step for the parameters of the previous segment .

In this chapter, the proposed design method is adapted to the coupling matrix formalism and several in-line filters have been designed to validate the theory presented in this chapter and the step-by-step design procedure detailed in the previous chapter [Martínez et al., 2013]. As a result, through the generalization of the step-by-step technique to the coupling matrix formalism, we open the possibility to use this procedure in the design of filters with alternative topologies more complex than the in-line topology.

3.2 Coupling matrix topology for in-line filters

The coupling matrix for in-line filters is shown in Figure 3.1 where there is coupling only between resonator i and i+1. Thus only the coupling values with the form:

$$M_{i,i+1} \quad or \quad M_{i+1,i} \qquad i \in \{1, N\} \tag{3.1}$$

and coupling elements M_{S1}, M_{1S}, M_{NL} and M_{LN} are non-zero.

$$M = \begin{bmatrix} 0 & M_{S1} & 0 & 0 & \cdots & 0 & 0 \\ M_{1S} & M_{11} & M_{12} & 0 & \cdots & 0 & 0 \\ 0 & M_{21} & M_{22} & M_{23} & \cdots & 0 & 0 \\ 0 & 0 & M_{32} & M_{33} & \cdots & 0 & 0 \\ \vdots & \vdots & \vdots & \vdots & \ddots & \vdots & \vdots \\ 0 & 0 & 0 & 0 & \cdots & M_{NN} & M_{NL} \\ 0 & 0 & 0 & 0 & \cdots & M_{LN} & 0 \end{bmatrix}$$

Figure 3.1: Coupling matrix topology for in-line filters.

Moreover elements from main diagonal different from M_{SS} or M_{LL} can be non-zero only for asynchronous filters where not all the resonators are tuned to the center frequency. As it is explained in the previous chapters, these elements are related to FIR elements in asynchronous filters.

All coupling matrices presented in this chapter have been obtained from the desired Chebyshev response. The synthesis of the Chebyshev response is briefly reviewed in the appendix A and it is discussed with more detail in [Cameron et al., 2007, Mendoza, 2006]. Similarly the synthesis of the coupling matrix for these filters is reviewed in [Cameron et al., 2007, Mendoza, 2006].

3.3 Filter design

In-line filters designed in this chapter have the structure shown in Figure 3.2. Standard waveguide WR-229/R-40 (width $A_{WG} = 58.17\ mm$ and height $B_{WG} = 29.083\ mm$) has been used for the input and output ports and all resonant cavities have the same width and height as the input and output waveguide. Also all coupling windows are inductive and its thickness is always set to 2 mm.

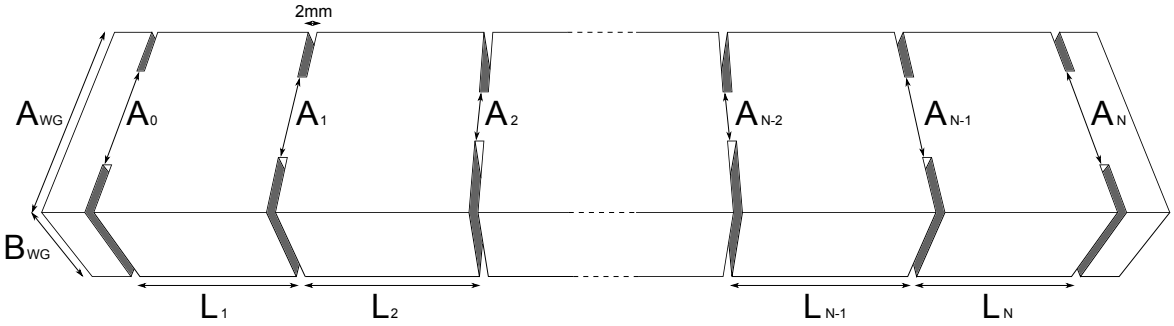

Figure 3.2: In-line filters structure with the parameters definition used in this chapter.

3.3.1 Design of odd order (N) filters

As an example, fifth-order in-line filter ($N = 5$) have been designed. Desired response is centered in C-band at 4 GHz, it have a bandwidth of 150 MHz and a refection level in the passband of $-20\ dB$. The coupling matrix in Figure 3.3 gives this desired response. As it is known, this coupling matrix is related to an in-line filter because only the coupling values between adjacent elements is non-zero.

$$M = \begin{bmatrix} 0 & 1.0137 & 0 & 0 & 0 & 0 & 0 \\ 1.0137 & 0 & 0.8653 & 0 & 0 & 0 & 0 \\ 0 & 0.8653 & 0 & 0.6357 & 0 & 0 & 0 \\ 0 & 0 & 0.6357 & 0 & 0.6357 & 0 & 0 \\ 0 & 0 & 0 & 0.6357 & 0 & 0.8653 & 0 \\ 0 & 0 & 0 & 0 & 0.8653 & 0 & 1.0137 \\ 0 & 0 & 0 & 0 & 0 & 1.0137 & 0 \end{bmatrix}$$

Figure 3.3: Coupling matrix which gives the desired fifth-order response.

This coupling matrix has to be scaled with the input and output impedance and the equivalent inductances of the waveguide structure in which the filter will be implemented. In order to apply equation (2.64) it is necessary to get the propagation constant at $f = f_0$ where f_0 is the center frequency of the filter. It can be noticed that all resonant cavities as well as the input and output waveguide have the same width. Then, only the mode TE_{10} can be excited in each cavity. As a result, every resonant cavity will exhibit the same propagation constant (β). This propagation constant is obtained by the equations (3.2) and (3.3).

$$\beta c_2 = \sqrt{kc_2^2 - k_c^2} = \sqrt{\left(\frac{\omega c_2}{c_0}\right)^2 - \left(\frac{\pi m}{A_{WG}} + \frac{\pi n}{B_{WG}}\right)^2} = 66.1616\ rad/s \tag{3.2}$$

$$\beta_0 = \sqrt{k_0^2 - k_c^2} = \sqrt{\left(\frac{\omega_0}{c_0}\right)^2 - \left(\frac{\pi m}{A_{WG}} + \frac{\pi n}{B_{WG}}\right)^2} = 64.1197\ rad/s \tag{3.3}$$

where βc_2, kc_2, and ωc_2 are referred to the upper cut-off frequency $fc_2 = 4.05GHz$ and β_0, k_0, ω_0 to the central frequency $fc = 4GHz$. Parameters A_{WG} and B_{WG} are the standard waveguide dimensions and m, n the TE_{10} mode index (therefore m=1, n=0).

Thus, the values of R_S, R_L and inductances from 1 to N are

$$R_S = \frac{\omega_0 \mu_0}{\beta_0} = 492.5587\ \Omega \tag{3.4}$$

$$L_i = \omega_0 \Delta L r_i = \omega_0 \Delta \frac{\omega c_2 \mu_0}{\beta c_2} \tan(\beta c_2 \lambda_g/2) \frac{1}{\omega_0 \left(\frac{\omega c_2}{\omega_0} - \frac{\omega_0}{\omega c_2}\right)} = 49.2693\ H \qquad i \in \{1, N\} \tag{3.5}$$

$$R_L = \frac{\omega_0 \mu_0}{\beta_0} = 492.5587\ \Omega \tag{3.6}$$

where $\lambda_g = \frac{2\pi}{\beta_0}$.

The scaled matrix (M') in Figure 3.4 has been obtained by scaling the original coupling matrix in Figure 3.3 with R_S, R_L and L_i values as it is explained in previous chapter.

$$M'_{S,1} = \sqrt{R_S L_1} M_{S,1} \tag{3.7}$$

$$M'_{i,i+1} = \sqrt{L_i L_{i+1}} M_{S,1} \qquad i \in \{1, N-1\} \tag{3.8}$$

$$M'_{N,L} = \sqrt{L_N R_L} M_{S,1} \tag{3.9}$$

$$M' = \begin{bmatrix} 0 & 157.9116 & 0 & 0 & 0 & 0 & 0 \\ 157.9116 & 0 & 42.6336 & 0 & 0 & 0 & 0 \\ 0 & 42.6336 & 0 & 31.3211 & 0 & 0 & 0 \\ 0 & 0 & 31.3211 & 0 & 31.3211 & 0 & 0 \\ 0 & 0 & 0 & 31.3211 & 0 & 42.6336 & 0 \\ 0 & 0 & 0 & 0 & 42.6336 & 0 & 157.9116 \\ 0 & 0 & 0 & 0 & 0 & 157.9116 & 0 \end{bmatrix}$$

Figure 3.4: Scaled coupling matrix of the designed fifth-order filter.

Firs task before starting the filter design is to get the partial responses as it is explained in previous chapter by segmenting the scaled coupling matrix of Figure 3.4. Once partials responses have been calculated by segmenting the filter coupling matrix, the filter structure can be dimensioned easily by a set of $N + 1$ steps.

- **Step 1:** In the first step, the width of the first coupling windows (A_0) is optimized to obtain the same response with the filter segment shown in Figure 3.5 as the response given by the first coupling matrix segment (Figure 3.6).

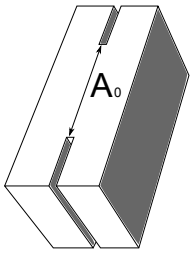

Figure 3.5: First segment of the filter structure. It is composed of only the first iris.

$$M'_1 = \begin{bmatrix} 0 & 138.3946 \\ 138.3946 & 0 \end{bmatrix}$$

Figure 3.6: First segment of the fifth-order scaled coupling matrix.

In this step there is only one parameters to optimize and the transmission response is quite simple. Thus by adjusting the structure in Figure 3.5 with a full-wave simulator it is almost immediate to obtain the width of first iris A_0. This value gives the required coupling specified by the matrix in Figure 3.6.

This parameter A_0 is related to the filter bandwidth. When the filter bandwidth increases, so does the width of the input/output coupling windows. Due to this, although in filters with a narrow bandwidth all coupling windows have a similar size, in wideband filters, the input and

output iris can be much wider meanwhile all other windows keep still a substantially smaller width.

After optimizing, the value of A_0 shown in Table 3.1 is achieved and the comparison between the transmission response given by the coupling matrix segment and by the first filter segment after optimizing is shown in Figure 3.7. It can be noted that this response only fits perfectly the theoretical partial response at the central frequency f_0. This is due to the dispersive behavior of the waveguide technology.

Parameter	Value (mm)
A_0	25.396

Table 3.1: Result of the optimized fifth-order filter parameters in step 1.

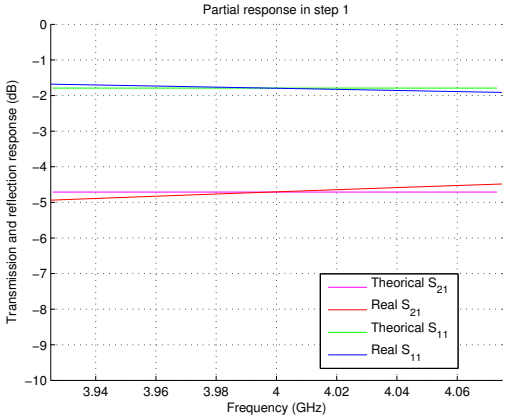

Figure 3.7: Comparison between the response given by the coupling matrix and by the filter segment in the step 1 of a fifth-order filter.

- **Step 2:** Once the optimum value of parameter A_0 is achieved, the second segment of filter structure is added. Then, only the parameters of this segment are optimized to obtain the response given by the second segment of the coupling matrix (Figure 3.8).

$$M_2' = \begin{bmatrix} 0 & 138.3946 & 0 \\ 138.3946 & 0 & 29.9395 \\ 0 & 29.9395 & 0 \end{bmatrix}$$

Figure 3.8: Second segment of the fifth-order filter scaled coupling matrix.

Adding the second filter segment, the structure shown in Figure 3.9 is obtained. In this case, due to the fact that the input and output aperture can be quite larger than the internal irises, specially for filters with large bandwidths, as previously discussed, the value of the parameter A_0 is not a good initial point for A_1. Nevertheless, since the structure in this step and its response are quite simple, the filter parameters can be manually modified in order to make its value closer to the final value and then the optimization will be faster. The cavity length must be shorter to increase resonant frequency and the iris width must be smaller to decrease coupling value taking into account that decreasing the iris width will also increase the resonant frequency.

With the values listed in Table 3.2, this filter segment gives the response shown in Figure 3.10a that is very close to the ideal response. Thus, by performing a final optimization of the parameter L_1 and A_1 the response in Figure 3.10b is obtained. It can be noticed that the obtained width for the second iris ($A1 = 14.327\ mm$) is too far from the value ($A_0 =$) obtained in the previous step.

- **Step 3:** The third coupling matrix segment is shown in Figure 3.11 and the structure of the filter segment as well as the unknown parameters in this step are shown in Figure 3.12.

With the initial parameters in Table 3.3 taken from the obtained parameters in the previous step, this structure gives the response in Figure 3.13a and by adjusting the parameters A_3 and L_3 the response in Figure 3.13b is achieved in a few seconds.

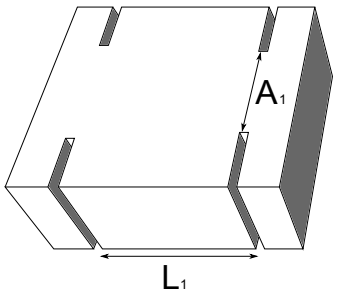

Figure 3.9: Second segment of the filter structure.

Parameter	Manual-adjusted value (mm)	Optimized value (mm)
L_1	43	42.715
A_1	13	14.327

Table 3.2: Obtained dimensions of the fifth-order filter parameters in step 2.

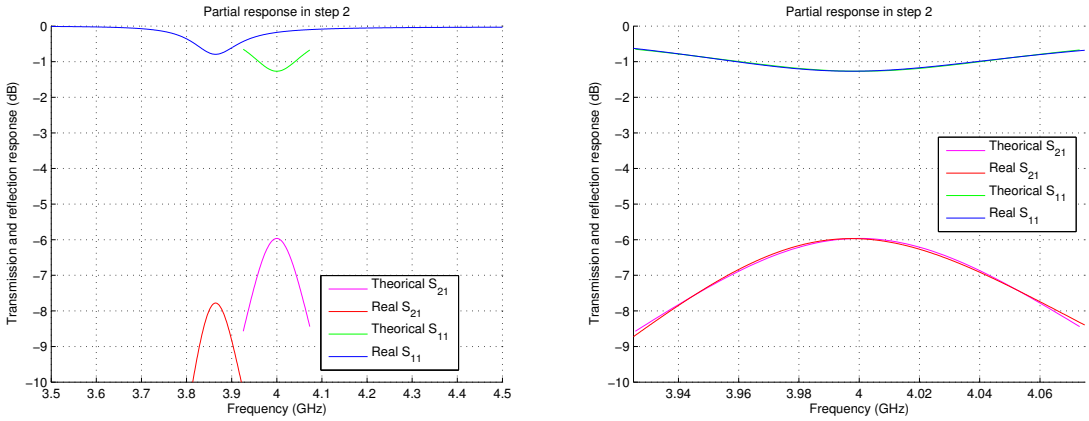

(a) Response before optimization (manually adjustements). (b) After optimization.

Figure 3.10: Given response in step 2 by the fifth-order filter segment.

$$M_3' = \begin{bmatrix} 0 & 138.3946 & 0 & 0 \\ 138.3946 & 0 & 29.9395 & 0 \\ 0 & 29.9395 & 0 & 20.4282 \\ 0 & 0 & 20.4282 & 0 \end{bmatrix}$$

Figure 3.11: Third segment of scaled coupling matrix.

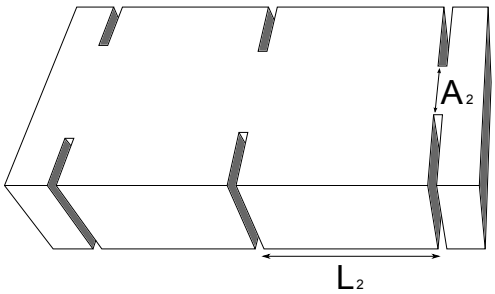

Figure 3.12: Third segment of the fifth-order filter structure.

Parameter	Initial value (mm)	Optimized value (mm)
L_2	42.715	46.751
A_2	14.327	12.637

Table 3.3: Relevant geometrical parameters for the fifth-order filter in step 3.

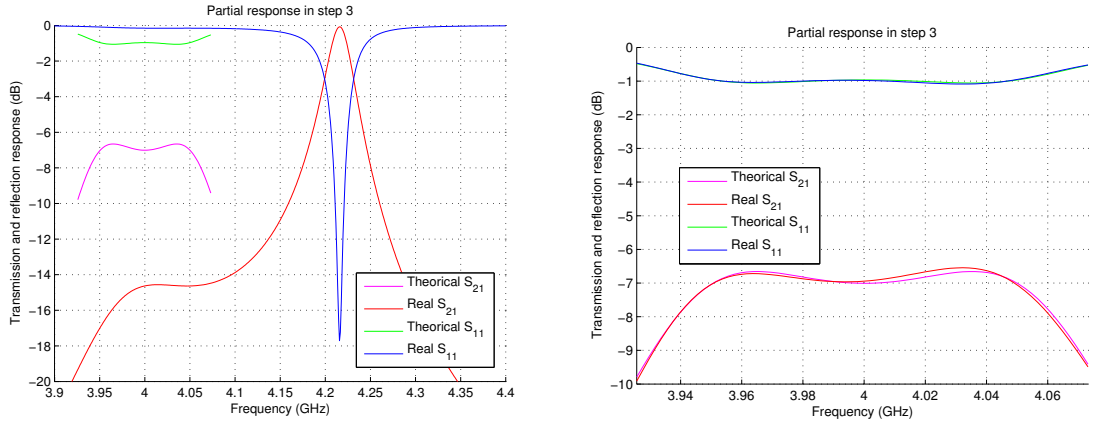

(a) Before optimization.

(b) After optimization.

Figure 3.13: Given response in step 3 for the fifth-order filter segment.

Parameter	Initial value (mm)	Optimized value (mm)
L_3	46.751	47.203
A_3	12.637	12.249

Table 3.4: Result of the fifth-order filter parameters in the step 4.

- **Step 4:** Figure 3.14 shows the fourth segment of the coupling matrix and Figure 3.15 shows the parameters adjusted in this step.

  It should be noted that when the parameters of the structure which is been adjusted are closer to the middle of the filter, its dimensions are more similar to the ones obtained in the previous step. Thus, if the initial parameters are taken from the parameters obtained in the previous step, the optimization is faster.

  In order to validate this assumption, it can be observed that the initial response in Figure 3.16a is closer to the target than the previous ones. Also the final parameter values are closer to their initial values as it is shown in Table 3.4. Indeed, the response in Figure 3.16b is obtained by slightly adjusting the parameters L_3 and A_3.

$$M_4' = \begin{bmatrix} 0 & 138.3946 & 0 & 0 & 0 \\ 138.3946 & 0 & 29.9395 & 0 & 0 \\ 0 & 29.9395 & 0 & 20.4282 & 0 \\ 0 & 0 & 20.4282 & 0 & 18.8053 \\ 0 & 0 & 0 & 18.8053 & 0 \end{bmatrix}$$

Figure 3.14: Fourth segment of the fifth-order filter scaled coupling matrix.

- **Step 5:** Table 3.5 lists the dimensions obtained in this step for the parameters shown in Figure 3.17. In addition, the responses given by the coupling matrix segment in Figure 3.18 and by the correspondent filter segment are shown in Figures 3.19a and 3.19b.

  As in previous steps, the obtained parameters in the last step have been taken as initial point. However in the final steps, as well as in the first steps, the change of the parameters in adjacent steps is greater than in the central ones. Due to this, and taking into account that the filter is symmetric[1], the dimensions of the correspondent cavity in the beginning of the filter could be a better initial point than the dimensions of the previous cavity in order to optimize the last steps of a symmetrical filter.

  In addition, it is important to note that this step affects the second half of the filter and the target responses in the second half of the filter are more complex. As a result, the design would have been easier if the second half of the filter is started from the end of the filter instead of from the beginning.

[1]The frequency response of symmetrical filters will be symmetric with symmetry axis in the center frequency. Its structure will be also symmetric. That is the reason why the dimensions of the first cavity are the same as the last cavity ones, the second cavity is the same as the second to last, etc.

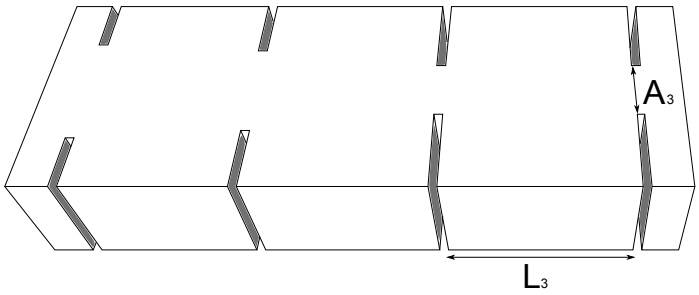

Figure 3.15: Fourth segment of the filter structure.

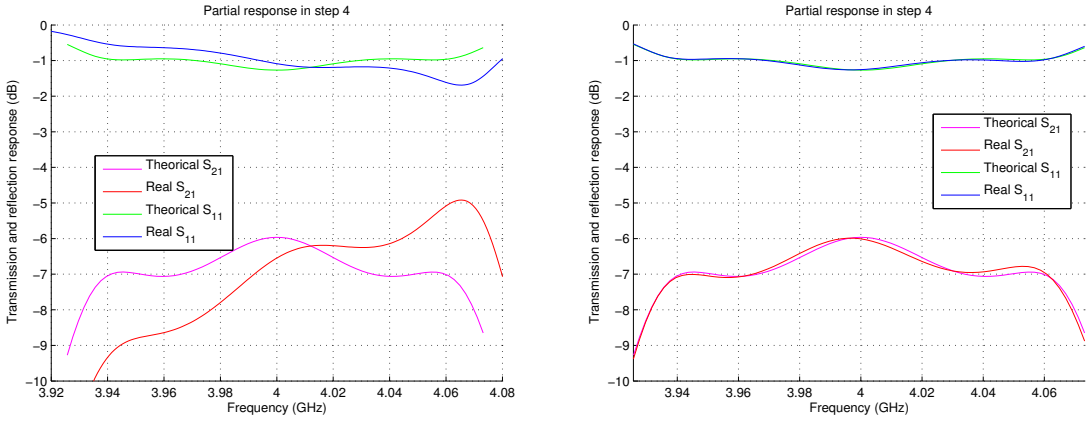

(a) Before optimization.

(b) After optimization.

Figure 3.16: Given response in the step 4 by the fifth-order filter segment.

Parameter	Initial value (mm)	Optimized value (mm)
L_3	47.203	47.278
A_3	12.249	12.165

Table 3.5: Result of the fifth-order filter parameters in step 5.

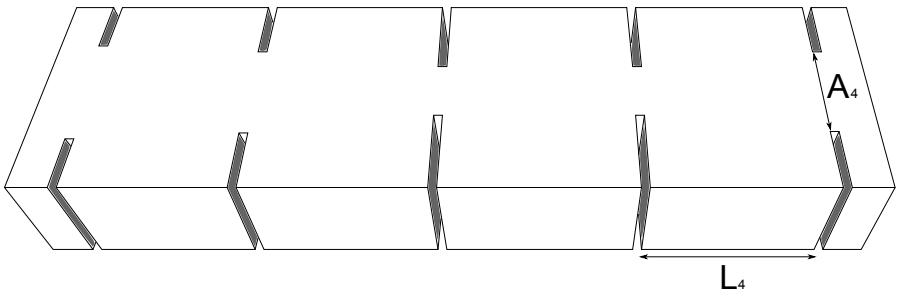

Figure 3.17: Fifth segment of the filter structure.

$$M_5' = \begin{bmatrix} 0 & 138.3946 & 0 & 0 & 0 & 0 \\ 138.3946 & 0 & 29.9395 & 0 & 0 & 0 \\ 0 & 29.9395 & 0 & 20.4282 & 0 & 0 \\ 0 & 0 & 20.4282 & 0 & 18.8053 & 0 \\ 0 & 0 & 0 & 18.8053 & 0 & 18.4655 \\ 0 & 0 & 0 & 0 & 18.4655 & 0 \end{bmatrix}$$

Figure 3.18: Fifth segment of the fifth-order filter scaled coupling matrix.

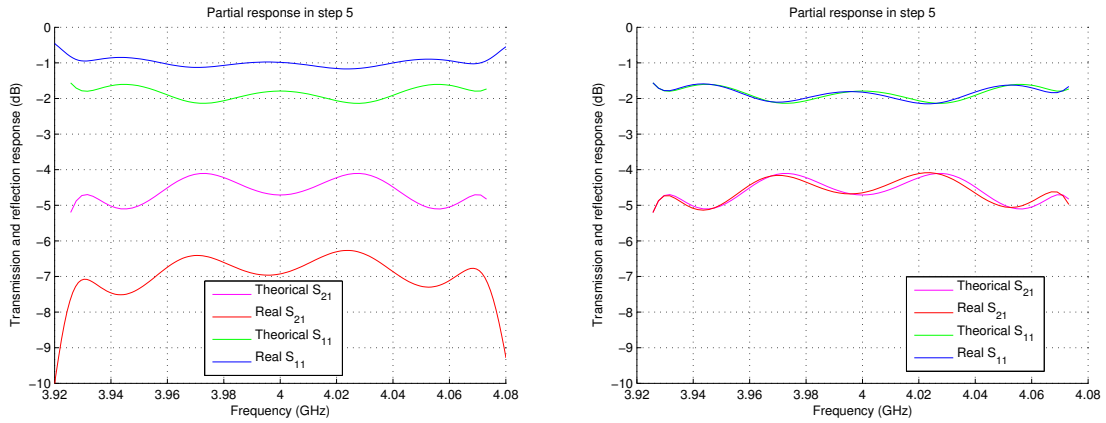

(a) Before optimization.

(b) After optimization.

Figure 3.19: Given response in step 5 by the fifth-order filter segment.

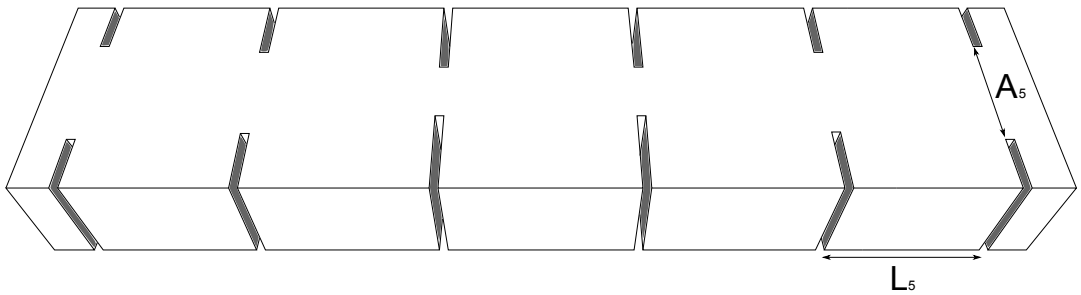

Figure 3.20: Complete filter structure (sixth segment) of a fifth-order filter.

- **Step 6:** The filter segment as well as the adjusted parameters in this step are shown in Figure 3.20 while the matrix in Figure 3.21 provides the target response. Figure 3.22a shows the transmission parameter obtained by using the dimensions calculated in the previous step as initial dimensions. Finally, the Figures 3.22b and 3.22c show the results obtained after optimizing the final parameters listed in Table 3.6.

  Since the partial response of the last steps are the most complex of the design process, the optimization in this last step is the most difficult in the design procedure. As it can be seen in Figure 3.22a, the initial filter response in this step taking the dimensions from the previous cavity as a initial point, is not too close to the goal. This is also due to the wider input and output as it is already mentioned. In this case the optimization of the last step is not so difficult due to the filter simplicity. However in more complex filters this last step to achieve the final filter response will be more difficult

  Thus, as it is desirable to avoid this last stages of filter design, hereinafter the filters design will be performed from the beginning to the middle for the first half of the structure and starting from the end to the middle for the second one. In that way, as only the target partial responses of first half of the filter will be used the design will be faster and easier.

  For symmetrical filters like the in-line filters designed in this chapter, the design from the beginning to the middle of the structure will always produce the same result as the design from the end to the middle. Thus the final filter dimensions can be achieved by dimensioning only the first half of the filter and copying the obtained parameters value to the second half. Figure 3.22d shows the filter response when the dimensions of the second half of the structure have been mirrored to the values obtained for the first half.

  In that way, it is achieved a symmetric structure and the filter design is performing reducing by half the number of steps and the required time. Moreover the final filter response will also be a little bit better.

$$M_6' = M' = \begin{bmatrix} 0 & 138.3946 & 0 & 0 & 0 & 0 \\ 138.3946 & 0 & 29.9395 & 0 & 0 & 0 \\ 0 & 29.9395 & 0 & 20.4282 & 0 & 0 \\ 0 & 0 & 20.4282 & 0 & 18.8053 & 0 \\ 0 & 0 & 0 & 18.8053 & 0 & 18.4655 \\ 0 & 0 & 0 & 0 & 18.4655 & 0 \end{bmatrix}$$

Figure 3.21: Complete scaled fifth-order filter coupling matrix (sixth segment).

Parameter	Initial value (mm)	Optimized value (mm)
L_3	47.278	47.279
A_3	12.165	12.249

Table 3.6: Result of the fifth-order filter parameters in step 6.

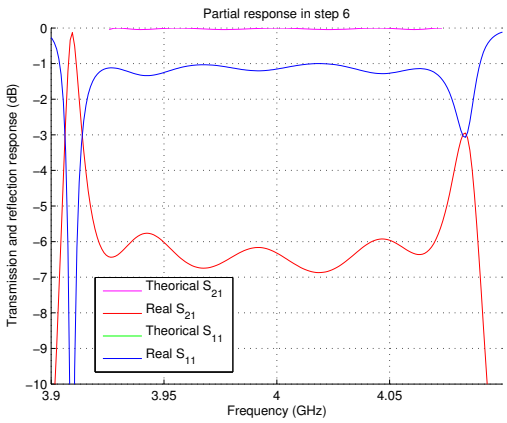

(a) Before optimization.

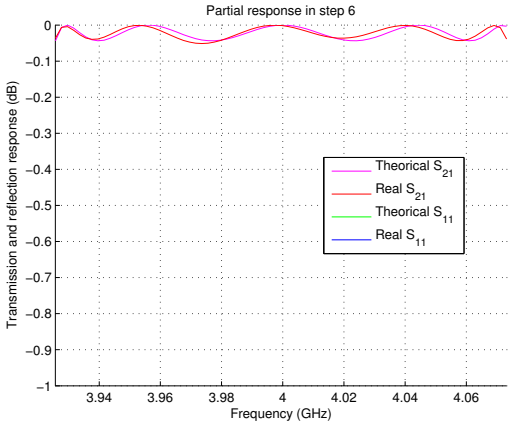

(b) After a final optimization (detailed view).

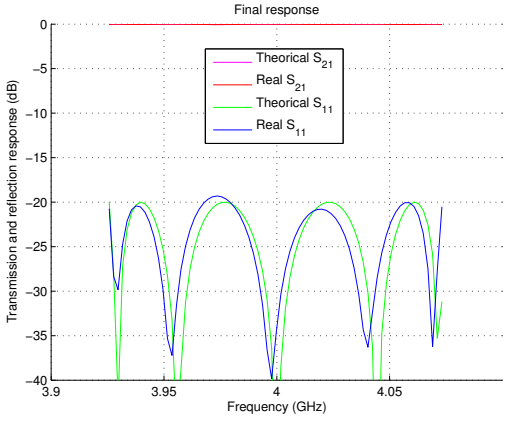

(c) After a final optimization in step 6 (global view).

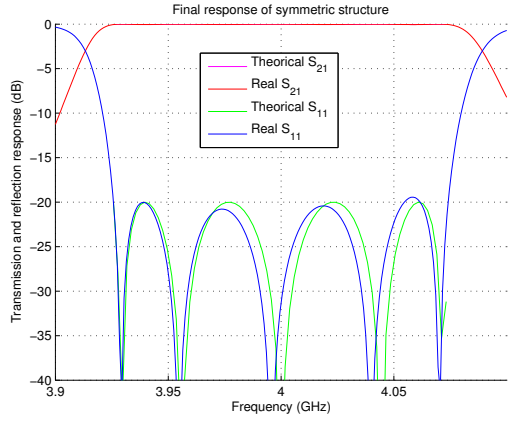

(d) Making filter symmetric by taking the parameters values of second half from the first half.

Figure 3.22: Total filter response obtained in step 6 by the designed fifth-order filter.

3.3.1.1 Summary of design procedure for odd order (N) filters

As it is shown in the above example, the design procedure for this kind of odd order (N) filters can be performed by a set of $\frac{N+1}{2}+1$ iterations.

$$\textit{Number of steps for N odd } = \frac{N+1}{2}+1 \tag{3.10}$$

where:

1. In **step 1** first iris width is adjusted to get the transmission value given by the first coupling matrix segment (first coupling value of complete matrix).
2. In **step k** with k from 2 to $\frac{N+1}{2}+1$ the **parameters L_{k-1} and A_{k-1}** are optimized to fit the response given by the *kth* segment of the coupling matrix.
3. Finally, since the structure is symmetric, the remaining task is to fix the dimensions of the second half of the filter to the values obtained for the first half as it is shown in equations (3.11) and (3.12).

$$A_k = A_{k-N} \quad k = \frac{N+1}{2} \text{ to } N \tag{3.11}$$

$$L_k = L_{k-N+1} \quad k = \frac{N+1}{2}+1 \text{ to } N \tag{3.12}$$

3.3.2 Design of even order (N) filters

In the same way as in the previous example, an even (N) order filter can be designed. In this section, it is a eighth-order in-line filter (N=8) whose response is centered in C-band at 4 GHz with a bandwidth of 100 MHz and a reflection level of -25 dB. The coupling matrix in Figure 3.23 gives this desired response. This coupling matrix is also related to an in-line filter since only the $M_{i,i+i}$ elements are non-zero like in the above example. Once again, this coupling matrix has to be scaled with the physical parameters of the waveguide structure in which the filter will be implemented, in the same way as the previous example. The scaled coupling matrix is shown in Figure 3.24.

$$M = \begin{bmatrix} 0 & 1.0873 & 0 & 0 & 0 & 0 & 0 & 0 & 0 & 0 \\ 1.0873 & 0 & 0.9103 & 0 & 0 & 0 & 0 & 0 & 0 & 0 \\ 0 & 0.9103 & 0 & 0.6211 & 0 & 0 & 0 & 0 & 0 & 0 \\ 0 & 0 & 0.6211 & 0 & 0.5718 & 0 & 0 & 0 & 0 & 0 \\ 0 & 0 & 0 & 0.5718 & 0 & 0.5614 & 0 & 0 & 0 & 0 \\ 0 & 0 & 0 & 0 & 0.5614 & 0 & 0.5718 & 0 & 0 & 0 \\ 0 & 0 & 0 & 0 & 0 & 0.5718 & 0 & 0.6211 & 0 & 0 \\ 0 & 0 & 0 & 0 & 0 & 0 & 0.6211 & 0 & 0.9103 & 0 \\ 0 & 0 & 0 & 0 & 0 & 0 & 0 & 0.9103 & 0 & 1.0873 \\ 0 & 0 & 0 & 0 & 0 & 0 & 0 & 0 & 1.0873 & 0 \end{bmatrix}$$

Figure 3.23: Coupling matrix which given the desired eighth-order response.

$$M' = \begin{bmatrix} 0 & 138.3946 & 0 & 0 & 0 & 0 & 0 & 0 & 0 & 0 \\ 138.3946 & 0 & 29.9395 & 0 & 0 & 0 & 0 & 0 & 0 & 0 \\ 0 & 29.9395 & 0 & 20.4282 & 0 & 0 & 0 & 0 & 0 & 0 \\ 0 & 0 & 20.4282 & 0 & 18.8053 & 0 & 0 & 0 & 0 & 0 \\ 0 & 0 & 0 & 18.8053 & 0 & 18.4655 & 0 & 0 & 0 & 0 \\ 0 & 0 & 0 & 0 & 18.4655 & 0 & 18.8053 & 0 & 0 & 0 \\ 0 & 0 & 0 & 0 & 0 & 18.8053 & 0 & 20.4282 & 0 & 0 \\ 0 & 0 & 0 & 0 & 0 & 0 & 20.4282 & 0 & 29.9395 & 0 \\ 0 & 0 & 0 & 0 & 0 & 0 & 0 & 29.9395 & 0 & 138.3946 \\ 0 & 0 & 0 & 0 & 0 & 0 & 0 & 0 & 138.3946 & 0 \end{bmatrix}$$

Figure 3.24: Scaled eighth-order filter coupling matrix.

All the partial responses required to perform the design procedure can be obtained from the scaled coupling matrix in Figure 3.24. However since the design will be performed only from the beginning of the filter structure to the middle due to the filter symmetry, only the first $\frac{N}{2}+2$ steps are required.

Once the first half of the filter is properly dimensioned, its dimensions can be duplicated to the other half in order to achieve the right final filter structure. Table 3.7 lists the parameters obtained in each step as well as the initial point of each parameter. These parameters are shown in Figure 3.25. It should be noted that the initial points of the parameters from L_2 to A_4 have been taken from the dimensions obtained in the previous step.

Finally, the Figures from 3.26a to 3.26i show the responses provided by each filter segment by taking the unknown parameter from the dimensions of the previous cavity as well as the responses obtained after optimizing the parameters of each segment.

Parameter	Initial	Step 1	Step 2	Step 3	Step 4	Step 5	FINAL
A0=A8 (mm)	30	25.396					25.396
L1=L8 (mm)	43		42.715				42.715
A1=A7 (mm)	13		14.327				14.327
L2=L7 (mm)	42.715			46.751			46.751
A2=A6 (mm)	14.327			12.637			12.637
L3=L6 (mm)	46.751				47.203		47.203
A3=A5 (mm)	12.637				12.249		12.249
L4=L5 (mm)	47.203					47.278	47.278
A4 (mm)	12.249					12.165	12.165

Table 3.7: Result of optimized parameters in each step of the eighth-order filter.

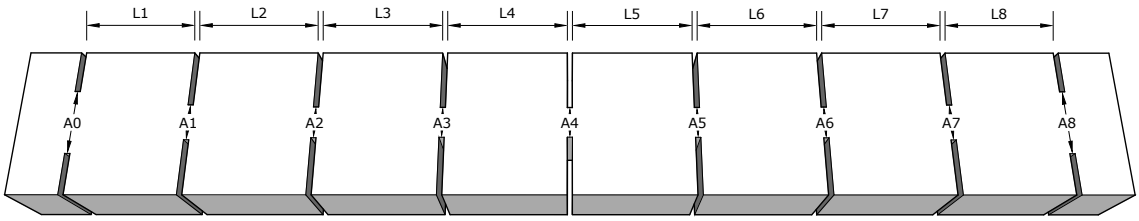

Figure 3.25: Structure and parameters of the designed eighth-order filter.

After finishing the step 5, the first half of the filter is correctly dimensioned. The remaining task, in order to achieve the complete filter structure and the final filter response, is to take the dimensions of the second half of the structure from the obtained dimensions in the first half listed in Table 3.7. With these dimensions the filter structure gives the response shown in Figure 3.26j.

3.3.2.1 Design procedure for even order (N) filters

To sum up, I will describe the general rule for the design procedure applied to filters of even order (N). Here the number of steps is:

$$\textit{Number of step for N even } = \frac{N}{2} + 1 \tag{3.13}$$

where:

1. In **step 1**, the first iris width is optimized to get the transmission value given by the first coupling matrix segment (first coupling value of complete matrix).

2. In **step k** with k from 2 to $\frac{N}{2} + 1$ the **parameters L_{k-1} and A_{k-1}** are optimized to fit the response given by the kth segment of the coupling matrix.

3. Finally, the dimensions of the second half of the structure are taken from the values obtained for the first half as it is shown in the expressions (3.14) and (3.15).

$$A_k = A_{k-N} \qquad k = \frac{N}{2} + 1 \text{ to } N \tag{3.14}$$

$$L_k = L_{k-N+1} \qquad k = \frac{N}{2} + 1 \text{ to } N \tag{3.15}$$

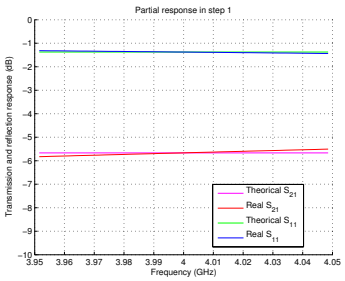

(a) Step 1, result.

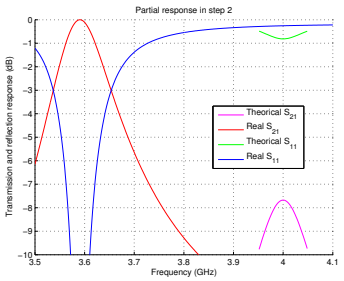

(b) Step 2, initial point.

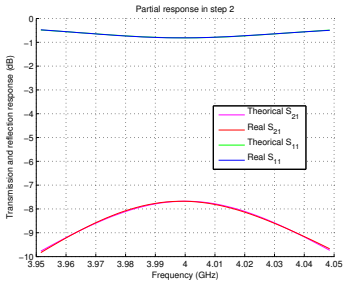

(c) Step 2, result.

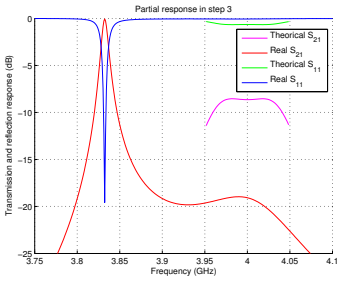

(d) Step 3, initial point.

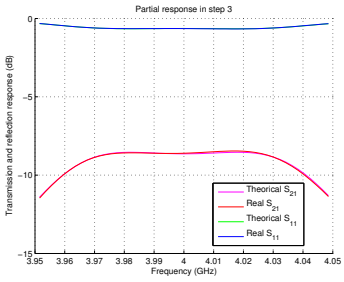

(e) Step 3, result.

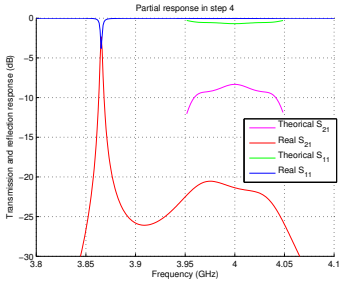

(f) Step 4, initial point.

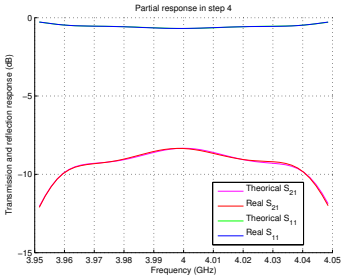

(g) Step 4, result.

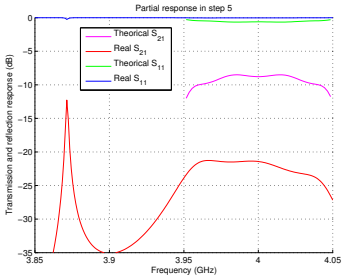

(h) Step 5, initial point.

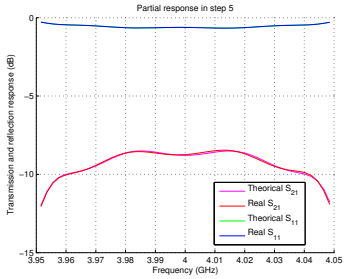

(i) Step 5, result.

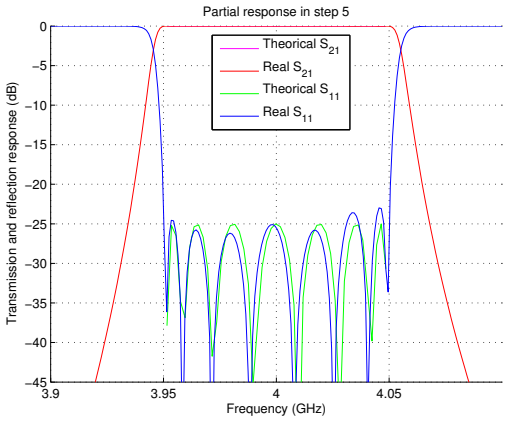

(j) Step 5, final response.

Figure 3.26: Partial responses en each step of the eighth-order filter.

3.4 Wideband in-line filters design

When addressing the issue of wide bandpass filter design, some problems appear due to the dispersive behavior of the waveguide. The electrical irises dimensions are frequency dependent and the synthesized values of the impedance inverters are only right at the filter center frequency. Due to this dispersive behavior, the slope parameter can not be fitted perfectly in a large bandwidth (as seen in Figure 2.14b with a fractional bandwidth $\Delta = 25\%$).

In this context, numerous authors have developed corrections to the slow parameters and more complex filters prototypes in order to perform successfully the design of wide band filters. As an example, some corrections of the slope parameters are presented in [Vanin et al., 2004] to overcome the mentioned drawback. Other authors optimize the filter prototype in each iteration in order to obtain the same behavior taking into account the dispersive behavior introduced by the waveguide structure [Soto et al., 2010].

Nevertheless, this kind of filters can be equally designed by the discussed step-by-step technique [Guglielmi and Melcon, 1993, Guglielmi, 1994] taking into account that the dispersive behavior of the waveguide will limit the maximum bandwidth, and also the accuracy that will be obtained for very wideband implementations. Moreover, since irises are wider in wideband filters, the interaction with the previous irises is larger. Thus when the *cavity* k is added in the *step* $k+1$; the *cavity* $k-1$ which has been optimized with an adapted load in *step* $k-1$ has to be re-optimized due to the load change. Thus, when adding a new segment to the structure that is being designed, it may be necessary to optimize, firstly the last added cavity and coupling window and then to refine the mentioned cavity and iris as well as the previous ones.

It should be noted that although in this case the number of parameters to optimize is twice the number in the previous section, the optimization is still easy as the initial values of these parameters are quite close to the target and only a small variation is required.

3.4.1 Wideband filters design procedure

In order to overcome the interaction between irises in wideband filters, a set of t iterations should be performed in each step k. The number t depends on the filter order and complexity and also on the fractional bandwidth Δ.

As it is known, in order to design a symmetric filter, k will take the value from 1 to $\frac{N+1}{2}+1$ for odd order filter and from 1 to $\frac{N}{2}+1$ for even odd filters. Iterations to be performed in a step k are:

1. Optimizations of parameters L_{k-t_1} and A_{k-t_1} where k is the index of last added cavity and $t_1 = 1$ for this first iteration.

2. Increase t index and perform a new optimization of parameters the L_{k-t_1}, A_{k-t_1}, L_{k-t_2} and A_{k-t_2} where $t_2 = 2$. Thereby, the problem of the irises interaction is solved and the filter segment response is refined to fit more accurately the target response for the step k.

3. A new optimization could be performed if the obtained response was not as accurate as desired. Then the t index has to be increased again $t_{i+1} = t_i + 1$ and two more parameters have to be added to the optimization. In each iteration the optimization is faster than in the previous iteration, as the initial parameters are much closer to the target than in the previous iteration. However it is necessary to take into account that the target response provided by the equivalent circuit with inductances and ideal impedance inverters shown in the previous chapter can not be fitted perfectly no matter how much iterations are performed. This fact is due to the dispersive behavior of the waveguide and also to the presence of spurious bands that are not modeled by the filter prototype. Finally the number of parameter optimized in each step k are:

$$L_{k-t} \; and \; A_{k-t} \qquad t \in [t_1 = 1, t_{max} \leq k] \tag{3.16}$$

In order to choose the proper value of t, it must be taken into account the size of the parameter variation. If the variation is insignificant as it often happens after the third or even the second iteration depending on the filter specifications, the result will be the same no matter how many iterations are performed. When this happens, the algorithm can be safely terminated.

In this chapter several wideband filters have been designed with a fractional bandwidth up to $\Delta = 25\%$, in all cases with a value $t_{max} = 2$. Firstly, a sixth-order filter with a fractional bandwidth of $\Delta = 12.5\%$ is designed to validate the proposed approach.

Next it is presented an eight-order filter in which the fractional bandwidth increases to $\Delta = 25\%$ in order to show the effectiveness of the step-by-step technique, and finally, it is presented an eleventh-order filter with the same frequency specifications as the one designed by the alternative procedure introduced in [Vanin et al., 2004].

3.4.2 Design of a sixth-order in-line filter with 500 MHz bandwidth

As an example, a sixth-order filter centered in C-band at frequency of 4GHz with 500 MHz bandwidth and a reflection level of -30 dB is designed. The coupling matrix that gives this response and the scaled coupling matrix are shown in Figures 3.27 and 3.28.

This design has been performed by 4 steps each one with two iterations. In the fist iteration only the unknown parameters are optimized taking the values of the parameter in last step as initial point. In the second iteration these parameters are optimized again as well as the width of the previous iris and the length of the previous cavity. The following list details this approach.

- **Step k=1:** First iris width is adjusted to obtain the first coupling level given by the coupling matrix. For convenience, the iris thickness is fix to 2 mm as in the other filters designed in this chapter.
- **Step k=2:** The parameters of the second segment are adjusted as well as the fist iris width ($A0$) obtained in the previous step. In this step, the obtained value in the previous step for the first iris has not been taken as initial point since as it is already mentioned, it can be quite wider due to the large bandwidth.
  - Iteration t=1: Parameters $L1$ and $A1$ are optimized. The initial point for this parameters is chosen in order to make the initial response close to the target.
  - Iteration t=2: Since the coupling windows are larger in wide band filters, the interactions between them increases. Thus, when a new segment is added, the effect in the previous step, which had been designed with an adapted load, has to be considered again. Due to this, in this iteration the parameters $L1$, $A1$ and $A0$ are readjusted. In can be seen in Table 3.8 that the variation of parameter $A0$ from previous step is quite small but important to increase the accuracy of the design process.
- **Step k=3:** This step has also been performed with two iterations.
  - Iteration t=1: Parameters $A2$ and $L2$ are optimized by taking as initial point the values of the parameters $A1$ and $L1$ obtained in the step 1.
  - Iteration t=2: Parameters $A2$ and $L2$ as well as $A1$ and $L1$ are adjusted to fit properly the target partial response. It can be seen in Table 3.8 that parameters $L1$ and $A1$ are slightly modified from 34.63 mm to 34.156 mm and from 26.71 mm to 26.728 mm respectively.
- **Step k=4:** In the same way as in previous step, parameters $L3$ and $A3$ are optimized in this step and parameters $L2$ and $A2$ are refined.
  - Iteration t=1: Parameters $L3$ and $A3$ are optimized taking the value of $L2$ and $A2$ as initial point.
  - Finally, parameters $L3$, $A3$, $L2$ and $A2$ are refined.

Obtained parameters in each step are shown in Table 3.8 and the filter response of each segment is shown in Figures from 3.29b to 3.29h.

The final response of this filter can be seen in Figure 3.29i. This response is really good taking into account that a 12.5% fractional bandwidth is achieved as it is shown in equation (3.17).

$$\Delta = \frac{500MHz}{4GHz} = 12.5\% \tag{3.17}$$

The final response obtained by classical design procedure, namely by dimensioning the filter cavities and irises separately would have been much poorer.

However, it would be desirable to get a final response that matches the theoretical response with the same accuracy as the result for the narrow bandwidth filters designed previously in this chapter. This can be done by performing a global optimization in which all filter parameters are refined. In this optimization the only single target is that the reflection level within the bandwidth must be below -30 dB as it is established in the filter specifications. The parameters values obtained are listed in Table 3.8 and the final response is shown Figure 3.29j. In this response all filter specifications are perfectly fulfilled.

It is important to note that this final optimization step converges fast to an optimum solution because the initial point provided by our design strategy is very close to the final geometry. Without this very good starting point, any optimization algorithm will fail in converging to the right solution. This shows the usefulness of the design strategy employed in this work.

The more noticeable effect in the response shown in Figure 3.29j is that the ripple in the passband given by the target response does not match the real ripple provided by the waveguide structure once the filter is properly designed. This is due to the dispersive behavior of the waveguide and also to the presence of spurious bands that are not modeled by the filter prototype based in ideal lumped elements.

$$M = \begin{bmatrix} 0 & 1.2017 & 0 & 0 & 0 & 0 & 0 & 0 \\ 1.2017 & 0 & 1.0511 & 0 & 0 & 0 & 0 & 0 \\ 0 & 1.0511 & 0 & 0.6921 & 0 & 0 & 0 & 0 \\ 0 & 0 & 0.6921 & 0 & 0.6463 & 0 & 0 & 0 \\ 0 & 0 & 0 & 0.6463 & 0 & 0.6921 & 0 & 0 \\ 0 & 0 & 0 & 0 & 0.6921 & 0 & 1.0511 & 0 \\ 0 & 0 & 0 & 0 & 0 & 1.0511 & 0 & 1.2017 \\ 0 & 0 & 0 & 0 & 0 & 0 & 1.20170 & \end{bmatrix}$$

Figure 3.27: Coupling matrix which given the desired sixth-order response.

$$M' = \begin{bmatrix} 0 & 344.2301 & 0 & 0 & 0 & 0 & 0 & 0 \\ 344.2301 & 0 & 175.1042 & 0 & 0 & 0 & 0 & 0 \\ 0 & 175.1042 & 0 & 115.3046 & 0 & 0 & 0 & 0 \\ 0 & 0 & 115.3046 & 0 & 107.6658 & 0 & 0 & 0 \\ 0 & 0 & 0 & 107.6658 & 0 & 115.3046 & 0 & 0 \\ 0 & 0 & 0 & 0 & 115.3046 & 0 & 175.1042 & 0 \\ 0 & 0 & 0 & 0 & 0 & 175.1042 & 0 & 344.2301 \\ 0 & 0 & 0 & 0 & 0 & 0 & 344.2301 & 0 \end{bmatrix}$$

Figure 3.28: Scaled sixth-order filter coupling matrix.

Parameter	Initial	Step 1	Step 2	Step 3	Step 4	FINAL
A0=A6 (mm)	30	38.860	36.353			36.185
L1=L6 (mm)	30		34.630	34.156		33.888
A1=A5 (mm)	25		26.710	26.728		26.675
L2=L5 (mm)	34.156			39.842	39.703	39.437
A2=A4 (mm)	26.728			23.735	23.749	23.663
L3=L4 (mm)	39.842				41.424	41.120
A3 (mm)	23.735				23.119	23.032

Table 3.8: Result of the wideband sixth-order filter parameters in each step.

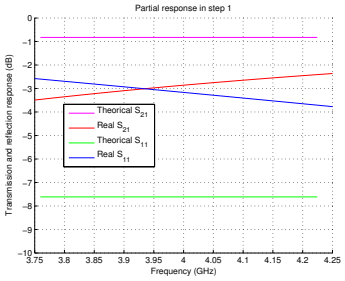

(a) Step 1, initial point.

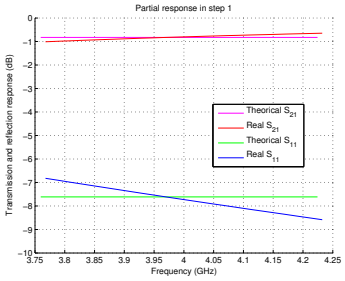

(b) Step 1, result.

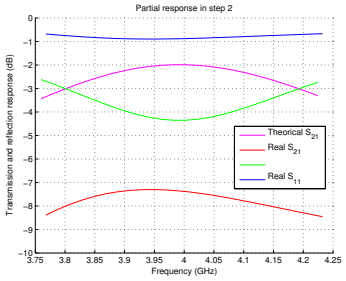

(c) Step 2, initial point.

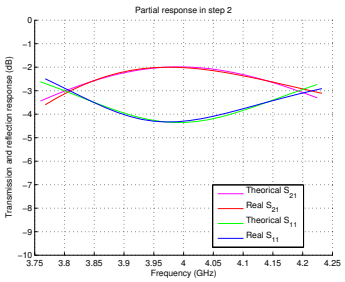

(d) Step 2, result.

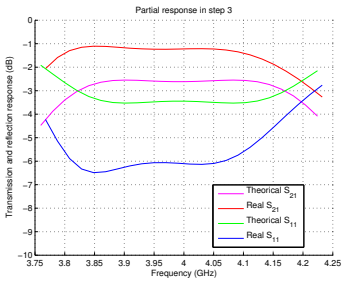

(e) Step 3, initial point.

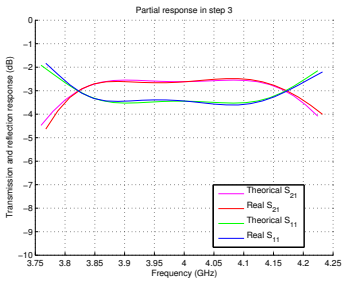

(f) Step 3, result.

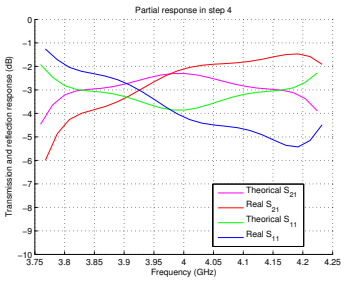

(g) Step 4, initial point.

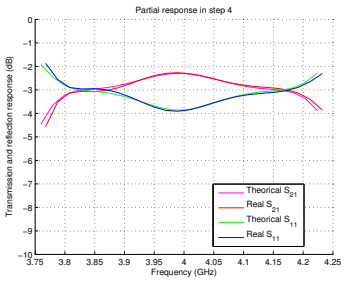

(h) Step 4, result.

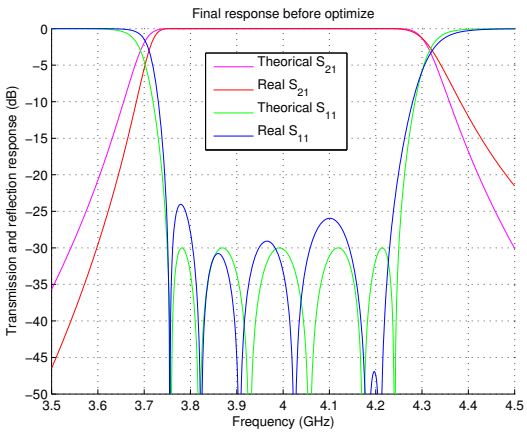

(i) Initial response of symmetric structure.

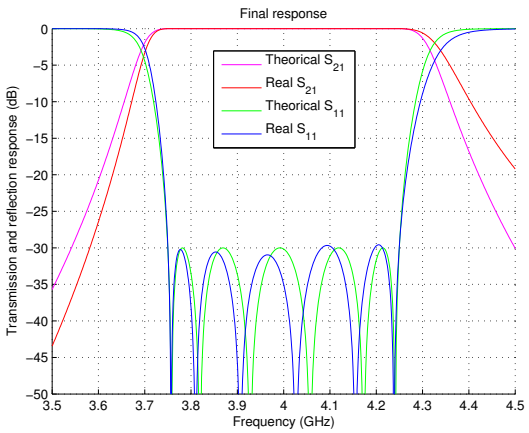

(j) Final response after optimize.

Figure 3.29: Partial responses in each step of the sixth-order filter.

3.4.3 Design of an eighth-order in-line filter with 1GHz bandwidth

In this example, designing a quite wideband waveguide filter is intended. It is an eighth-order filter with 4GHz of central frequency (C-band), a reflection level of 30 dB as the preview example but with 1 GHz bandwidth. This large bandwidth and the central frequency give a fractional bandwidth of 25% which is difficult to design with traditional design techniques.

$$\Delta = \frac{1GHz}{4GHz} = 0.25 \tag{3.18}$$

This design has been performed by 5 steps each one with two iterations and one final step to fit the final target response. Finally, a global optimization has been required to fulfill properly all the specifications as it has been done in the previous example.

The coupling matrix that has been used is the one in Figure 3.30 and the scaled coupling matrix in Figure 3.31. The values for the parameters obtained in each step are listed in Table 3.9 meanwhile Figures from 3.32a to 3.32e show the partial responses in each step.

Figure 3.32f shows the result obtained after the design procedure which is much poorer than the obtained in the last example due to the larger fractional bandwidth. Finally, Figure 3.32g shows the final response after performing a global optimization with the only single target of the reflection level in the passband. For this large bandwidth, the filter response begin to be deteriorated. That is once again due to waveguide dispersion and to the presence of spurious bands. Looking at the partial responses in Figure 3.32 it can be noted that it is not possible to fit accurately the partial responses, especially in the right edge of the passband as a result of both, the dispersive behavior and the proximity of the spurious band.

It can be noticed that the ripple provided by the waveguide structure is almost out of phase with the ripple in target response. This effect is also caused by the presence of the spurious bands. As a result of the large bandwidth the spurious bands are wider and closer to the filter passband. Moreover, when the filter is more selective, the transmission poles are closer to the passband edges. That is re reason why the rejection in the stop-band above the filter passband decreases meanwhile the rejection below the passband increases. Thus, the positions of the transmission poles are shifted to lower frequencies. In this way, the ripple in the passband provided by the filter prototype which has a symmetry axis in the filter central frequency can not be fitted properly.

It would be necessary a more complex filter prototype which models the spurious band and provides a target response that takes into account the shifting of the transmission poles to lower frequencies. In this way, with a filter prototype that provides the proper response with the right ripple within the bandwidth, then it could be possible to obtain the right partial responses by segmenting this filter prototype.

$$M = \begin{bmatrix}
0 & 1.1785 & 0 & 0 & 0 & 0 & 0 & 0 & 0 & 0 \\
1.1785 & 0 & 1.0075 & 0 & 0 & 0 & 0 & 0 & 0 & 0 \\
0 & 1.0075 & 0 & 0.6554 & 0 & 0 & 0 & 0 & 0 & 0 \\
0 & 0 & 0.6554 & 0 & 0.5930 & 0 & 0 & 0 & 0 & 0 \\
0 & 0 & 0 & 0.5930 & 0 & 0.5798 & 0 & 0 & 0 & 0 \\
0 & 0 & 0 & 0 & 0.5798 & 0 & 0.5930 & 0 & 0 & 0 \\
0 & 0 & 0 & 0 & 0 & 0.5930 & 0 & 0.6554 & 0 & 0 \\
0 & 0 & 0 & 0 & 0 & 0 & 0.6554 & 0 & 1.0075 & 0 \\
0 & 0 & 0 & 0 & 0 & 0 & 0 & 1.0075 & 0 & 1.1785 \\
0 & 0 & 0 & 0 & 0 & 0 & 0 & 0 & 1.1785 & 0
\end{bmatrix}$$

Figure 3.30: Coupling matrix which given the desired eighth-order response.

$$M' = \begin{bmatrix}
0 & 501.2895 & 0 & 0 & 0 & 0 & 0 & 0 & 0 & 0 \\
501.2895 & 0 & 370.1114 & 0 & 0 & 0 & 0 & 0 & 0 & 0 \\
0 & 370.1114 & 0 & 240.7537 & 0 & 0 & 0 & 0 & 0 & 0 \\
0 & 0 & 240.7537 & 0 & 217.8528 & 0 & 0 & 0 & 0 & 0 \\
0 & 0 & 0 & 217.8528 & 0 & 213.0042 & 0 & 0 & 0 & 0 \\
0 & 0 & 0 & 0 & 213.0042 & 0 & 217.8528 & 0 & 0 & 0 \\
0 & 0 & 0 & 0 & 0 & 217.8528 & 0 & 240.7537 & 0 & 0 \\
0 & 0 & 0 & 0 & 0 & 0 & 240.7537 & 0 & 370.1114 & 0 \\
0 & 0 & 0 & 0 & 0 & 0 & 0 & 370.1114 & 0 & 501.2895 \\
0 & 0 & 0 & 0 & 0 & 0 & 0 & 0 & 501.2895 & 0
\end{bmatrix}$$

Figure 3.31: Scaled eighth-order filter coupling matrix.

Parameter	Initial	Step 1	Step 2	Step 3	Step 4	STEP 5	FINAL
A0=A8 (mm)	30	54.780	41.129				42.151
L1=L8 (mm)	30		31.161	31.348			29.999
A1=A7 (mm)	30		34.452	33.351			33.971
L2=L7 (mm)	31.161			35.088	35.313		34.211
A2=A6 (mm)	34.452			30.962	30.418		30.801
L3=L6 (mm)	35.088				36.839	37.136	36.263
A3=A5 (mm)	30.962				29.892	29.417	29.719
L4=L5 (mm)	36.839					37.450	36.979
A4 (mm)	29.892					29.628	29.451

Table 3.9: Result of the wideband eighth-order filter parameters in each step.

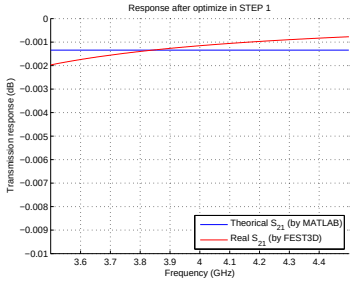

(a) Step 1, result.

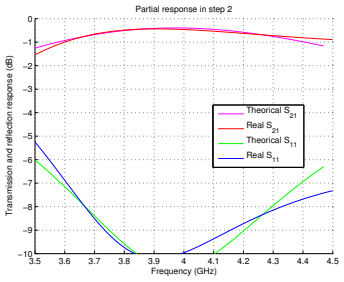

(b) Step 2, result.

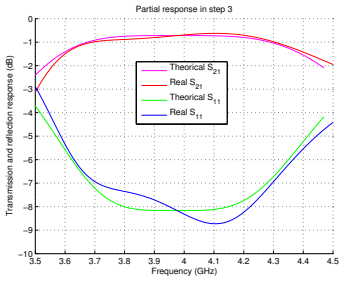

(c) Step 3, result.

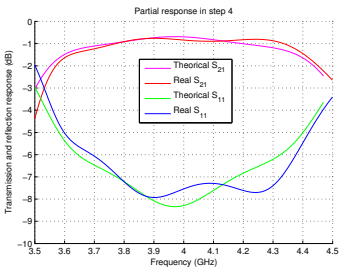

(d) Step 4, result.

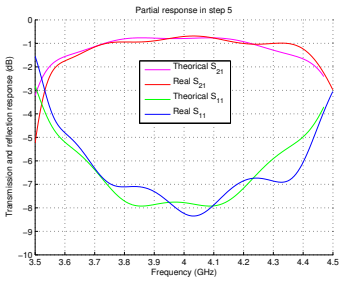

(e) Step 5, result.

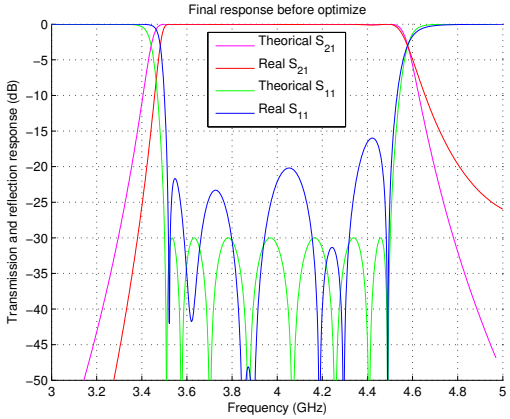

(f) Initial response of symmetric structure.

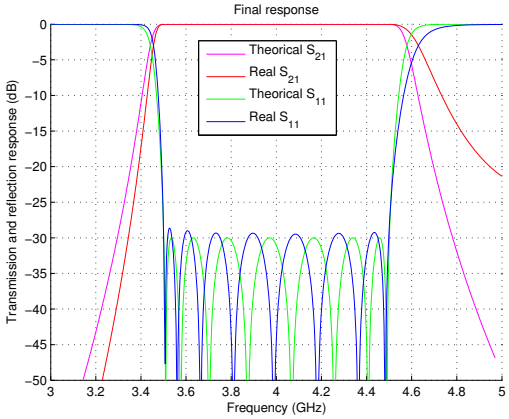

(g) Final response after optimizing.

Figure 3.32: Partial responses in each step of the eighth-order filter.

3.4.4 Eleventh-order in-line filter with 2.5GHz bandwidth

Finally, I will show the design of an eleventh-order filter centered at 13.25 GHz with a bandwidth of 2.5 GHz and a return losses of -25 dB similarly to the filter presented in [Vanin et al., 2004] by using corrections of the slope parameters. In this example the fractional bandwidth reach 18.9 %.

$$\Delta = \frac{2.5GHz}{13.25GHz} = 18.88 \tag{3.19}$$

The approach followed in this example is right the same as used in the previous ones and the obtained response is shown in Figure 3.34a. The final result has been achieved after a global optimization by imposing the condition that the reflection parameter should be below -25 dB in the passband regardless of the target response. The final filter dimensions are listed in Table 3.10 and the filter parameters are shown in Figure 3.33. Figure 3.34b shows the response provided by this filter with the mentioned dimensions.

Parameter name	Parameter value (mm)	Parameter name	Parameter value (mm)
$A_0 = A_{11}$	12.068	$L_1 = L_{11}$	9.175
$A_1 = A_{10}$	9.255	$L_2 = L_{10}$	10.725
$A_2 = A_9$	8.367	$L_3 = L_9$	11.266
$A_3 = A_8$	8.089	$L_4 = L_8$	11.442
$A_4 = A_7$	7.988	$L_5 = L_7$	11.505
$A_5 = A_6$	7.953	L_6	11.521

Table 3.10: Final parameters values of the designed eleventh-order filter.

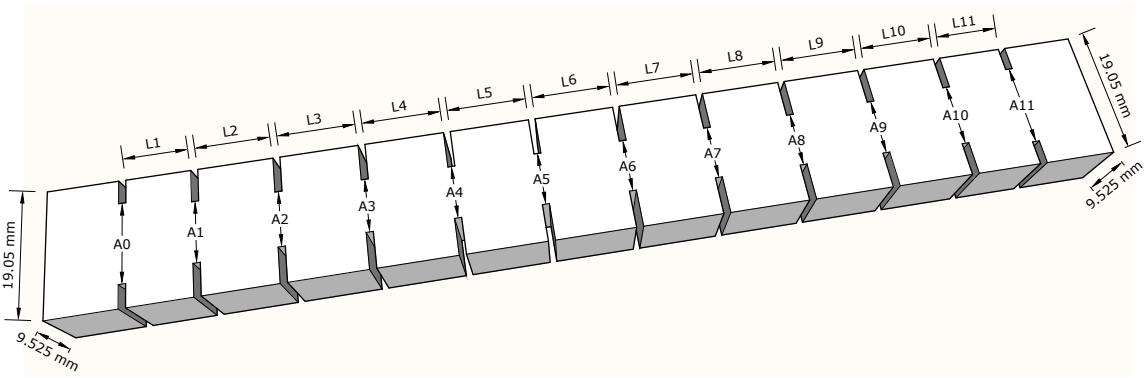

Figure 3.33: Structure of the designed eleventh-order filter.

At this point the final result shown in Figure 3.34b is achieved and the filter structure is properly dimensioned. Then it would be desirable to know how accurate the partial target responses are for this kind of wideband filters. Thus, this filter is segmented in order to compare the real partial responses given by the real filter structure with the partial responses obtained by segmenting the coupling matrix. In this way it is possible to notice how and at what point the theoretical responses are incorrect for wide band filters. Partial responses obtained are shown in Figures from 3.35a to 3.35k and Figure 3.35l shows the final result obtained with these partial responses.

In these partial responses, as it was already known, the main effect is the shifting to lower frequencies of the transmission poles. However a small scaling error can also be noticed. It can be noted in all partial responses in Figures from 3.35b to 3.35k that the real transmission coefficient (S_{21}) is always below the target in the left side of the passband and above the target response in the right passband edge.

In conclusion, in order to perform the design of wideband filters more accurately and to avoid the final global optimization it would be needed some corrections of the target responses. These

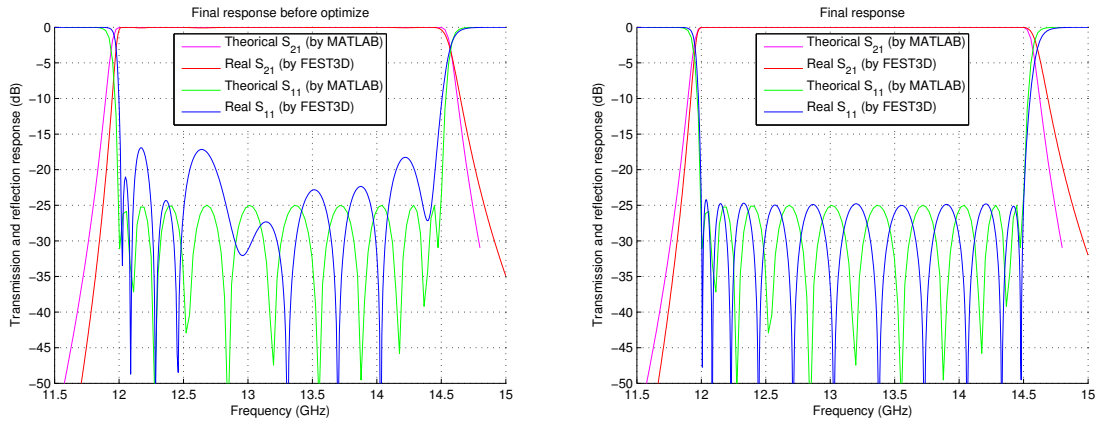

(a) Before opmization.

(b) After a global optimization.

Figure 3.34: Final response of the eleventh-order filter.

corrections should involve, firstly a non-linear frequency transformation that shifts to lower frequencies the transmission poles within the passband, and secondly a frequency dependent scaling that corrects the transmission and reflection levels.

3.5 Conclusions

In this chapter a design procedure for microwave filters has been presented based on the segmentation of the structure in a step-by-step fashion. The main contribution of this theory is the adaptation of the design technique introduced for the first time by [Guglielmi and Melcon, 1993, Guglielmi, 1994] to the general formalism given by the coupling matrix. Thus the filters design possibilities are expanded, since it could be applied not only for the design of in-line filters, but also for other more complex coupling topologies as it will be shown in the next chapter.

Moreover, several examples of filters designed in waveguide technology have been presented, showing the effectiveness of the technique and the validity of the presented approach.

Finally, with regard to the wideband filters design, it has been shown some effects of non-linear mechanisms such as the dispersive behavior of the waveguide or the variation of the rejection in the stop-band due to the presence of the spurious bands. Despite this, the filters responses obtained after concluding the design procedure are close enough to the target response. Thus, it is only necessary a slight variation in the dimensions of the structure. As a result, a global optimization of the filter structure leads easily to the proper dimensions that provide the desired responses.

In this context, some authors have developed mathematical corrections for the filter prototypes in order to represent more accurately the behavior of wideband filter [Vanin et al., 2004]. Nevertheless it has been demonstrated that the presented approach is still useful for the design of filters with a fractional bandwidth up to 25% in spite of the fact that the partial responses provided by the coupling matrix do not take into account these non-linear effects. Indeed, the eleventh-order filter designed in this chapter is the same filter as the one designed in [Vanin et al., 2004] through using corrections of the slope parameters.

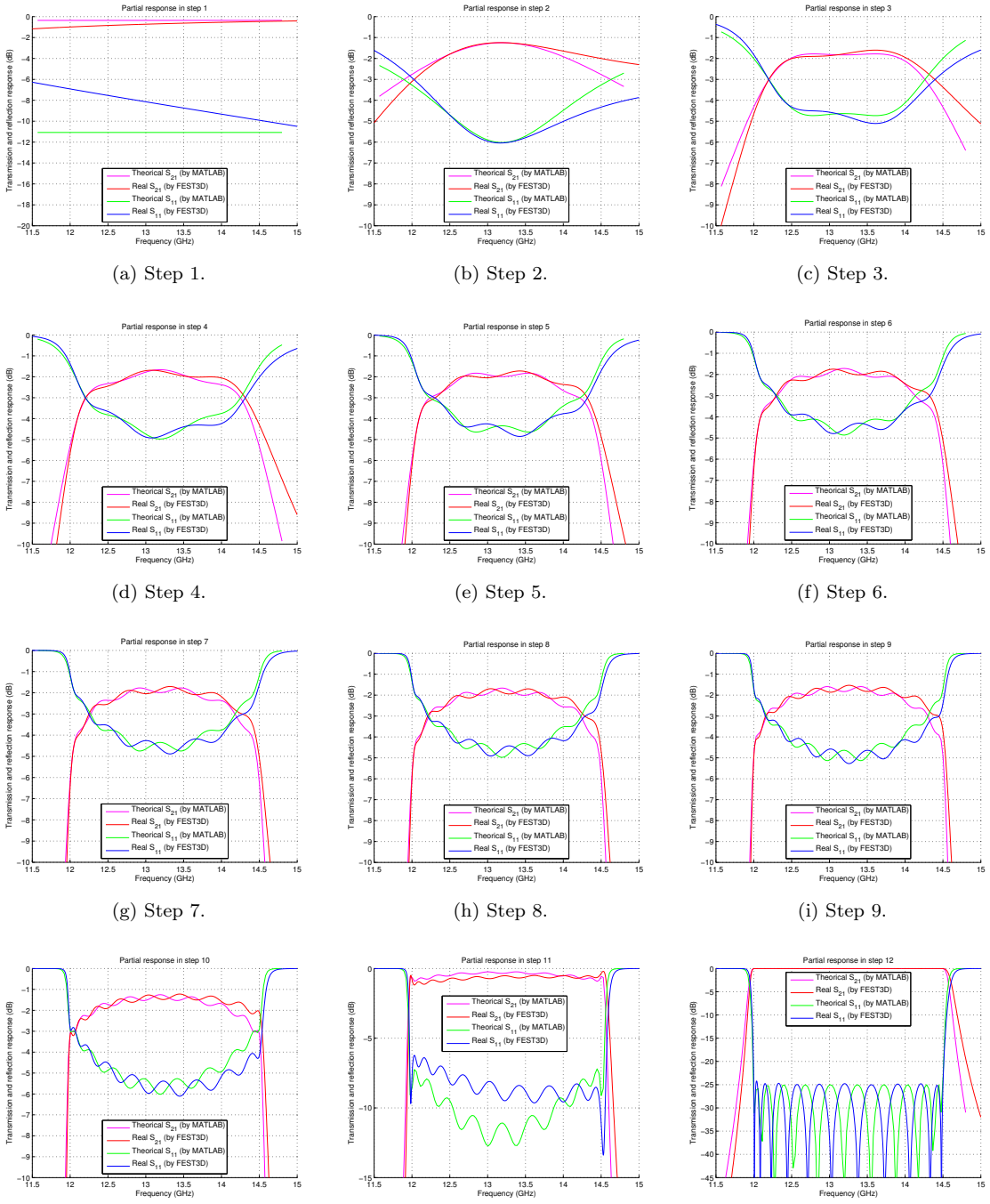

(a) Step 1. (b) Step 2. (c) Step 3.

(d) Step 4. (e) Step 5. (f) Step 6.

(g) Step 7. (h) Step 8. (i) Step 9.

(j) Step 10. (k) Step 11. (l) Step 12.

Figure 3.35: Real partial response in each step after segmenting the final eleventh-order filter.

4 DUAL-MODE FILTERS DESIGN

4.1 Introduction

Classical dual-mode filters are based on dual mode resonant cavities which employ two orthogonally polarized modes in its physical realization. Thus, each dual mode cavity provides two electrical resonances, which are inde pendent of each other. This leads to a considerable size reduction compared to filters composed of single mode cavities. Moreover, a dual-mode is able to provide a transmission zero depending on the coupling topology. Thus, it is possible to achieve high selectivity filtering functions and structures of compact size [Cameron et al., 2007].

The number of transmission zeros provided by a coupling structure is given by the filter order minus the minimum number of resonances in the path between the input and the output.

$$TZ = N - min(P) \tag{4.1}$$

where TZ is the number of transmission zeros provided by the coupling structure, N is the total number of resonances and $min(P)$ the minimum number of resonators in a given path between the input and the output.

For instance, an in-line filter (Figure 4.1a)can not provide any transmission zero as the only path between the input and the output is composed by all of the resonators in the filter structure. However, in a transversal coupling topology there is coupling between the input and all resonators as well as between all resonators and the output (Figure 4.1b). Thus, the minimum path in a pure transversal topology is always 1 and the number of transmission zeros is the filter order minus 1.

$$TZ_{\text{Transversal topology}} = N - 1 \tag{4.2}$$

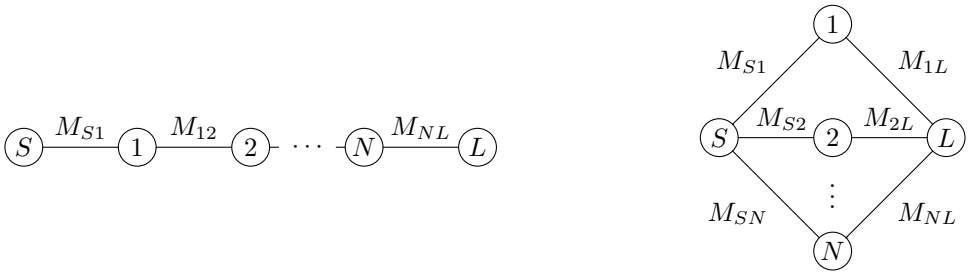

(a) In-line topology.

(b) Transversal topology.

Figure 4.1: Coupling-routing diagram of in-line and transversal topologies.

Due to its compact size and reduced mass, dual-mode filters became popular in the early 70s [Wanselow, 1975, Cameron and Rhodes, 1981, Fiedziuszko, 1982] in the field of satellite communications. Since then, they have been widely used in satellite transponders to achieve advanced filtering functions by a fairly simple structure. Classical dual-mode filters are implemented by cylindrical

cavities which support two orthogonally polarized TE_{11n} mode resonances. These two resonances are tuned by two tuning screws set 90º apart around the circumference of the cavity and define the polarization directions. This type of filters are well known and deeply studied due to its huge spread [Cogollos et al., 2010, Cogollos et al., 2012, Hu and Wu, 2013].

Figure 4.2 shows an example of a dual-mode filter formed by two cylindrical cavities. In this example, the vertical mode in the first cavity (mode 1) is excited by a horizontal input iris. Once the vertical mode exist in the cavity the horizontal resonance (mode 2) is excited by introducing a perturbation in the symmetry of the structure made by some element such as a screw or a notch like in Figure 4.2. This element distorts the field of the first resonance and produce field components in the direction of the second resonance. Thus producing the coupling between the two.

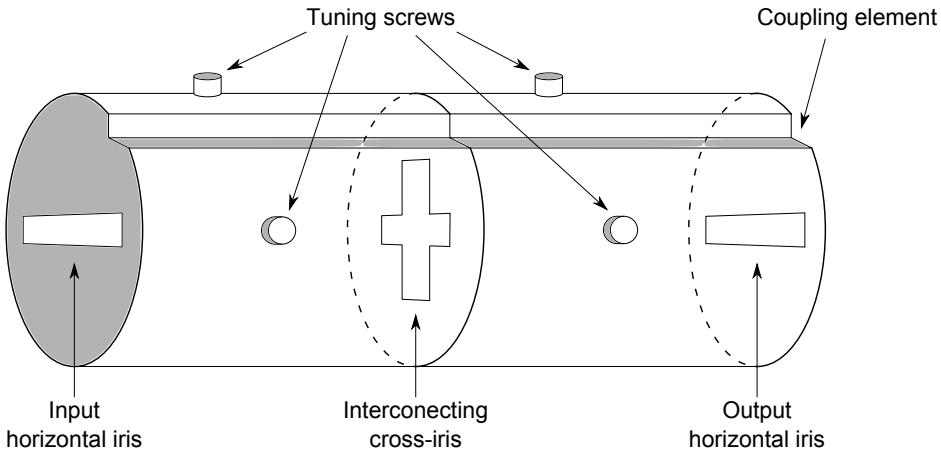

Figure 4.2: Dual mode filter with two cylindrical resonators.

The diagram of Figure 4.3 shows the coupling topology of the filter from Figure 4.2. The cross-iris plate between the cavities provides the inter-cavity couplings M_{14} and M_{23}. The horizontal slot of the cross-iris provides the coupling M_{14} between vertical modes 1 and 4. Moreover the vertical slot gives the coupling M_{23} between the horizontal modes 2 and 3. Since each slot of the cross-iris has a reduced width, the horizontal slot affects almost exclusively to the coupling between the vertical polarized modes and the vertical slot to the horizontally polarized resonances. Thus, the cross-polarization couplings (M_{13} and M_{24}) are negligibly small.

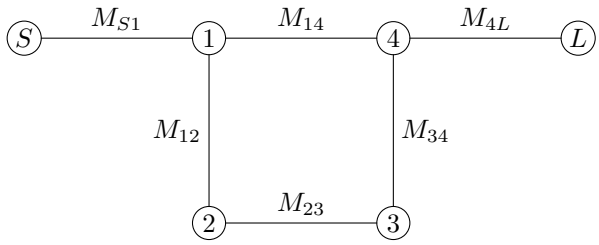

Figure 4.3: Coupling diagram of the dual-mode filter with two cylindrical resonators.

Nevertheless, the design of these filters is still fairly complex due to the number of coupling and tuning elements required. In addition, as a result of the coupling structure and the circular waveguide technology, these filters involve a complex and costly manufacturing process. Similarly, it is possible to find another dual-mode cavities with rectangular waveguide technology, however all of them are based on the same principles. They use rectangular cavities in which two orthogonally polarized modes are excited, one of them by the input coupling window and the other one by additional coupling elements. For instance a cut edge [Liang et al., 1992] or a coupling screw. In spite of the rectangular structure, these cavities still keep some drawbacks from the circular implemented dual-mode cavities. They require the same coupling elements as the circular cavities and it is still necessary to dimension the whole 3D structure since both the width and height of the dual-mode cavities as well as the length must be adjusted.

4.2 All inductive dual-mode resonators

Dual mode filters designed in this chapter are based on the *full inductive* dual-mode resonators introduced by Guglielmi [Guglielmi et al., 2001]. Instead of orthogonal polarized modes as in classical dual-mode filters, all inductive dual-mode resonant cavities are based on the presence of two higher order modes which resonate within a rectangular cavity. In order to achieve the desired behavior with two transmission poles and one transmission zero, the first resonant mode have to see an electrical path of λ_g and the second one a length of $\lambda_g/2$. Then, the field of the second resonant mode change the sign going from the resonator input aperture to the output, and the field of the first mode keep the same sign since it sees a variation of two $\lambda_g/2$ from the input to the output. In this way, since the second resonant mode changes the sign from the input to the output, a destructive interference occurs in the resonator output producing a transmission zero at one specific frequency.

Figure 4.4 shows an example of a second-order filter structure with all-inductive technology. This kind of filters are formed by rectangular waveguide cavities inter-coupled by inductive irises. Each rectangular dual-mode resonator has to be micro-metrically and particularly accurately dimensioned in order to make desired modes $TE_{m_1n_1p_1}$ and $TE_{m_2n_2p_2}$ exist independently, and resonate at the right frequency within each cavity. Moreover both modes in first cavity are excited by a single inductive input iris critically dimensioned to bring the required amount of coupling to each mode in dual-mode cavity. The inter-cavity couplings are also provided by a single coupling window which is specially dimensioned and property placed in order to achieve the proper straight coupling between the same modes in both cavities (if the resonant modes in both cavities are the same) and the right cross-mode coupling between the unlike modes.

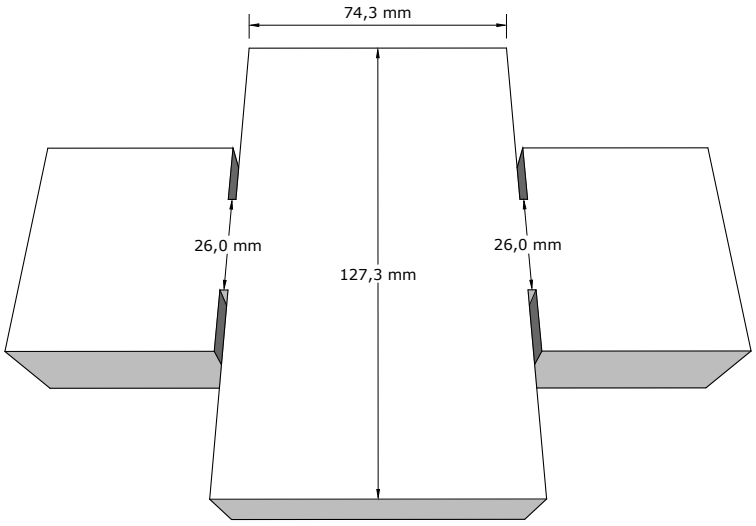

Figure 4.4: Dual-mode resonant cavity with the modes TE_{301} and TE_{201}.

Several advantages are provided by inductive dual-mode filters since their structure can be simpler than cylindrical waveguide implementing dual-mode filters. Moreover, the complete structure have inductive behavior, then the simulation and optimization process are extremely simple. In addition due to the all inductive configuration, this kind of dual-mode filters can be implemented quite easily by other technologies such as *Substrate Integrated Waveguide (SIW)* [Cassivi et al., 2002]. However these advantages come at the expense of reduced spurious free bands and some degradation in the unloaded Q, in spite of the fact that it is possible to change the Q_U factor by changing the waveguide height value [Guglielmi et al., 2001, Cameron et al., 2007].

Since the whole structure has an inductive behavior, the modal index relative to the cavity height has to be equal to zero. Thus, resonant modes in a inductive cavity can be:

$$\begin{aligned} First\ mode: &\quad TE_{m_1 0 p_1} \\ Second\ mode: &\quad TE_{m_2 0 p_2} \end{aligned} \tag{4.3}$$

Moreover, in order to provide a transmission zero, it is necessary to impose the above mentioned constraint. The first resonant mode has to see an electrical path of λ_g from the input to the output

meanwhile the second one a length of $\lambda_g/2$. In this way, the first mode field keeps the same sign in the output as in the input and the second mode changes the sign going from the input to the output. According to this condition: $p_1 = 2$ and $p_2 = 1$.

Indexes m_1 and m_2 must be chosen properly to be able to excite only the two desired modes. The most common options are using the TE_{301} and TE_{102} modes as well as the modes TE_{201} and TE_{102}. The first option gives a simpler structure because both modes can be excited by a non-offset iris[1]. This structure is the one shown in Figure 4.4. However the coupling level to the mode TE_{301} can not be adjusted independently of the coupling to the mode TE_{102}. The second option provides more freedom in the coupling level to each mode by adjusting the iris width and offset at a expense of a more complex structure. The required structure to use the modes TE_{102} and TE_{201} is shown in Figure 4.5. The fact of using coupling windows with offset makes the filter design more difficult and the filter response very sensitive to small changes in the filter dimensions.

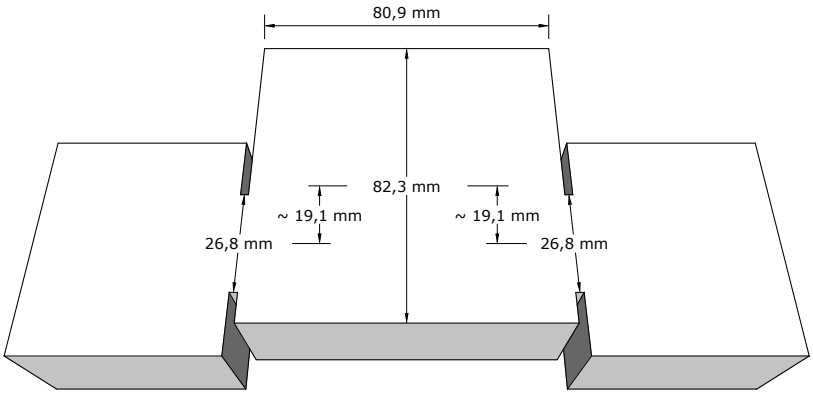

Figure 4.5: Dual-mode resonant cavity with the modes TE_{201} and TE_{201}.

Each one of the presented structures implements the second-order transversal topology shown in Figure 4.6. It can be seen that there is only coupling between the source and both resonant modes and between these modes and the output. Moreover, the resonant modes in the dual-mode cavity (modes 1 and 2 in Figure 4.6) have to be properly isolated. As a result both structures produce a second-order response with one transmission zero. Figure 4.7 shows the kind of response obtained with both dual-mode technologies.

Furthermore, it can be noticed the difference in the distance from the passband of the transmission zero provided by each technology. The technology with non-offset cavities introduced a transmission zero at a given distance from the passband that can not be controlled[2]. Conversely the technology with offset in the irises allows to adjust the zero position by changing the offset value.

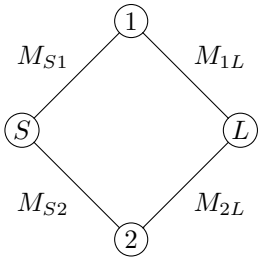

Figure 4.6: Coupling-routing diagram of a second-order inductive dual-mode filter.

[1]It can be proven that with a symmetrical aperture, only the resonant modes TE_{MN} or TM_{MN} are excited where M has to be an odd index and N an even index. If it is desired to excite the modes TE/TM_{QN} with Q even it is necessary to introduce some asymmetry in the XZ plane. Similarly, in order to excite the modes TE/TM_{MP} with P odd an asymmetry in the YZ plane is required. Thus only when there are some asymmetries in both XZ and YZ planes, the modes TE_{QP} or TM_{QP} ($TE_{01,02...}$; $TE/TM_{21,23...}$; etc.) are excited.

[2]In inductive dual-mode cavities, the distance from the passband of the transmission zeros is given by the relation between the coupling level to the first resonant mode (mode TE_{102}) and the coupling to the second mode (either the mode TE_{301} or TE_{201}). If it is not possible to vary this relation, then the relative distance from the passband of the transmission zeros will be fixed to a given value.

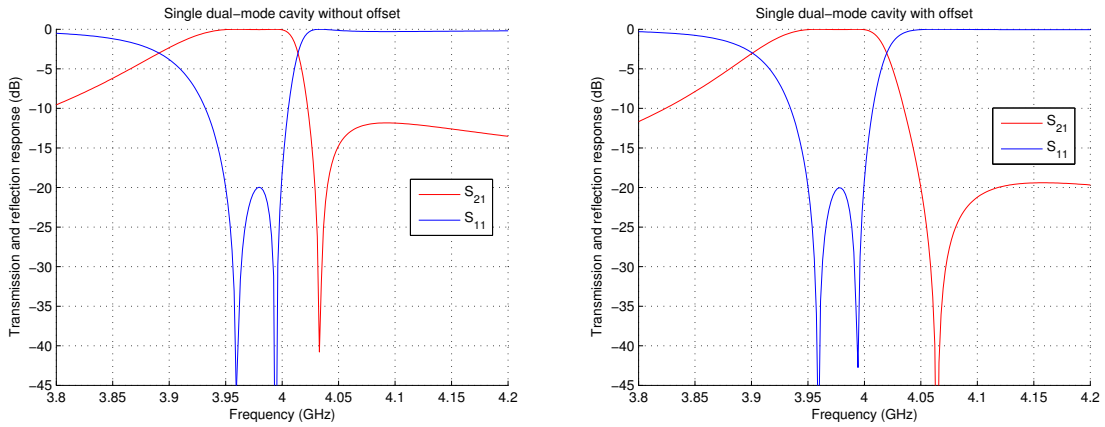

(a) With modes TE_{301} and TE_{102}.

(b) With modes TE_{201} and TE_{102}.

Figure 4.7: Electrical response of a single dual-mode cavity.

4.2.1 Technology with modes TE_{301} and TE_{102}.

This technology uses wider cavities with centered irises to excite the modes TE_{301} and TE_{102}. With regard to the modes TE_{101} and TE_{201}, the first one resonates at a too low frequency due to the physical dimensions of the cavity and the second one is not excited due to the centered input aperture.

This approach provides a simpler structure an a higher quality factor Q. However it is not possible to place the transmission zero as desired as the position of the transmission zero is given by the relation between the coupling to the first and second mode in the dual-mode cavity. Thus, since in this kind of cavities, the windows aperture varies both the coupling to the first and the second mode at the same time, the position of the transmission zero is fixed at a given frequency.

The behavior in Figure 4.7a is obtained with this technology where it is easy to know the resonant frequency of each mode and how the transmission zero is produced. Figure 4.8 shows the electric field patterns at frequencies in which each mode resonate and at the frequency where the transmission zero is produced.

4.2.2 Technology with modes TE_{201} and TE_{102}.

This technology allows more compact-size filters since the cavity width required by the mode TE_{201} to resonate at the desired frequency is lower than the width required by the mode TE_{301}. Moreover the coupling level to each mode is more controllable due to an available extra parameter which can be adjusted. In this structure it is possible to adjust irises width and offset to achieve the right coupling level to both modes TE_{201} and TE_{102}. For instance, if it is desired to increased the coupling to the mode TE_{201} while keeping the coupling level to the mode TE_{102}, then it is necessary to increase the windows aperture, what will raise the coupling to both modes. After that, by increasing the offset a higher coupling to the mode TE_{201} will be achieved at the expense of the coupling level to the mode TE_{102}. However, the main drawbacks is the more complex design process due to the extra parameters.

Figure 4.9 shows the size of this kind of cavities and the field patterns within them at different frequencies.

4.3 Coupling matrix topology for inductive dual-mode filters

Figure 4.10 shows the coupling-route diagram of a fourth-order filter with two dual-mode cavities interconnected by a single coupling window (Figure 4.11). This coupling window has to provide the right amount of straight couplings (M_{13} and M_{24}) and the proper cross-mode couplings (M_{23} and M_{14}) by itself. If it is desired to add more dual-mode resonators, the coupling iris which will interconnect the new resonator with the previous one has to provide the desired coupling value between both two modes in the last resonators and the two in the previous resonator.

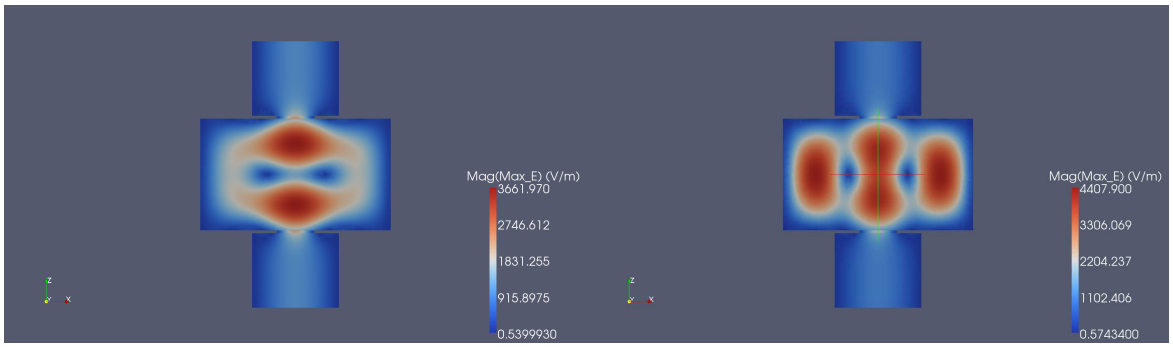

(a) First reflection zero (Mode TE_{102}). (b) Second reflection zero (Mode TE_{301}).

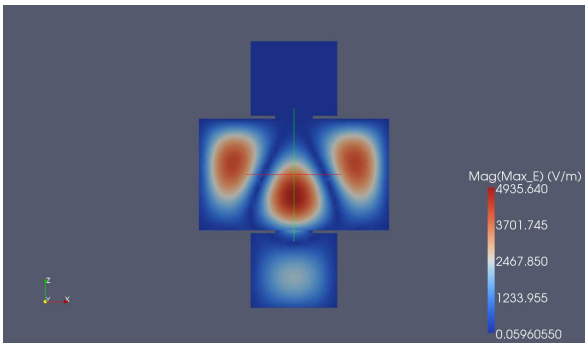

(c) Transmission zero.

Figure 4.8: Field patterns of a dual-mode cavity with the modes TE_{301} and TE_{102}.

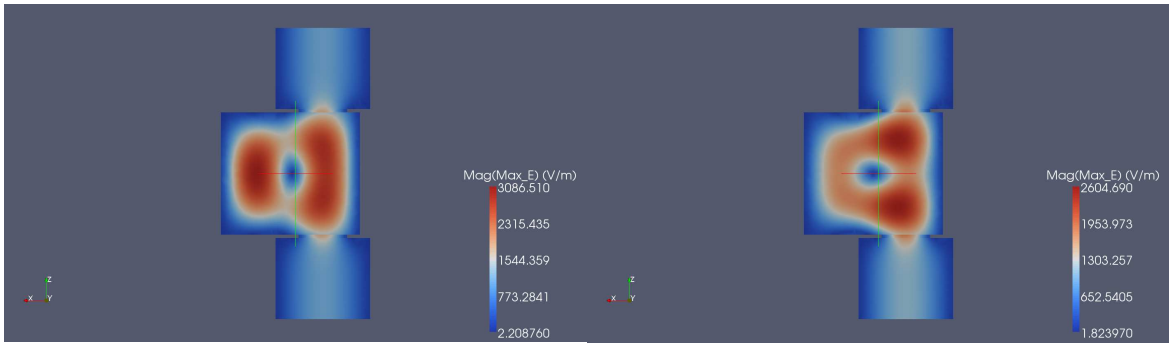

(a) First reflection zero (Mode TE_{102}). (b) Second reflection zero (Mode TE_{201}).

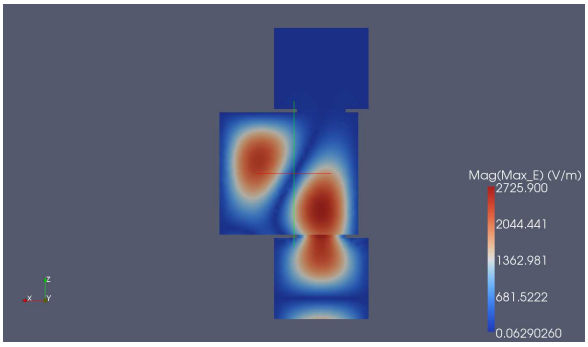

(c) Transmission zero.

Figure 4.9: Field patterns of dual-mode cavity with the modes TE_{201} and TE_{102}.

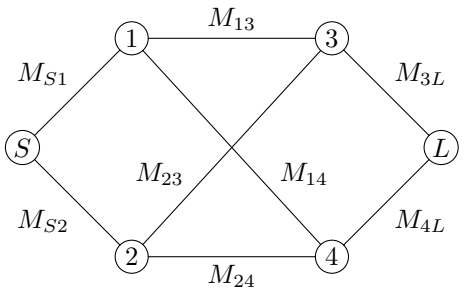

Figure 4.10: Coupling-routing diagram of a fourth-order inductive dual-mode filter with two dual-mode cavities.

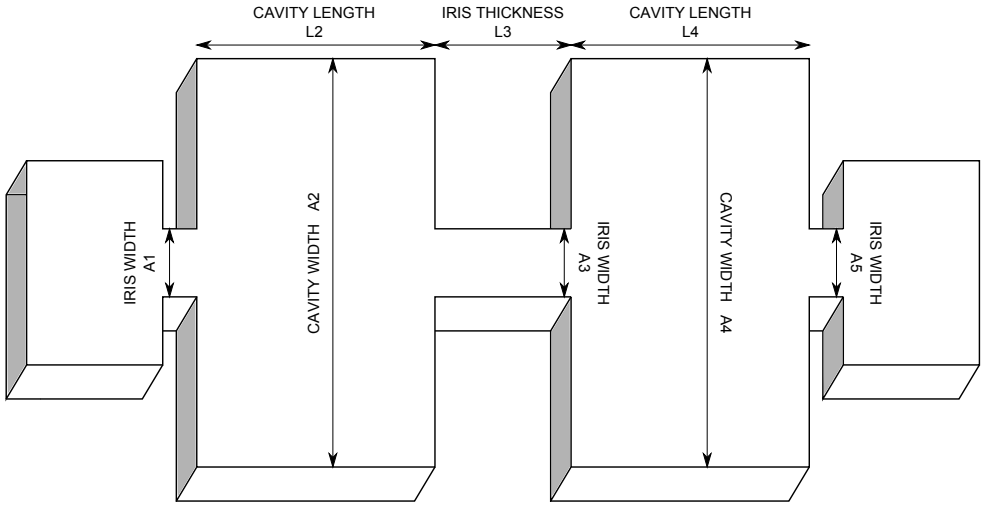

Figure 4.11: Dual mode fourth-order filter with two dual-mode cavities and parameters of its structure.

Figure 4.12 shows the generalized coupling route topology for dual-mode filters with only dual-mode cavities. In this diagram there are non-zero coupling values between each two modes in a dual-mode cavity and each mode in the next cavity as well as in the previous one. Moreover, the modes which resonate in a dual-mode cavity are isolated to each other. The coupling matrix shown in Figure 4.13 corresponds to a dual-mode filter formed only by dual-mode cavities (whose topology is shown in Figure 4.12). It can be seen that there is no coupling between the modes that resonate in the same cavity (modes 1 and 2, modes 3 and 4, modes 5 and 6...).

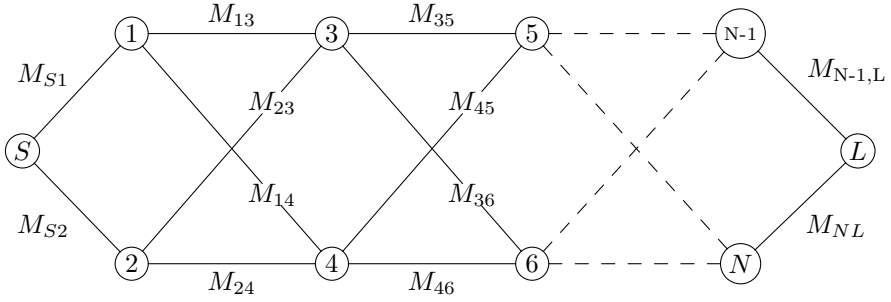

Figure 4.12: Generalized coupling-routing diagram for an inductive dual-mode filter with only dual-mode cavities.

$$M = \begin{bmatrix} 0 & M_{S1} & M_{S2} & 0 & 0 & 0 & 0 & 0 & \cdots & 0 & 0 \\ M_{1S} & M_{11} & 0 & M_{13} & M_{14} & 0 & 0 & 0 & \cdots & 0 & 0 \\ M_{2S} & 0 & M_{22} & M_{23} & M_{24} & 0 & 0 & 0 & \cdots & 0 & 0 \\ 0 & M_{31} & M_{32} & M_{33} & 0 & M_{35} & M_{36} & 0 & \cdots & 0 & 0 \\ 0 & M_{41} & M_{42} & 0 & M_{44} & M_{45} & M_{46} & 0 & \cdots & 0 & 0 \\ 0 & 0 & 0 & M_{53} & M_{54} & M_{55} & 0 & M_{57} & \cdots & 0 & 0 \\ 0 & 0 & 0 & M_{63} & M_{64} & 0 & M_{66} & M_{67} & \cdots & 0 & 0 \\ 0 & 0 & 0 & 0 & 0 & M_{75} & M_{76} & M_{77} & \cdots & 0 & 0 \\ \vdots & \vdots & \vdots & \vdots & \vdots & \vdots & \vdots & \vdots & \ddots & \vdots & \vdots \\ 0 & 0 & 0 & 0 & 0 & 0 & 0 & 0 & \cdots & M_{NN} & M_{NL} \\ 0 & 0 & 0 & 0 & 0 & 0 & 0 & 0 & \cdots & M_{LN} & 0 \end{bmatrix}$$

Figure 4.13: Coupling matrix of a dual-mode filter with only dual-mode cavities.

Finally, it should be commented that all coupling matrices for the dual-mode filters designed in this chapter have been obtained by applying rotations to the transversal coupling matrix as it is explained in [Mendoza et al., 2014].

4.4 Generalization of the design procedure

In the last chapter the step-by-step procedure was adapted to the context of the coupling matrix for in-line coupling topologies. However, by adapting the step-by-step [Guglielmi and Melcon, 1993, Guglielmi, 1994] technique to the coupling matrix, it is also possible to implement any coupling structure whose topology can be represented by the generalized coupling matrix shown in (4.4).

$$M = \begin{bmatrix} 0 & M_{S1} & M_{S2} & \cdots & M_{SN} & M_{SL} \\ M_{1S} & M_{11} & M_{12} & \cdots & M_{1N} & M_{1L} \\ M_{2S} & M_{21} & M_{22} & \cdots & M_{2N} & M_{2L} \\ \vdots & \vdots & \vdots & \ddots & \vdots & \vdots \\ M_{NS} & M_{N1} & M_{N2} & \cdots & M_{NN} & M_{NL} \\ M_{LS} & M_{L1} & M_{L2} & \cdots & M_{LN} & 0 \end{bmatrix} \tag{4.4}$$

Here, we do a generalization of the design approach for any coupling topology. Thus it can be used in the design of more complex coupling topologies, far beyond than the in-line filters already investigated.

As it is already reviewed, elements $M_{Si} = M_{iS}$ represent the input couplings from the source to the $i-th$ resonator, elements $M_{ij_{(i\neq j)}}$ represent the couplings between the $i-th$ and the $j-th$ resonators and $M_{jL} = M_{Lj}$ elements represent the output coupling from the $j-th$ resonator to

the load. Finally, elements in the main diagonal (M_{ii}) are related to frequency-invariant reactance (FIR) elements in both filter prototypes shown in Figure 4.14. These elements are used to introduce a frequency shift in the resonant frequency of each resonator with respect to the center frequency of the filter. They are needed in asynchronously tuned topologies.

The generalized coupling matrix in equation (4.4) represents the low-pass network shown in Figure 4.14a, when all matrix elements are normalized in the following form:

$$R_S = R_L = L_i = 1 \tag{4.5}$$

$$B_i = M_{ii} \tag{4.6}$$

It was discussed in chapter 2 that although this coupling matrix gives the total response of a given filter, in the application of the step-by-step procedure, the partial responses related to specific parts of the filter structure can not be extracted from the normalized coupling matrix. Therefore, coupling matrix scaling is necessary in order to be able to segment the global coupling matrix, and to obtain the right partial responses. The scaled coupling matrix will still represent the lowpass prototype shown in Figure 4.14a. However, inductors, FIR elements and loads of this lowpass prototype will be scaled using the information provided by the real resonators of the bandpass prototype shown in Figure 4.14b, This bandpass prototype is obtained with the classical bandpass to lowpass transformation [Matthaei and Yones, 1980, Cameron et al., 2007].

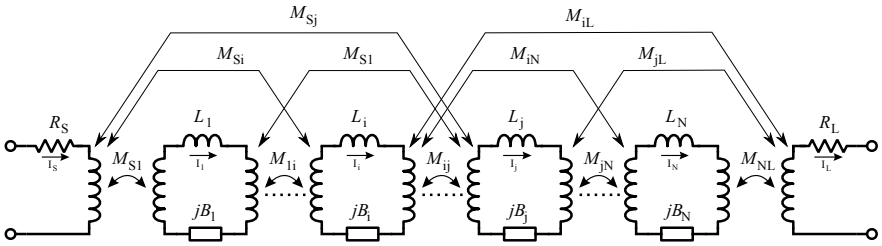

(a) Low pass prototype.

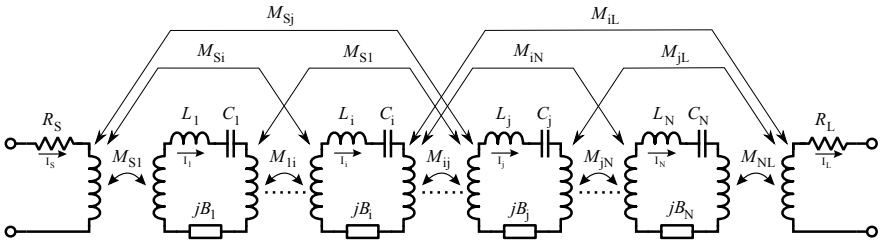

(b) Band pass prototype.

Figure 4.14: Lumped-elements prototypes.

4.4.1 Coupling matrix scaling

Firstly, it is necessary to scale the filter coupling matrix with the R_S, R_L and L_i values which better fit the physical technology in which this filter will be implemented. When this scaling is done, the matrix M' is obtained. It should be noted that it is necessary to distinguish two different cases as follows:

- Input and output element scaling.

$$M'^2_{S,i} = R_{IN} L_i M^2_{S,i} \tag{4.7}$$

$$M'^2_{i,L} = R_{OUT} L_i M^2_{i,L} \tag{4.8}$$

  where R_{IN} is the filter input impedance and the R_{OUT} the filter output impedance.

- Scale for other elements.

$$M'^2_{i,j} = L_i L_j M^2_{i,j} \tag{4.9}$$

This new matrix M' can be segmented to obtain the internal transfer functions of the filter. It is also important to note that the element M'_{ll} of a segment of size (lxl) has to be has to be set to zero because the resonant cavity that is taken as the filter output becomes a non-resonating node.

4.4.2 Computation of the lumped elements values

The only remaining task is to obtain the values R_{IN}, R_{OUT} and L_i to do the previously proposed scaling. These values must be obtained from the physical structure in which the desired band-pass filter will be implemented. Since the required values are from the lumped elements of the low-pass prototype, they can not be directly obtained from the filter structure as it implements a bandpass filter.

Therefore, firstly the values of the lumped elements of the band-pass prototype in Figure 4.14b are obtained from the filter structure and then the low-pass prototype in Figure 4.14a will be obtained by applying the "band-pass to low-pass" transformation. In this way, R_{IN} and R_{OUT} are just the band-pass filter input and output reference impedances and L_i elements are computed as follows:

$$L_i = \frac{\Delta}{\omega_1'} X_i = \frac{\Delta}{\omega_1'} \omega_0 Lr_i \tag{4.10}$$

where $\Delta = \frac{\omega_2 - \omega_1}{\omega_0}$ is the filter fractional bandwidth, $\omega_1' = 1$ the normalized cut-off frequency of the low-pass prototype and Lr_i the lumped inductances of the band-pass prototype obtained from the physical filter structure. Finally X_i refers to the slope parameter of each electrical resonator.

4.4.3 Example for waveguide technology

Here is an example of how the values Lr_i can be obtained from a band-pass filter in waveguide technology. As it is explained in chapter 2, it is necessary to get the value of the lumped elements in Figure 4.15b that provide the same slope parameter as the transmission line in Figure 4.15a. As both circuits resonate at the same frequency, equating the input impedances Z_{IN_i} and $Z_{IN_{i_{eq}}}$ at other frequency, for instance the upper cut-off frequency (ω_2),it is possible to get an approximate expression for the inductances in Figure 4.15b.

As it is known, the waveguide input impedance in Figure 4.15a at the frequency ω_2 is expressed by (4.11). Here, the right resonator in waveguide technology and the proper resonating mode $MODE = TE_{mnp}\ or\ TM_{mnp}$ must be considered.

(a) Transmission line equivalent.

(b) Lumped component equivalent.

Figure 4.15: Equivalent circuits to the waveguide resonator.

$$Z_{IN_i} = j \frac{\omega_2 \mu_0}{\beta_{2_{MODE}}} \tan\left(\beta_{2_{MODE}} \cdot l_0\right) \tag{4.11}$$

The propagation constant of the corresponding mode at the frequency ω_2 ($\beta_{2_{MODE}}$) is given by (4.12), l_0 by the equation (4.13) and λ_{g_0} is shown in expression (4.14).

$$\beta_{2_{MODE}} = \sqrt{\left(\omega_2 \sqrt{\epsilon\mu}\right)^2 - \left(\frac{m\pi}{a}\right)^2 - \left(\frac{n\pi}{b}\right)^2} \tag{4.12}$$

$$l_0 = \frac{\lambda_{g_0}}{2} p \tag{4.13}$$

$$\lambda_{g_0} = \frac{2\pi}{\beta_{MODE}(\omega = \omega_0)} \tag{4.14}$$

Finally, the input impedance for the LC lumped-element resonator in Figure 4.15b at the frequency ω_2 takes the following expression:

$$Z_{IN_{i_{eq}}} = j \frac{1}{\omega_0 Cr} \left(\frac{\omega_2}{\omega_0} - \frac{\omega_0}{\omega_2}\right) = j\omega_0 Lr \left(\frac{\omega_2}{\omega_0} - \frac{\omega_0}{\omega_2}\right) \tag{4.15}$$

In expression (4.15) as well as in (4.11), the upper cut-off frequency (ω_2) has been used in order to make the filter resonators to exhibit an inductive behavior. Equating (4.15) and (4.11) the expression for Lr_i is obtained, namely:

$$Lr_i = \frac{\omega_2 \mu_0}{\beta_{2_{TE_{mnp}}}} \tan\left(\beta_{2_{MODE}} \frac{\lambda_{g_0}}{2} p\right) \left[\omega_0 \left(\frac{\omega_{C2}}{\omega_0} - \frac{\omega_0}{\omega_{C2}}\right)\right]^{-1} \tag{4.16}$$

Once the coupling matrix is scaled, by using a step by step procedure, the first single iris can be dimensioned separately to obtain the coupling level to each mode in the first cavity given by the M_{Si} coupling elements. An additional difficulty in this step is to select a proper width for the dual mode cavity, which will act now as the output port. Remember that this width controls the resonant frequencies of the mode TE_{201}. Therefore, the exact width for this cavity is not known at this stage. A good strategy is to perform the optimization of the input iris taking the output waveguide width as an initial theoretical value. Theoretical width and length values of each dual-mode cavity are obtained by imposing that each mode in the cavity resonates at the same frequency with a slight frequency shift due to the FIR elements represented by the coupling matrix main diagonal.

We get the resonant frequency of both modes in each cavity with equation (4.17) and taking into account that $B = -M_{ii} \cdot BW$ in each dual-mode cavity.

$$fr_i = f_0 + \Delta f_i = \frac{1}{2} \cdot \left(B_i + \sqrt{B_i^2 + 4 \cdot f_0^2}\right) \tag{4.17}$$

Moreover, resonant frequency of each resonant mode in every waveguide cavity can be expressed as follow:

$$f_{r_i} = \frac{1}{2\sqrt{\epsilon\mu}} \sqrt{\left(\frac{m_i}{a}\right)^2 + \left(\frac{n_i}{b}\right)^2 + \left(\frac{p_i}{l}\right)^2} \tag{4.18}$$

where m_i, n_i and p_i are the modal index of the ith resonant mode in each dual-mode cavity. From expression (4.18) next equations are obtained, namely:

$$a^2 = \frac{m_i^2}{\epsilon_r \mu_r \left(2f_{r_i}\right)^2 - \left(\frac{n_i}{b}\right)^2 - \left(\frac{p_i}{l}\right)^2} \tag{4.19}$$

$$b^2 = \frac{n_i^2}{\epsilon_r \mu_r \left(2f_{r_i}\right)^2 - \left(\frac{m_i}{a}\right)^2 - \left(\frac{p_i}{l}\right)^2} \tag{4.20}$$

$$l^2 = \frac{p_i^2}{\epsilon_r \mu_r \left(2f_{r_i}\right)^2 - \left(\frac{m_i}{a}\right)^2 - \left(\frac{n_i}{b}\right)^2} \tag{4.21}$$

By applying the expression from (4.19) to (4.21) to each resonant mode i in a given cavity, it is possible to obtain the theoretical dimensions a, b, and l. With this theoretical values, the cavity dimensions are quite close to the final value. Thus, when segmenting a cavity with several modes within it, it is possible to dimension the input window using the theoretical cavity width and height. Then, when optimizing the whole cavity, its dimensions are adjusted taking theoretical parameters as initial values.

It should be noted that although the cavity length must be decreased due to the influence of the input and output aperture, the initial cavity width and height are quite close to its final value, thus the target partial responses obtained from the theoretical cavity width are still valid even though the cavity width is slightly modified in a later optimization step.

Finally, when the initial theoretical dimensions of all resonant cavities are known, it is possible to compute the target response for each mode in each cavity Then the step-by-step approach previously discussed [Guglielmi et al., 1991] can be applied. However it is necessary to take into consideration that in each step, if there are several modes in the output waveguide, then the coupling to all of these modes must be adjusted simultaneously[3].

[3]The main difference when segmenting the structure by a dual-mode cavity is that there are two modes propagating in the output port. Thus, both transmission parameters have to be adjusted, namely the transmission coefficient from mode 1 in the input waveguide to mode 1 in the output and from input the mode 1 to the output mode 2. Regarding the coupling matrix, it must be segmented to obtain the target partial responses for each resonant mode in the cavity by removing the row and column related to the other mode. In appendix D it is discussed how to optimize both resonant modes simultaneously by using the electromagnetic software FEST3D.

4.5 Inductive dual-mode filters design procedure

Currently dual-mode filters design is fairly complex due to the number of parameters to optimize and to the complex shape of useful filter responses. To get the right response of an inductive dual-mode cavity it is necessary to dimension both its width and length in order to adjust the resonant frequency of each mode that resonates in this cavity. This procedure can be simplified by using an intelligent design strategy.

Below, the design procedure presented in the last section is particularized for the all-inductive technology introduced for the first time by Guglielmi [Guglielmi et al., 2001]. Moreover, some filters are designed with different orders and transmission zeros. All filters designed in this chapter are centered at 3.9 GHz, in C-band, with 100 MHz bandwidth and a reflection level of -15 dB. These filters are feed by the standard waveguide $WR-229$ which has a width of 58.17 mm and a height of 29.083 mm. Furthermore, some filters implemented with both technologies introduced in sections 4.2.1 and 4.2.2 are presented. With these technologies the resonant modes are either the mode TE_{102} and the mode TE_{301} or the modes TE_{102} and TE_{201}.

First of all, the coupling matrix must be scaled before the step-by-step procedure can be applied. In order to scale the coupling matrix as it is already explained, it is important to match properly each element in the coupling matrix with each resonant mode in the filter structure. There are two possible options in each dual-mode cavity, matching the first row and column in the coupling matrix with the first resonant mode in the dual-mode cavity or vice versa.

In the normalized coupling matrix, the coupling element related to the first mode (TE_{10p_1}) is always greater than the one related to second one ($TE_{m_2 01}$). Thus the first mode in the cavity (TE_{10p_1}) is related to the higher coupling value and the second mode ($TE_{m_2 01}$) is related to the lower value.

Once this matching is right, the coupling matrix can be scaled by the same way as it is done for in-line filters.

- Input and output element scaling.

$$M'^2_{S,i} = R\frac{\Delta}{\omega'_1}X_i M^2_{S,i} = R\frac{\Delta}{\omega'_1}\omega_0 Lr_i M^2_{S,i} \tag{4.22}$$

$$M'^2_{i,L} = R\frac{\Delta}{\omega'_1}X_i M^2_{i,L} = R\frac{\Delta}{\omega'_1}\omega_0 Lr_i M^2_{i,L} \tag{4.23}$$

  where R is the characteristic impedance of the TE_{10} mode in the input and output waveguide.

- Scaling for other elements.

$$M'^2_{i,j} = \frac{\Delta}{\omega'_1}X_i\frac{\Delta}{\omega'_1}X_j M^2_{i,j} = \left(\frac{\Delta}{\omega'_1}\right)^2 \omega_0^2 Lr_i Lr_j M^2_{i,j} \tag{4.24}$$

When computing the inductances Lr_i it is necessary to consider the right resonant mode in the dual-mode cavity either the mode $TE_{m_2 01}$ or TE_{10p_1}. Then, the inductances of the BPP are expressed by (4.25).

$$Lr_{TE_{m_i 0 p_i}} = \frac{\omega_2 \mu_0}{\beta_{2_{TE_{m_i 0 p_i}}}} \tan\left(\beta_{2_{TE_{m_i 0 p_i}}}\frac{\lambda_g}{2}p_i\right)\left[\omega_0\left(\frac{\omega_{C2}}{\omega_0}-\frac{\omega_0}{\omega_{C2}}\right)\right]^{-1} \tag{4.25}$$

Finally, it is necessary to obtain the initial dimensions a and l of each dual-mode cavity in order to compute the propagation constant $\beta_{2_{TE_{m_i 0 p_i}}}$ of each resonant mode. By equating the expression (4.21) for both resonant modes in a dual-mode cavity and with the constraint that the eigenvalue relative to the dimension b is equal to zero, the formula (4.26) is obtained. Similarly, the formula (4.27) is obtained by equating the expression (4.19) for both resonant modes [Cameron et al., 2007].

$$a^2 = \frac{1}{2\epsilon\mu}\frac{(m_2 p_1)^2-(m_1 p_2)^2}{(p_1 f_{r_2})^2-(p_2 f_{r_1})^2} \tag{4.26}$$

$$l^2 = \frac{1}{2\epsilon\mu}\frac{(m_2 p_1)^2-(m_1 p_2)^2}{(m_2 f_{r_1})^2-(m_1 f_{r_2})^2} \tag{4.27}$$

4.6 Third-order dual-mode filter without offsets in the irises

As a first example, a simple third-order dual-mode filter is designed. It is formed by a dual-mode cavity with modes TE_{102} and TE_{301} and a single mode cavity with the resonant mode TE_{101}.

Figure 4.16 shows the desired filter structure in this section. Each parameter to optimize is also shown in Figure 4.16. The unknown parameters are the input and output iris width, the dual-mode cavity length and width, the single mode cavity length and the central iris width and length[4]. Other known parameters are the input and output irises thickness (2 mm), and single mode cavity width (58.17 mm as standard $WR-229$ used for the input and output waveguides). This structure implements the coupling topology shown in Figure 4.17.

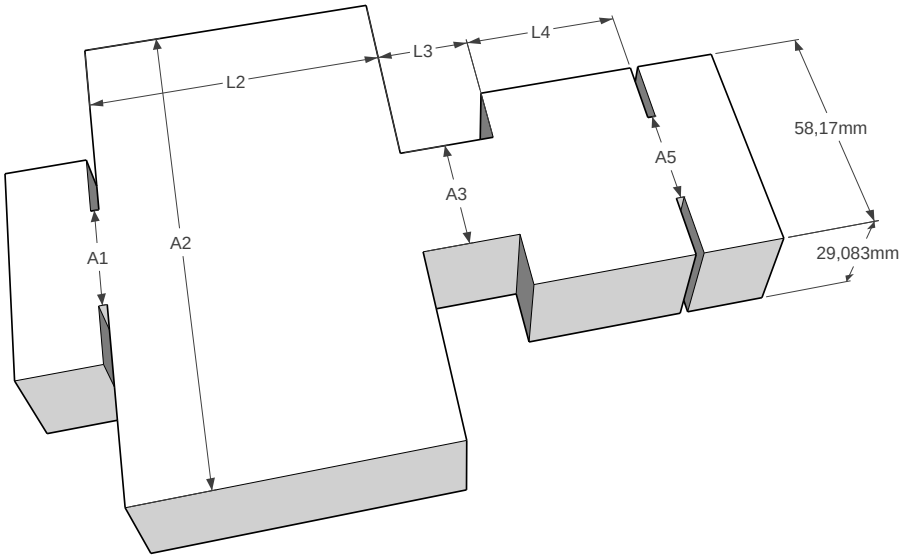

Figure 4.16: Desired filter structure and parameters to be optimized for the third-order dual-mode filter with non-offset irises (scaled drawing).

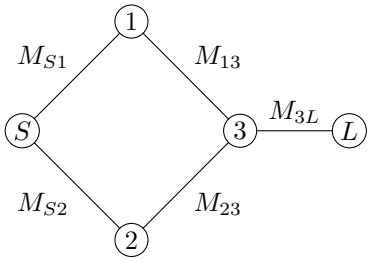

Figure 4.17: Coupling-routing diagram of a third-order dual-mode filter.

4.6.1 Filter specifications and coupling matrix scaling

This filter is centered at 3.9 GHz in C-band with 100 MHz bandwidth, a reflection level of -15 dB and also with a transmission zero above the filter passband. The coupling matrix in Figure 4.18a represents the above described third-order dual-mode filter. It should be commented that the synthesis of all coupling matrices presented in this work has been performed as it is described in [Mendoza et al., 2014].

[4]Even though the input and output coupling value can be obtained by adjusting only the input and output irises width, it should be noted that this is not true for the central iris. The reason is that the two irises of the dual-mode cavity have to exhibit a similar width in order to keep the orthogonality of the two modes excited in the dual mode cavity. If both dual-mode cavity apertures were too different, the field pattern in the dual-mode cavity would be distorted and it would not be possible to adjust the resonant frequency of both modes simultaneously. Thus, since the inner coupling values are smaller, it is necessary to increase the central iris thickness to achieve the required coupling value without making the irises width too much different.

$$M = \begin{array}{c} \begin{matrix} NR & TE_{102} & TE_{301} & TE_{101} & NR \end{matrix} \\ \begin{bmatrix} \mathbf{0} & 0.8101 & -0.4902 & 0 & 0 \\ 0.8101 & \mathbf{0.5548} & 0 & 0.8793 & 0 \\ -0.4902 & 0 & \mathbf{-1.0616} & 0.3048 & 0 \\ 0 & 0.8793 & 0.3048 & \mathbf{0.1216} & 0.9468 \\ 0 & 0 & 0 & 0.9468 & \mathbf{0} \end{bmatrix} \end{array}$$

(a) Original coupling matrix.

$$M' = \begin{array}{c} \begin{matrix} NR & TE_{102} & TE_{301} & TE_{101} & NR \end{matrix} \\ \begin{bmatrix} \mathbf{0} & 108.430 & -133.013 & 0 & 0 \\ 108.430 & \mathbf{19.637} & 0 & 31.465 & 0 \\ -133.013 & 0 & \mathbf{-155.628} & 21.752 & 0 \\ 0 & 31.465 & 21.752 & \mathbf{4.297} & 127.355 \\ 0 & 0 & 0 & 127.355 & \mathbf{0} \end{bmatrix} \end{array}$$

(b) Scaled coupling matrix.

Figure 4.18: Coupling matrix of the third-order dual-mode filter with a transmission zero above the passband.

In this matrix, the second and third rows and columns are related with both resonant modes in dual-mode cavity. In this matrix the coupling to each mode in the first dual-mode cavity is given by $M_{S1} = 0.81$ and $M_{S2} = -0.49$. Thus, the higher one (M_{S1}) is related to the mode TE_{102} and the corresponding column and row in coupling matrix have to be scaled with the TE_{102} mode slope parameters. Then, the row and column related to the second mode in the coupling matrix have to be scaled with the TE_{301} mode slope parameters.

Another possibility would be to pay attention to the sign of the coupling elements in the coupling matrix. As it is discussed in section 4.2, the mode TE_{301} changes the sign going from the input to the output while the TE_{102} keeps the same sign. Thus regarding to the signs in the coupling matrix, the column in which the sign changes from the input to the output of the dual-mode cavity corresponds to the mode TE_{301} meanwhile the column in which the sign does not change correspond to the mode TE_{102}. It can be seen in Figure 4.18a that the TE_{102} keeps the same sign from the input to the output coupling of the dual-mode cavity ($0.81 \rightarrow 8.88$) while the mode TE_{301} changes the sign ($-0.49 \rightarrow 0.3$).

Thus, there are two possibilities to identify the resonant modes related with each column and row in the coupling matrix. However, it will be easier to pay attention to the absolute value of the normalized couplings as the coupling to the mode TE_{102} will always be greater in the normalized coupling matrix as it is shown in Figure 4.19. It is a fact that the coupling to the mode TE_{301} increases when placing the transmission zero further from the passband, however the coupling to both modes in the dual-mode cavity (elements M_{S1} and M_{S2}) only reach the same value when the transmission zero is located at infinity (Figure 4.19).

The labels in Figure 4.18a indicates which mode corresponds to each column in the coupling matrix according to the matching done (The label NR refers to a non-resonating node). In this way, it is also possible to know which element of the main diagonal (highlighted in Figure 4.18a) is related to the frequency shifting of each resonant mode due to the above mentioned FIR elements.

Firstly, it is necessary to obtain the resonant frequency of each mode in the dual-mode cavity using the equation (4.17). Then, next results are obtained.

$$f_{r_1} = f_{0_1} + \Delta f_1 = \frac{1}{2} \cdot \left(B_{TE_{301}} + \sqrt{B_{TE_{301}}^2 + 4 \cdot f_0^2} \right) = 3.9534\ GHz \tag{4.28}$$

$$f_{r_2} = f_{0_2} + \Delta f_2 = \frac{1}{2} \cdot \left(B_{TE_{102}} + \sqrt{B_{TE_{102}}^2 + 4 \cdot f_0^2} \right) = 3.8726\ GHz \tag{4.29}$$

Knowing that BW=100 MHz, f_0=3.9 GHz and according to the matching done in Figure 4.18a:

$$B_{TE_{301}} = -M_{22} \cdot BW \tag{4.30}$$

$$B_{TE_{102}} = -M_{11} \cdot BW \tag{4.31}$$

Once the resonant frequencies are obtained, the initial dimensions of the dual-mode cavity are

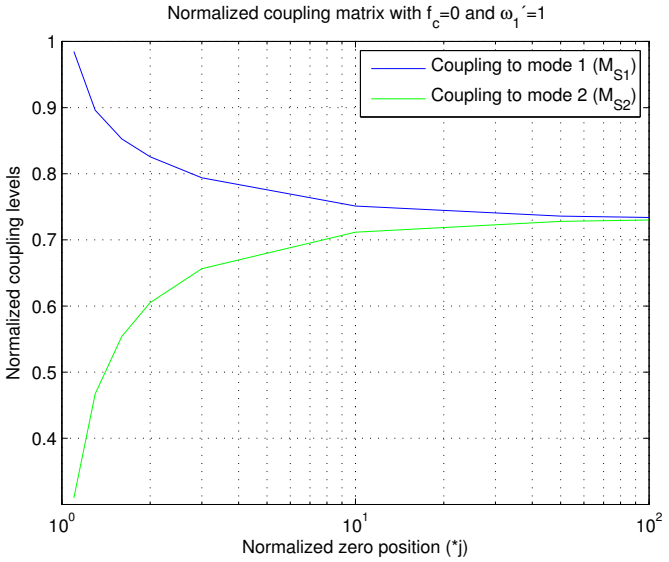

Figure 4.19: Coupling to the first mode (TE_{102}) and to the second one (either TE_{301} or TE_{301}) in a dual-mode cavity.

obtained from (4.26) and (4.27) namely:

$$a^2 = \frac{1}{2\epsilon\mu}\frac{(m_2p_1)^2 - (m_1p_2)^2}{(p_1f_{r_2})^2 - (p_2f_{r_1})^2} = 128.7\ mm \tag{4.32}$$

$$l^2 = \frac{1}{2\epsilon\mu}\frac{(m_2p_1)^2 - (m_1p_2)^2}{(m_2f_{r_1})^2 - (m_1f_{r_2})^2} = 81.2\ mm \tag{4.33}$$

Finally, by using the theoretical values above calculated, it is possible to obtain the propagation constant β of each resonant mode. Moreover through the expression (4.25), the values of the inductances needed to scale the coupling matrix in Figure 4.18a are obtained using the expressions from (4.22) to (4.24). The scaled coupling matrix is shown in Figure 4.18b.

4.6.2 Forward design

As opposed to the design of in-line filters where the filter structure is symmetric, the design of dual-mode filter has to be done forward and backward, since the structure is not symmetrical anymore. The forward design is performed by segmenting the filter structure from the input to the output. Since there are two resonant cavities, it is necessary to perform two forward steps.

- **First forward step.** In the first forward step, only the first coupling window is adjusted. It is shown in Figure 4.20a. The standard waveguide $WR-229$ is used as input waveguide and the theoretical value above calculate is used as the output waveguide width. At this point, it is not possible to optimize the width of the dual-mode cavity as it controls the resonant frequency of the mode TE_{301} within it. Since the mode TE_{301} is not resonating in this segment, there is no information in order to adjust the width of the cavity. However, the theoretical value calculated in equation (4.32) can be used to perform this step of the design procedure.

  Figures 4.21a and 4.21b show the matrices that provide the target response for the modes TE_{102} and TE_{301} respectively. However, as is can be noticed in Figure 4.22a, since there is only one parameter to adjust in this optimization, it is not possible to adjust the coupling to both modes at the same time. Thus, only the coupling to mode TE_{102} is reached in this step by adjusting the first iris width. The obtained iris width is shown in Table 4.1a.

  The aperture thickness is fixed to 2 mm and only the width is adjusted in order to achieve the desired coupling to both modes in the output waveguide namely modes TE_{10} and TE_{30}. Figure 4.22a shows the achieved result in this first design step. Here, the coupling to both resonant modes should be adjusted simultaneously to reach the responses provided by both coupling matrix segments in Figure 4.21 (see appendix D).

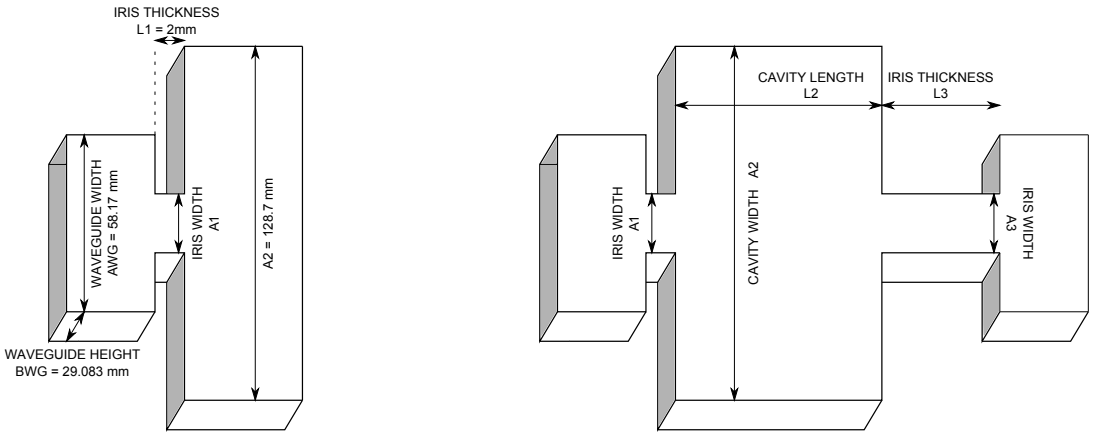

(a) First segment. (b) Second segment.

Figure 4.20: Filter segments in the forward design of the third-order non offset filter.

$$M' = \begin{bmatrix} NR & NR \\ 0 & 108.430 \\ 108.430 & 0 \end{bmatrix} \qquad M' = \begin{bmatrix} NR & NR \\ 0 & -133.013 \\ 108.430 & 0 \end{bmatrix}$$

(a) For output mode TE_{102}. (b) For output mode TE_{301}.

Figure 4.21: First segment of the coupling matrix for each resonant mode.

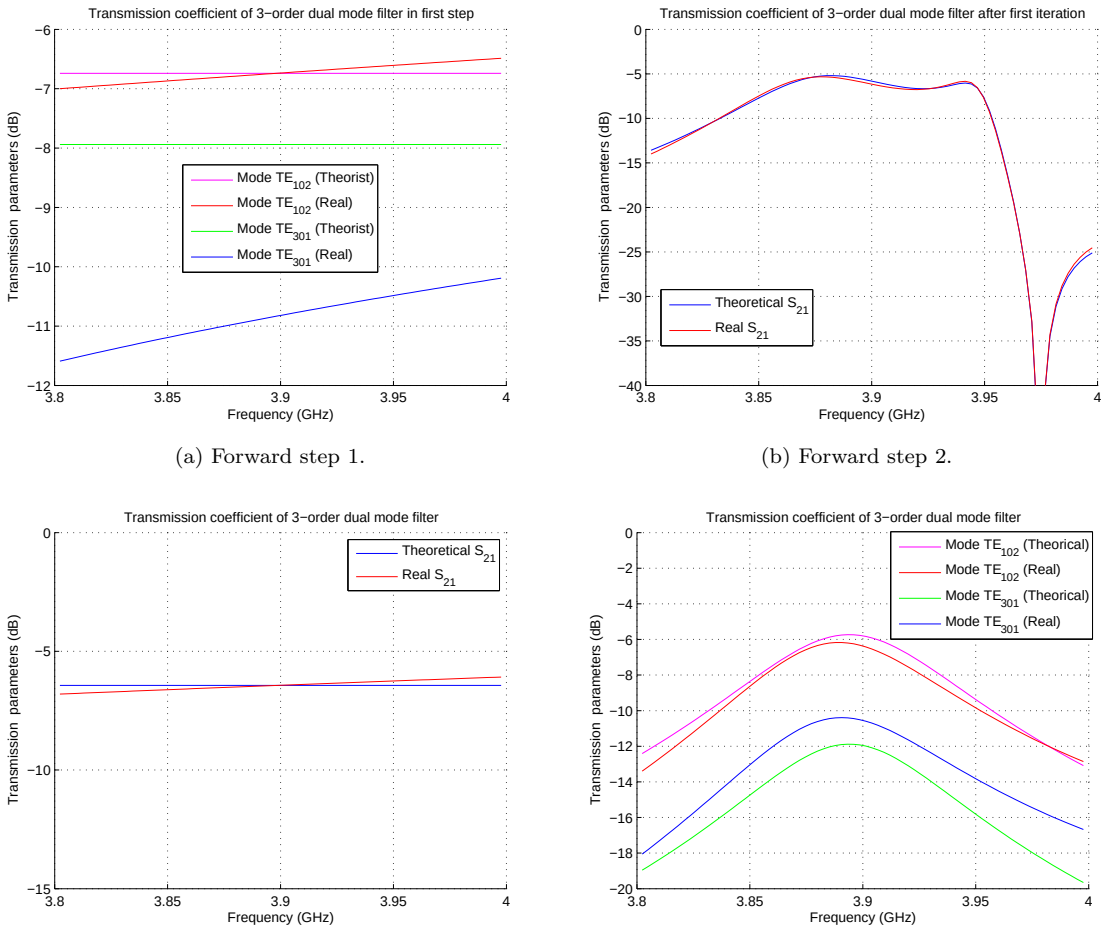

(a) Forward step 1. (b) Forward step 2.

(c) Backward step 1. iteration. (d) Backward step 2.

Figure 4.22: Real and theoretical response in each forward step of the third-order non-offset dual-mode filter.

- **Second forward step.** In step two, the second structure segment (Figure 4.20b) is added and a new optimization is performed with the parameters which have not been optimized in the previous step to reach the second partial target response. However, it is necessary to do an extra iteration and modify the first iris width in order to obtain the right result. This iteration is necessary since the interaction between adjacent elements are stronger in dual-mode filters in the same way as it was in wideband filters.

  Thus, in the first optimization, the parameters A_2, L_2, A_3 and L_3 shown in Figure 4.20b are adjusted while in the second optimization the parameter A_1 is also refined. The obtained parameters in each optimization are listed in Table 4.1a. In this case, since in this step there is only one resonant mode in the output cavity, the partial target response can be fitted perfectly as it can be seen in Figure 4.22. The scaled coupling matrix that provides the target response in this step is shown in Figure 4.23.

$$M' = \begin{array}{c} \begin{matrix} NR & TE_{102} & TE_{301} & NR \end{matrix} \\ \left[\begin{matrix} 0 & 108.430 & -133.013 & 0 \\ 108.430 & 19.637 & 0 & 31.465 \\ -133.013 & 0 & -155.628 & 21.752 \\ 0 & 31.465 & 21.752 & 4.297 \\ 0 & 0 & 0 & 0 \end{matrix}\right] \end{array}$$

Figure 4.23: Scaled matrix in the forward step 2 of the third-order dual-mode filter without offset.

4.6.3 Backward design

The next task is to segment the filter structure from the end to the beginning in order to make de design easier. Moreover, in the backward design of this filter there are only two parameters to optimize since the central iris dimensions are known from the forward design and it will be fixed in order not to perturb the partial response already archived.

- **First backward step.** As in the first forward step, in the first backward step there is only one parameter to optimize, namely the width of the filter output iris. The structure optimized in this step is shown in Figure 4.24a where the input and output waveguides are the standard waveguide $WR-229$ and the iris is 2 mm thick. The matrix in Figure 4.25 gives the target response for this segment.

  After optimizing the iris width, the parameter values in Table 4.1b and the transmission response in Figure 4.22c are obtained.

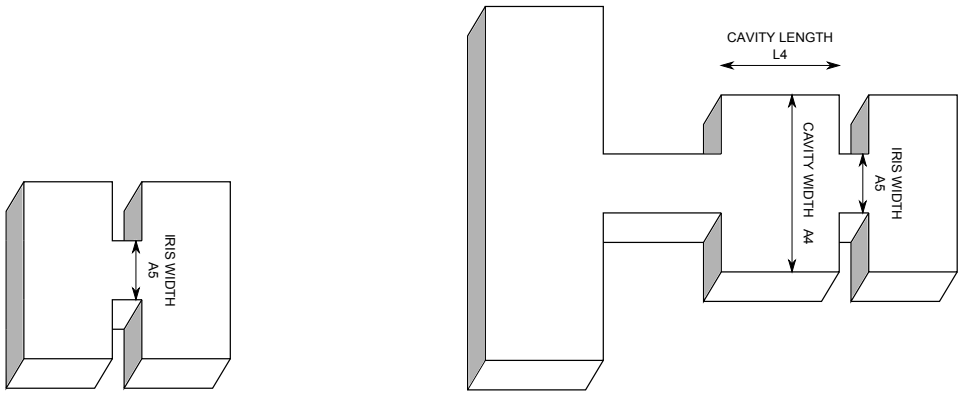

(a) First segment. (b) Second segment.

Figure 4.24: Filter segments in the backward design of the third-order non offset filter.

$$M' = \begin{array}{c} \begin{matrix} NR & NR \end{matrix} \\ \left[\begin{matrix} 0 & 127.355 \\ 127.355 & 0 \end{matrix}\right] \end{array}$$

Figure 4.25: Scaled matrix in the backward step 1 of the third-order dual-mode filter without offset.

- **Second backward step.** Here, the first cavity width and the central iris dimensions are known and fixed from the forward step. Thus, the parameters to optimize are only the ones shown in Figure 4.24b. In the same way as in the forward design, in first instance, only the cavity length and width are adjusted. Then a second iteration is performed to refine the last iris width (A_5). The target responses in this step are given by the coupling matrices in Figures 4.26a and 4.26b.

  Finally, the obtained dimensions are listed in Table 4.1b and the partial response provided by this segment is shown in Figure 4.22d. Again we can observe that the right coupling level is obtained only for the mode TE_{102}. As mentioned before, this is because with a centered iris it is not possible to adjust independently the coupling to the two modes of the dual mode cavity. Remember that this limitation is related to the impossibility to place the transmission zero at any arbitrary distance from the passband.

$$M = \begin{array}{c} \begin{matrix} TE_{102} & TE_{101} & NR \end{matrix} \\ \begin{bmatrix} 0 & 31.465 & 0 \\ 31.465 & 4.297 & 127.355 \\ 0 & 127.355 & 0 \end{bmatrix} \end{array}$$

(a) For mode TE_{102}.

$$M' = \begin{array}{c} \begin{matrix} TE_{301} & TE_{101} & NR \end{matrix} \\ \begin{bmatrix} 0 & 21.752 & 0 \\ 21.752 & 4.297 & 127.355 \\ 0 & 127.355 & 0 \end{bmatrix} \end{array}$$

(b) For mode TE_{301}.

Figure 4.26: Second matrix segment of the third-order dual-mode filter in the backward step 2.

Parameter	Initial	Step 1	Step 2
A1	30	29.2319	27.4388
A2	128.7		129.2186
L2	81.2		74.9663
A3	29.2379		29.8135
L3	20		24.8787

(a) Forward design.

Parameter	Initial	Step 1	Step 2
A5	24.8467	29.2319	24.9406
L4	40		39.8967
A4	58.17		
L3	29.8135		
A3	24.8787		
A2	129.2186		

(b) Backward design.

Table 4.1: Result of the optimized third-order non-offset filter parameters in each step.

4.6.4 Results

Once the forward and backward designs have been completed, the final filter structure can be composed using the parameters obtained in both forward and backward designs. Although the final response, shown in Figure 4.27a may not be as good as it would be desired, with an extra optimization in which only the parameters L_4 and A_5 are adjusted, the response in Figure 4.27b can be reached.

The final structure and its physical dimensions are shown in Table 4.2 and Figure 4.16.

Parameter	Value (mm)	Parameter	Value (mm)
A1	27.4531	L2	74.9603
A2	129.2196	L3	24.9089
A3	29.8232	L4	39.8272
A5	24.8965		

Table 4.2: Parameters value of filter structure in Figure 4.16.

4.7 Third-order dual-mode filter with offsets in the irises

Next designed example, is a third-order dual-mode filter with offset in the irises. It is formed by a dual-mode cavity with the modes TE_{102} and TE_{201} and a single mode cavity with the mode TE_{101}

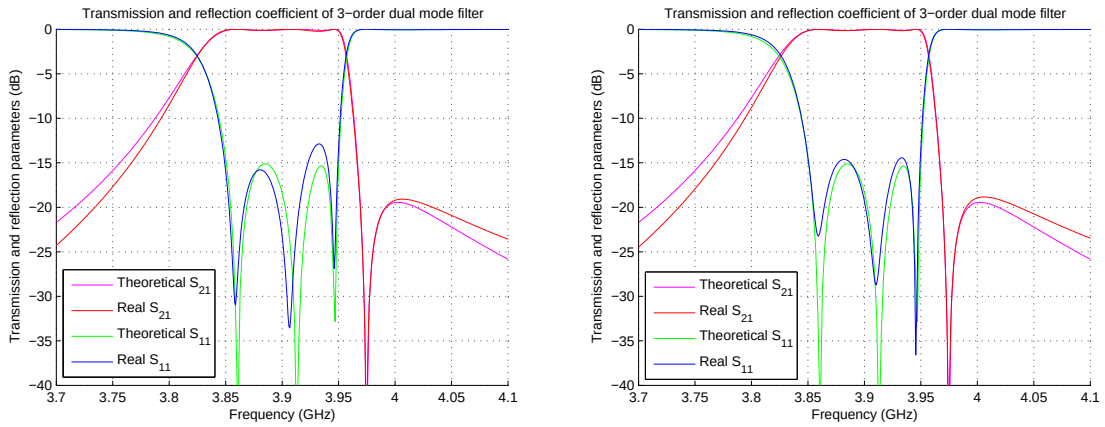

(a) After ensambling the complete filter.

(b) After a final optimization.

Figure 4.27: Final response of the third-order non-offset filter.

(Figure 4.28). This structure is quite similar to the one implemented in the previous example. However, in order to excite the mode TE_{201}, it is necessary to introduce offset in the input and output apertures of the dual-mode cavity (see section 4.2.1). Thus there are two more parameters to optimize which made the design process more complex.

In Figure 4.28 the parameters adjusted in this structure are shown namely the offset of both apertures of the dual-mode cavity, the irises width and the dual-mode cavity width and length. In addition the central iris thickness must also be adjusted in order to keep similar widths in the input and output iris of the dual-mode cavity as it happened in the previous example.

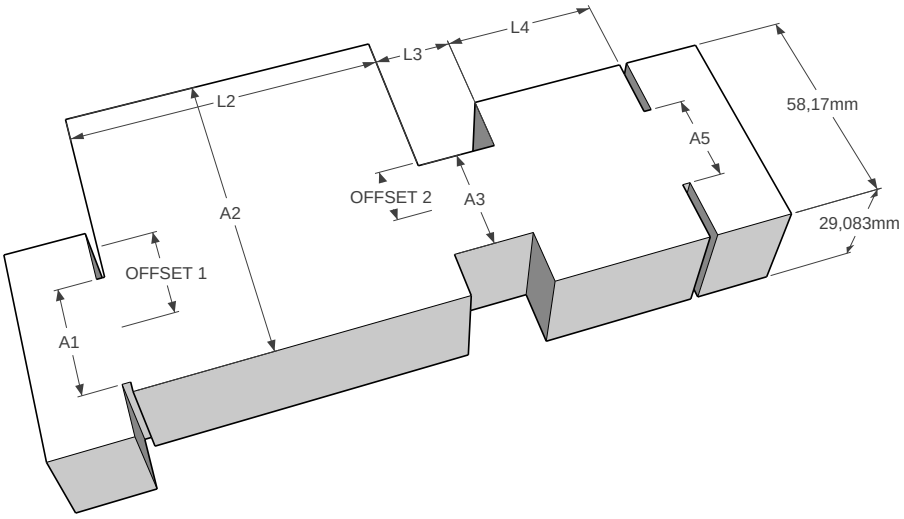

Figure 4.28: Filter structure of the third order dual mode filter with offset (scaled drawing).

4.7.1 Filter specification and coupling matrix

The band specifications are the same as in the previous example. This filter is centered at 3.9 GHz in C-band with 100 MHz bandwidth and a reflection level of -15 dB. The transmission zero is located above the filter bandpass again.

With this technology, it is possible to place the transmission zero further from the passband. Thus the response supplied by the coupling matrix in Figure 4.29 which introduces a more distant transmission zero from the passband, is implemented. In Figure 4.29, it is also indicated which resonant mode corresponds to each column of the coupling matrix. It can be noted that the coupling

to the mode TE_{102} ($|M_{S1}| = 0.7594$) is greater than the coupling to the mode TE_{201} ($|M_{S2}| = 0.5633$) as it is explained in the previous section.

$$M' = \begin{bmatrix} NR & TE_{102} & TE_{201} & TE_{101} & NR \\ \mathbf{0} & 0.7594 & -0.5633 & 0 & 0 \\ 0.7594 & \mathbf{0.6873} & 0 & 0.7908 & 0 \\ -0.5633 & 0 & \mathbf{-1.0158} & 0.4281 & 0 \\ 0 & 0.7908 & 0.4281 & \mathbf{0.0828} & 0.9455 \\ 0 & 0 & 0 & 0.9455 & \mathbf{0} \end{bmatrix}$$

Figure 4.29: Coupling matrix of the third-order dual-mode filter with with a more distant from the passband transmission zero from the passband.

The desired response given by the above introduced coupling matrix is shown in Figure 4.30. Moreover it is compared with the target function in the last example. It can be noted that both responses have identical in-band specifications. However the response for the filter with the TE_{201} mode provides a transmission zero further from the passband. Then a better rejection in the stop band is achieved at the expense of a lower frequency selectivity.

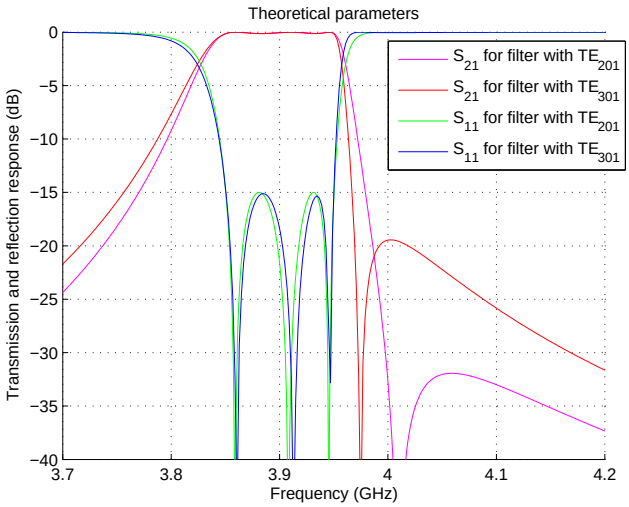

Figure 4.30: Ideal filter responses of the two last investigated filters..

4.7.2 Forward design

The first task to do is to get the initial values of the dual-mode cavity width and length that make the two modes resonate in the dual mode cavity at the right frequencies. Then it is necessary to scale the filter coupling matrix in order to get the target partial responses. By proceeding as described in the previous case and given that in this example $TE_{m_1 0 p_1} = TE_{102}$ and $TE_{m_2 0 p_2} = TE_{201}$ it is easy to obtain the theoretical dimensions of the dual-mode cavity with the expressions (4.35) and (4.35).

$$a^2 = \frac{1}{2\epsilon\mu} \frac{(m_2 p_1)^2 - (m_1 p_2)^2}{(p_1 f_{r_2})^2 - (p_2 f_{r_1})^2} = 84.3 \ mm \tag{4.34}$$

$$l^2 = \frac{1}{2\epsilon\mu} \frac{(m_2 p_1)^2 - (m_1 p_2)^2}{(m_2 f_{r_1})^2 - (m_1 f_{r_2})^2} = 87.4 \ mm \tag{4.35}$$

With these theoretical dimensions it is possible to obtain the lumped-elements of the low-pass prototype needed to scale the coupling matrix in Figure 4.29 in the same way as in previous example.

Next, as in the previous example, two forward steps are performed since this filter is composed of two cavities.

- **First forward step.** In the first step, the first coupling window is adjusted to achieve the proper coupling level to each mode in the dual-mode cavity as in the last example. However now there are two parameters (the first iris aperture and offset shown in Figure 4.31a). Both parameters must be adjusted in this first step to reach the target coupling value to each mode simultaneously.

In the structure shown in Figure 4.31a, the iris aperture controls the coupling level to both modes at the same time while by adjusting the offset, it is possible to change the relation between the coupling level to each mode. If the offset increases, the coupling to the mode TE_{201} will increase at the expense of the coupling to the mode TE_{102} and vice versa. Regarding to the iris thickness, it is again fixed to 2 mm thick.

It must be noted in Figure 4.32a that the obtained coupling levels to each mode in the first cavity do not reach the target coupling levels. Indeed, even though it could be possible to get the right coupling to both modes if the coupling to the TE_{201} mode was not higher than the coupling to the TE_{102} mode, the required coupling to second mode (TE_{201}) is too high due to the too further position of the transmission zero.

With such high coupling levels (about $-6.5\ dB$) it is not possible to obtain a coupling level to the second mode (TE_{201}) higher than the coupling to the first mode (TE_{102}). This is because in order to obtain such coupling levels it is required a coupling iris with a very large width, which limits the maximum available offset to the dual-mode cavity. In order to raise the coupling to the TE_{201} mode above the coupling level to TE_{102} mode, it is necessary to increase the width of the iris in order to get higher couplings to both modes and also to increase the offset to reduce the coupling to TE_{102} mode. Since the available maximum offset is limited and decreases when iris width increases, the maximum coupling level to the second resonant mode that can be obtained by keeping the coupling to the first mode is limited.

This issue that will be explained more in detail in chapter 6 is related with the maximum bandwidth that can be implemented with this structure, as the bandwidth is directly controlled by the filter input and output coupling levels.

Nevertheless, although the response shown in Figure 4.32a obtained after optimizing the parameters listed in Table 4.3a does not reach the goal, the obtained result is good enough to achieve the desired filter response as the first iris will be readjusted in the second iteration. Due to the stronger interactions in the dual-mode cavity, when the second segment is added to the filter structure, the first coupling may be affected. In order to compensate for this effect, it is necessary to decrease the aperture of the first window what leads to an extended available range for the offset, and thus for the position of the transmission zero. As a result, the partial response in the forward step 2 is properly fitted.

- **Second forward step.** In the second forward step, it is only necessary to optimize four parameters namely the dimensions of the dual-mode cavity (length and width), the offset of the second iris and its thickness. These parameters are shown in Table 4.31b. Moreover the first iris width and offset adjusted in the previous step are refined. This is done by two iterations in the same way as in the previous example.

  In the first iteration, the optimized parameters are the width and height of the dual-mode cavity and also the offset and the thickness of the dual-mode cavity output aperture. For that, the theoretical dual-mode dimensions above calculated are taken as starting points for this optimization. The initial value for the offset of the output aperture is taken from the previous step while the iris thickness is chosen to make the response closer to the target. The second iris width is fixed to be the same as the width of the first one. In this way, both apertures of the dual-mode cavity will keep the same width.

  In this step, the dimensions width ($A2$) and height ($L2$) control the resonant frequency of each mode. It is even possible to move the transmission zero to the other side of the passband by changing the resonant frequency of each mode in the dual-mode cavity. Indeed if the resonant frequency of the mode TE_{201} is lower than the resonant frequency of the mode TE_{102}, the transmission zero will be below the passband. However if the mode TE_{201} resonates above the mode TE_{102}, the transmission zero will be above the passband. With regard to the distance of the transmission zero from the passband, it is given by the second offset ($OFFSET2$). This parameter ($OFFSET2$) has to be similar to the first offset ($OFFSET1$) and the greater the second offset is, the further from the passband the transmission zero will be.

  In the second iteration, the previously optimized parameters are adjusted and also the first aperture width and offset are slightly modified to get the response shown in Figure 4.32b. The obtained parameters are listed in Table 4.3a. It can be noted that the first and second iris widths are fixed to the same value. As discussed previously this is needed to maintain orthogonality between the two modes excited in the dual-mode cavity.

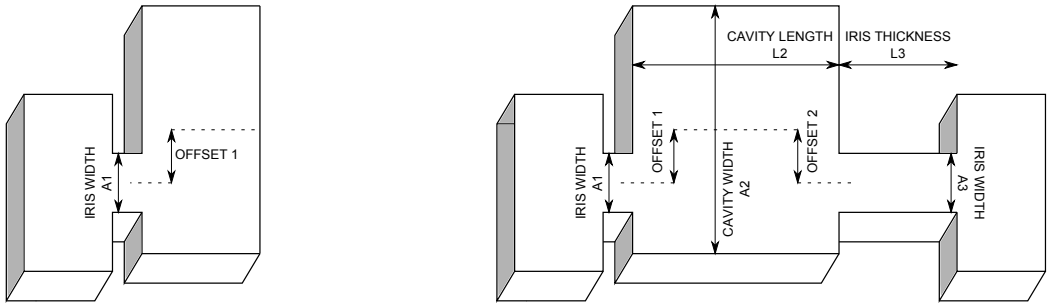

(a) First segment. (b) Second segment.

Figure 4.31: Filter segments in the forward design of the third-order filter with offset in the irises.

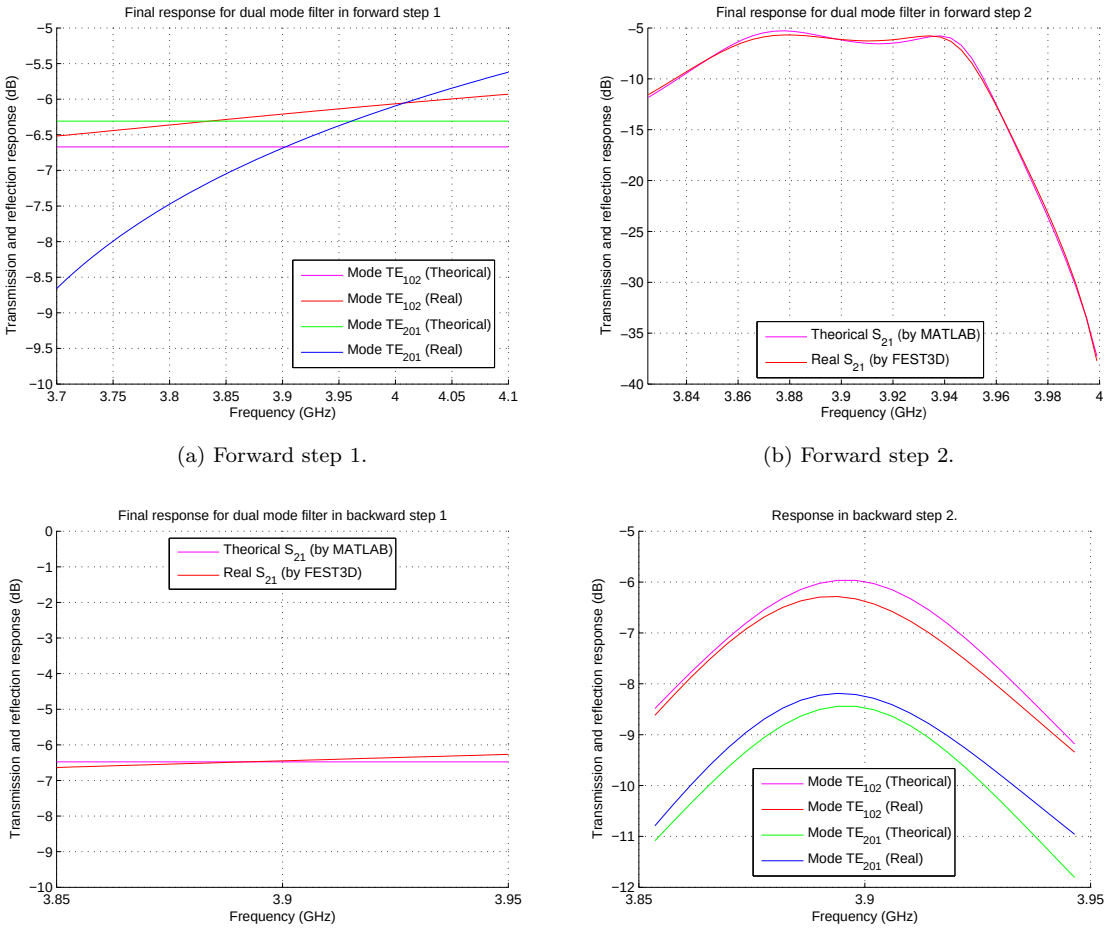

(a) Forward step 1. (b) Forward step 2.

(c) Backward step 1. iteration. (d) Backward step 2.

Figure 4.32: Real and theoretical response in each forward step of the third-order dual-mode filter with offset.

4.7.3 Backward design

The approach in the backward design is right the same as in the forward stages, however the design is easier due to the fewer parameters to optimize as the central iris dimensions will be fixed to the values obtained in the forward design.

- **First backward step.** Since the iris thickness is fixed to 2 mm, in this step there is one single parameter to optimize and only one resonant mode in the output cavity. Figure 4.33a shows the filter structure in this step while the partial response obtained can be seen in Figure 4.32c.
- **Second backward step.** The structure and the parameters adjusted in this step are shown in Figure 4.33b. The central iris and output cavity keep the size obtained in the forward design in order to avoid having to perform a global optimization. Thus, there are only two parameters to optimize and it is done in two iterations. Firstly the length of the single-mode cavity which is unknown is optimized. Then both parameters, the single-mode cavity length and the last iris width are adjusted.

  The obtained response is shown in Figure 4.32d and the adjusted parameters are listed in Table 4.3b. It can be noted that there is a small error in the level of the scattering parameters from Figure 4.32d. This issue will be addressed later.

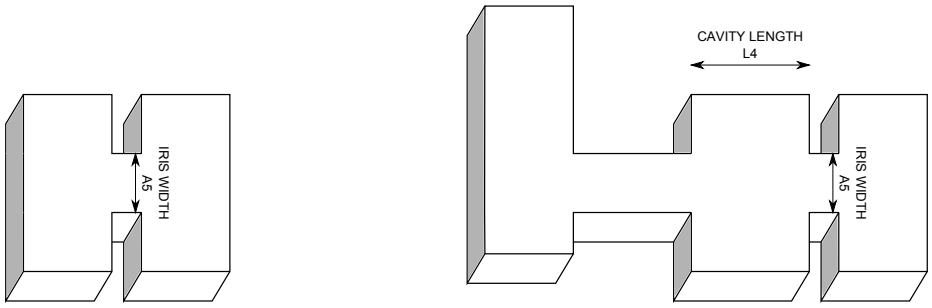

(a) First segment. (b) Second segment.

Figure 4.33: Filter segments in the backward design of the third-order filter with offset.

Parameter	Initial	Step 1	Step 2
A1 = A3	30	30.8173	29.4044
OFFSET 1	-15	-23.7414	-22.8208
A2	84.3		83.4674
L2	87.4		82.3651
L3	20		22.7716
OFFSET 2	23.7414		19.4357

(a) Forward design.

Parameter	Initial	Step 1	Step 2
A5	29.4044	24.8250	
L4	40		40.0433
A4	58.17		
L3	22.7716		
A3	29.4044		
A2 (Output)	83.4674		

(b) Backward design.

Table 4.3: Dimensions of the optimized third-order filter with iris offset in each step.

4.7.4 Results

Since the central iris parameters gotten in the forward stages have not been modified in the backward design, after assembling both halves of the filter structure, the obtained response is almost perfect and it is not necessary to do any more. The final structure and its physical dimensions are shown in Table 4.4 and Figure 4.28.

The final structure is shown in Figure 4.4. It can be noted that almost the maximum offset is applied in the input window. Thus the transmission zero can not be placed further from the passband in this structure with the given bandwidth. This is due to the the fact that the input iris is related to the filter bandwidth. This issue has already been discussed in section 3.3 and will be explained more in detail in chapter 6.

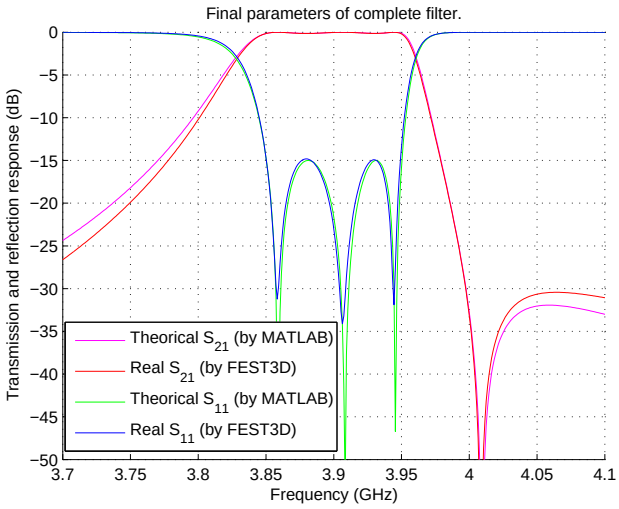

Figure 4.34: Final response of the third-order dual-mode filter with offset.

Parameter	Value (mm)	Parameter	Value (mm)	Parameter	Value (mm)
A1	29.4044	L2	82.3651	OFFSET 1	-22.8208
A2	83.4674	L3	22.7716	OFFSET 2	19.4357
A3	29.4044	L4	40.0433		
A5	24.8250				

Table 4.4: Parameters value of the filter structure in Figure 4.28.

4.8 Fourth-order dual-mode filter with two dual-mode cavities and offset technology

Next, a fourth-order filter is designed to validate the theory that is introduced in this chapter. This filter implements the coupling topology shown in Figure 4.10 and the filter structure is shown in Figure 4.35. It is composed of two dual-mode cavities with the modes TE_{201} and TE_{102} and with offset in the input and output apertures to both dual-mode cavities. The input and output irises will have similar dimensions while the central iris must be thicker in order to keep the same width as the input or the output one.

Since all irises apertures have to be similar in width and in order to make the design easier, the width of all coupling windows will be fixed to the same value. This value is the one obtained in the forward design.

4.8.1 Filter specifications and coupling matrix

The filter is centered at 3.9 Ghz in C-band with 100 MHz bandwidth and a reflection level of -15 dB. Also, this filter provides two transmission zeros in both passband edges improving in this way the filter selectivity. The desired response for this filter is given by the $(6x6)$ coupling matrix in Figure 4.36a which exhibits the "all-dual-mode" topology shown in Figure 4.13.

The first issue in this example, is to match each mode in each dual-mode cavity with the proper coupling value in the dual-mode matrix. In the forward design, since the coupling value $M_{S1} = -0.7458$ is higher than the value $M_{S2} = -0.5106$, the first mode in the coupling matrix corresponds to the mode TE_{102} in the resonant cavity and the second mode in the coupling matrix is related to the TE_{201} mode.

The same happens in the backward design, the coupling $M_{L3} = 0.5046$ refers to mode TE_{201} and the coupling $M_{L4} = -0.7499$ is related to the fundamental mode (TE_{102}). Thus, the matrix in Figure 4.36b is obtained after scaling the above coupling matrix.

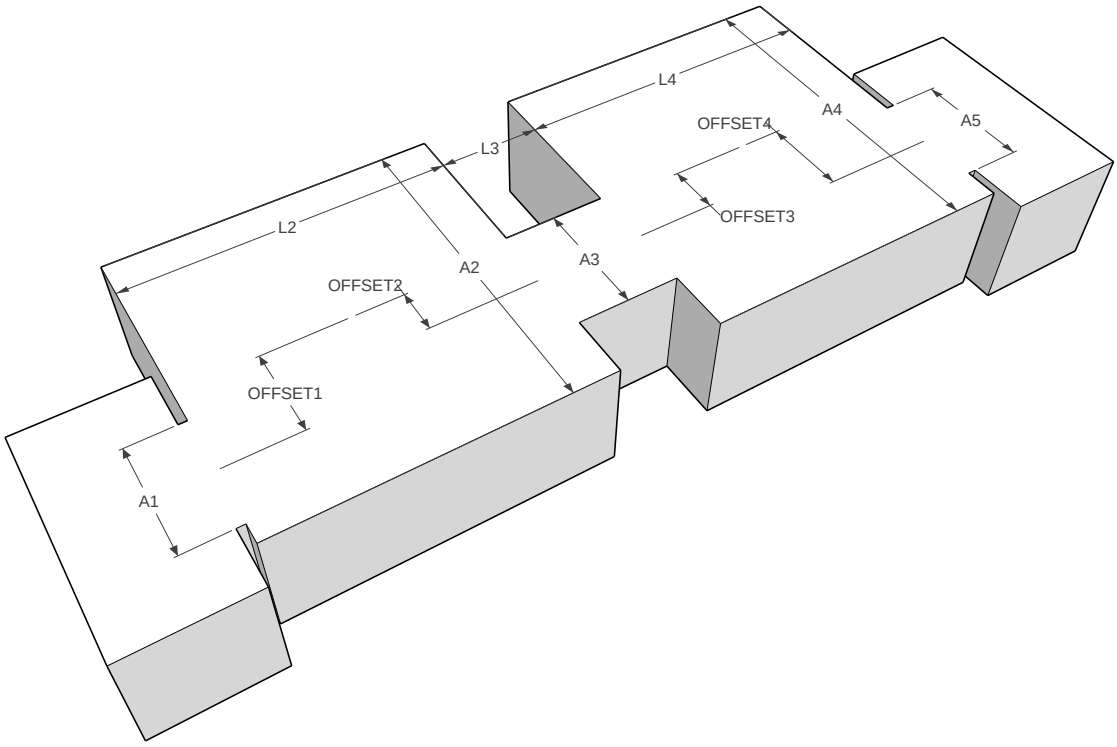

Figure 4.35: Filter structure of the fourth-order filter with two transmission zeros (scaled drawing).

$$M = \begin{bmatrix} \boldsymbol{NR} & \boldsymbol{TE_{102}} & \boldsymbol{TE_{201}} & \boldsymbol{TE_{201}} & \boldsymbol{TE_{102}} & \boldsymbol{NR} \\ \mathbf{0} & -0.7458 & -0.5106 & 0 & 0 & 0 \\ -0.7458 & \mathbf{-0.4743} & 0 & -0.2441 & -0.5770 & 0 \\ -0.5106 & 0 & \mathbf{1.0160} & 0.1081 & 0.2555 & 0 \\ 0 & -0.2441 & 0.1081 & \mathbf{-1.0197} & 0 & 0.5046 \\ 0 & -0.5770 & 0.2555 & 0 & \mathbf{0.4637} & -0.7499 \\ 0 & 0 & 0 & 0.5046 & -0.7499 & \mathbf{0} \end{bmatrix}$$

(a) Original coupling matrix.

$$M' = \begin{bmatrix} \boldsymbol{NR} & \boldsymbol{TE_{102}} & \boldsymbol{TE_{201}} & \boldsymbol{TE_{201}} & \boldsymbol{TE_{102}} & \boldsymbol{NR} \\ \mathbf{0} & -107.5500 & -138.8788 & 0 & 0 & 0 \\ -107.5500 & \mathbf{-19.6525} & 0 & -20.9941 & -24.6033 & 0 \\ -138.8788 & 0 & \mathbf{149.7591} & 17.5356 & 20.5483 & 0 \\ 0 & -20.9941 & 17.5356 & \mathbf{-182.0387} & 0 & 151.0422 \\ 0 & -24.6033 & 20.5483 & 0 & \mathbf{20.3472} & -111.2866 \\ 0 & 0 & 0 & 151.0422 & -111.2866 & \mathbf{0} \end{bmatrix}$$

(b) Scaled coupling matrix.

Figure 4.36: Coupling matrix of the fourth-order dual-mode filter with two transmission zeros.

4.8.2 Forward design

Firstly, it is necessary to get the initial values to be used in both cavities from equations (4.26) and (4.27). Thus, the theoretical values of both dual-mode cavities are the ones listed in Table 4.5.

As it happened in the previous examples, the theoretical width of both dual-mode cavities will be quite close to the final width. However this fact is not valid for the length of the cavities. Due to the thickness of the central iris, the electrical lengths of the cavities is enlarged and it is necessary to decrease the lengths of both cavities in order to compensate for this effect.

	First cavity	Second cavity
Width (mm)	87.7	84.4
Length (mm)	85	87.1

Table 4.5: Theoretical dimensions of the dual-mode cavities.

- **First forward step.** In the first forward segment, the first aperture thickness is fixed and only the iris width and the input offset to the first dual-mode cavity are adjusted. Values of 2 mm for the iris thickness and 87.7 mm for the first cavity width (output port in the step 1) are taken in this step. The structure of the segment in this step is shown in Figure 4.37a.

  In this step, it is quite easy to adjust the first iris width and offset to obtain the response shown in Figure 4.38a. Here, the offset controls the relation between the coupling to the first and the second mode meanwhile the iris aperture controls the coupling to both modes in the same way as in the previous example. Since this filter is composed only by dual-mode cavities, all coupling windows must have the same width. Thus all irises width will be fixed to the width obtained in this step, shown in Table 4.6a.

- **Second forward step.** The approach in this step is similar to the design procedure of the second forward segment in the previous section since it is necessary to optimize both the width and length of the first dual-mode cavity and the thickness and offset of the central iris, as well as to refine the first iris and offset adjusted in the previous step by a second iteration. However there are some important differences.

  Firstly, the width of the standard waveguide can not be used in the output port. Instead the theoretical width of the second dual-mode cavity, above calculated (84.4 mm) will be used. This is because the mode TE_{201} needs to be excited.

  Secondly, the output offset needs to be adjusted in order to excite the mode TE_{201}. Thus, there are five parameters to optimize in the first iteration, namely the width and length of the first dual-mode cavity and the thickness and both offsets of the central iris. These parameters are listed in Table 4.6a while the filter structure is shown in Figure 4.37b. With the dimensions of the dual-mode cavity it is possible to adjust the resonant frequency of each mode while the second offset controls the position of the transmission zero from the passband as it was explained in the previous example. However the extra parameter in this design controls the coupling to each mode in the output waveguide. The output offset ($OFFSET3$) controls the relations between the coupling to each mode and the iris thickness ($L3$) the coupling to both ones. Thus it is necessary to adjust the output offset to get the right separation between both curves in Figure 4.38b while the coupling level and shape can be achieved by adjusting the iris thickness ($L3$).

  Finally, a second iteration is performed to refine the first iris and there is another difference with the previous example. Since the irises thickness is fixed to the value obtained in the previous step (28.2723 mm), in order to adjust the first coupling, the first iris thickness is slightly modified. As it was already discussed, the coupling in the first iris will be lowered in this iteration, thus it is necessary to increase the iris thickness. As a result the parameters adjusted in the second iteration are the first iris thickness and offset, the dual-mode cavity width and length as well as the thickness and both offsets of the second iris. After that, the partial response achieved in this step is shown in Figure 4.38b.

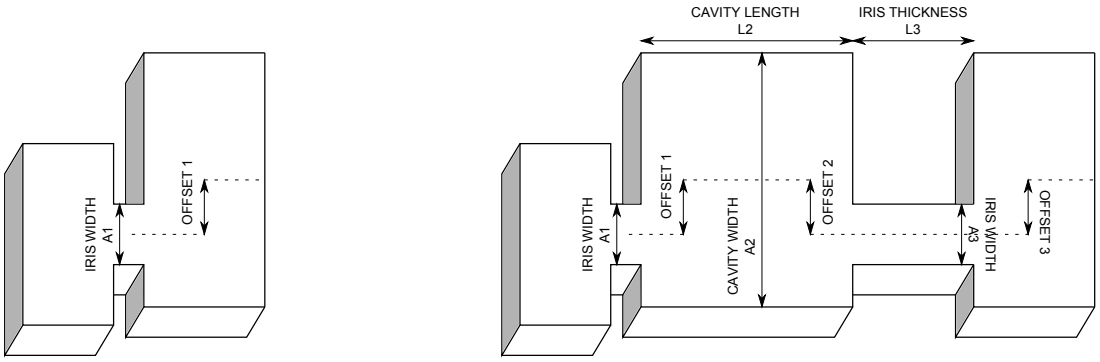

(a) First segment.

(b) Second segment.

Figure 4.37: Filter segments in the forward design of the fourth-order filter whit two transmission zeros.

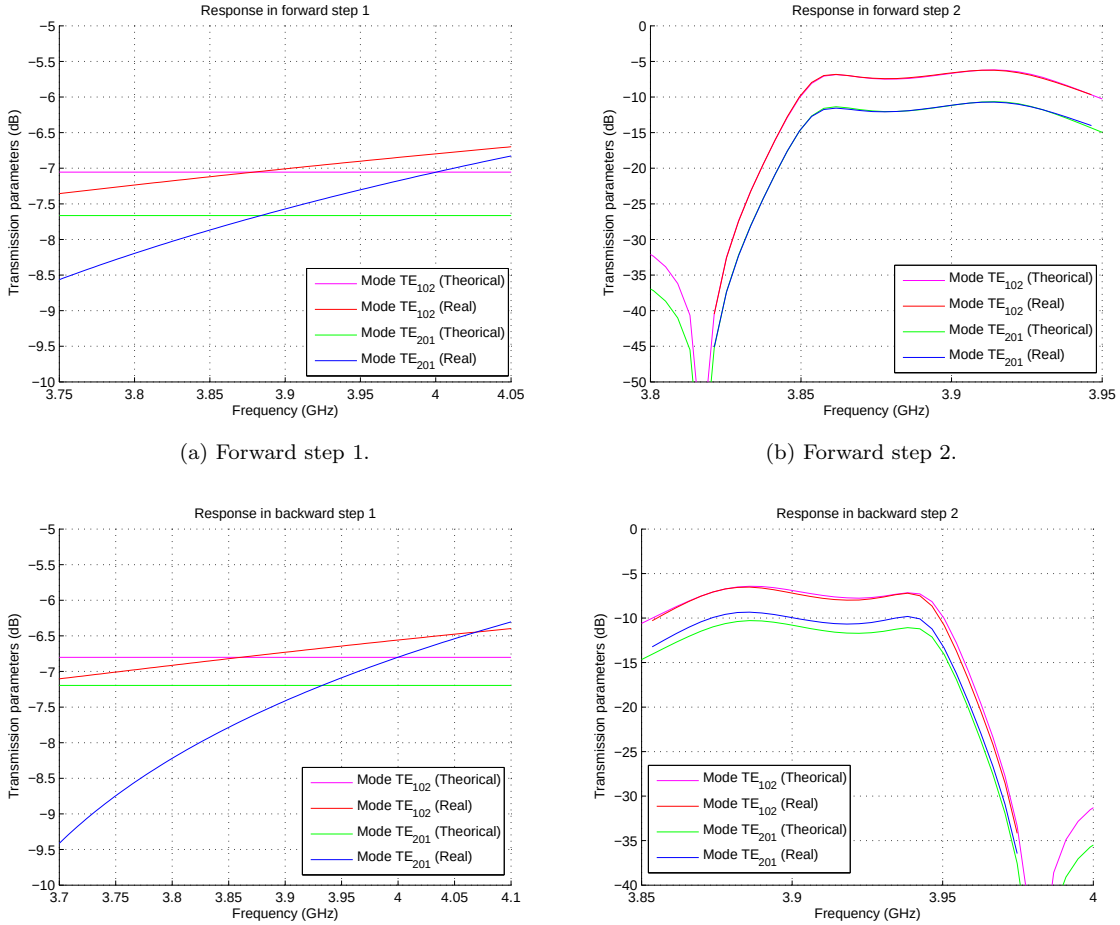

(a) Forward step 1.

(b) Forward step 2.

(c) Backward step 1. iteration.

(d) Backward step 2.

Figure 4.38: Real and theoretical response in each step of the fourth-order dual-mode filter with two transmission zeros.

4.8.3 Backward design

In the same way as in the forward design, the backward design is composed of two steps and each one will be equally performed by two iterations.

- **First backward step.** The approach in the first backward step is the same as in the first forward step. However the width of the output waveguide is taken from the theoretical width of the second cavity. Moreover, the width of the last iris is fixed to the same value as the first and second one. Thus the thickness of the last iris ($A5$) and last offset ($OFFSET4$) are adjusted in order to reach the target coupling levels.

  The parameters optimized in this step are shown in Figure 4.39a and Table 4.6b meanwhile the partial response obtained is shown in Figure 4.39a.

- **Second backward step.** In this example, the filter is designed starting from the forward stage. Thus the parameters of the central iris and the central offsets are fixed to the dimensions obtained in the forward design and there will be necessary to adjust only four parameters. The width and height of the dual-mode cavity ($A4$ and $L4$) as well as the thickness of the last iris ($L5$) and the last offset ($OFFSET4$). Parameters $A4$ and $L4$ control the resonant frequency of each mode within this cavity and will be optimized in a first iteration. In a second iteration these dimensions will be readjusted together with parameters $L5$ and $OFFSET4$.

  The structure in this step is shown in Figure 4.39b and the parameters adjusted are listed in Table 4.6b.

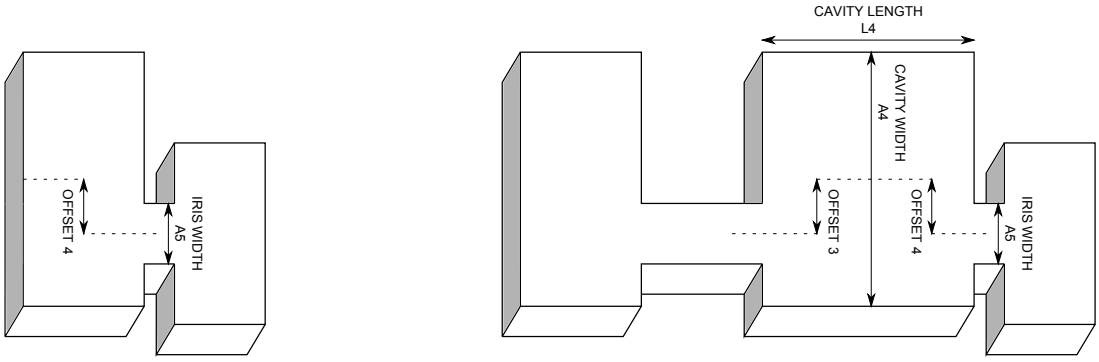

(a) First segment.

(b) Second segment.

Figure 4.39: Filter segments in the backward design of the fourth-order filter with two transmission zeros.

It should be noted in the result shown in Figure 4.38d that there is a small error in the obtained target response. This error is not in the response shape but in the level. In fact, this error will exist in the last step of all filters of this kind. The source of this error, for the moment remains unknown.

Moreover, this result indicates that the design is properly performed. It has been observed that when the shape of the target response is incorrect after the last step, then the global design will fail. If this happens, then it is necessary to perform the design starting from the other side. In that case, the backward design should be performed first and the dimensions obtained for the central iris should be kept when performing the forward design.

As it is already said, this issue will be discussed more in detail in chapter 6.

4.8.4 Results

When performing the backward design, the final result shown in Figure 4.40a is achieved after binding together both halves of the filter structure.

Table 4.7a shows the parameters value after performing the design procedure. If it is desired to refine this response, it can be possible to do a global optimization to adjust all parameters. However, it is important to remember that all irises widths should remain unchanged.

After a global optimization, the response in Figure 4.40b is obtained. The final structure and its physical dimensions are shown in Table 4.7b and Figure 4.35.

Parameter	Initial	Step 1	Step 2
A1=A3=A5	30	28.2723	
OFFSET 1	-15	-21.3424	-20.8709
L1	2		2.6688
A2	87.7		87.2401
L2	85		79.3510
L3	20		20.2667
OFFSET 2	15		16.6338
OFFSET 3	-15		-13.1863
A4 (Output port)	84.4		

(a) Forward design.

Parameter	Initial	Step 1	Step 2
L5	2	1	1.9153
OFFSET 4	20.8709	22.3673	22.9560
A4	84.4		84.0647
L4	87.1		81.5282
L3	20.2667		
A1=A3=A5	28.2723		
OFFSET 3	-13.1863		
OFFSET 2	16.6338		
A2 (Output port)	87.2401		

(b) Backward design.

Table 4.6: Dimensions of the optimized fourth-order filter with two transmission zeros in each step.

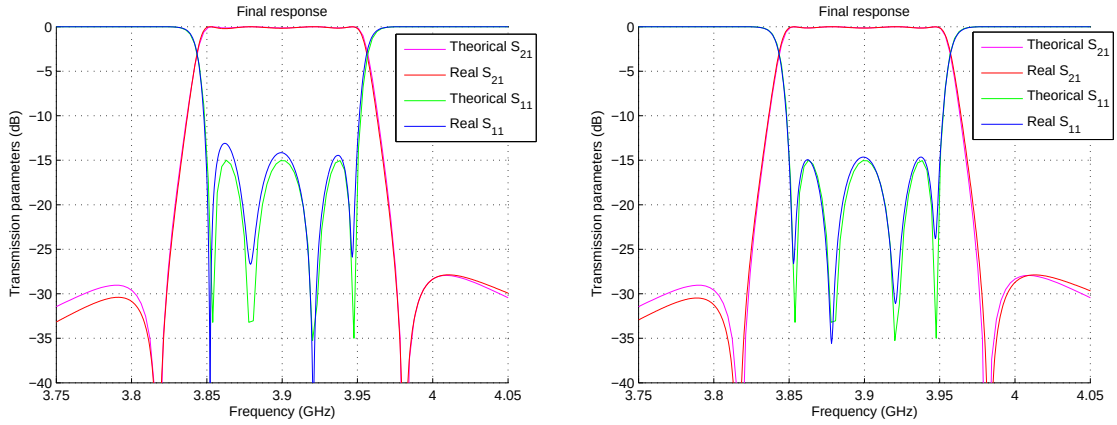

(a) Result of the design approach.

(b) After a glogal optimization.

Figure 4.40: Final response of the fourth-order filter with two transmission zeros.

Parameter	Value (mm)	Parameter	Value (mm)	Parameter	Value (mm)
A1	28.2723	L1	2.6688	OFFSET 1	-20.8709
A2	87.2401	L2	79.3510	OFFSET 2	16.6338
A3	28.2723	L3	20.2667	OFFSET 3	-13.1863
A4	84.0647	L4	81.5282	OFFSET 4	22.9560
A5	28.2723	L5	1.9153		

(a) Dimensions of filter which gives the response in Figure 4.40a

Parameter	Value (mm)	Parameter	Value (mm)	Parameter	Value (mm)
A1	28.2723	L1	2.4448	OFFSET 1	-20.7518
A2	87.3046	L2	79.2377	OFFSET 2	16.4940
A3	28.2723	L3	20.3719	OFFSET 3	-13.4022
A4	84.0244	L4	81.5219	OFFSET 4	22.5832
A5	28.2723	L5	1.7657		

(b) Dimensions of filter structure in Figure 4.35 which provides the response in Figure 4.40b.

Table 4.7: Final dimensions of the fourth-order filter with two transmission zeros.

4.9 Sixth-order dual-mode filter with two dual-mode cavities and offset technology

Finally, it has been designed a sixth-order filter composed of three dual-mode cavities with the same specifications as in the previous example. The desired structure for this filter is composed by three dual-mode cavities with the modes TE_{201} and TE_{102} and offset in the couplings windows (Figure 4.41). The coupling topology implemented by this filter is shown in Figure 4.42. To the author knowledge, this is the first example of a physical design of a sixth-order filter using the all-dual mode topology shown in Figure 4.41.

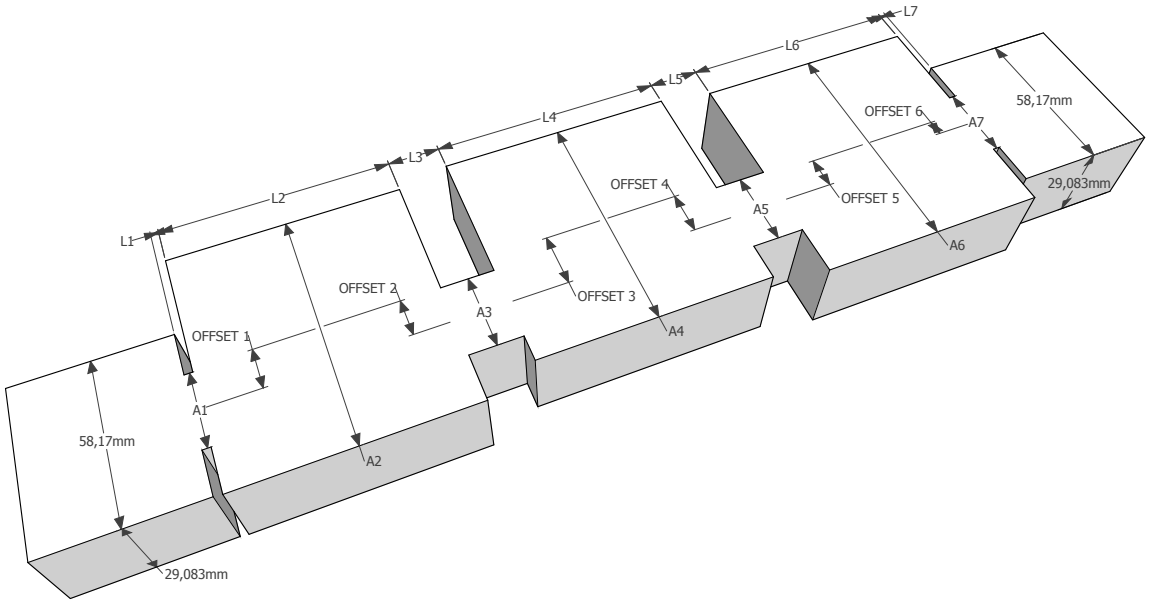

Figure 4.41: Filter structure of the designed sixth-order filter with offset (scaled drawing).

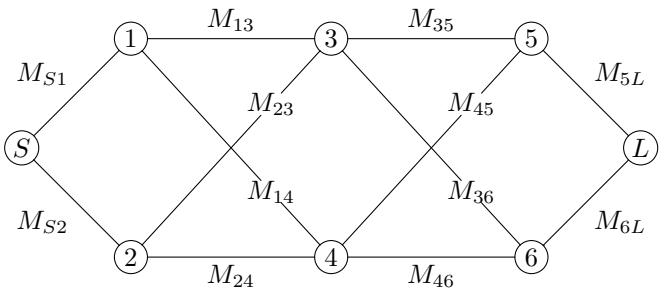

Figure 4.42: Coupling-routing diagram for an inductive dual-mode filter with three dual-mode cavities.

4.9.1 Filter specifications and coupling matrix

The filter is centered at 3.9 Ghz in C-band with 100 MHz bandwidth and a reflection level of -15 dB. This filter provides three transmission zeros located at 3.825 GHz, 3.958 GHz and 3.97 GHz. The target response of this filter is given by the $(8x8)$ coupling matrix in Figure 4.43 which also have the "all-dual-mode" topology shown in Figure 4.13.

In this matrix, each row and column is identified with the proper resonant mode in the filter structure by following the rule of the absolute value of the coupling in each cavity. Labels in Figure 4.43 indicate which resonant mode corresponds to each column in the coupling matrix. As in the previous examples, the labels NR refer to "non-resonating nodes". Once this matching is done, the matrix is scaled as it is explained previously in this chapter.

$$M = \begin{bmatrix} \boldsymbol{NR} & \boldsymbol{TE_{102}} & \boldsymbol{TE_{201}} & \boldsymbol{TE_{102}} & \boldsymbol{TE_{201}} & \boldsymbol{TE_{201}} & \boldsymbol{TE_{102}} & \boldsymbol{NR} \\ \mathbf{0} & -0.7559 & -0.4618 & 0 & 0 & 0 & 0 & 0 \\ -0.7559 & \mathbf{-0.3648} & 0 & 0.5123 & 0.3061 & 0 & 0 & 0 \\ -0.4618 & 0 & \mathbf{1.0172} & -0.1470 & -0.0878 & 0 & 0 & 0 \\ 0 & 0.5123 & -0.1470 & \mathbf{0.2939} & 0 & -0.0659 & 0.5696 & 0 \\ 0 & 0.3061 & -0.0878 & 0 & \mathbf{-0.8115} & 0.0333 & -0.2877 & 0 \\ 0 & 0 & 0 & -0.0659 & 0.0333 & \mathbf{-1.0343} & 0 & 0.3897 \\ 0 & 0 & 0 & 0.5696 & -0.2877 & 0 & \mathbf{0.2617} & 0.7954 \\ 0 & 0 & 0 & 0 & 0 & 0.3897 & 0.7954 & \mathbf{0} \end{bmatrix}$$

Figure 4.43: Coupling matrix of a sixth-order dual-mode filter with three transmission zeros.

4.9.2 First segment

Firstly, it is necessary to get the initial dimensions to be used in the three cavities of the filter. These dimensions are listed in Table 4.8.

	First cavity	Second cavity	Third cavity
Width (mm)	87.7	84.7	84.4
Length (mm)	85.1	86.7	86.8

Table 4.8: Theoretical dimensions of the dual-mode cavities in the sixth-order filter with three transmission zeros.

Here, first iris width and input offset are adjusted while fixing iris thickness to 1 mm. An initial width of 87.7 mm is taken for the output cavity in the forward design as shown in Figure 4.44a meanwhile a width of 84.4 mm is used in the backward design (Figure 4.44b).

In this way, for the forward segment we come to the result: $width = 26\ mm$ and $offset = 18.6\ mm$. Since all irises apertures have to be similar, the width of all coupling windows will be fixed to the same value. This value should be slightly greater than the one obtained when fixing the iris thickness to 1 mm in order to prevent the iris thickness to get below 1 mm, which is not convenient from the manufacturing point of view. Consequently, the input and output irises will be similar and the central iris will have to be thicker in order to keep the same width as the input or output ones.

By setting all irises width to 27 mm and by optimizing the iris thickness and offset it is possible to obtain the results listed in Table 4.9a for the forward segment and in Table 4.9b for the backward one as well as the partial responses shown in Figure 4.45.

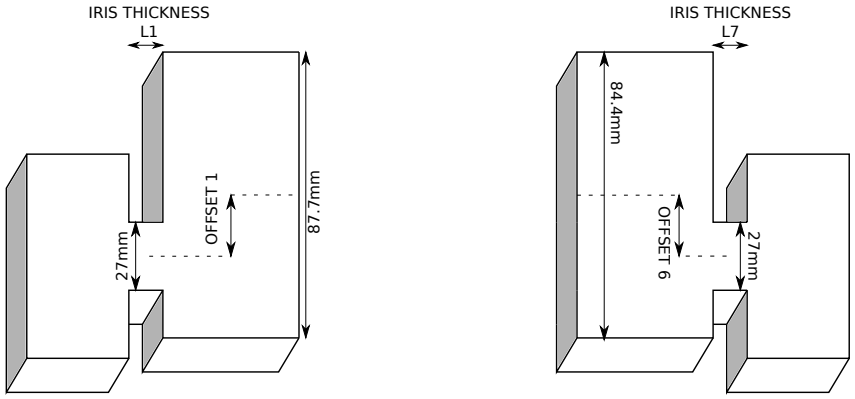

(a) Forward segment. (b) Backward segment.

Figure 4.44: Structure in the step 1 of the sixth-order dual-mode filter with three transmission zeros.

4.9.3 Second segment

Here, the parameters shown in Figures 4.46a and 4.46b as well as in Tables 4.10a and 4.10b are adjusted by two iterations in the same way as in the previous example. In the first iteration the optimized parameters are the thickness ($L3$) and both offsets ($OFFSET2$ and $OFFSET3$) of the central iris and the width ($A2$) and length ($L2$) of the first cavity for the forward segment.

Parameter	Initial (mm)	Optimized (mm)
L_1	1	1.9223
$OFFSET_1$	0	-18.7766

(a) Forward segment.

Parameter	Initial (mm)	Optimized (mm)
L_7	1	1.9590
$OFFSET_6$	0	16.4050

(b) Backward segment.

Table 4.9: Dimensions in the step 1 of the sixth-order dual-mode filter with three transmission zeros.

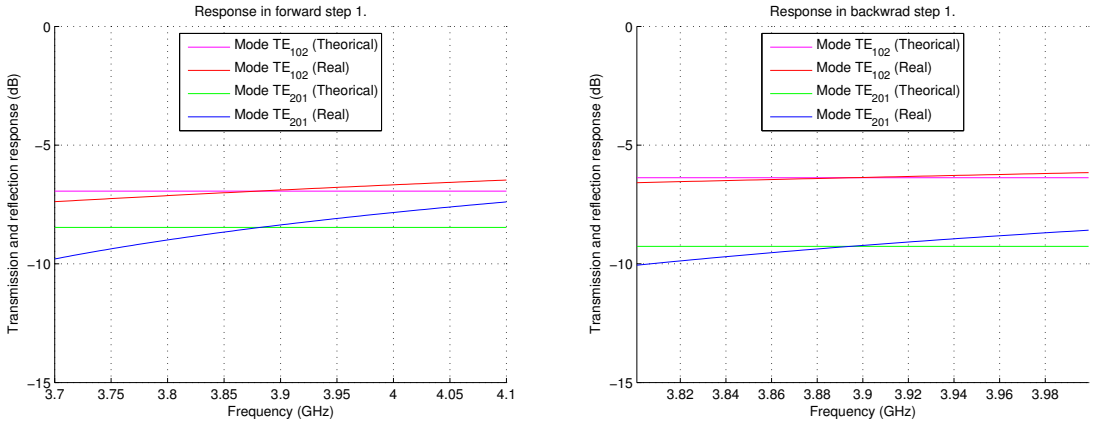

(a) Forward segment. (b) Backward segment.

Figure 4.45: Real and theoretical response in the step 1 of the sixth-order dual-mode filter with three transmission zeros.

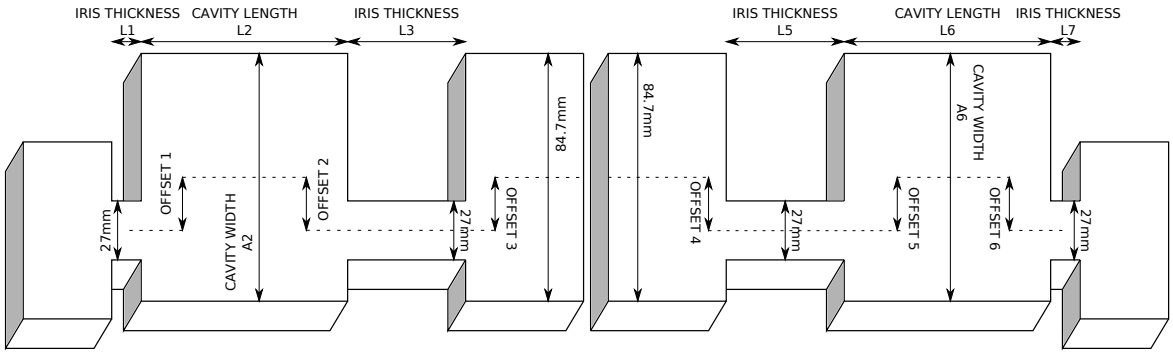

(a) Forward segment. (b) Backward segment.

Figure 4.46: Structure in the step 2 of the sixth-order dual-mode filter with three transmission zeros.

It is important to clarify that this is the more complex optimization in the design of this type of filters since it is required to optimize five parameters simultaneously. That is the reason why it is advisable to perform a manual adjustment that provides a starting point as close as possible to the desired result. Then, it will be necessary to use an electromagnetic optimizer that can deal with these five parameters.

In this step, each parameter has the same effect in the response as discussed previously. The width and height of the dual-mode cavity along with the offset control the resonant frequency of each mode as well as the position of the transmission zero from the passband. The output iris and offset control the coupling to each mode in the output waveguide. For the backward segment, the analogue parameters are optimized, namely $OFFSET4$, $OFFSET5$, $L5$, $L6$ and $A6$ (see Figures 4.46a and 4.46b).

Once these parameters are adjusted, a new optimization is performed adding the parameters $L1$ and $OFFSET1$ in the forward segment and $L7$ and $OFFSET6$ in the backward one. The obtained responses are shown in Figure 4.47a for the forward segment and in Figure 4.47b for the backward segment.

Parameter	Initial (mm)	Optimized (mm)
L_1	1.3344	2.4091
$OFFSET_1$	-18.6110	-14.0843
L_2	85.1	78.5887
A_2	87.7	88.1138
$OFFSET_2$	14.0926	12.6829
L_3	15	17.7259
$OFFSET_3$	-14.0926	-20.1172

(a) Forward segment.

Parameter	Initial (mm)	Optimized (mm)
L_7	1.9590	3.1478
$OFFSET_6$	16.4050	6.1287
L_6	86.8	79.2352
A_6	84.4	85.6717
$OFFSET_5$	-16.4697	-11.2968
L_5	15	18.2483
$OFFSET_4$	16.4697	15.4172

(b) Backward segment.

Table 4.10: Dimensions in the step 2 of the sixth-order dual-mode filter with three transmission zeros.

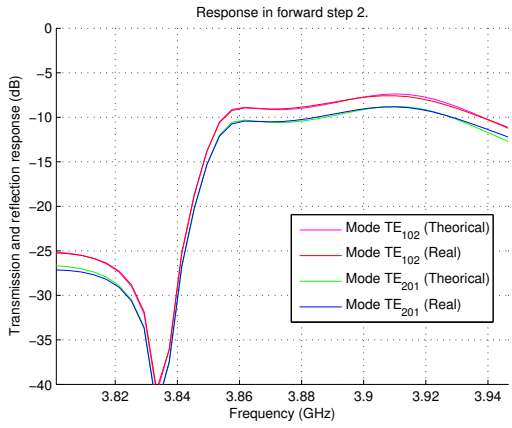

(a) Forward segment.

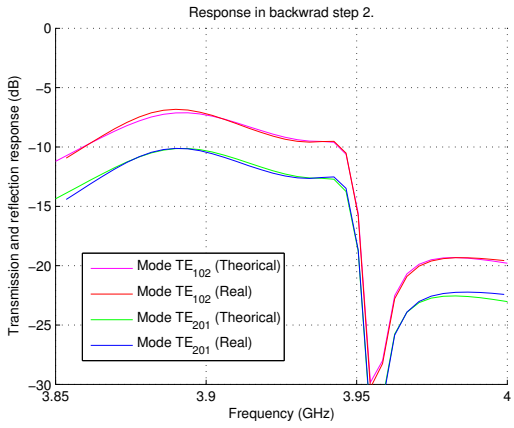

(b) Backward segment.

Figure 4.47: Real and theoretical response in the step 2 of the sixth-order dual-mode filter with three transmission zeros.

4.9.4 Result

Finally, the only unknown parameters are the width and height of the central cavity ($A4$ and $L4$). These two parameters could be adjusted in the third forward step as well as in the backward one to fit the resonant frequencies of the resonant modes inside the central cavity. However, both the third backward and the third forward segment lead to different solutions and only one of them will provide the right response when the filter is assembled together.

Both filter segments in backward and forward design will produce an incorrect response when they are compared with the target. However in one of them the error will reside in the shape of the partial response meanwhile in the other segment there will be an error in the level of the scattering parameters. It is necessary to take this issue into account since after assembling both halves of the filter, the final response will be the correct one in only one of the two situations. It has been observed, that the right solution is the one that contains an error in the level of the partial response and not in the shape.

In this example, by using the structure of the third forward segment, shown in Figure 4.48 the response in Figure 4.49 is obtained with the dimensions listed in Table 4.11. In this response, it can be noted that there is a scaling error in the response of the mode TE_{201}. However this is the expected result as the filter response of the complete structure is the one shown in Figure 4.50a. This response achieves a rather good fulfillment of the filter specifications.

If a global optimization is performed the response in Figure 4.50b is achieved that fit perfectly the target specifications. The dimensions of the final structure after performing a global optimization are shown in Table 4.12 and Figure 4.41.

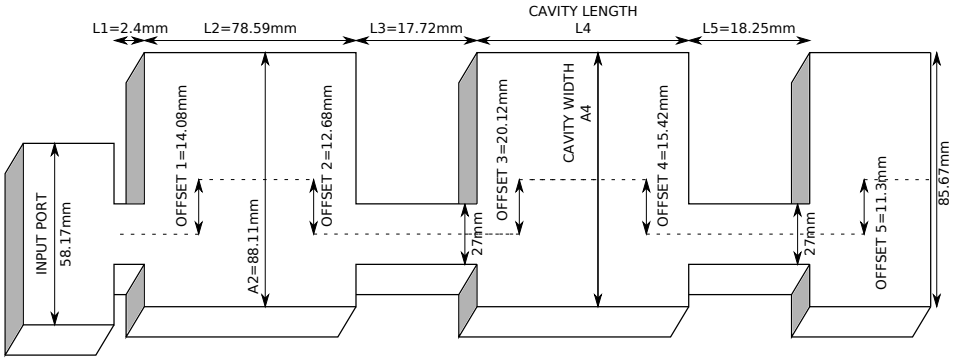

Figure 4.48: Structure view and parameters in step 3 of the sixth-order filter with three transmission zeros.

Parameter	Initial (mm)	Optimized (mm)
L_4	86.7	81.7919
A_4	84.7	84.3689

Table 4.11: Dimensions in the forward step 3 of the sixth-order dual-mode filter with three transmission zeros.

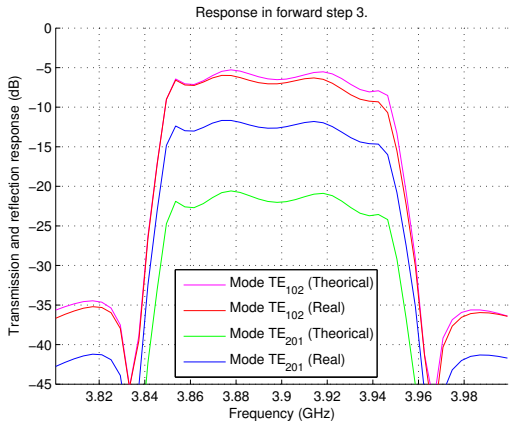

Figure 4.49: Real and theoretical response in the step 3 of the sixth-order dual-mode filter with three transmission zeros.

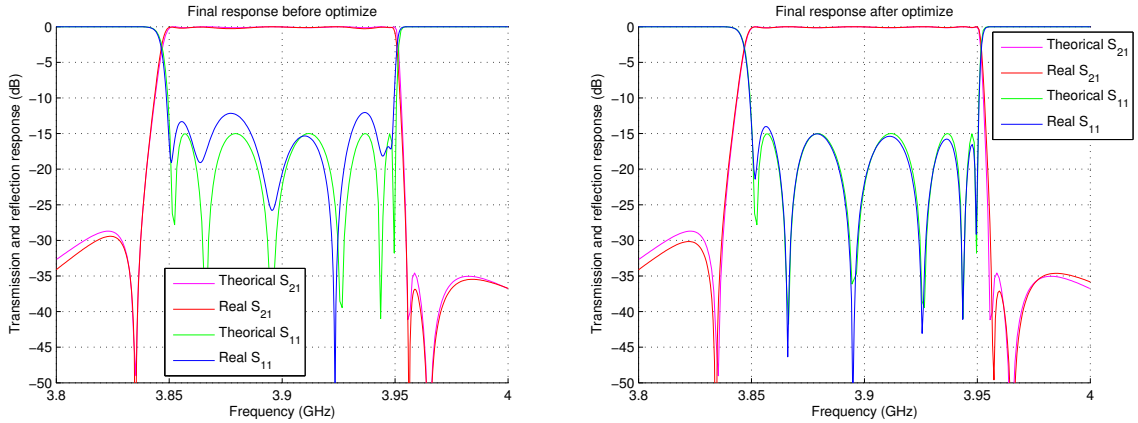

(a) Before optimize.

(b) After optimize.

Figure 4.50: Final response of the sixth-order filter with three transmission zeros.

Parameter	Value (mm)	Parameter	Value (mm)	Parameter	Value (mm)
A1	27	L1	2.6180	OFFSET 1	-14.5558
A2	87.9650	L2	78.6984	OFFSET 2	13.5367
A3	27	L3	17.9728	OFFSET 3	-19.2441
A4	84.3784	L4	81.6128	OFFSET 4	15.4064
A5	27	L5	17.9802	OFFSET 5	-11.5682
A6	85.6801	L6	79.1820	OFFSET 6	5.6998
A7	27	L7	2.3167		

Table 4.12: Parameters value of filter structure in Figure 4.35.

4.10 Conclusions

In this chapter, the adaptation of the step-by-step design procedure [Guglielmi and Melcon, 1993, Guglielmi, 1994] to the formalism of the coupling matrix has been generalized. Thus this approach is now useful to design any coupling topology represented by the coupling matrix. Moreover, the design could be implemented in any technology by using the coupling matrix of the topology that is intended to implement, and by segmenting the physical structure.

It should be noted that if the topology is too much complex, the segmenting of the structure can not be chosen arbitrarily but it is necessary to cut the structure by the points where the target partial response can be obtained by segmenting the coupling matrix. In this work, as the designed filters are implemented in waveguide technology, they have been segmented by the resonant cavities. Thus it is possible to consider these resonant cavities as the output port in each segment and to obtain the partial response by segmenting the coupling matrix.

Moreover, in order to validate this generalized procedure, some filters have been presented with the all-inductive dual-mode topology introduced for the first time in [Guglielmi et al., 2001]. Furthermore, this topology is extended for the first time to any number of dual-mode cavities. The extended topology is represented by the coupling diagram of Figure 4.12 where only dual-mode cavities have been used. However these filters with only dual-mode cavities present some important drawbacks such as the thicker inner irises or the limitation on the maximum bandwidth that can be achieved, and the maximum distance of the transmission zeros from the passband. This is due to the fact that all irises of the dual-mode cavities must have the same width which is fixed to a given value. As a result, since the input and output couplings are quite larger as compared to the inner coupling, the inner windows have to be thicker in order to decrease the coupling level, and at the same time keeping the the same width.

The last effect leads also to a limitation on the distance where the transmission zeros can be placed from the passband. In order to place the transmission zeros further from the passband, it is necessary to get a stronger coupling to the second mode in the dual-mode cavities keeping at the same level the coupling to the first one. To achieve that, it would be necessary to increase the offsets in order to obtain higher coupling to the mode TE_{201}. However, due to the thicker irises, the offset range is limited and so the position of the transmission zeros.

To overcome this drawback, it would be desirable a filter structure that favors the coupling to the mode TE_{201}. For instance, if a dielectric strip is placed inside the cavity, going from the input to the output, the electric field of the mode TE_{102} would confine in the center of the cavity. In that way the available range for the offset would increase and then, the transmission zeros could be placed further from the passband.

However, in spite of the discussed drawbacks, these dual-mode filters offer some advantages such as the reduction in volume and mass, the higher Q and the lower insertion loss. This advantages are due to the fact that the volume of the resonant cavities is increased and the number of irises, that will introduce losses in the real prototype, is reduced by half as compared to in-line filters [Guglielmi et al., 2001, Cameron et al., 2007].

Finally, it should be noted that all filters designed in this chapter have a reflection level of $-15\ dB$ what may seem a little poor. Nevertheless, it is not relevant in the design procedure as it can be set to a higher value at the expense of a reduction of the maximum bandwidth and a lower rejection in the stop band. In practice, it would be necessary to reach a trade-off between the bandwidth, the reflection level in the passband and the rejection in the stopband, taking into account that the rejection in the stopband will be greater when placing the transmission zeros further from the passband (at the cost of some selectivity close to the passband).

5 MULTIPLEXERS DESIGN

5.1 Introduction

Due to the already mentioned overcrowding electromagnetic spectrum and its multiuser environment the allocated frequency bands are highly channelized. Furthermore, the high-power amplifiers used in satellite payloads require a narrow band signal in order to avoid the effects introduced by the non-linearity of these devices and operate with high efficiency. As a result, multiplexers are needed in order to separate a wideband signal into a given number of narrow band channels. In addition, multiplexers are also used in order to combine a group of narrowband channels into a wideband signal that can be transmitted through a common antenna.

In this way, the simplified block diagram of a satellite payloads system (figure 5.1) is composed by a receiver (uplink) antenna, a low-noise amplifier (LNA) to compensate the losses due to the uplink propagation, an input multiplexer that separates the received signal into narrowband channels, the amplification chain composed by high power amplifiers that amplify each channel separately and the output multiplexer which recombines the amplified channels into a single signal that can be transmitted back to the earth through the downlink antenna [Cameron et al., 2007]. However, it is possible to distinguish between three categories of multiplexing applications.

- **Input multiplexers or channelizers (demultiplexers).** They split a received broadband signal into a given number of narrowband channels. This task is performed after the broadband amplification of the received signal by a LNA. Thus, extremely low insertion losses are not a crucial condition.
- **Output multiplexers or combiners (multiplexer).** They are used to recombine the frequency channels after the high power amplification. In this application, insertion losses are a critical parameter since it has a direct impact on the transmitted signal. In addition, microwave filters used in these multiplexers must be able to operate at high frequencies and must provide a high rejection in the stopbands to suppress the inter-modulation products generated by the high power amplifiers (HPAs).
- **Transmit-receive diplexers.** A diplexer is a two channel multiplexer frequently used to share a single antenna between the transmitter and the receiver. In these applications, the insertion losses of the receive filter contribute directly to the overall noise figure of the receiver since it is placed before the LNA. Thus, both the insertion losses of the transmit filter as well as the insertion losses of the receive filter are important. Moreover, it is necessary a good handling of high power and a high rejection between the two channels.

The design and implementation of multiplexer systems is linked to the synthesis and design process of microwave filters and it has evolved as a result of the improvements made in the field of filters design. Nevertheless, there are different configurations of multiplexers system that offer various degrees of interaction between the multiplexer system and the filter design [Cameron et al., 2007].

5.1.1 Hybrid coupled multiplexers

This configuration is based on the directional property of the 90° hybrid (figure 5.2). The input wideband signal goes through a directional coupler what divides the signal between two identical

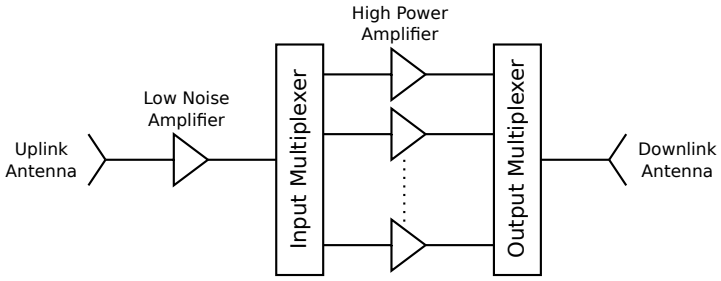

Figure 5.1: Simplified satellite payloads diagram.

filters in the first channel. At the output of these filters, the signals coming from each path are recombined by another hybrid. This hybrid cancels the received signals in one of its outputs as a result of a destructive interference meanwhile in the other output a constructive interference occurs and the filtered signal is retrieved. Similarly the reflected signals of both filters go back through the first 90° hybrid that recombines these signals in the path to the next channel and cancels it in the return path.

As a result, since the reflected signal of each channel goes exclusively to the next one, the interactions between channels are minimized. This fact allows the filters design independently of the multiplexer design. Moreover, it also allows the modular design since it is possible to add new channels to the designed multiplexer as well as to replace a given channel at a later time.

However, this configuration results in a too bulky and heavy structure since two 90° hybrid and two filters are required in each channel. Another drawback is the tight tolerances needed in the manufacturing process of the directional couplers and the two filtering paths in each channel. In fact, in order to assure that both signals are added constructively at the output, it is necessary to use two identical hybrids and two identical filters. Furthermore, additional tuning elements may be necessary in order to compensate for the phase deviation between the two paths [Cameron et al., 2007].

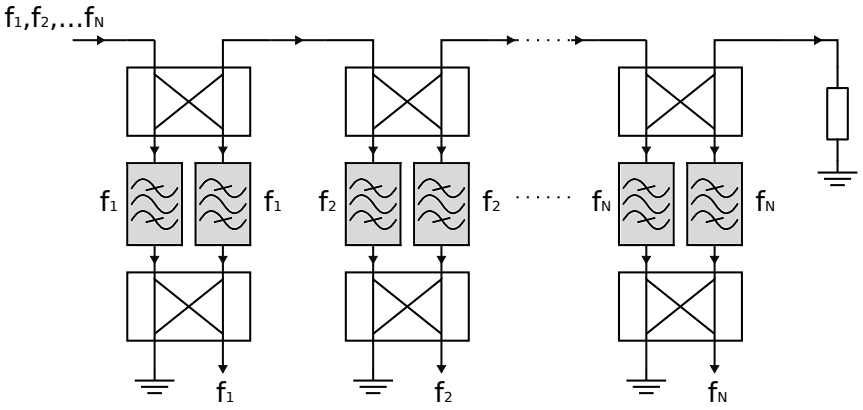

Figure 5.2: Hybrid coupled multiplexer.

5.1.2 Circulator-coupled multiplexers

This configuration is shown in Figure 5.3. This approach keeps the advantages provided by multiplexers with directional couplers related to the modular design. It is possible to design each channel independently of the multiplexer structure due to the unidirectional property of the circulator as well as to add new channels at any time. In addition, this structure overcomes the drawback present in the multiplexer with directional filters in terms of the need of two filters in each channel and the high accuracy required in the manufacturing process of both filters. This fact leads to a size reduction since each channel is composed only by a circulator and the corresponding filter.

With regard to the drawback of this multiplexer, it is important to take into account the increase in the insertion losses of each channel. The insertion losses in the first channel will be the sum of the insertion losses of the first filter and the insertion losses introduced by the first circulator. The second channel will have the insertion losses due to the second filter as well as the loses due to the two first

circulators and so forth. In this way, each channel will exhibit higher losses than the previous one and the maximum number of channel will be given by the maximum admissible losses. Thus it will not be an adequate option for channelizers or demultiplexers. [Cameron et al., 2007].

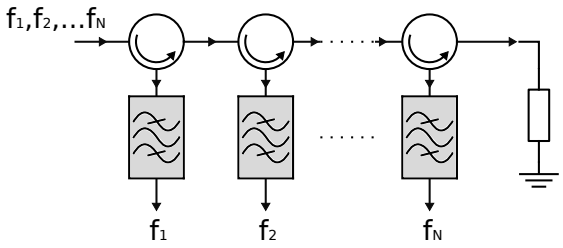

Figure 5.3: Circulator coupled multiplexer.

5.1.3 Directional filters multiplexers

A directional filter is a four-port device in which one port is terminated in a load and the other three ports act as a circulator with a band-pass filter. Thus the directional filters shown in Figure 5.4 perform the same task as each circulator together with the corresponding filter in the circulator-coupled multiplexer (figure 5.3). The output signal of each directional filter is obtained in the channel output meanwhile the reflected signal goes to the next channel. However, due to the properties of the directional filters, they can only be used with narrowband channels [Neubauer et al., 2002, Cameron et al., 2007].

This approach offers some advantages with respect to the previous options. These multiplexers keep the modular property as the channels can be added independently from the design of the multiplexer structure. Moreover, it is obtained a reduction in size from the hybrid-coupled multiplexer (figure 5.2). Finally, this configuration overcome the problem of the cumulative losses from the circulator-coupled multiplexer (figure 5.3).

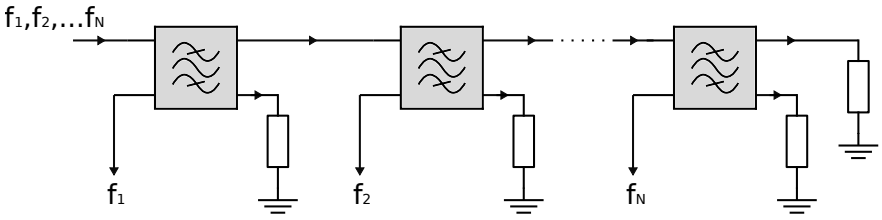

Figure 5.4: Multiplexer with directional filters.

5.1.4 Manifold-coupled multiplexers

These multiplexers are composed of a bandpass filter for each channel interconnected by transmission lines (figure 5.5). With a manifold configuration, channels are not isolated from each other and the reflected signal of a given filter will perturb the response of the other filters. As a result, this approach is not amenable for a modular structure since it is necessary to design the multiplexer with all the channels at once. In this way it is possible to optimize both the channels filters and the length of the transmission lines in order to obtain the right phase of the input signal to each filter and compensate for the interactions between them. In this context, some authors have developed optimization methods to achieve the desired behavior [Morini et al., 1997, Accatino and Mongiardo, 2002, Uhm et al., 2005, Montejo-Garai et al., 2005a] and also synthesis techniques for the whole multiplexer [Macchiarella and Tamiazzo, 2011].

If it is desired to add new channels or to change the frequency allocation of the current ones, then it is necessary to perform a new synthesis and to design a new multiplexer. Moreover the design and implementation procedure become more difficult when the number of channels increases.

This configuration is widely implemented for space applications since this approach offers the best result in terms of miniaturization of the structure and absolute insertion losses in each channel. Furthermore the inability to perform a modular design is not a drawback in the space sector where the manufactured devices can not be modified [Hu et al., 2013, Cameron et al., 2007].

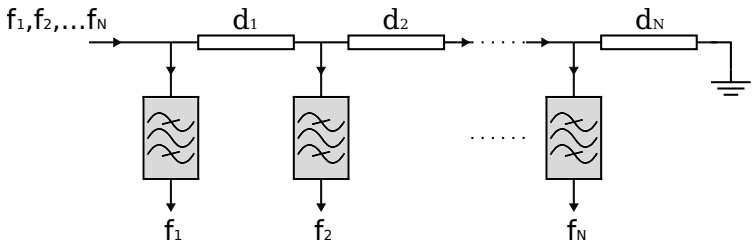

Figure 5.5: Manifold multiplexer.

5.1.5 Star junction multiplexers

Finally, star-junction multiplexers is the approach that has been used in this work. In star-junction multiplexers, the filter of each channel is directly coupled to the input port (figure 5.6). The junction between the channels and the feeding port must be properly dimensioned to provide the right coupling to each channel and to compensate for the interaction between them. Thus this configuration is not amenable to a modular design as it happened with the manifold multiplexers (figure 5.5). It is usually necessary to perform the synthesis of the whole structure with all the filters connected before starting the design procedure [Macchiarella and Tamiazzo, 2006, Macchiarella and Tamiazzo, 2010, Macchiarella, 2011]. Moreover, in order to modify the channels configuration it is necessary to perform a new synthesis and a new design of the whole multiplexer. Another drawback of this structure comes from the fact that the maximum number of channels coupled to the input port is given by the geometry of the junction and the presence of high order modes within it (for instance in the case of a waveguide implementation, as it is addressed in this work).

With regard to the advantages, this type of multiplexers achieves the most compact size while keeping the lower insertion loss as compared to manifold multiplexers. In addition, the modular structure is not relevant in the space sector, that is why star-junction multiplexers are commonly used for satellite applications when a reduced number of channels is required such as diplexers or triplexers [Gál et al., 2013, Li et al., 2013, Cheng et al., 2013, Ezzeddine et al., 2012].

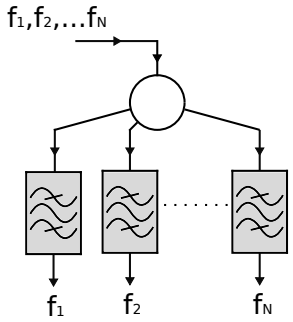

Figure 5.6: Star multiplexer.

5.2 Diplexer with in-line filters

A diplexer is a three port device used to combine or separate two channels, for instance the transmitted and received signals of a common antenna. Usually, diplexers are composed of a different filter for each channel and a T-junction. This T-junction provides the right coupling to each channel and should be properly dimensioned in order to compensate for the strong interaction between both filters [Cameron et al., 2007].

Diplexers with in-line filters are well known and easy to design because of the simplicity of these filters . However, it may not be the best choice to implement a diplexer due to the large guard band needed as a result of the low selectivity of in-line filters.

Nevertheless, several of these diplexers have been designed in this chapter by using the strong capabilities of the developed design technique based on the structure segmentation [Guglielmi and Melcon, 1993, Guglielmi, 1994]. In this way considerable advantages are obtained in terms of ease of design and accuracy of the achieved target response avoiding the need of performing the optimization

of the whole diplexer.

The first step in the design of these diplexers consist on the design of the filters for each channel separately according to the previously studied procedure. Once the filters are designed, it is not necessary to use the partial responses obtained from the coupling matrix anymore, since we now have the actual partial responses that can be obtained by segmenting each designed filter.

Firstly, the diplexer junction is optimized starting with an appropriate starting point which is manually optimized and provides a proper coupling level to each channel. Then, this junction is optimized taking the responses obtained by segmenting the separately-designed filters as target responses.

Although the parameters obtained will be a good starting point, it is not the final structure as the diplexer junction will be significantly affected when the filters on each channel are added.

Next it is necessary to add the second segment of each filter and to optimize both the length of the first cavity and the parameters obtained in the previous step. It should be noted that although the output iris in this segment will also be modified, it will be the last modification, since when the variation of the last iris in each filter is small or even negligible, the remainder structure of each filter can be added to obtain the desired response without requiring any further optimization.

5.2.1 In-line filters

The required filter for each channel of every diplexer is initially designed isolate. Below the filters used in in-line diplexers are presented. All of them are third-order filters with a reflection level of -20 dB and 100 MHz bandwidth. The coupling matrix in Figure 5.7 gives the normalized response of all in-line filters used in this chapter. This response is frequency-shifted by the lowpass-to-bandpass transformation to obtain the target response for each channel. The passband of the first channel goes from 3.85 GHz to 3.95 GHz, the second channel from 4.05 GHz to 4.15 GHz and regarding the last one, used for the design of a triplexer in section 5.3, its passband goes from 4.25 GHz to 4.35 GHz. The obtained filtering functions are shown in Figure 5.8.

$$M = \begin{bmatrix} 0 & 1.0825 & 0 & 0 & 0 \\ 1.0825 & 0 & 1.0303 & 0 & 0 \\ 0 & 1.0303 & 0 & 1.0303 & 0 \\ 0 & 0 & 1.0303 & 0 & 1.0825 \\ 0 & 0 & 0 & 1.0825 & 0 \end{bmatrix}$$

Figure 5.7: Coupling matrix used for all in-line filters in diplexers design.

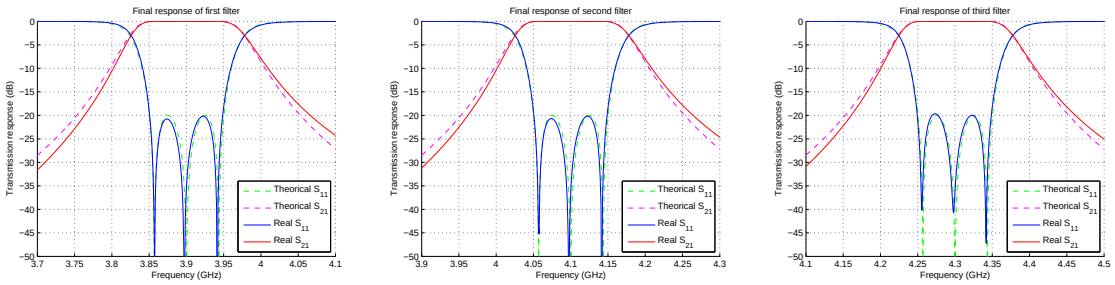

(a) Channel 1. (b) Channel 2. (c) Channel 3.

Figure 5.8: In-line filters for each channel.

These three in-line filters have been used to compose two diplexers, one of them with all inductive technology (H-plane junction) and the other one enlarging the input waveguide height to make the diplexer junction (E-plane diplexer). Moreover, an E-plane triplexer is also presented in section 5.2.4.

5.2.2 H-plane diplexer

In the first example an H-plane diplexer is designed (with all-inductive technology). The filters centered at 3.9 GHz and 4.1 GHz shown in Figure 5.8a and 5.8b have been used in the first and second channels.

The structure obtained for the diplexer is shown in Figure 5.9. Here, the input iris of each channel is not necessary since the first segment of each filter, together with the diplexer junction act as a resonator. Therefore, these input irises have been removed in both channels.

Once the filters are designed independently, when both channels and the diplexer junction are assembled, the first cavity of each channel must be readjusted to compensate for the interactions produced by the diplexer junction.

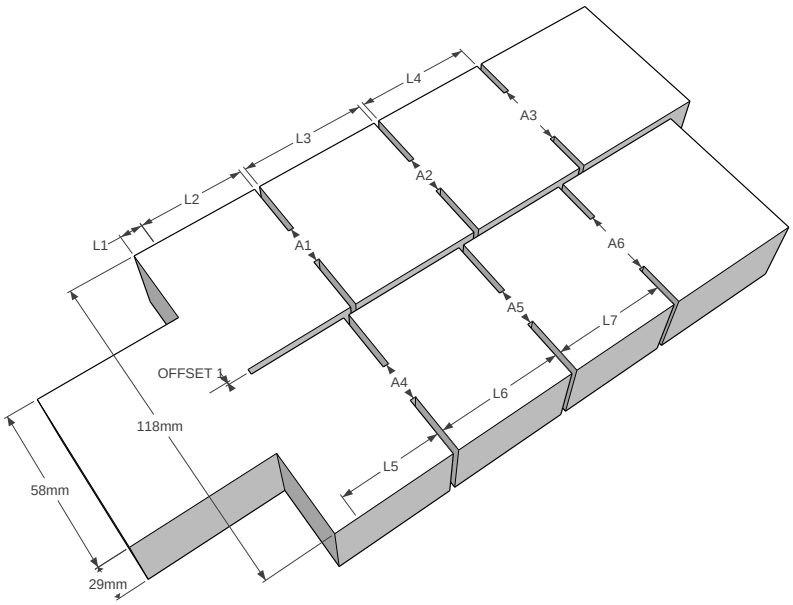

Figure 5.9: H-plane diplexer.

The optimization process is as follows:

1. **STEP 1: Optimization of the diplexer junction.** Parameters $Offset1$ and $L1$ are optimized taking the diplexer output in the first cavity of each channel. The aim is to get an initial coupling level to each channel similar to the coupling provided by the first iris (removed in this structure) of each of the isolated filters in their respective passbands. With two parameters either the width or the height of the junction and the offset it is possible to achieve the right coupling level to each channel. Thus only the above two parameters are adjusted since the width of the junction is set to 118.34 mm (Figure 5.9 in order to have a 2 mm separation between both physical channels.

   Table 5.1 shows the values of the parameters obtained in STEP 1 and Figure 5.10a shows the coupling level to each channel provided by the diplexer junction as well as the level obtained in the isolated filters. It can be observed that the required coupling to both channels are recovered with the H-plane junction.

2. **STEP 2: Optimization of the first resonator.** In this step the first cavity and the second iris of each filter is optimized while the output is taken in the second cavity. Thus there will be a resonator in each channel. At this point the optimization is performed in several iterations:

   (a) Firstly the length of the first cavity of each filter (parameters $L2$ and $L5$) is decreased to compensate the effective length introduced by the junction. In the first channel, the length of the first cavity has been reduced from 44.32 mm to 38.81 mm while in the second channel from 41 mm to 34.89 mm.

   (b) Both parameters $L2$ and $L5$ are adjusted as well as the size of the junction ($offset1$ and $L1$) obtained in the previous step. The goal is to get the same response as the one provided by the isolated filters when the output is taken in the second cavity.

	PARAMETER (MM)	INITIAL	STEP 1	STEP 2	STEP 3	FINAL
JUNCTION	OFFSET1	0	0.4185	0.9003		0.9003
	L1	5	10.0707	8.0719		8.0719
CHANNEL 1	L2	44.3268		38.8189	38.8868	38.8868
	A1	15.6122		15.4601	15.3615	15.3615
	L3	48.0065			48.1263	48.1263
	A2	15.6122			15.5692	15.5692
	L4	44.3268				44.3268
	A3	26.1039				26.1039
CHANNEL 2	L5	41.0093		34.8725	34.8072	34.8072
	A4	14.4727		14.2761	14.3085	14.3085
	L6	44.3121			44.3208	44.3208
	A5	14.4227			14.4426	14.4426
	L7	41.0093				41.0093
	A6	24.6622				24.6622

Table 5.1: Parameters value in each step of the H-plane in-line diplexer.

It should be noted that the output iris in this STEP (parameters $A2$ and $A5$ will not be modified. In addition when it is possible to get the target response without modifying the output windows, the rest of each filter can be added without having to perform any other modifications. Nevertheless, since the result obtained in this step is not as accurate as it would be desired, parameters $A2$ and $A5$ have also been adjusted and a final optimization has been performed.

Table 5.1 shows the value of the parameters obtained in the STEP 2 and Figure 5.10b shows the response obtained by cutting both channels by the second cavity compared with the response obtained with the isolated filters.

3. **STEP 3. Final adjustment.** Finally the parameters $L2$, $A1$, $L5$, $A4$, $L3$, $A2$, $L6$, $A5$ have been adjusted to get the result shown in Figure 5.10c. As it is shown in Table 5.1 the variation of these parameters is in the range of tens of microns and the variation of the filter response is almost negligible. Thus the optimization is quite fast since the previous derived procedure resulted in a starting point very close to the final optimized structure.

The dimensions of the final structure obtained are listed in Table 5.1 and the response provided by the diplexer is shown in Figure 5.10d. It can be observed that the design procedure has been very effective, since the target response is almost perfectly recovered.

5.2.3 E-plane diplexer

I now address another example similar to the above one, however in this case the two waveguides are stacked in the E-plane (Figure5.11).

1. **STEP 1: Diplexer junction optimization.** Just the same as in the above example but in this case the parameters $OFFSET1$, $L1$ and the junction height $B1$ are optimized. As initial values of these parameters, we have taken: $OFFSET1 = 0$, $L1 = 5$ and $B1 = 61$.

   Table 5.2 lists the values of the parameters obtained in STEP 1 and Figure 5.12a the coupling level to each channel given by the diplexer junction as compared to the coupling of the isolated filters. It can be observed that the right coupling to both channels are successfully retrieved.

2. **STEP 2. Optimization of the first resonator.** The performed iterations in this step are the same as in the previous example. Here, the parameters $L1$, $B1$, $OFFSET1$, $L2$, $A1$, $L5$ and $A4$ have been adjusted. In this case it has also been made an extra iteration in the same way as in the previously designed H-plane diplexer.

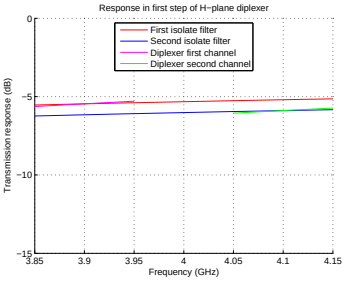

(a) First step.

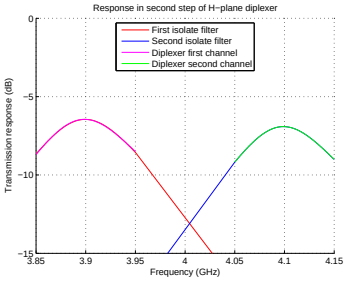

(b) Second step.

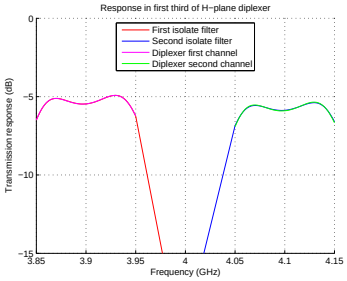

(c) Third step.

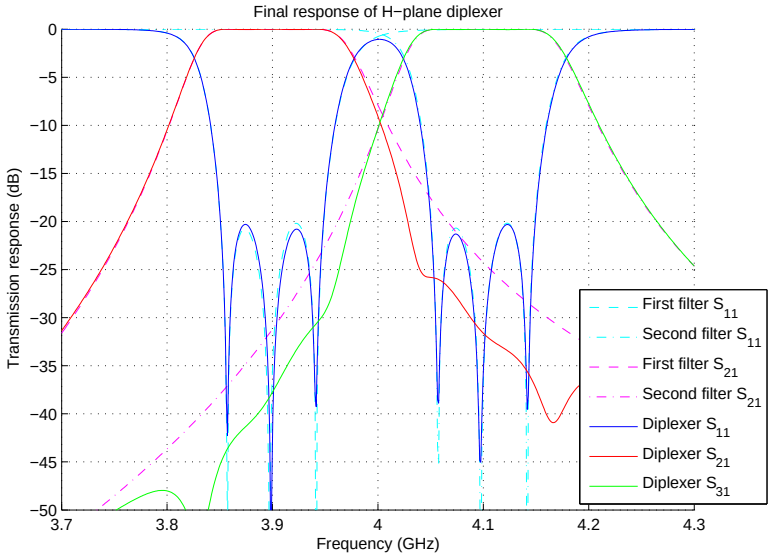

(d) Final response.

Figure 5.10: Response in each step of the H-plane in-line diplexer.

3. **STEP 3. Final adjustment.** It is performed as in the above example, with the difference that here the widths $A2$ and $A5$ need not to be modified since their variations are negligible. In this STEP the output iris is unchanged. Thus the rest of both filters can be added and the final response is recovered without the need to perform to perform any further modification.

The dimensions of the final structure obtained are listed in Table 5.2 and the response provided by the diplexer is shown in Figure 5.12d. It can be seen that the final response is almost perfect by optimizing a reduced number of parameters in each step due to the design procedure.

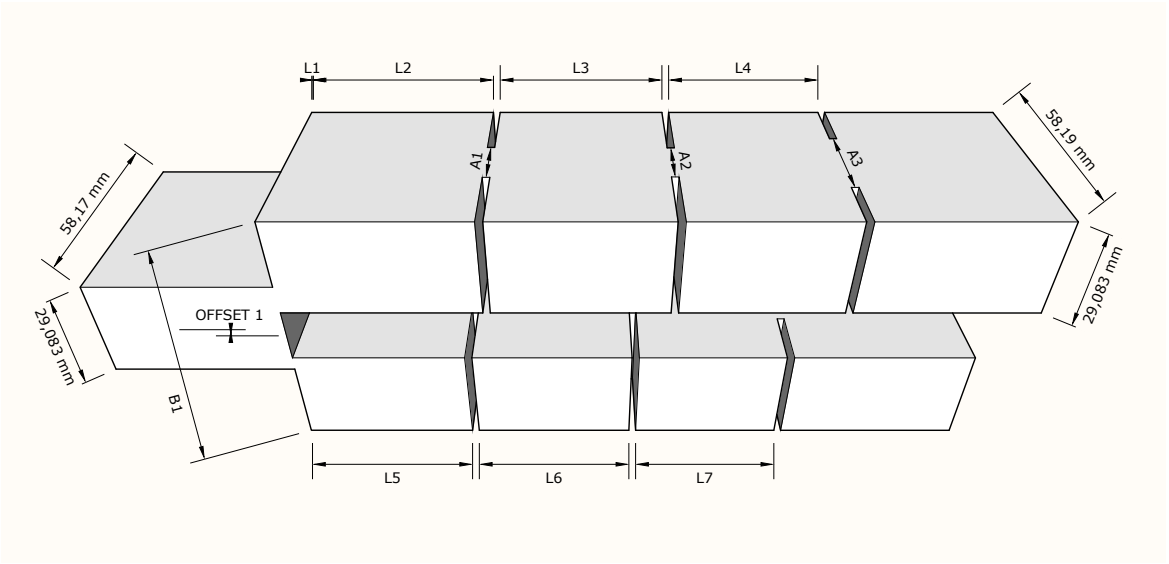

(a) First channel view.

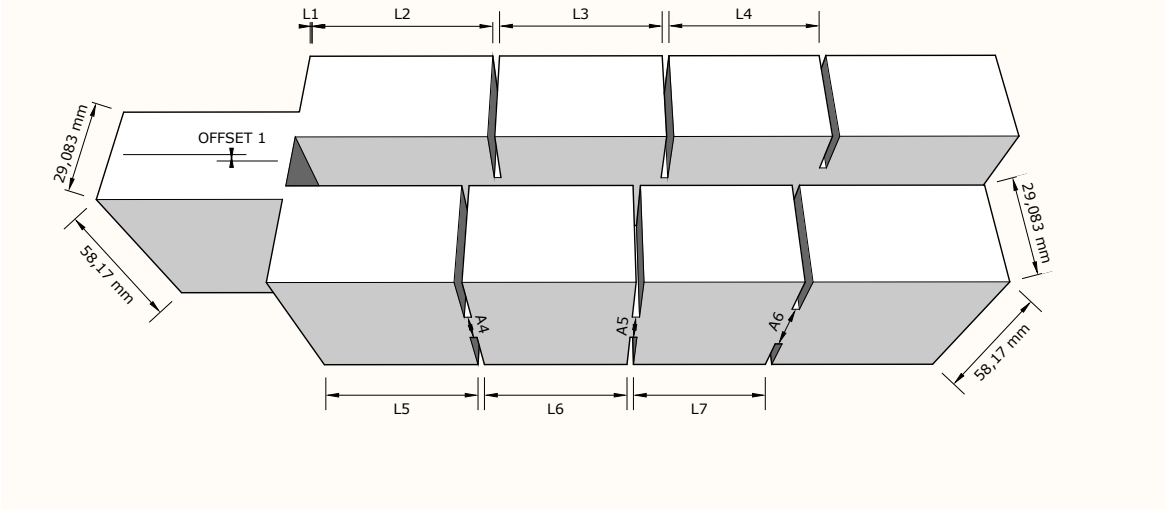

(b) Second channel view.

Figure 5.11: E-plane diplexer.

5.2.4 E-plane triplexer

As a final example of star multiplexers using in-line filters, a triplexer with three in-line filters has been designed. The filters that have been used are shown in Figure 5.8. These filters have been stacked in the E-plane as in the previous example. With this example the advantages obtained by using the segmentation technique are clearly shown since the design of a quite complex structure with a considerable number of parameters is performed by a very simple procedure.

1. **STEP 1: Diplexer junction optimization.** Here there is the only difference with the previous example. To optimize the triplexer junction it is necessary to choose proper initial

	PARAM. (mm)	INITIAL	STEP 1	STEP 2	STEP 3	FINAL
JUNCTION	OFFSET1	0	-0.0202	-2.1922		-2.1922
	B1	61	73.0483	74.3020		74.3020
	L1	5	0.2267	0.2066		0.2066
CHANNEL 1	L2	44.3268		53.6956	53.7834	53.7834
	A1	15.6122		16.0731	16.0338	16.0338
	L3	48.0065			48.0369	48.0369
	A2	15.6122				15.6122
	L4	44.3268				44.3268
	A3	26.1039				26.1039
CHANNEL 2	L5	41.0093		47.6260	47.6288	47.6288
	A4	14.4227		14.4344	14.4415	14.4415
	L6	44.3121			44.3654	44.3654
	A5	14.4227				14.4227
	L5	41.0093				41.0093
	A6	24.6622				24.6622

Table 5.2: Parameters value in each step of the E-plane in-line diplexer.

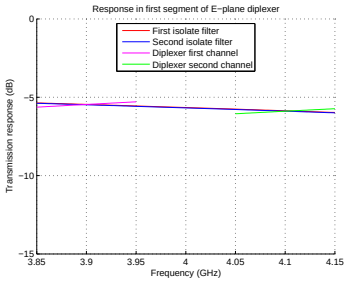

(a) First step.

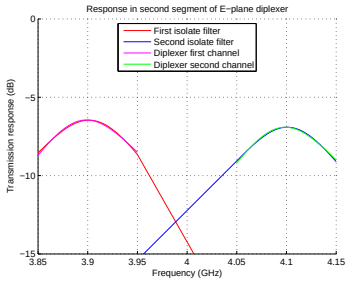

(b) Second step.

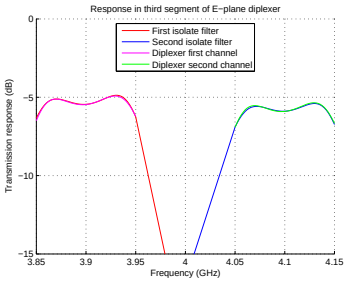

(c) Third step.

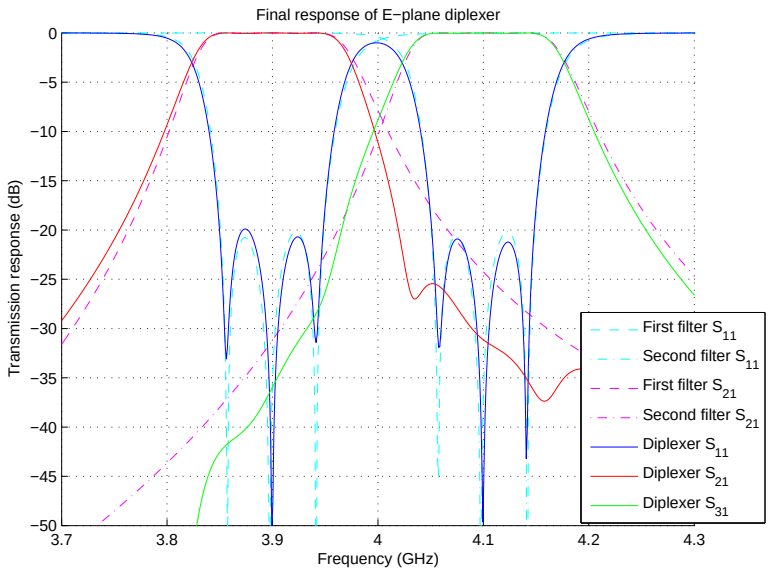

(d) Final response.

Figure 5.12: Response in each step of the E-plane in-line diplexer.

values for the parameters ($D1$, $D2$ y $L1$) that provide a constant level of coupling to each of the channels in its passband. This is necessary to prevent that higher order modes resonate inside the junction. Thus, we will try to make the union as small as possible to avoid having resonant modes within the junction since these resonances would spoil the filter responses.

Table 5.3 shows the value of the initial and obtained parameters in STEP 1 and Figure 5.14a shows the coupling level to each channel that is provided by the triplexer junction and also the required coupling level obtained by segmenting each isolated filter. It can be observed that the required coupling is retrieved in each channel.

2. **STEP 2. Optimization of the first resonator.** As in the previous case we perform an optimization of the parameters listed in Table 5.3. The response obtained is shown in Figure 5.14b.

3. **STEP 3. Final adjustment.** Finally, a final optimization is performed with the parameters listed in Table 5.3 (Figure 5.14c).

The dimensions of the final structure are listed in Table 5.3 and the response provided by the triplexer can be seen in Figure 5.14d.

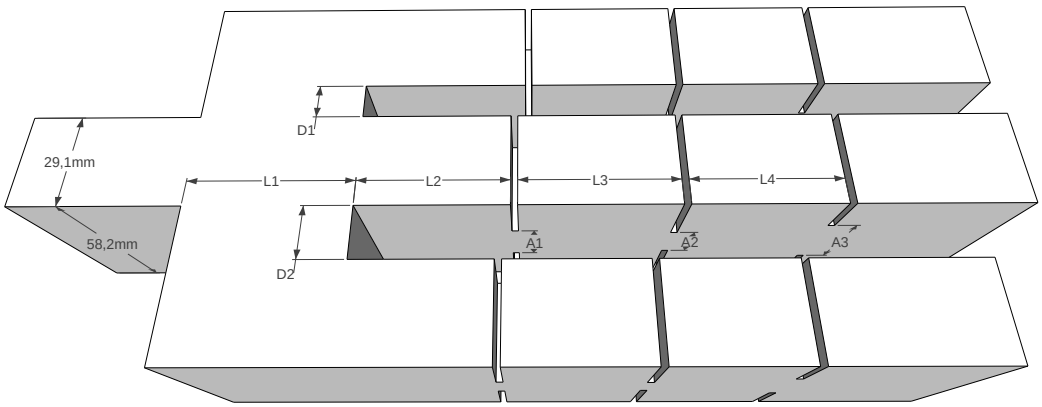

(a) First channel view.

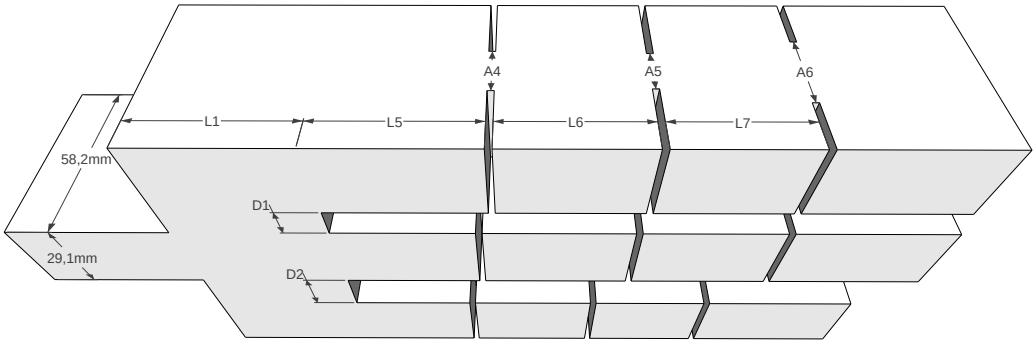

(b) Second channel view.

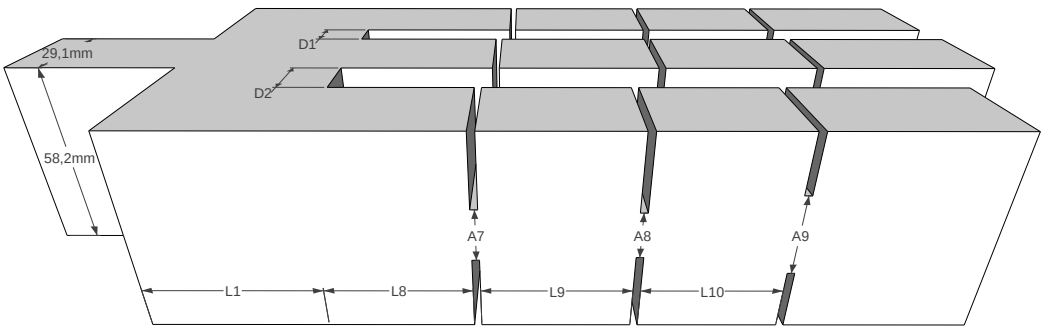

(c) Third channel view.

Figure 5.13: E-plane triplexer.

	PARAM. (mm)	INITIAL	STEP 1	STEP 2	STEP 3	FINAL
JUNCTION	D1	5	10.1439	10.7466	10.8279	10.8279
	D2	10	14.0919	16.1195	16.1197	16.1197
	L1	20	55.9849	48.6647	48.6543	48.6543
CHANNEL 1	L2	44.3268		44.6371	44.2891	44.2891
	A1	15.6122		18.9854	19.1839	19.1839
	L3	48.0065			46.8363	46.8262
	A2	15.6122			15.7126	15.6867
	L4	44.3268				44.2805
	A3	26.1039				26.0128
CHANNEL 2	L5	41.0093		48.8500	48.6095	48.6095
	A4	14.4227		16.1078	16.0551	16.0551
	L6	44.3121			43.8809	43.8664
	A5	14.4227			14.4333	14.4484
	L7	41.0093				40.9387
	A6	24.6622				24.7686
CHANNEL 3	L8	38.2312		40.3053	40.0607	40.0607
	A7	13.4465		15.3053	15.2521	15.2521
	L9	41.2397			40.7683	40.7541
	A8	13.4466			13.4422	13.4509
	L10	38.2773				38.1912
	A9	23.3240				23.4293

Table 5.3: Parameters value in each step of the E-plane in-line triplexer.

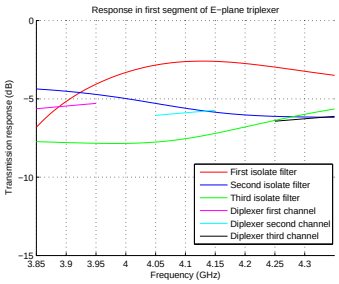

(a) First step.

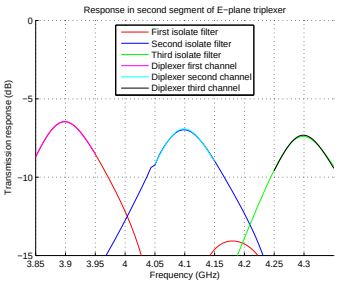

(b) Second step.

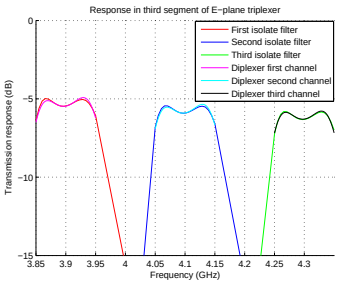

(c) Third step.

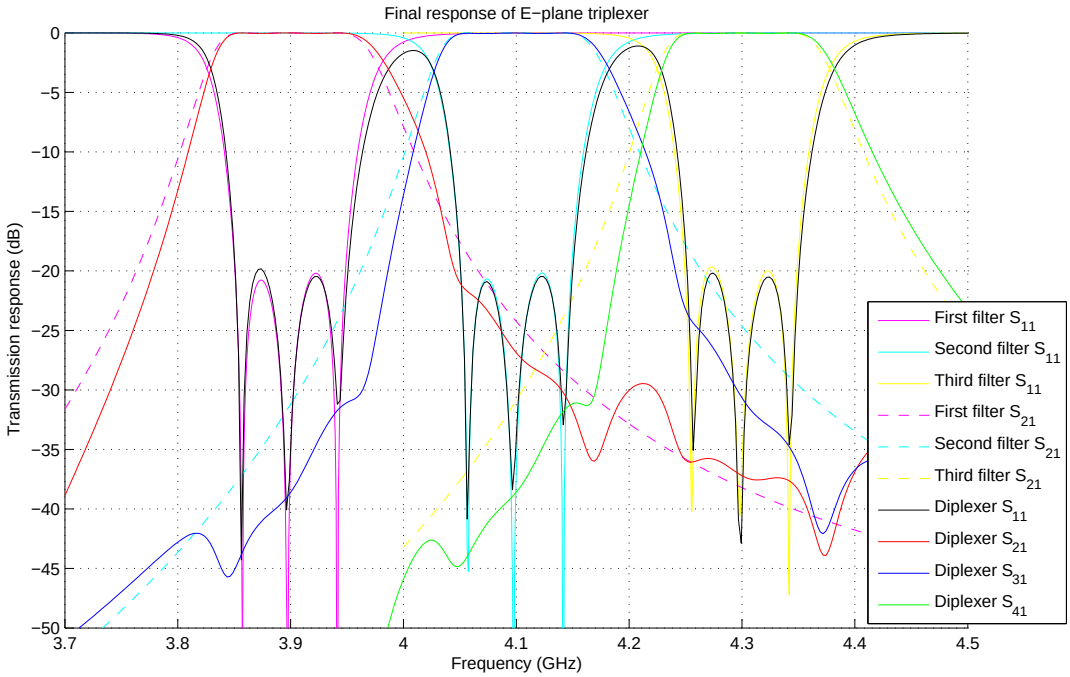

(d) Final response.

Figure 5.14: Response in each step of the E-plane in-line triplexer.

5.3 Diplexer with dual-mode filters

As we have seen in the previous chapter, dual-mode cavities allow us to introduce transmission zeros at the edges of the filter passband increasing the selectivity of the filter at the expense of a reduced rejection in the stopband. The possibility of increasing the selectivity by introducing transmission zeros will reduce the required guard band between channels and even can eliminate it. In this way it would be possible to get adjacent channels. Some authors have already designed diplexers using dual-mode filters to introduce transmission zeros in order to increase the rejection between channels [Ezzeddine et al., 2012, Cheng et al., 2013].

However, by extending the segmentation technique introduced by Guglielmi [Guglielmi and Melcon, 1993, Guglielmi, 1994] to the design of multiplexers, it is possible to design the dual-mode filters separately without taking into account the diplexer structure. Afterwards the designed filters are attached to the diplexer junction and the first cavity is reoptimized to retrieve the first partial response of each filter, following the strategy of the step-by-step design technique derived in this work.

Firstly we will implement two diplexers with third-order dual-mode filters. These filters will be the ones already designed in the previous chapter which consist of a dual-mode cavity and a single-mode one (Figures 4.16 and 4.28). To increase the rejection between channels and reduce the guard band, the filter at lower frequency will have a transmission zero above the passband while the upper channel will introduce a transmission zero below the passband. Thus a much greater selectivity between between both frequencies bands can be achieved.

The best frequency specifications for these filters are those in which the transmission zero introduced by each channel coincides with the beginning of the passband of the adjacent channel. Then the guard band between channels is minimized. However in this section we have tried to make a comparison between two diplexers built with the two third-order dual-mode filters designed in the previous chapter. These filters are the third-order dual-mode filter using the mode TE_{301} and the one that uses the TE_{201} mode. Thus the different rejection levels obtained when placing the transmission zeros close to the passband or far from it are highlighted.

That is the reason why both diplexers keep the same frequency specifications. With these specifications, the diplexer formed by filters with the TE_{201} mode will satisfy the condition that the transmission zeros coincide with the beginning of the adjacent channel pass-band. Nevertheless the diplexer composed of filters with the TE_{301} mode will not due to the higher rejection between channels provided by this technology.

These diplexers have been built by coupling both filters to the diplexer junction through the single-mode cavity. Thus the junction structures obtained in the diplexers with in-line filters can be reused. In addition, the optimization is much easier if the filters are attached to the junction by the single-mode cavity since the two resonant modes of the dual mode cavity are not disturbed by the junction.

Finally an example of a diplexer with only dual mode cavities is shown in all-inductive technology. It consists of two fourth-order dual-mode filters with a transmission zero at each side of the passband similar to the one designed in the previous chapter (Figure 4.35). In this way, it is shown the procedure to follow if it is necessary to attach the diplexer junction to a dual-mode cavity and not to a single-mode as in the previous cases.

5.3.1 E-plane diplexer with TE_{102} and TE_{301} modes

This diplexer is composed of two third-order filters with the TE_{301} mode which provide one transmission zero on each channel. These filters are the one designed in the previous chapter (Figure 4.16) for the first channel and a identical one with 100 Mhz bandwidth but frequency-shifted and with the transmission zero below the passband for the second channel. The obtained diplexer structure is shown in (Figure 5.15).

Each of the filters have a bandwidth of 100 MHz and a reflection level of -15 dB. Moreover, the passband of each channel will be centered at 3.9 GHz and 4.1 GHz.

The design process is exactly the same as for the diplexer with two channels stacked in the E-plane which has been presented in the previous section. In the first iteration the junction is optimized to achieve the appropriate coupling level to each channel. As initial dimensions for the junction, we

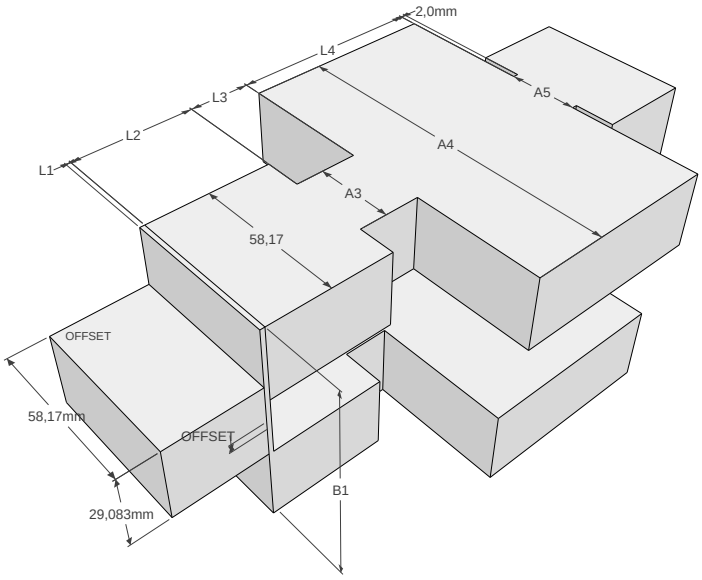

(a) Top view.

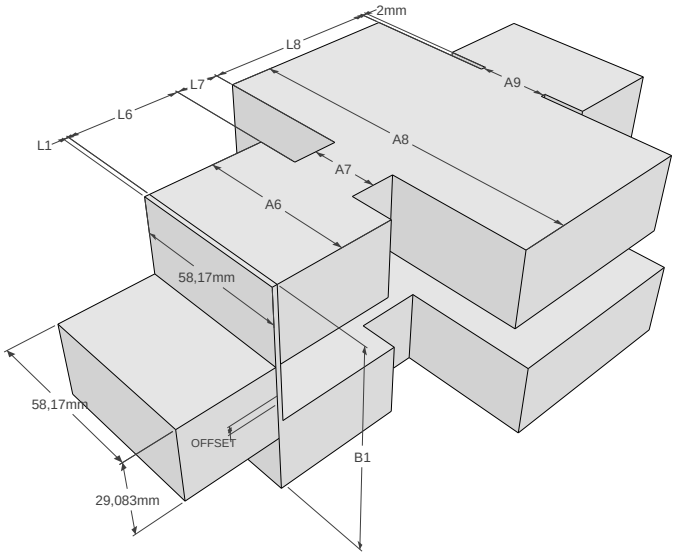

(b) Bottom view.

Figure 5.15: E-plane diplexer with the TE_{102} and TE_{301} modes.

	PARAM. (mm)	INITIAL	STEP 1	STEP 2	FINAL
JUNCTION	OFFSET	0	-0.2561	-2.4666	-3.2495
	L1	5	17.5530	1.3801	1.7583
	B1	80	78.5199	80.4175	81.0365
CHANNEL 1	L2	29.8272		47.2720	47.1257
	L3	24.9089		23.8345	23.5291
	A3	29.8232		29.5293	29.7092
	L4	74.9603			75.0503
	A4	129.2196			129.2142
	A5	27.4531			27.0362
	L5	2			2
CHANNEL 2	L6	28.8761		43.8748	43.3239
	L7	17.0073		17.0073	16.9945
	A7	25.7832		25.7832	25.7473
	L8	71.6192			71.6192
	A8	129.4929			129.4929
	A9	26.7285			26.7285
	L9	2			2

Table 5.4: Parameters value in each step of the third-order diplexer with the TE_{301} mode.

have taken similar values to those obtained in the previous section for the in-line diplexer.

1. **STEP 1: Optimization of the diplexer junction.** Parameters ($B1$, $L1$ and $OFFSET$) shown in Figure 5.15 are optimized. Table 5.4 lists the value of the initial and obtained parameters in STEP 1 and Figure 5.16a shows the coupling level to each channel provided by the diplexer junction compared to the coupling level obtained with the isolated filters. It can be observed that the right coupling could be obtained for both channels at the center frequency of each channel.

2. **STEP 2. Optimization of the first resonator.** In this step, two iterations have also been made:

   (a) Optimization of the above parameters $B1$, $L1$ and $OFFSET$ (Figure 5.15) together with the lengths $L2$ and $L6$. The objective is to compensate the length of the diplexer junction by decreasing the length of the single-mode cavities.

   (b) Optimization of the above parameters along with the central iris.

3. **STEP 3. Final adjustment.** Since the central iris is optimized, the next step should be to optimize the dual mode cavity. However, as the result is almost perfect, a global optimization has been made to obtain the response shown in Figure 5.16c.

5.3.2 H-plane diplexer with TE_{102} and TE_{201} modes

In this example another diplexer will be built, this time with all-inductive technology. Here, the third-order dual-mode filter with the TE_{201} mode designed in the previous chapter has been used for the first channel. Similarly to the previous example the same filter with 100 Mhz bandwidth but frequency-shifted and with the transmission zero below the passband has been used for the second channel. The desired structure for this diplexer is shown in Figure 5.17.

The design process is exactly the same as in the previous cases thus a detailed explanation is not required. The parameters modified in each step are listed in Table 5.5. It can be seen that in the design of the complete diplexer, only five parameters have been modified with respect to the two

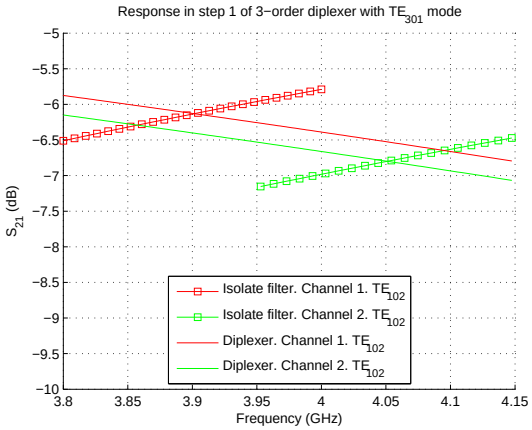

(a) First step.

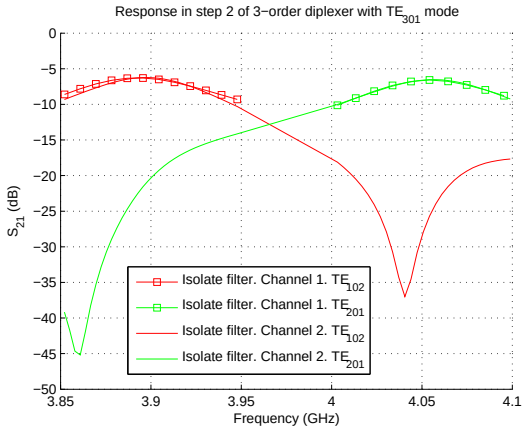

(b) Second step.

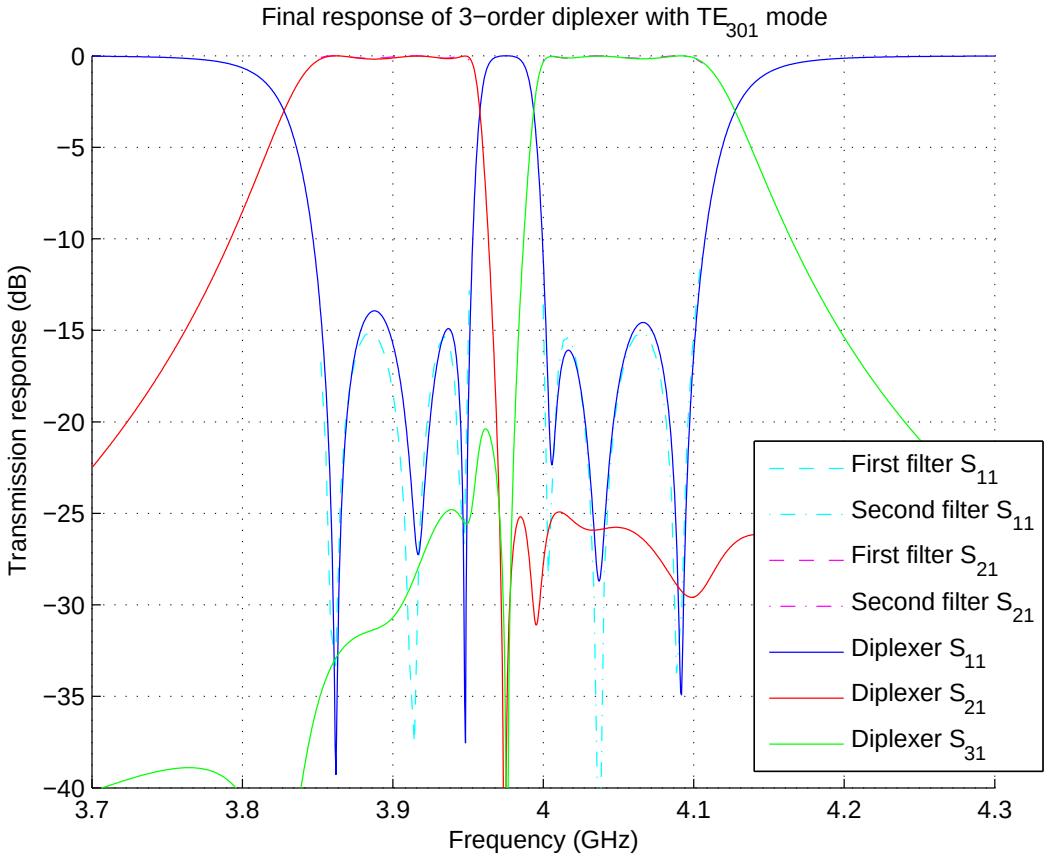

(c) Final response.

Figure 5.16: Response in each step of the third-order diplexer with the TE_{301} mode.

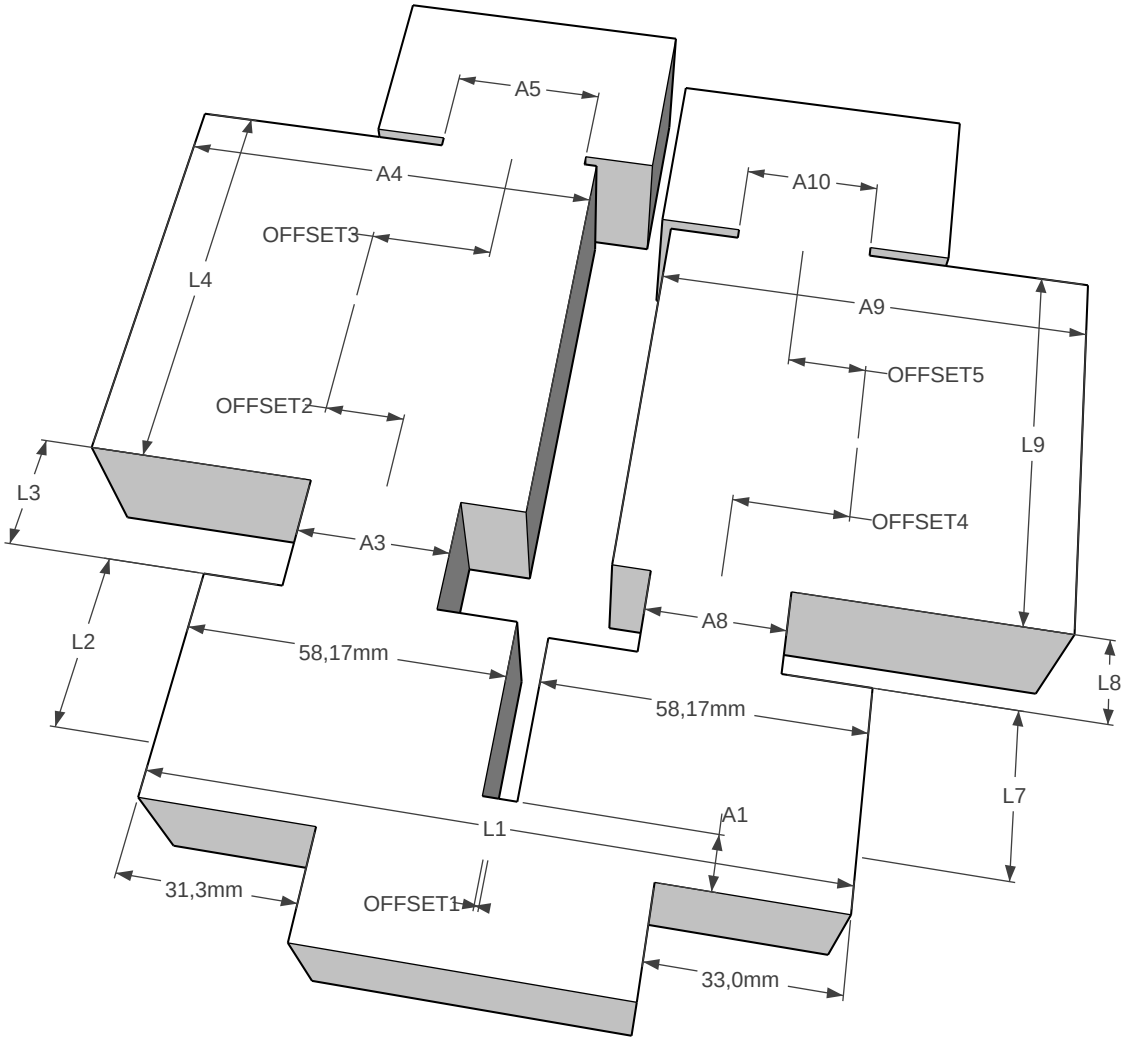

Figure 5.17: H-plane diplexer with the TE_{102} and TE_{201} modes.

	PARAM. (mm)	INITIAL	STEP 1	STEP 2	FINAL
JUNCTION	OFFSET1	0	0.2935	0.7685	0.7685
	A1	10	9.0723	9.4698	9.4698
	L1	120	120.0551	121.4496	121.4496
CHANNEL 1	L2	40.17331		32.9866	32.9866
	L3	23.0809			23.0809
	A3	29.3832			29.3832
	OFFSET2	17.9348			17.9348
	L4	82.1140			82.1140
	A4	83.4731			83.4731
	OFFSET3	-23.7414			-23.7414
	A5	30.8173			30.8173
CHANNEL 2	L7	39.0980		31.5082	31.5082
	L8	15.3330			15.3330
	A8	25.4069			25.4069
	OFFSET4	21.0894			21.0894
	L9	76.7551			76.7551
	A9	84.0853			84.0853
	OFFSET5	-14.5871			-14.5871
	A10	26.5414			26.5414

Table 5.5: Parameters value in each step of the third-order diplexer with TE_{201} mode.

filters designed separately. The variations of these parameters were performed by two iterations, thus due to this and since the initial values of these parameters are very close to the final dimensions, the optimization of the diplexer is extremely fast.

Next it is commented each step of the design procedure:

1. **STEP 1: Optimization of the diplexer junction.** Parameters $A1$, $L1$ and $OFFSET1$ (Figure 5.17) are optimized. Table 5.5 list the values of the initial and obtained parameters in STEP 1. Figure 5.18a shows the coupling level provided by the diplexer junction compared with the levels obtained with the isolated filters. Once more, it can be seen that the required coupling is perfectly fitted within the whole bandpass of each channel.

2. **STEP 2. Optimization of first resonator.** The above parameters ($A1$, $L1$ and $OFFSET1$) together with the lengths $L2$ and $L7$ are optimized. The goal is to compensate for the length of the junction by decreasing the length of the single-mode cavities.

The design concludes at this point without changing any other parameter since the partial response in step 2 is already quite good. Moreover as the central couplings of both filters have not been modified, the field in the dual-mode cavities has not been disturbed. Thus they do not need to be modified.

As a result, based on the designs of both filters separately, it is only required the variation of five parameters to obtain the final design of the diplexer. This final response is shown in Figure 5.18c.

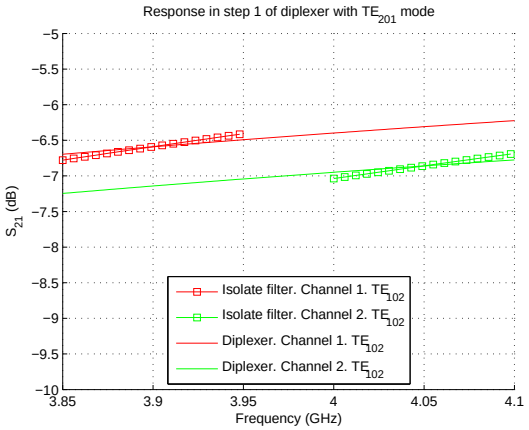

(a) First step.

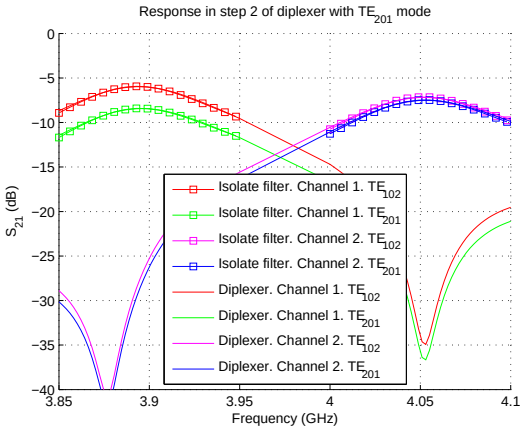

(b) Second step.

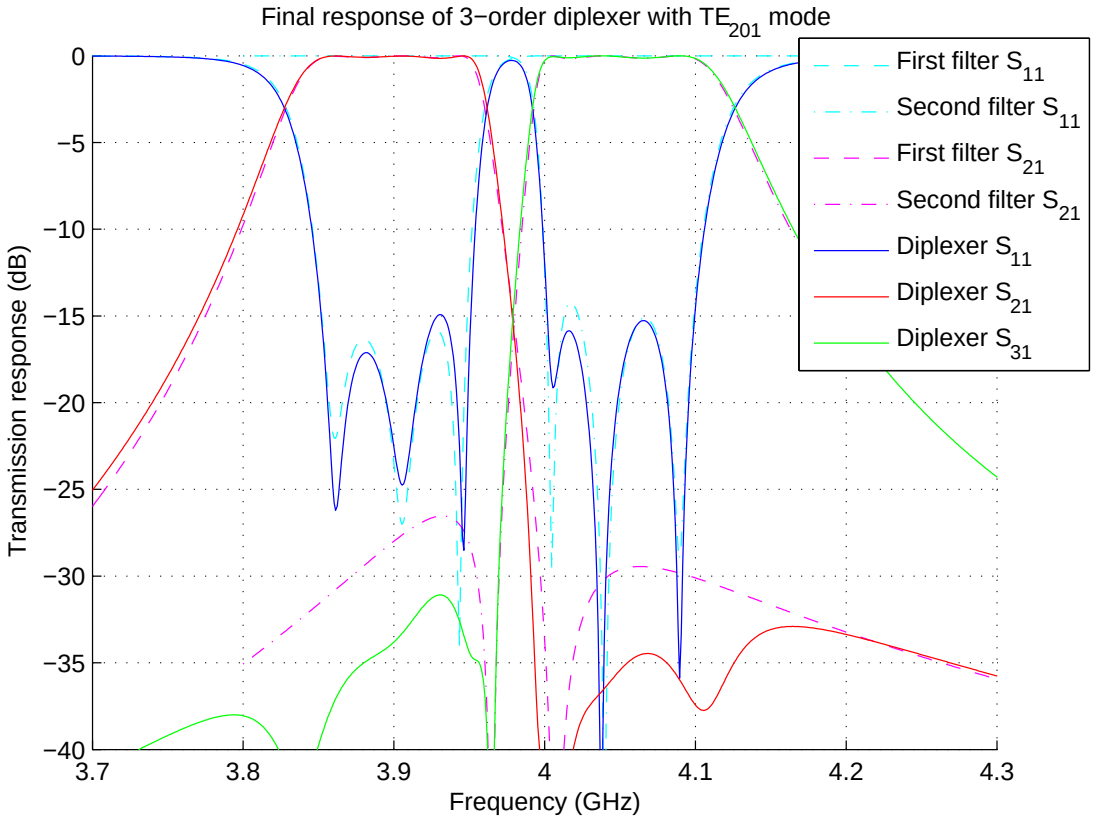

(c) Final response.

Figure 5.18: Response in each step of third-order diplexer with TE_{201} mode.

5.3.3 Isolated fourth-order filters

Finally, it is shown an example of an all-inductive diplexer built with two fourth-order dual-mode filters with a transmission zero at each side of the passband. An example of the type of filters used in this diplexer have been already presented in the previous chapter (Figure 4.35). These filters are only composed of dual-mode cavities, then it is not possible to bind the filters with the diplexer junction by a single mode cavity. This leads to a more complex design procedure as compared to the previous diplexers. I will now explain the procedure to follow if it is necessary to make the diplexer junction coupled not to a single-mode cavity but to a dual-mode one.

When trying to build this diplexer exclusively with dual-mode cavities, the following drawbacks appear:

1. The input iris can not be removed since in order to adjust the coupling to both modes independently, the windows width as well as the offset are necessary.

2. If the input iris is kept in both filters, the level of coupling provided by the whole "diplexer junction + input irises" drastically decreases and it is necessary to re-optimize the first iris to compensate for this effect.

3. The width of all coupling windows should be the same in each filter to assure orthogonality between the two modes in the dual-mode cavities. Therefore this parameter can not be modified.

A possible solution could be to increase the width of all windows to obtain a higher coupling level but then you reach the limit on the offset of input and output windows. This is because by increasing the width of the windows, the level of coupling to the TE_{102} mode increases faster than the coupling to the TE_{201} mode. Therefore it is necessary to increase the appropriate offset to get the right coupling to both modes. As it is not possible to increase the width of the windows, if it is necessary to increase the input coupling to both filters, another option is to reduce the thickness.

Obviously the thickness of the windows can not be reduced more than 1-2 mm due to manufacturing constrains. Consequently for this reduction to be possible, the design of the isolated filters is done using thicker (12 mm) input windows. However, as already mentioned, in order to make the irises thicker it is necessary to increase the width of the windows and therefore the maximum offset available in the coupling windows decreases. To make it possible, the bandwidth of each channel has been cut in half. Thus the required coupling level in the input windows is lower and therefore it is possible to design these filters with input irises 12 mm thick.

The designed filters to implement this diplexer are shown in Figure 5.19. As it can be noted, in addition to the thickness of the irises, the offset of the output waveguides have been increased to the maximum value. Thus the physical separation between both channels (and then the footprint) in the final structure (Figure 5.20) is as small as possible. This is very desirable since it will increase even more the input coupling to each channel.

Tables 5.6 and 5.7 list the dimensions of the designed filters shown in Figure 5.19. As can be seen from filters in Fig 5.19, almost the maximum offset in the input waveguides ($OFFSET1$) has been applied. This means that 50 MHz is about the maximum bandwidth that can be obtained with these filters once the thickness of the input irises is set to 12 mm and the reflection level to -15 dB.

PARAM.	VALUE (mm)	PARAM.	VALUE (mm)	PARAM.	VALUE (mm)
L1	12	A1	33.3764	OFFSET 1	-22.7458
L2	76.0893	A2	83.3790	OFFSET 2	10.8975
L3	62.6362	A3	34.4835	OFFSET 3	-13.9907
L4	75.1232	A4	86.5948	OFFSET 4	25.2384
L5	20.2057	A5	35.9806	OFFSET 5	-11.0260

Table 5.6: Parameters of the first-channel isolated filter with two transmission zeros.

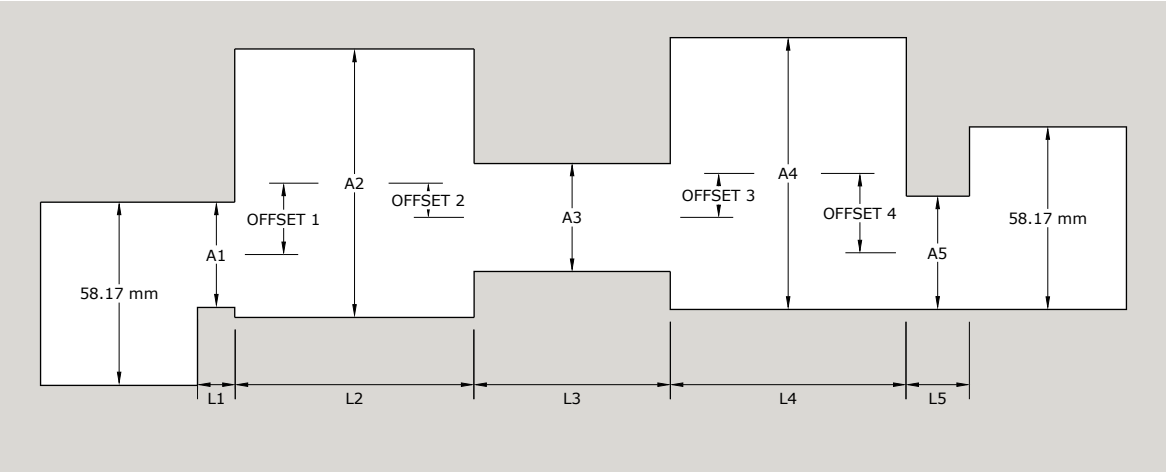

(a) First channel.

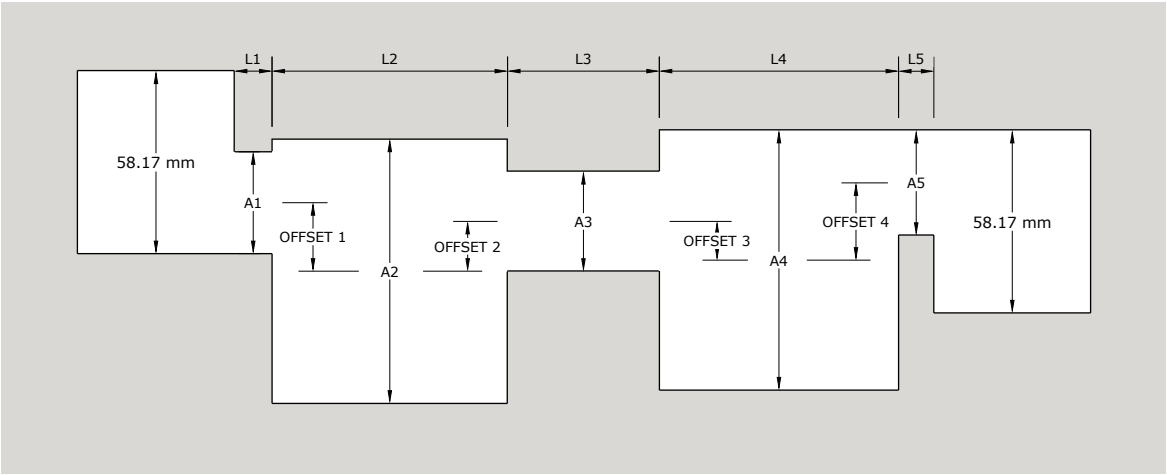

(b) Second channel.

Figure 5.19: Isolated fourth-order filters with two transmission zeros.

PARAM.	VALUE (mm)	PARAM.	VALUE (mm)	PARAM.	VALUE (mm)
L1	12	A1	32.4553	OFFSET 1	21.8275
L2	75.0864	A2	84.1389	OFFSET 2	-15.8649
L3	48.3765	A3	31.7523	OFFSET 3	12.3771
L4	76.2731	A4	82.7299	OFFSET 4	-26.6194
L5	11.2486	A5	33.4146	OFFSET 5	12.3395

Table 5.7: Parameters of the second-channel isolated filter with two transmission zeros.

5.3.4 H-plane diplexer with fourth-order dual mode filters

Once the filters for each channel are designed with 12 mm thick irises and with the maximum offset in the output waveguides, it is quite easy to build the diplexer.

The desired structure is shown in 5.20. It can be seen how by applying the maximum offset to the output waveguides, it is possible to achieve a minimum channel spacing (about 2 mm).

Moreover, as it is already mentioned above, the junction of this diplexer, without the input irises, is modeled as an iris of equal width but with a larger equivalent thickness. The approach to follow when binding both filters to the junction that is modeled as a thicker iris of equal width, is to decrease the thickness of the input iris in order to compensate for the equivalent thickness of the junction. Then it is possible to retrieve the response provided by the isolated filters after the first coupling. This is the reason to design the filters with input irises 12 mm thick.

The optimization process is divided in two steps:

- **STEP 1: Optimization of the diplexer junction.** Firstly, the diplexer is cut by the first dual-mode cavity. The output is taken in the first cavity of each channel and the parameters to be optimized are only $A1$, $L1$, $L2$ y $L7$ (Figure 5.20). The aim is to decrease the thickness of the input iris of each channel in the same value as the equivalent thickness of the junction. Table 5.8 shows both the initial and obtained parameters in STEP 1. It can be seen that in the first channel it has been necessary to reduce the first iris thickness from 12 mm to 6.123 mm meanwhile the first iris of the second channel has been reduced from 12 mm to 2.597 mm. Moreover, in this optimization the restriction of the minimum value for the parameter $A1$ has been imposed that ensures a minimum manufacturable separation of about 2 mm between the two channels.
- **STEP 2: Readjustment of the first cavity.** Once the junction has been optimized, the first cavity needs a little adjustment as it is still perturbed by the diplexer junction. For this, the diplexer is cut by the second cavity in both channels. Thus the second dual-mode cavity acts as the filter output. In this step, parameters $A1$, $L1$, $L2$, $L7$ obtained in the previous step as well as $A2$, $OFFSET1$, $L3$, $A3$, $A7$, $OFFSET6$, $L8$ and $OFFSET8$ (Figure 5.20) are optimized. Table 5.8 shows the values of these parameters and it can be noted that their variations are quite small. Thus the optimization is quite fast due to the so good starting point, although at first glance it may seems a complicated structure. Once this optimization has been done it is not necessary to modify any other parameters since the central iris is unchanged and the second cavity is not perturbed.

Table 5.8 lists the final dimensions of the diplexer and Figure 5.21 shows the partial and final responses.

5.4 Conclusions

In this chapter we have done a brief review of the different multiplexer configurations in the framework of the space sector. In addition, the segmentation technique already discussed [Guglielmi and Melcon, 1993, Guglielmi, 1994, Martínez et al., 2013] has been applied to the design of star-junction multiplexer with in-line and dual-mode topologies. For these designs, the filters are designed separately by using the same design procedure as described in the previous chapters. Following the same step-by-step design strategy, afterwards the complete diplexer is built by cutting the filters by the first cavity and by optimizing the diplexer junction and the first segment of each channel to retrieve the correspondent partial response. As a result, the diplexer is dimensioned easily and efficiently and it is not necessary to perform the synthesis of the whole diplexer.

Finally, we have studied the procedure to follow if it is necessary to design a diplexer with the all inductive dual-mode technology with only dual mode cavities [Guglielmi et al., 2001] by coupling the diplexer junction to a dual-mode cavity instead of to a single-mode one.

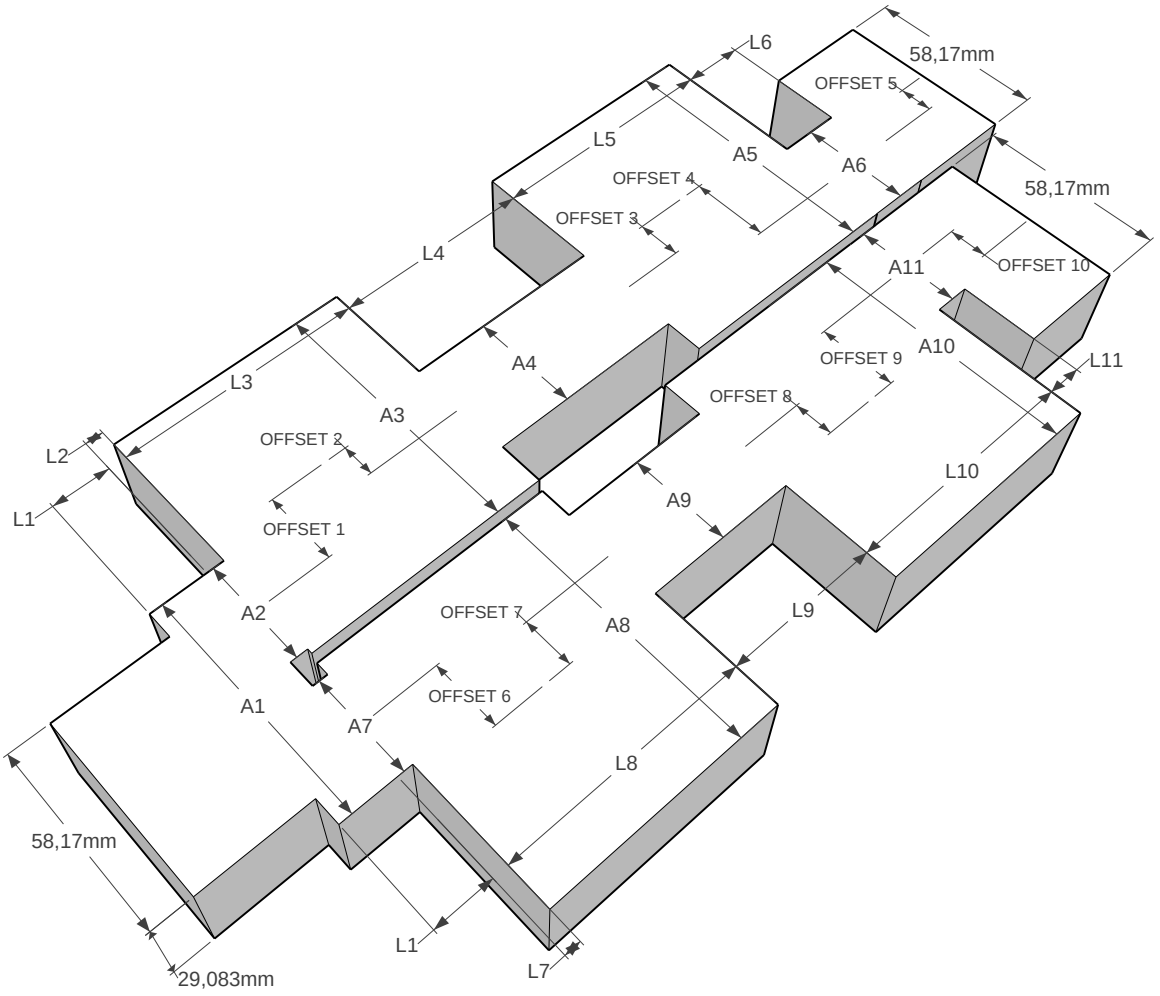

Figure 5.20: H-plane diplexer with fourth-order dual mode filters and two transmission zeros in each channel.

	PARAM. (mm)	INITIAL	STEP 1	STEP 2	FINAL
JUNCTION	A1	75.5	76.7654	75.5	75.5
	L1	20	32.0144	17.6642	17.6642
CHANNEL 1	L2	12	6.1230	5.3876	5.3876
	A2	33.3764		34.4807	34.4807
	OFFSET 1	-22.7458		-23.7838	-23.7838
	L3	76.0893		76.1492	76.1492
	A3	85.3790		85.3329	85.3329
	OFFSET 2	10.8975			10.8975
	OFFSET 3	-13.9907			-13.9907
	L4	62.6362			62.6362
	A4	34.4835			34.4835
	L5	75.1232			75.1232
	A5	86.5948			86.5948
	OFFSET 4	25.2384			25.2384
	OFFSET 5	-11.0260			-11.0260
	L6	20.2057			20.2057
	A6	35.9806			35.9806
CHANNEL 2	L7	12	2.5974	4.6505	4.6505
	A7	32.4553		32.1863	32.1863
	OFFSET 6	21.8275		21.7757	21.7757
	L8	75.0864		75.1393	75.1393
	A8	84.1389		84.1177	84.1177
	OFFSET 7	-15.8649			-15.8649
	OFFSET 8	12.3371			12.3371
	L9	48.3765			48.3765
	A9	31.7523			31.7523
	L10	76.2731			76.2731
	A10	82.7299			82.7299
	OFFSET 9	-24.6194			-24.6194
	OFFSET 10	12.3395			12.3395
	L11	11.2486			11.2486
	A11	33.4146			33.4146

Table 5.8: Parameters value in each step of the diplexers with fourth-order filters and two transmission zeros in each channel.

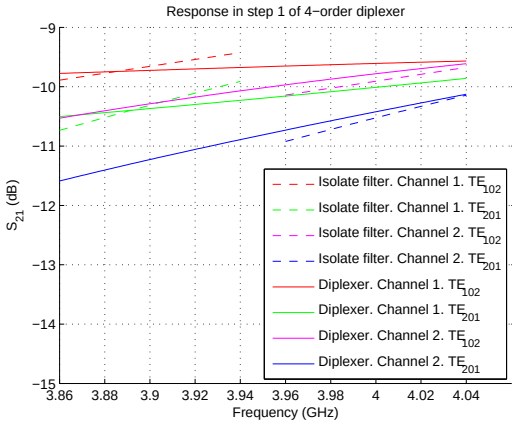

(a) First step.

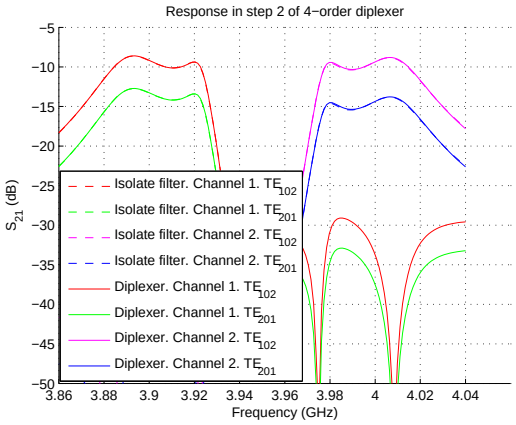

(b) Second step.

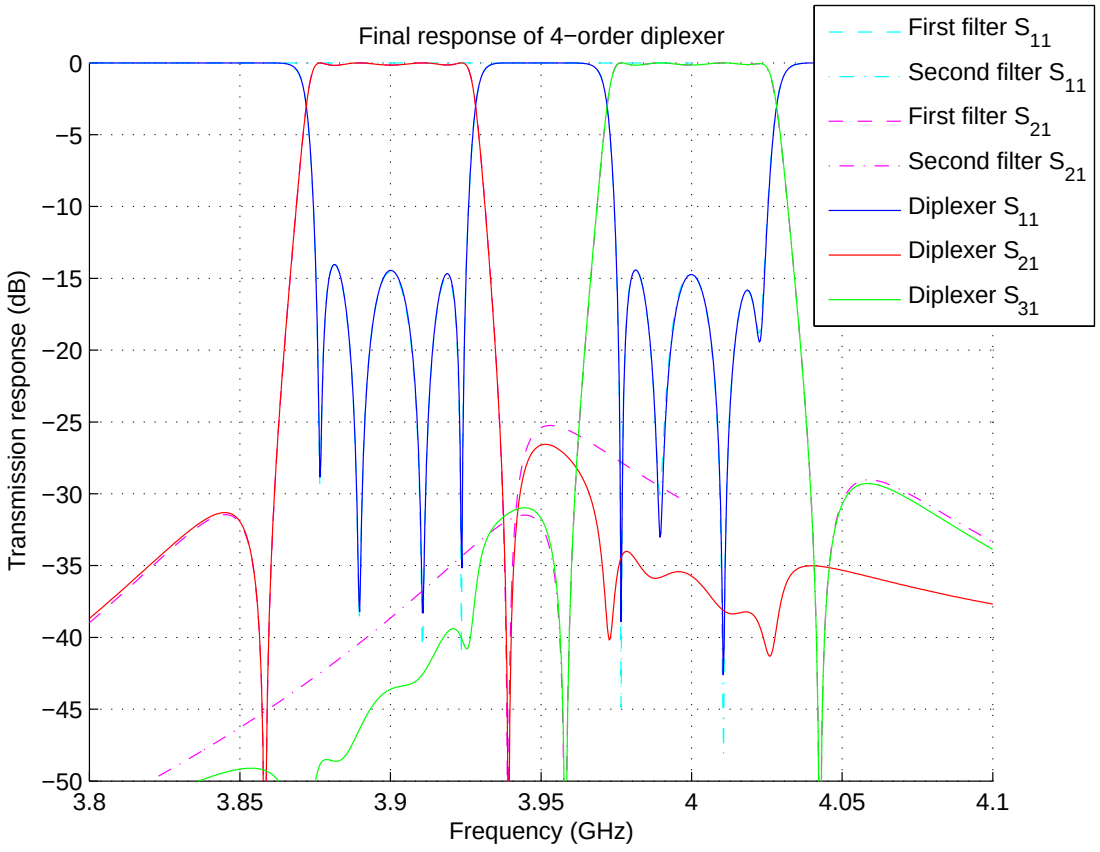

(c) Final response.

Figure 5.21: Final response of the diplexer with fourth-order filters and two transmission zeros in each channel.

6

DUAL-MODE FILTER WITH INPUT-OUTPUT SINGLE-MODE CAVITIES

6.1 Introduction

As discussed in the previous chapters, the design of filters with dual-mode cavities in all-inductive technology has some important drawbacks. The main drawback has been advanced in Chapter 4 and limited the bandwidth of the designed filters due to the impossibility to further increase the coupling to the second mode in the cavity while maintaining the coupling level to the first mode. Indeed, in the previously designed kind of dual-mode filters, the bandwidth is limited by the maximum input and output offset available. This is because the greater filter bandwidth, the higher input (M_{Si}) and output (M_{jL}) coupling values. Then, the width of the input coupling needs to be increased, and this limits seriously the offsets that can be obtained.

Moreover, the more distant from the passband the transmission zero is, the greater the required coupling to the TE_{201} becomes. However, to increase the coupling to the TE_{201} mode above the coupling level to the TE_{102} mode, it is necessary to enlarge the width of the iris in order to get higher couplings to both modes and also to increase the offset to reduce the coupling to the TE_{102} mode. As applicable maximum offset is limited and decreases when iris width gets larger, the maximum coupling level to the second resonant mode that can be obtained while maintaining the coupling to the first mode is limited by this parameter. Thus, both the bandwidth and the position of the transmission zeros are limited.

Another drawback is that since external and internal coupling levels are quite different and all coupling windows in dual-mode cavities must have the same width to maintain orthogonality between the two modes of dual-mode cavities, the internal windows are quite thicker than the input and output windows. Thus the filter footprint becomes too large when the number of dual-mode cavities increases.

To overcome these drawbacks, we have proposed for the first time a new topology in which single-mode cavities have been added to the filter input and output.

6.2 Adding input and output single-mode cavities

By adding single-mode input and output cavities the problem of the higher required coupling values when increasing the filter bandwidth is solved. These high coupling values can be easily obtained by coupling to an input and output single-mode cavity where no offset is required. In this way, the couplings to the dual-mode cavities are internal couplings that are always much smaller than the input and output couplings, especially when the bandwidth increases.

In addition, due to the smaller couplings, there is a larger offset range available. Then it is possible to overcome the limitation of the maximum coupling level to the second mode while keeping the coupling to the first one. This fact limited the maximum distance from the passband of the transmission zeros.

By studying the behavior of standard coupling levels M_{ij} while varying the position of the transmission zeros it is seen that the coupling to the second mode (TE_{201}) is always smaller than the coupling to the first one (TE_{102}). In spite of the fact that the coupling level to the second mode in a dual-mode cavity increases when moving further from the passband the transmission zero, this level

is always smaller and only if the transmission zero is placed at infinity frequency, then both modes reach the same coupling level. Figure 6.1a shows the coupling levels to the first and the second mode in a dual-mode cavity as a function of the normalized position of the transmission zero with respect to the passband. It can be seen that the couplings to both modes reaches the same level when the transmission zeros are located at the infinity.

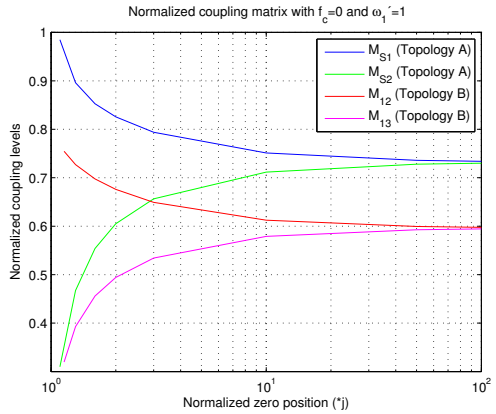

(a) Couplings levels in the normalized coupling matrix.

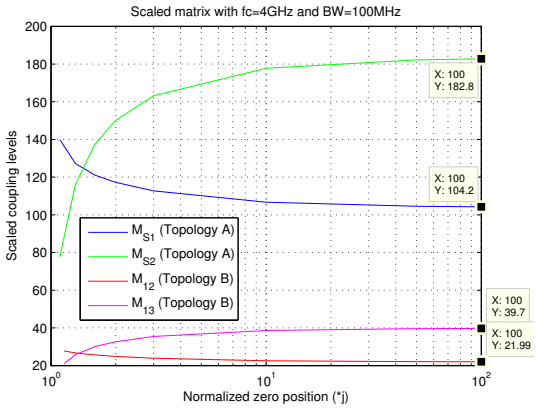

(b) Couplings levels in the scaled coupling matrix with a bandwidth of 100 MHz.

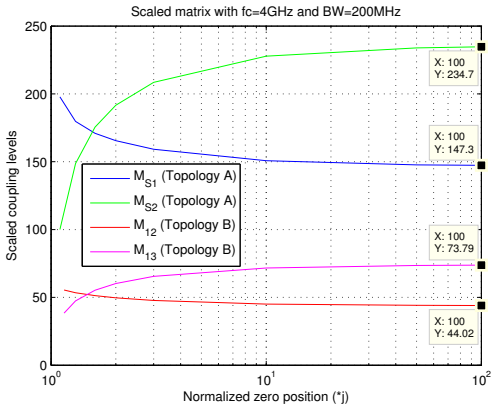

(c) Couplings levels in the scaled coupling matrix with a bandwidth of 200 MHz.

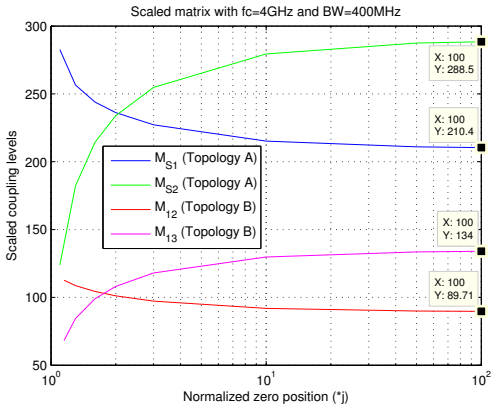

(d) Couplings levels in the scaled coupling matrix with a bandwidth of 400 MHz.

Figure 6.1: Input couplings to the first dual-mode cavity in both topologies. Both topologies A and B are shown in Figure 6.2.

However, unlike normalized couplings shown in Figure 6.1a, when the matrix is scaled, the input coupling to the second mode can rise above the coupling level to the first mode. This fact is shown in Figure 6.1b, where a bandwidth of 100 MHz and a central frequency of 4 GHz have been considered. It should be noted the different coupling levels to both resonant modes in a dual-mode cavity when this cavity is placed at the filter input (Topology A in figure 6.2) or between single-mode cavities (Topology B in figure 6.2).

Furthermore, it can be seen in Figure 6.1c and 6.1d the behavior of the coupling levels that rise when the bandwidth increases. If single-mode cavities are added to the filter input and output the level of coupling required by this topology with a bandwidth of 400 MHz (topology B in Figure 6.1d) is even lower than the level required by the topology without single-mode cavities with a bandwidth of 100 MHz (topology A in Figure 6.1b). Thus the margin for the implementable bandwidth is considerably extended.

Finally, it is important to consider the relation R between the coupling to the second mode (TE_{201})

and with respect to the first one (TE_{102}).

$$R = \frac{M_{S2}}{M_{S1}} \quad \text{In the topology A} \tag{6.1}$$

$$R = \frac{M_{13}}{M_{12}} \quad \text{In the topology B} \tag{6.2}$$

This relation R is related to the required offset of a dual-mode cavity in order to introduce a transmission zero at a given frequency. Thus if the relation R decreases, the required offset is lower and then, the maximum distance from the passband where the transmission zero can be placed is increased.

The value R is also linked to the filter bandwidth. Figure 6.3 shows the relation between the coupling to each mode in both topologies when the bandwidth increases. In the topology with single-mode cavities (Topology B), the relation between the coupling to the second mode and the coupling to the first one is greater. Thus the coupling to the mode TE_{201} is higher as compared to the couplings to the mode TE_{102}. This means that the required offset is larger for topology B. Nevertheless this is not a problem in the topology with single-mode cavities due to the smaller irises. Moreover, it can also be noted in Figure 6.3 that when the bandwidth increases, the couplings to both modes are more similar. This means that the coupling to the mode TE_{102} rises faster than the coupling to the mode TE_{201}. Thus the relation R decreases. This fact together with the smaller couplings to the dual-mode cavities in the topology with single-mode cavities (Topology B) make easier the design of dual-mode filters with larger bandwidth.

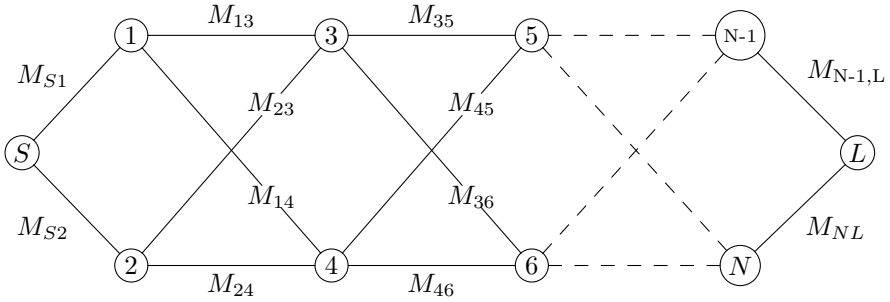

(a) Topology A: Dual-mode filters with only dual-mode cavities.

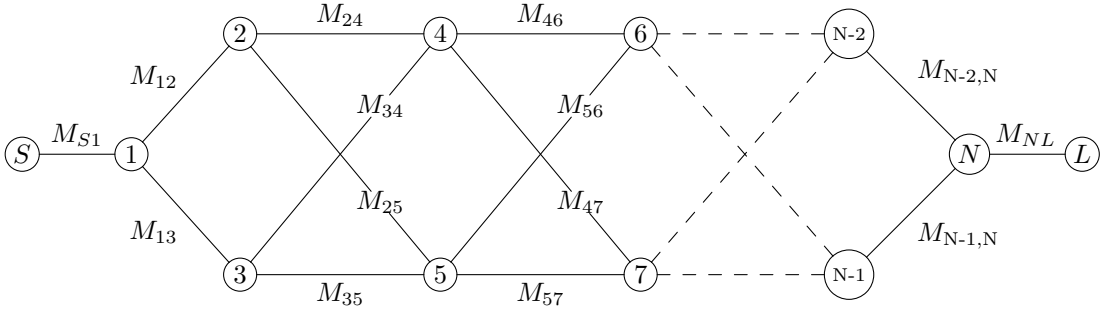

(b) Topology B: Dual-mode filters with single-mode cavities in the filter input and output.

Figure 6.2: Generalized coupling-routing diagram for both topologies of all-inductive dual mode filters.

6.2.1 Coupling matrix for this topology

The coupling matrices shown in this section remain the same topology all-dual-mode previously shown. However, by adding single-mode cavities at the input and output of the filter, the dual-mode cavities are isolated from the large input and output couplings.

Figure 6.2b shows the generalized coupling-routing diagram for the topology all-dual-mode with input and output single-mode cavities. Moreover, Figure 6.4 shows the coupling matrix which implements this topology.

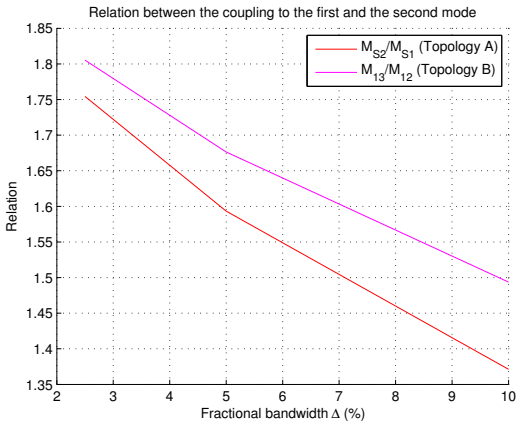

Figure 6.3: Relation between the coupling to the second mode (TE_{201}) and to the first mode (TE_{102}) in the dual-mode cavity. Both topologies A and B are shown in Figure 6.2.

$$M = \begin{bmatrix} 0 & M_{S1} & 0 & 0 & 0 & 0 & 0 & 0 & 0 & \cdots & 0 & 0 \\ M_{1S} & M_{11} & M_{12} & M_{13} & 0 & 0 & 0 & 0 & 0 & \cdots & 0 & 0 \\ 0 & M_{21} & M_{22} & 0 & M_{24} & M_{25} & 0 & 0 & 0 & \cdots & 0 & 0 \\ 0 & M_{31} & 0 & M_{33} & M_{34} & M_{35} & 0 & 0 & 0 & \cdots & 0 & 0 \\ 0 & 0 & M_{42} & M_{43} & M_{44} & 0 & M_{46} & M_{47} & 0 & \cdots & 0 & 0 \\ 0 & 0 & M_{52} & M_{53} & 0 & M_{55} & M_{56} & M_{57} & 0 & \cdots & 0 & 0 \\ 0 & 0 & 0 & 0 & M_{64} & M_{65} & M_{66} & 0 & M_{68} & \cdots & 0 & 0 \\ 0 & 0 & 0 & 0 & M_{74} & M_{75} & 0 & M_{77} & M_{78} & \cdots & 0 & 0 \\ 0 & 0 & 0 & 0 & 0 & 0 & M_{86} & M_{87} & M_{88} & \cdots & 0 & 0 \\ \vdots & \vdots & \vdots & \vdots & \vdots & \vdots & \vdots & \vdots & \vdots & \ddots & \vdots & \vdots \\ 0 & 0 & 0 & 0 & 0 & 0 & 0 & 0 & 0 & \cdots & M_{NN} & M_{NL} \\ 0 & 0 & 0 & 0 & 0 & 0 & 0 & 0 & 0 & \cdots & M_{LN} & 0 \end{bmatrix}$$

Figure 6.4: Coupling matrix of a dual mode filter with dual-mode cavities and single-mode cavities in the filter input and output.

6.3 Design example

In this section, a sixth-order filter with two transmission zeros in the real plane is designed. This filter will be centered at 19.09 GHz with a reflection level of -22 dB and a bandwidth of 300 MHz. The transmission zeros will be placed at 18.91 GHz and 19.3 GHz.

The coupling matrix which gives this response is shown in Figure 6.5 and the ideal response provided by this matrix appears in Figure 6.6.

$$M = \begin{bmatrix} 0 & -1.0324 & 0 & 0 & 0 & 0 & 0 & 0 \\ -1.0324 & -0.0059 & 0.7788 & 0.3655 & 0 & 0 & 0 & 0 \\ 0 & 0.7788 & -0.2165 & 0 & -0.2509 & -0.4926 & 0 & 0 \\ 0 & 0.3655 & 0 & 0.9484 & 0.0967 & 0.1899 & 0 & 0 \\ 0 & 0 & -0.2509 & 0.0967 & -0.9004 & 0 & 0.4286 & 0 \\ 0 & 0 & -0.4926 & 0.1899 & 0 & 0.2889 & -0.7460 & 0 \\ 0 & 0 & 0 & 0 & 0.4286 & -0.7460 & -0.0059 & 1.0324 \\ 0 & 0 & 0 & 0 & 0 & 0 & 1.0324 & 0 \end{bmatrix}$$

Figure 6.5: Coupling matrix which provides the sixth-order response.

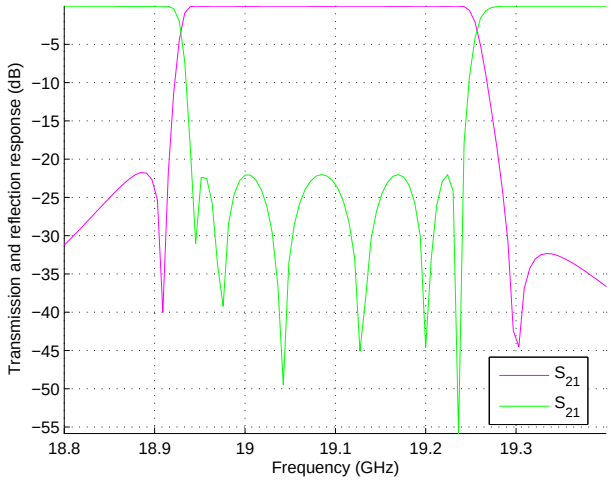

Figure 6.6: Ideal response of the sixth-order filter with input and output single-mode cavities.

The first task is to match each resonant mode in each dual-mode cavity with the correspondent row and column in the coupling matrix. This matrix consists of eight rows and eight columns. The first and last ones correspond to the input and output ports of the filter while the central ones represent each of the resonances.

As it is known, in this kind of dual-mode cavities it is provided a greater coupling to the TE_{102} mode than to the TE_{201} mode. Thus the third row and column represent the resonant mode TE_{102} and the fourth row and column correspond to mode TE_{201} in the first dual-mode cavity since the coupling value $S_{12} = 0.7788$ is higher than the value $S_{13} = 0.3655$. With regard to the second resonant cavity, the fifth row and column correspond to the mode TE_{201} while the sixth ones correspond to the mode TE_{102}.

According to this, the matching of the resonant modes with the coupling values remains as shown in Figure 6.7.

6.3.1 Structure view

When single-mode cavities are placed in the filter input and output, the input and output couplings are no longer a problem. Moreover the internal coupling levels are much smaller and can be easily obtained with the coupling windows to the dual-mode cavities. With regard to the thicker internal

$$M = \begin{bmatrix} & Source & TE_{101} & TE_{102} & TE_{201} & TE_{201} & TE_{102} & TE_{101} & Load \\ Source & 0 & -1.0324 & 0 & 0 & 0 & 0 & 0 & 0 \\ TE_{101} & -1.0324 & -0.0059 & 0.7788 & 0.3655 & 0 & 0 & 0 & 0 \\ TE_{102} & 0 & 0.7788 & -0.2165 & 0 & -0.2509 & -0.4926 & 0 & 0 \\ TE_{201} & 0 & 0.3655 & 0 & 0.9484 & 0.0967 & 0.1899 & 0 & 0 \\ TE_{201} & 0 & 0 & -0.2509 & 0.0967 & -0.9004 & 0 & 0.4286 & 0 \\ TE_{102} & 0 & 0 & -0.4926 & 0.1899 & 0 & 0.2889 & -0.7460 & 0 \\ TE_{101} & 0 & 0 & 0 & 0 & 0.4286 & -0.7460 & -0.0059 & 1.0324 \\ Load & 0 & 0 & 0 & 0 & 0 & 0 & 1.0324 & 0 \end{bmatrix}$$

Figure 6.7: Matching of each resonance in the sixth-order filter with each value of the coupling matrix.

irises, since the internal required couplings are quite similar to each other, the internal coupling windows can keep almost the same thickness which is set to the minimum manufacturable value namely between $1-2\ mm$. Indeed, the filter structure is the one shown in Figure 6.8.

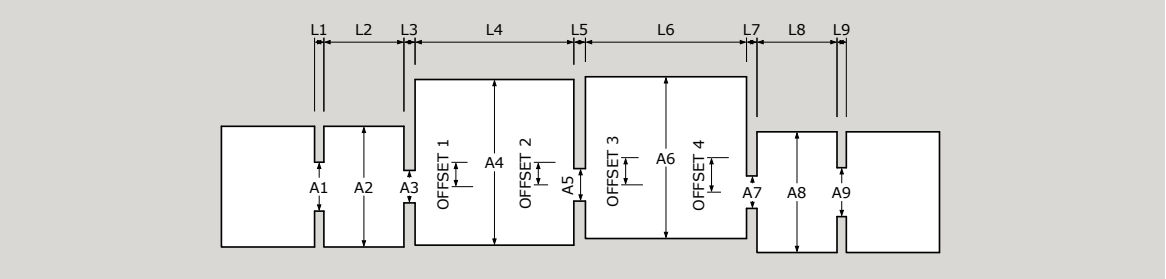

Figure 6.8: Designed sixth-order filter with 2 TZ by adding dual-mode cavities to the filter input and output.

6.3.2 Design procedure

The approach for designing this filter is exactly the same as it was developed in Chapter 4. Firstly, the first half of the filter is dimensioned by the forward design, and by the backward design the second part of the filter is obtained.

Next it is to get the initial values to be used in both cavities. With the expressions introduced in chapter 4, we get the resonant frequency of both modes in each cavity taking into account that $B = -M_{ii} \cdot BW$ in each dual-mode cavity.

$$fr = f_0 + \Delta f = \frac{1}{2} \cdot \left(B + \sqrt{B^2 + 4 \cdot f_0^2} \right) \tag{6.3}$$

Thus according to the matching done in the previous section:

- In the first dual-mode cavity:

$$B_{TE_{102}} = -M_{22} \cdot BW = -(-2.2165) \cdot 100\ MHz = 221.65\ MHz \tag{6.4}$$
$$B_{TE_{201}} = -M_{33} \cdot BW = -(0.9484) \cdot 100\ MHz = -94.84\ MHz \tag{6.5}$$

$$fr_{TE_{102}} = f_0 + \Delta f_{TE_{102}} = \frac{1}{2} \cdot \left(B_{TE_{102}} + \sqrt{B_{TE_{201}}^2 + 4 \cdot f_0^2} \right) = 3.9108\ GHz \tag{6.6}$$
$$fr_{TE_{201}} = f_0 + \Delta f_{TE_{201}} = \frac{1}{2} \cdot \left(B_{TE_{201}} + \sqrt{B_{TE_{201}}^2 + 4 \cdot f_0^2} \right) = 3.8529\ GHz \tag{6.7}$$

- In the second dual-mode cavity:

$$B_{TE_{102}} = -M_{55} \cdot BW = -(0.2889) \cdot 100\ MHz = -28.89\ MHz \tag{6.8}$$
$$B_{TE_{201}} = -M_{44} \cdot BW = -(-0.9004) \cdot 100\ MHz = 90.04\ MHz \tag{6.9}$$

$$fr_{TE_{201}} = f_0 + \Delta f_{r_{TE_{201}}} = \frac{1}{2} \cdot \left(B_{TE_{201}} + \sqrt{(B_{TE_{201}}^2 + 4 \cdot f_0^2)} \right) = 3.8856\ GHz \tag{6.10}$$
$$fr_{TE_{201}} = f_0 + \Delta f_{r_{TE_{201}}} = \frac{1}{2} \cdot \left(B_{TE_{201}} + \sqrt{(B_{TE_{201}}^2 + 4 \cdot f_0^2)} \right) = 3.9453\ GHz \tag{6.11}$$

Finally by applying the equations (4.26) and (4.27) which impose that each resonant mode resonate at the right frequency given by the diagonal of the coupling matrix, the initial dimensions listed in Table 6.1 are obtained.

$$a^2 = \frac{1}{2\epsilon\mu}\frac{(m_2p_1)^2 - (m_1p_2)^2}{(p_1 f_{r_2})^2 - (p_2 f_{r_1})^2} \tag{6.12}$$

$$l^2 = \frac{1}{2\epsilon\mu}\frac{(m_2p_1)^2 - (m_1p_2)^2}{(m_2 f_{r_1})^2 - (m_1 f_{r_2})^2} \tag{6.13}$$

Where:

$$Mode\ 1 = TE_{m_1 0 p_1} = TE_{102} \tag{6.14}$$

$$Mode\ 2 = TE_{m_1 0 p_2} = TE_{201} \tag{6.15}$$

	First dual-mode cavity	Second dual-mode cavity
Width (mm)	17.8	17.4
Length (mm)	17.5	17.7

Table 6.1: Initial dimensions of the dual mode cavities.

6.3.3 First segment

In the first step, the input iris is adjusted in the forward segment and the output one in the backward segment. It can be noted that since $M_{S1} = M_{6L} = -1.0324$ in the matrix from Figure 6.5, then both input and output irises are identical. Figure 6.9 shows the structure optimized in the first step of both forward and backward designs and Table 6.2 lists the obtained widths for the first and last iris. It can be seen that the result is the same for both parameters. The obtained response in the first step is shown in Figures 6.10a and 6.10b.

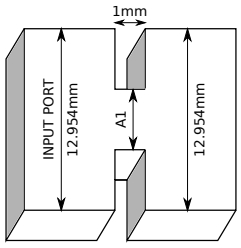

(a) Forward segment.

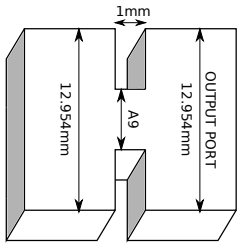

(b) Backward segment.

Figure 6.9: Structure in the first step of the sixth-order dual mode filter.

Parameter	Initial (mm)	Optimized (mm)
A_1	6	5.219

(a) Forward segment.

Parameter	Initial (mm)	Optimized (mm)
A_9	6	5.219

(b) Backward segment.

Table 6.2: Dimensions in step 1 of the sixth-order dual mode filter.

6.3.4 Second segment

Here, the single-mode cavity and the second iris length as well as output offset are adjusted in the second forward segment (Figure 6.11a). In the backward segment the parameters to optimize are the last offset, the thickness "L5" and the length "L6" (Figure 6.11b). Here, the width af all irises is fixed to 3.486 mm in order to keep the irises thickness between 1-2 millimeters. In this step, the first iris does not need to be modified. The obtained dimensions are listed in Table 6.3 and Figure 6.12 shows the partial responses obtained in the forward and backward step 2.

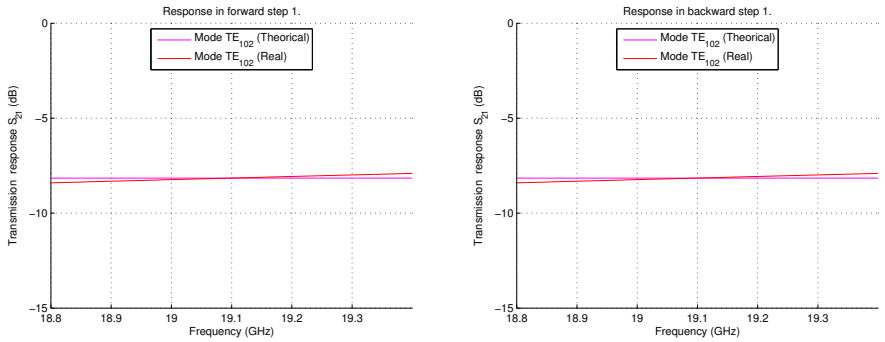

(a) Forward segment. (b) Backward segment.

Figure 6.10: Real and theoretical response in step 1 of the sixth-order dual mode filter.

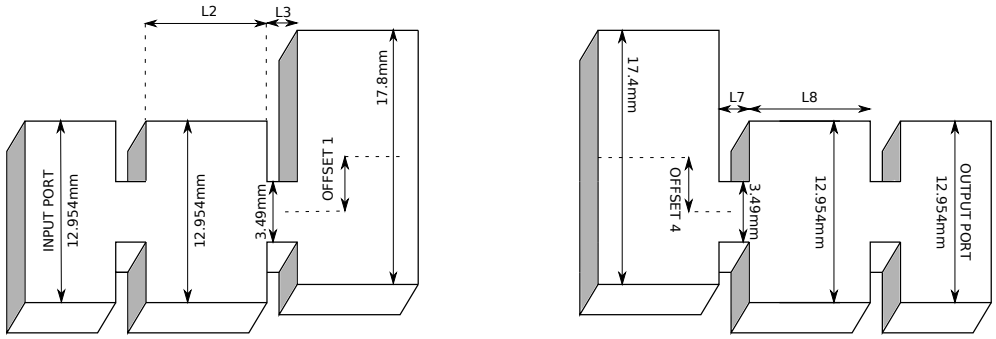

(a) Forward segment. (b) Backward segment.

Figure 6.11: Structure in the second step of the sixth-order dual mode filter.

Parameter	Initial (mm)	Optimized (mm)
L_2	9	8.6046
$L3$	1	1.2
$OFFSET1$	0	-2.7129

(a) Forward segment.

Parameter	Initial (mm)	Optimized (mm)
L_8	9	8.6057
L_7	1	1.1438
$OFFSET4$	0	3.5085

(b) Backward segment.

Table 6.3: Dimensions in step 2 of the sixth-order dual mode filter.

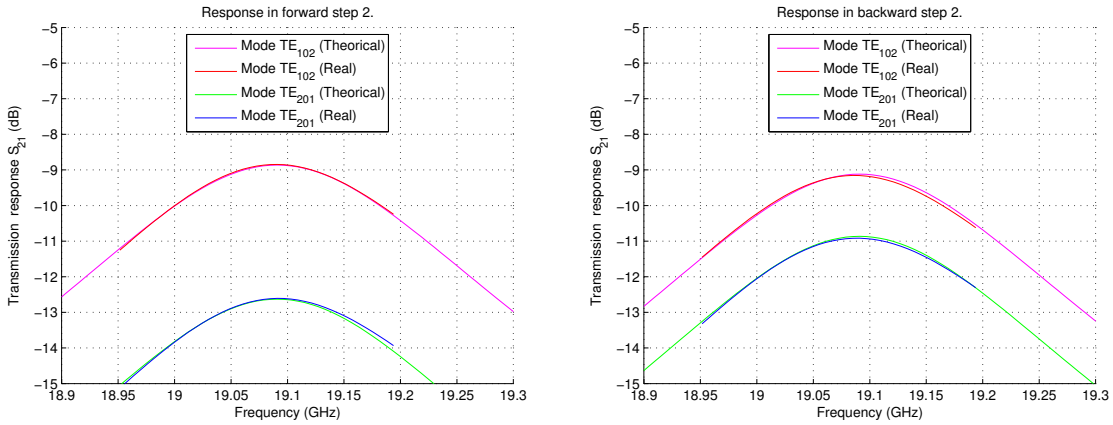

(a) Forward segment. (b) Backward segment.

Figure 6.12: Real and theoretical response in step 2 of the sixth-order dual mode filter.

6.3.5 Third segment

In the step 3, the central iris and the width and length of the first dual-mode cavity in the forward design or the second one in the backward design are optimized. Since the central iris is common to both forward and backward design, it only needs to be optimized either in the forward or in the backward segment. Once the thickness and offsets of the central iris are calculated in the forward or backward segment, the dimensions of the central iris in the other segment will be fixed to the obtained values. Then it will be necessary to optimize only two parameters namely the width and length of the remaining dual-mode cavity (Figure 6.13).

According to this, there are two possible approaches when performing the last step of the filter design, in this case the step 3:

1. The first option is to **perform first the forward step** as usual adjusting the parameters shown in Figure 6.13a and then to optimize the backward segment (figure 6.13b while keeping the dimensions obtained in the forward segment for the central iris. These dimensions are $OFFSET\ 2$, $L5$, $OFFSET\ 3$ and the width of the first dual-mode cavity $L4$. Thus by adjusting only the unknown parameters ($L6$ and $A6$) in the backward step, it is possible to reach a good final result.

   Table 6.4 lists the achieved dimensions when performing the forward step 3 before the backward one. Figure 6.14a shows the partial response after performing the forward design and Figure 6.14b the response obtained in the backward segment by adjusting only the dimensions of second dual-mode cavity (parameters $L6$ and $A6$).

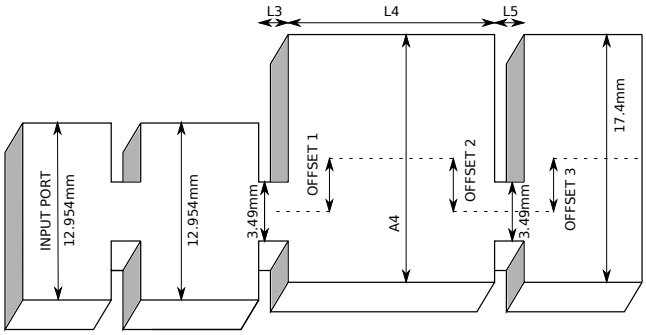

(a) Forward segment.

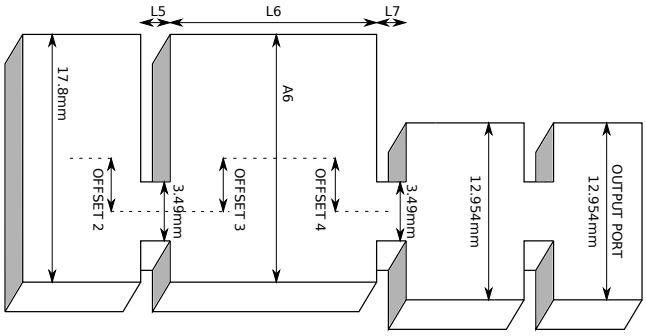

(b) Backward segment.

Figure 6.13: Structure in the third step of the sixth-order dual mode filter.

Parameter	Initial (mm)	Optimized (mm)
L_3	1.2	1.2154
$OFFSET1$	-2.7129	-2.6571
L_4	17.5	17.0464
A_4	17.8	17.7757
$OFFSET2$	2.7129	2.4510
$L5$	1.2	1.2296
$OFFSET3$	-2.7129	-3.0813

(a) Forward segment.

Parameter	Initial (mm)	Optimized (mm)
L_6	17.7	17.2901
A_6	17.4	17.3633

(b) Backward segment.

Table 6.4: Dimensions in step 3 performing firstly the forward design and then the backward design.

2. The other option is to perform **firstly the backward design** (figure 6.13b) and then the forward one (figure 6.13a) keeping the parameters obtained in the backward design and optimizing only the unknown parameters, namely $L4$ and $A4$ (the dimensions of the first dual-mode cavity). In this way the obtained dimensions of the central iris are slightly different to the ones achieved when performing the forward design in the first place. Thus the final response will be a little different.

   The result obtained by performing the backward step in the first place is shown in Table 6.5a and Figure 6.15a. Finally, the result obtained in the forward step by optimizing the dimensions of the first dual-mode cavity (parameters $L4$ and $A4$) is shown in Table 6.5b and Figure 6.15b).

Parameter	Initial (mm)	Optimized (mm)
L_7	1.1438	1.1532
$OFFSET4$	3.5085	3.6534
L_6	17.7	17.2916
A_6	17.4	17.3639
$OFFSET3$	-3.5085	-2.9682
$L5$	1.1438	1.2496
$OFFSET2$	3.5085	2.2353

(a) Backward segment.

Parameter	Initial (mm)	Optimized (mm)
L_4	17.5	17.0392
A_4	17.8	17.7869

(b) Forward segment.

Table 6.5: Parameters in step 3 performing the backward design before the forward one.

Both of the presented design options, starting the final step either by the forward design or by the backward one are valid in order to achieve the final filter structure. Nevertheless, as forward and backward designs provide two solutions slightly different for the central iris, both solutions have been used in the other segment in order to compare both results. Table 6.6 compares the value of the parameters obtained in both forward and backward design. It should be noted that both design options achieve two different solutions for the central iris (parameters $OFFSET$ 2, $L5$ and $OFFSET$ 3) and one of them is clearly better in order to obtain the proper final response without the need of a global optimization as it can be seen in Figure 6.16. This Figure shows the final response reached when the step 3 is performed starting by the forward design (Figure 6.16a) or by the backward one (Figure 6.16b).

Parameter	Value from forward design	Value from backward design
$OFFSET2$	2.4510	2.2353
$L5$	1.2296	1.2496
$OFFSET3$	-3.0813	-2.9682

Table 6.6: Comparison of the central iris dimensions obtained in both forward and backward design.

As the result shown in Figure 6.16a is clearly better than the one in Figure 6.16b, this filter should be designed starting by the forward half. It can be demonstrated that in all filters of this kind, two different responses can be obtained starting the final step either by the forward segment or by the backward one. In addition, one of them is much better than the other.

However, it is possible to identify the right response by looking at the result of the last design step. In can be seen that the response of the backward step 3 (Figure 6.14b) when performing first the forward design have a little error in the level of the transmission parameters. Similarly, with regard to the response in Figure 6.15b obtained by performing first the backward design, the error is not in the level but in the shape. Then, considering this fact, the final filter response will be right only if the last filter segment is designed by the option that provides an error in the level of the partial response. If the final partial response exhibits an error in the shape of the scattering parameters, then it means that the final step should be repeated starting by the opposite end of the filter.

6.3.6 Results

The dimensions listed in Table 6.7 and Figure 6.18 are obtained by taking the structure which provides the response shown in Figure 6.16a and performing a global optimization of the filter. The final response provided by this filter after optimization is shown in Figure 6.17. The final response of this filter is almost perfect as the response without a final optimization shown in Figure 6.16a is quite close to the desired target.

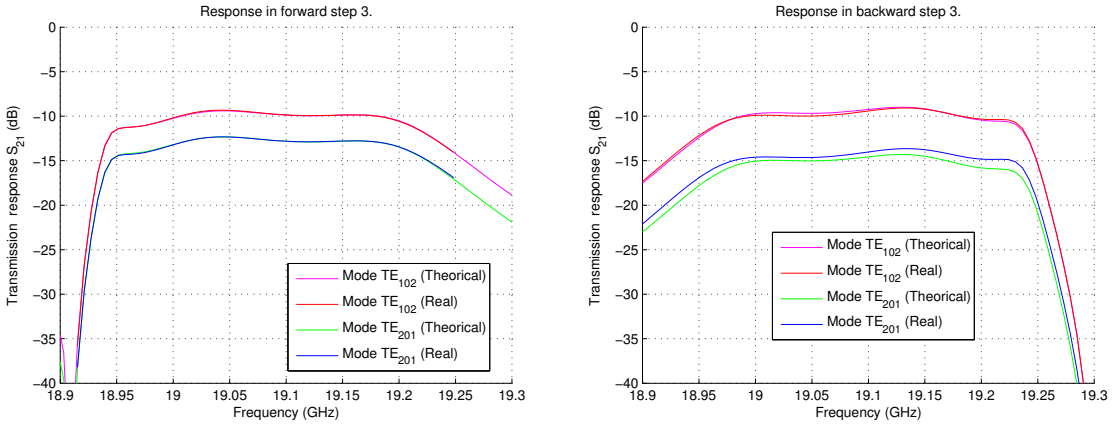

(a) Forward segment. (b) Backward segment.

Figure 6.14: Real and theoretical response in step 3 performing firstly the forward design and then the backward design.

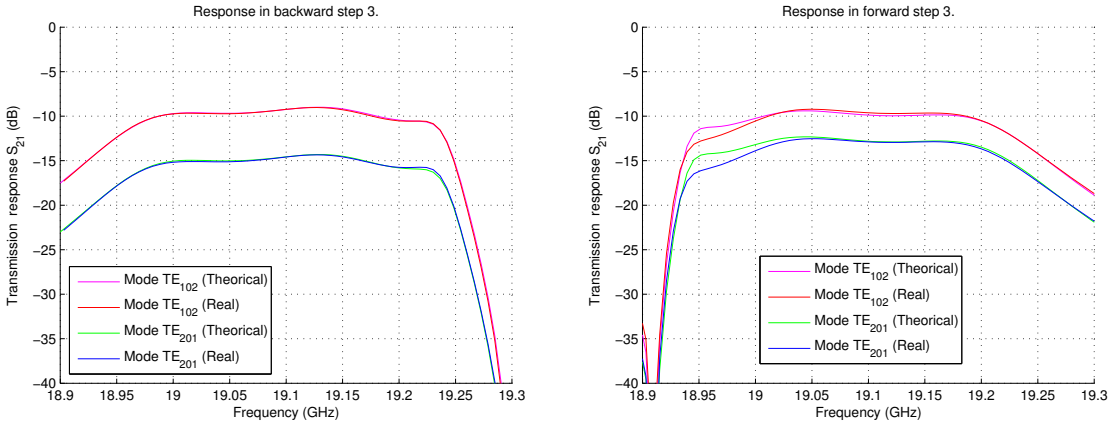

(a) Backward segment. (b) Forward segment.

Figure 6.15: Real and theoretical response in step 3 performing the backward design before the forward one.

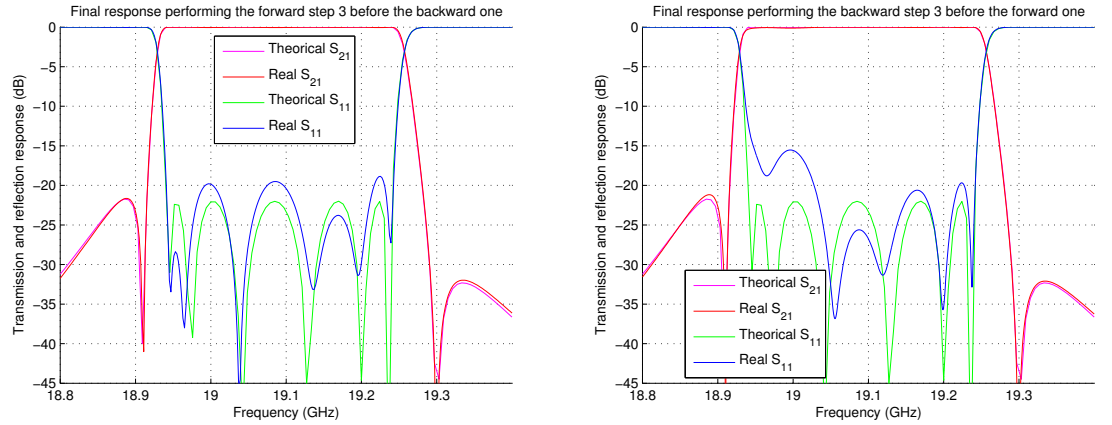

(a) Performing firstly the forward step. (b) Performing firstly the backward step.

Figure 6.16: Final filter response with each one of the results listed in Table 6.6.

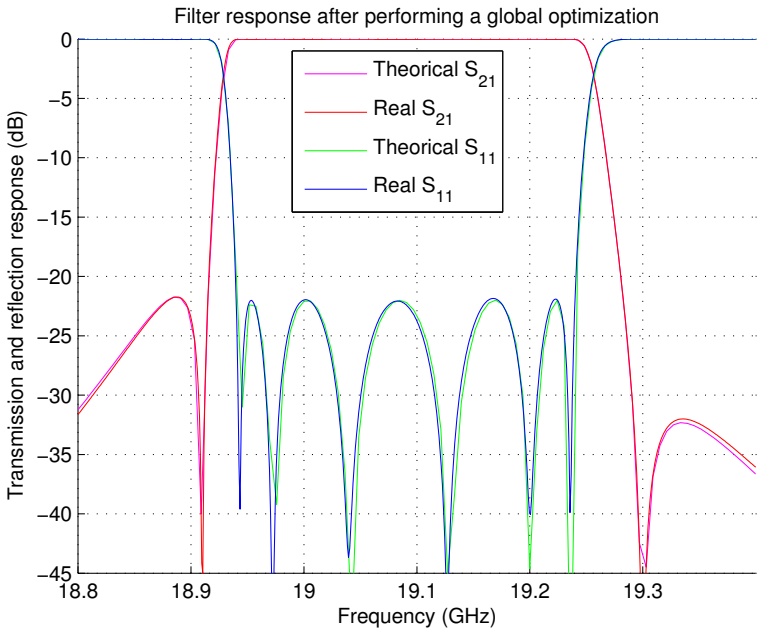

Figure 6.17: Final filter response after performing a global optimization.

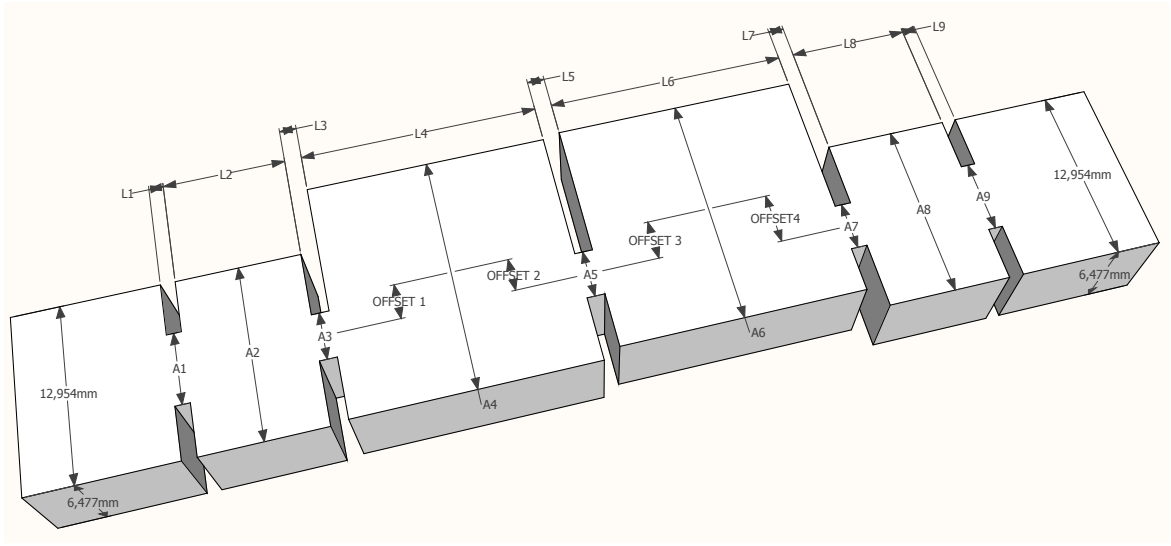

Figure 6.18: Final filter structure.

Parameter	Value (mm)	Parameter	Value (mm)	Parameter	Value (mm)
A1	5.249	L1	1	OFFSET 1	-2.6107
A2	12.954	L2	8.591	OFFSET 2	2.4166
A3	3.486	L3	1.1968	OFFSET 3	-2.9206
A4	17.7796	L4	17.0421	OFFSET 4	3.7072
A5	3.486	L5	1.2437		
A6	17.3622	L6	17.2910		
A7	3.486	L7	1.1230		
A8	12.954	L8	8.589		
A9	5.249	L9	1		

Table 6.7: Parameters value of the filter structure in Figure 6.18.

6.4 Designed filters

In order to validate the proposed approach and to show the advantages of placing single-mode cavities at the filter input and output, several dual-mode filters have been designed though repeating the procedure presented. These filters have different characteristics in terms of order and transmission zeros in order to fit the frequency specifications of a real satellite application.

The given frequency specification for this specific satellite application, are as follows:

- Input/output waveguide WR51 (12.954mm x 6.477mm)
- Bandwidth: from 19.00 GHz to 19.152 GHz
- Insertion losses: less than 0.8 dB at centre band
- Reflection in the passband: less than 22 dB
- Rejection: Table 6.8 lists the rejection required in each frequency range.

Frequency range (GHz)		Rejection (dB)
From:	To:	
0	18.5	-50
18.5	18.9	-20
19.3	19.6	-25
19.6	45.0	-50 (with a lowpass filter)

Table 6.8: Rejection required in each frequency range.

Figure 6.19 shows the mask obtained from the previous specifications and from the rejection values listed in Table 6.8.

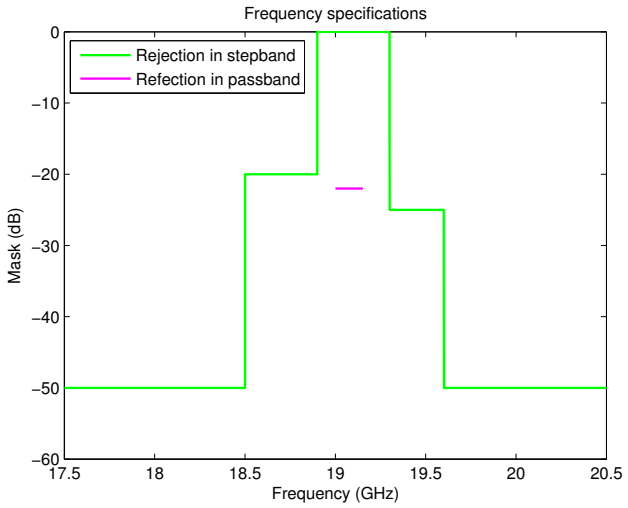

Figure 6.19: Reflection and rejection levels required.

All the following filters will fit these specifications, included the one designed in the previous section. The designed filters goes from one of fifth-order and one transmission zero (5-1-0)[1] to a tenth-order filter with four transmission zeros (10-4-0).

It should be noticed that sixth-order is the minimum option in order to have two transmission zeros and to include a single-mode cavity in both the filter input and output. Nevertheless two fifth-order filters have been designed, one with a single transmission zero (5-1-0) and another one with two transmission zeros and thick irises (5-2-0).

It is also important to note that the filters with higher order have better specifications of bandwidth and reflection level in order to achieve a better fulfillment of the specification for the satellite application. However, they are more complex and exhibit higher sensitivity. The frequency specifications of all designed filters are shown in Table 6.9.

[1]The nomenclature (A-B-C) is related to the filter order and the number of transmission zeros. “A” refers to the number of poles of the given filter, “B” refers to the number of transmission zeros in the real axis and “C” indicates the number of complex transmission zeros (located in the complex plane)

Order	Reflection	Transmission zeros	Central frequency	Bandwidth
5	-25 dB	18.89 GHz	19.075 GHz	180 MHz

(a) Filter 1 (5-1-0).

Order	Reflection	Transmission zeros	Central frequency	Bandwidth
5	-22 dB	18.9 and 19.36 GHz	19.076 GHz	240 MHz

(b) Filter 2 (5-2-0).

Order	Reflection	Transmission zeros	Central frequency	Bandwidth
6	-22 dB	18.91 and 19.30 GHz	19.09 GHz	300 MHz

(c) Filter 3 (6-2-0).

Order	Reflection	Transmission zeros	Central frequency	Bandwidth
8	-24 dB	18.93 and 19.278 GHz	19.1 GHz	300 MHz

(d) Filter 4 (8-2-0).

Order	Reflection	Transmission zeros	Central frequency	Bandwidth
8	-24 dB	18.92, 18.93 and 19.275 GHz	19.086 GHz	300 MHz

(e) Filter 5 (8-3-0).

Order	Reflection	Transmission zeros	Central frequency	Bandwidth
10	-22 dB	18.907 and 19.293 GHz	19.097 GHz	360 MHz

(f) Filter 6 (10-2-0).

Order	Reflection	Transmission zeros	Central frequency	Bandwidth
10	-22 dB	18.906, 18.914, 19.286 and 19.296 GHz	19.098 GHz	360 MHz

(g) Filter 7 (10-4-0).

Table 6.9: Specifications of all filters designed in this section.

6.4.1 Filter 1 (5-1-0)

The first option is a fifth-order filter centered at 19.075 GHz with a bandwidth of 180 MHz. The filter has a reflection level of -25 dB in the passband and a transmission zero placed at 18.89 GHz.

The coupling matrix that provides this response is shown in Figure 6.20. Figure 6.21 shows the full-wave response provided by this filter. Finally the waveguide structure of this filter is shown in Figure 6.34a. This

$$M = \begin{bmatrix} 0 & -1.1192 & 0 & 0 & 0 & 0 & 0 \\ -1.1192 & -0.0276 & 0.9711 & 0 & 0 & 0 & 0 \\ 0 & 0.9711 & -0.0390 & 0.5679 & -0.3771 & 0 & 0 \\ 0 & 0 & 0.5679 & -0.4973 & 0 & -0.7885 & 0 \\ 0 & 0 & -0.3771 & 0 & 0.8482 & -0.5668 & 0 \\ 0 & 0 & 0 & -0.7885 & -0.5668 & -0.0276 & 1.1192 \\ 0 & 0 & 0 & 0 & 0 & 1.1192 & 0 \end{bmatrix}$$

Figure 6.20: Coupling matrix of filter 1 (5-1-0).

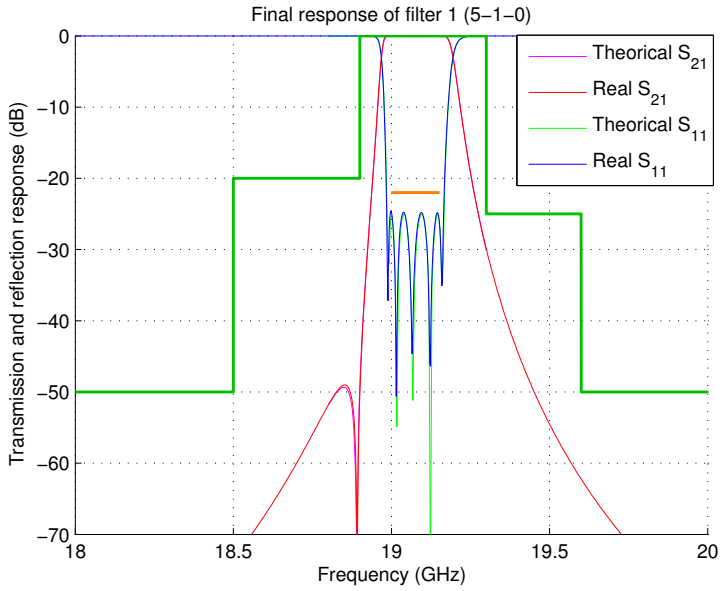

Figure 6.21: Response of filter 1 (5-1-0).

filter has enough margin in the passband and in the mask edges to take into account a possible frequency shifting due to the manufacturing errors. However the bandwidth is not wide enough to assure a flat passband in the response from Figure 6.21 since the passband edges will be rounded in the real prototype when losses are considered.

There is also some margin in the reflection level in the passband. This is to avoid adding tuning screws in the manufactured prototype since although the real filter will not be equirriple due to manufacturing tolerances, it could still fulfill the specifications.

6.4.2 Filter 2 (5-2-0)

The second option is a fifth-order filter centered at 19.076 GHz like the previous filter. However now a second transmission zero will be implemented while relaxing the reflection level at -22 dB. In this way it is possible to increase the bandwidth from 180 MHz to 240 MHz in order to have a flatter bandpass in the manufactured filter in spite of higher losses. In this filter the transmission zeros are located at 18.9 GHz and 19.36 GHz.

The coupling matrix of this filter is shown in Figure 6.22. Figure 6.23 shows the full-wave response provided by this filter and the waveguide structure of this filter is shown in Figure 6.34b as well as the dimensions in Table 6.10b. In this solution there is not any margin in the reflection level, thus if the filter is

$$M = \begin{bmatrix} 0 & -1.0484 & 0 & 0 & 0 & 0 & 0 \\ -1.0484 & -0.0143 & 0.7246 & -0.5166 & 0 & 0 & 0 \\ 0 & 0.7246 & 0.4099 & 0 & 0.1418 & 0.5458 & 0 \\ 0 & -0.5166 & 0 & -0.8589 & 0.1046 & 0.4027 & 0 \\ 0 & 0 & 0.1418 & 0.1046 & 1.1340 & 0 & 0.5765 \\ 0 & 0 & 0.5458 & 0.4027 & 0 & -0.5119 & -0.8757 \\ 0 & 0 & 0 & 0 & 0.5765 & -0.8757 & 0 \end{bmatrix}$$

Figure 6.22: Coupling matrix of filter 2 (5-2-0).

prototyped, then it will be imperative to add tuning screws to the resonant cavities in order to compensate for the manufacturing errors.

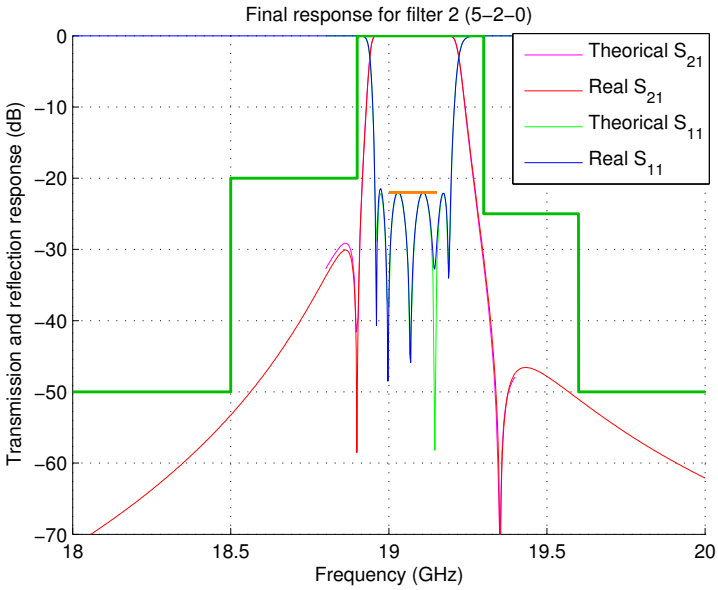

Figure 6.23: Response of filter 2 (5-2-0).

With regard to the possible frequency shifting in the manufactured breadboard, there is still some margin in the edges of the mask, however it has been decreased in order to have a larger bandpass.

6.4.3 Filter 3 (6-2-0)

This is a sixth-order filter centered at 19.09 GHz with a reflection level in the passband of -22 dB and two transmission zeros at 18.91 GHz and 19.30 GHz. The bandwidth has also been increased from the previous example to 300 MHz.

The coupling matrix of this filter is shown in Figure 6.24. Figure 6.25 shows the full-wave response provided by this filter. The waveguide structure of this filter is shown in Figure 6.34c and its dimensions are listed in Table 6.10c. In this filter there is a larger margin in the bandwidth at a expense of a margin slightly

$$M = \begin{bmatrix} 0 & -1.0324 & 0 & 0 & 0 & 0 & 0 & 0 \\ -1.0324 & -0.0059 & 0.7788 & 0.3655 & 0 & 0 & 0 & 0 \\ 0 & 0.7788 & -0.2165 & 0 & -0.2509 & -0.4926 & 0 & 0 \\ 0 & 0.3655 & 0 & 0.9484 & 0.0967 & 0.1899 & 0 & 0 \\ 0 & 0 & -0.2509 & 0.0967 & -0.9004 & 0 & 0.4286 & 0 \\ 0 & 0 & -0.4926 & 0.1899 & 0 & 0.2889 & -0.7460 & 0 \\ 0 & 0 & 0 & 0 & 0.4286 & -0.7460 & -0.0059 & 1.0324 \\ 0 & 0 & 0 & 0 & 0 & 0 & 1.0324 & 0 \end{bmatrix}$$

Figure 6.24: Coupling matrix of filter 3 (6-2-0).

greater than 10 MHz in each edge of passband. In addition there is no margin in the reflection level. Thus, tuning screws will be necessary.

6.4.4 Filter 4 (8-2-0)

The fourth filter is an eighth-order filter centered at 19.1 GHz with a reflection level in the passband of -24 dB, two transmission zeros at 18.93 GHz and 19.278 GHz and a bandwidth of 300 MHz.

The coupling matrix of this filter is shown in Figure 6.26. Figure 6.27 shows the full-wave response provided by this filter and the waveguide structure of this filter is shown in Figure 6.34d as well as the dimensions in Table 6.11d.

By increasing the filter order, the rejection level in the stop band increases as well. Thus it is possible to place the transmission zeros closer to the passband and to enlarge the filter selectivity in order to have a larger margin in both edges of the mask and even some margin in the reflection level.

6.4.5 Filter 5 (8-3-0)

The main difference between this filter and the previous one is the presence of a third transmission zero. This filter keeps the bandwidth of 300 MHz and the reflection level of -24 dB. However it is centered at 19.086 GHz with tree transmission zeros at 18.92, 18.93 and 19.275 GHz.

The coupling matrix of this filter is shown in Figure 6.28. Figure 6.29 shows the full-wave response provides by this filter and the waveguide structure of this filter is shown in Figure 6.34e and Table 6.11e.

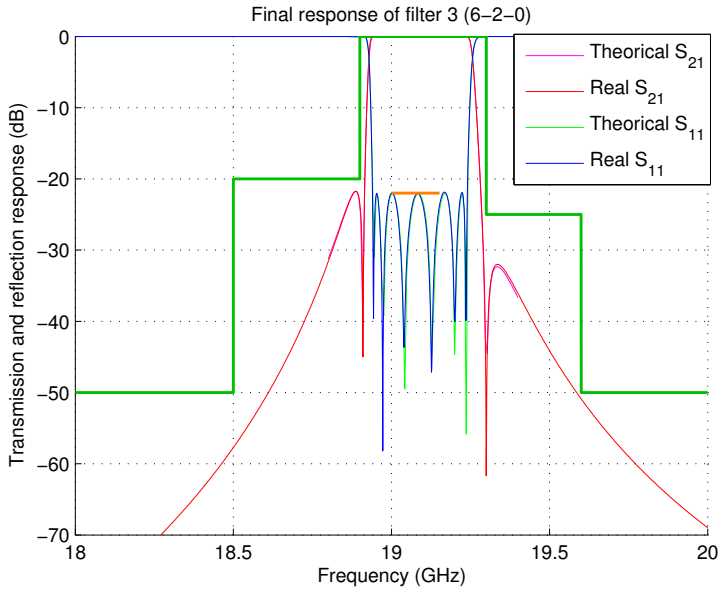

Figure 6.25: Response of filter 3 (6-2-0).

$$M = \begin{bmatrix}
0 & 1.0603 & 0 & 0 & 0 & 0 & 0 & 0 & 0 & 0 \\
1.0603 & -0.0014 & 0.8776 & 0 & 0 & 0 & 0 & 0 & 0 & 0 \\
0 & 0.8776 & -0.0014 & 0.5549 & -0.2370 & 0 & 0 & 0 & 0 & 0 \\
0 & 0 & 0.5549 & -0.1693 & 0 & -0.2062 & -0.4686 & 0 & 0 & 0 \\
0 & 0 & -0.2370 & 0 & 0.9180 & -0.0814 & -0.1849 & 0 & 0 & 0 \\
0 & 0 & 0 & -0.2062 & -0.0814 & -0.8969 & 0 & -0.2564 & 0 & 0 \\
0 & 0 & 0 & -0.4686 & -0.1849 & 0 & 0.1957 & 0.5462 & 0 & 0 \\
0 & 0 & 0 & 0 & 0 & -0.2564 & 0.5462 & -0.0014 & -0.8776 & 0 \\
0 & 0 & 0 & 0 & 0 & 0 & 0 & -0.8776 & -0.0014 & 1.0603 \\
0 & 0 & 0 & 0 & 0 & 0 & 0 & 0 & 1.0603 & 0
\end{bmatrix}$$

Figure 6.26: Coupling matrix of filter 4 (8-2-0).

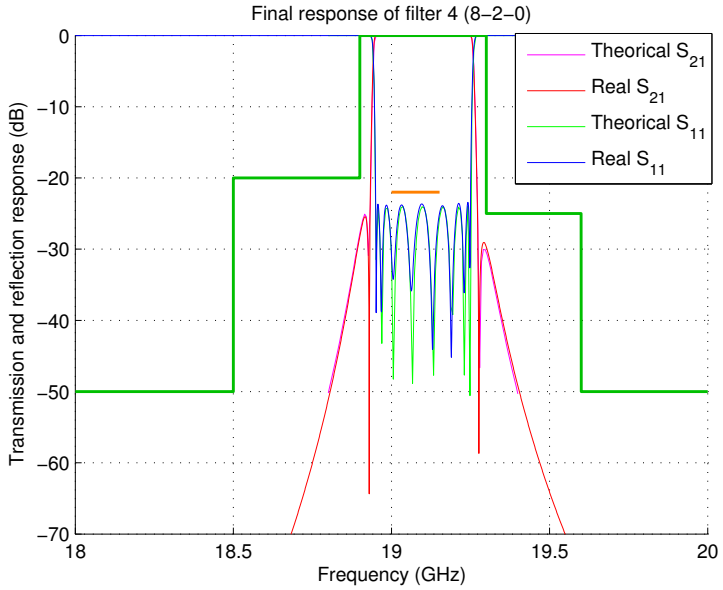

Figure 6.27: Response of filter 4 (8-2-0).

$$M = \begin{bmatrix}
0 & 1.0591 & 0 & 0 & 0 & 0 & 0 & 0 & 0 & 0 \\
1.0591 & -0.0124 & 0.8007 & 0.3545 & 0 & 0 & 0 & 0 & 0 & 0 \\
0 & 0.8007 & -0.2003 & 0 & -0.2411 & -0.4816 & 0 & 0 & 0 & 0 \\
0 & 0.3545 & 0 & 0.9421 & 0.0703 & 0.1405 & 0 & 0 & 0 & 0 \\
0 & 0 & -0.2411 & 0.0703 & -0.8975 & 0 & 0.0357 & -0.2540 & 0 & 0 \\
0 & 0 & -0.4816 & 0.1405 & 0 & 0.1637 & -0.0710 & 0.5060 & 0 & 0 \\
0 & 0 & 0 & 0 & 0.0357 & -0.0710 & 0.9953 & 0 & 0.2545 & 0 \\
0 & 0 & 0 & 0 & -0.2540 & 0.5060 & 0 & -0.1061 & 0.8379 & 0 \\
0 & 0 & 0 & 0 & 0 & 0 & 0.2545 & 0.8379 & -0.0124 & 1.0591 \\
0 & 0 & 0 & 0 & 0 & 0 & 0 & 0 & 1.0591 & 0
\end{bmatrix}$$

Figure 6.28: Coupling matrix of filter 5 (8-3-0).

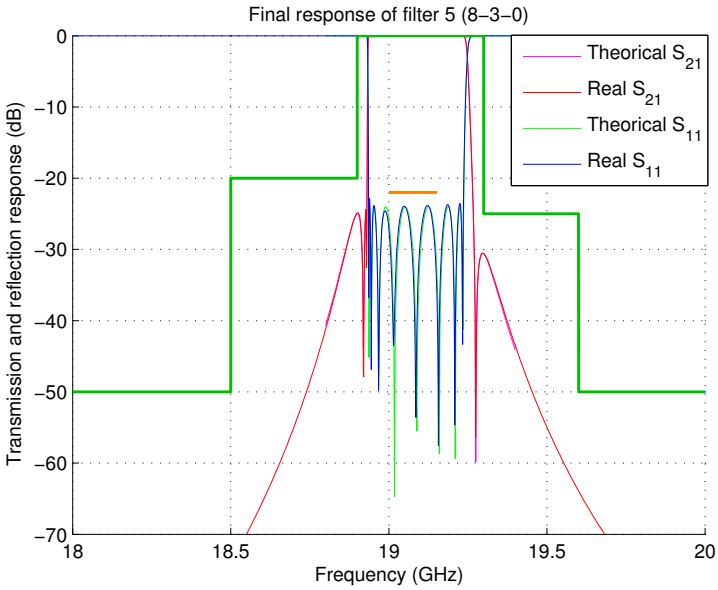

Figure 6.29: Response of filter 5 (8-3-0).

By placing two transmission zeros below the bandpass a extremely high selectivity is achieved in this side. Then the margin with regard to the mask is increased. Moreover the central frequency has been decreased in order to have approximately the same margin in each side of the filter.

6.4.6 Filter 6 (10-2-0)

This is a tenth-order filter centered at 19.097 GHz with a bandwidth of 360 MHz and a reflection level of -22 dB. This filter provides two transmission zeros at 18.907 GHz and 19.293 GHz.

The coupling matrix of this filter is shown in Figure 6.30. Figure 6.31 shows the full-wave response provided by this filter and the waveguide structure of this filter is shown in Figure 6.35f and Table 6.11f.

$$M = \begin{bmatrix}
0 & 1.0184 & 0 & 0 & 0 & 0 & 0 & 0 & 0 & 0 & 0 & 0 \\
1.018 & -0.0008 & 0.8361 & 0 & 0 & 0 & 0 & 0 & 0 & 0 & 0 & 0 \\
0 & 0.8361 & -0.0008 & -0.5868 & 0 & 0 & 0 & 0 & 0 & 0 & 0 & 0 \\
0 & 0 & -0.5868 & -0.0008 & -0.5129 & 0.1756 & 0 & 0 & 0 & 0 & 0 & 0 \\
0 & 0 & 0 & -0.5129 & -0.1099 & 0 & -0.1742 & -0.4685 & 0 & 0 & 0 & 0 \\
0 & 0 & 0 & 0.1756 & 0 & 0.9296 & -0.0570 & -0.1534 & 0 & 0 & 0 & 0 \\
0 & 0 & 0 & 0 & -0.1742 & -0.0570 & -0.9090 & 0 & 0.1950 & 0 & 0 & 0 \\
0 & 0 & 0 & 0 & -0.4685 & -0.1534 & 0 & 0.1341 & -0.5059 & 0 & 0 & 0 \\
0 & 0 & 0 & 0 & 0 & 0 & 0.1950 & -0.5059 & -0.0008 & -0.5868 & 0 & 0 \\
0 & 0 & 0 & 0 & 0 & 0 & 0 & 0 & -0.5868 & -0.0008 & 0.8361 & 0 \\
0 & 0 & 0 & 0 & 0 & 0 & 0 & 0 & 0 & 0.8361 & -0.0008 & 1.0184 \\
0 & 0 & 0 & 0 & 0 & 0 & 0 & 0 & 0 & 0 & 1.0184 & 0
\end{bmatrix}$$

Figure 6.30: Coupling matrix of filter 6 (10-2-0).

Although here there is no margin in the reflection level, the advantage of this response is the large bandwidth of 360 MHz almost as large as the maximum space is the mask (400 MHz). Moreover there is still remaining a margin of 10 MHz in each edge of the mask as a result of the high selectivity.

In this response it is also important to take into account the high filter order that allows placing the transmission zeros quite close to the passband since the rejection level in the stopband increases.

6.4.7 Filter 7 (10-4-0)

Finally, a tenth-order filter with four dual-mode cavities and input/output single-mode cavities is designed. The central frequency is 19.098 GHz, the bandwidth is 360 MHz and the reflection level is -22 dB.

The coupling matrix of this filter is shown in Figure 6.32. Figure 6.33 shows the full-wave response provided by this filter. Moreover the waveguide structure of this filter is shown in Figure 6.35g and finally the dimensions of the filter structure are listed in Table 6.11g. The interest of this filter is the presence of four transmission zeros. By placing two of them in each side of the passband, the rejection level in the stopband increases. Thus it is possible to place the zeros even closer to the passband to achieve a extremely high selectivity.

With this response, the margin in each edge of the mask has been increased to 15 MHz while keeping the bandwidth of 360 MHz and the reflection level of -22 dB. Taking into account that the maximum space in the mask is 400 MHz and there is a margin of 15 MHz in each side, the transition band is just of 5 MHz in each edge of the passband.

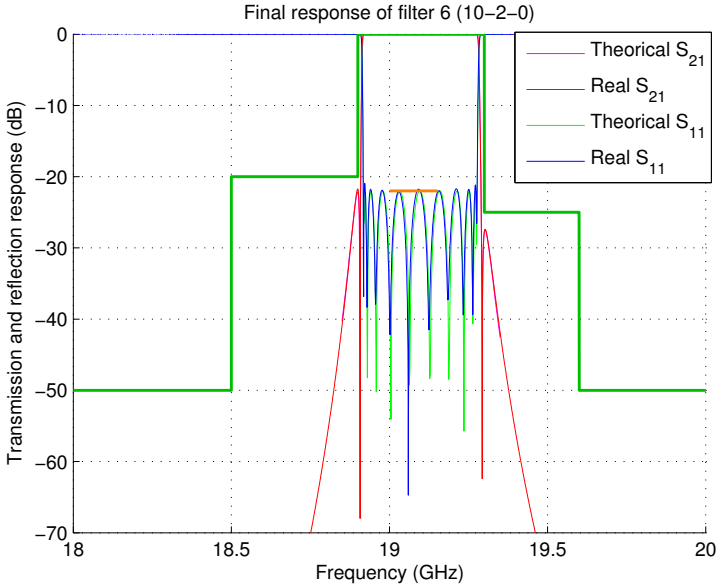

Figure 6.31: Response of filter 6 (10-2-0).

$$M = \begin{bmatrix}
0 & -1.0157 & 0 & 0 & 0 & 0 & 0 & 0 & 0 & 0 & 0 & 0 \\
-1.0157 & -0.0006 & 0.7736 & -0.3052 & 0 & 0 & 0 & 0 & 0 & 0 & 0 & 0 \\
0 & 0.7736 & -0.1489 & 0 & 0.1612 & 0.5069 & 0 & 0 & 0 & 0 & 0 & 0 \\
0 & -0.3052 & 0 & 0.9524 & 0.0400 & 0.1259 & 0 & 0 & 0 & 0 & 0 & 0 \\
0 & 0 & 0.1612 & 0.0400 & -0.9518 & 0 & 0.0255 & -0.1226 & 0 & 0 & 0 & 0 \\
0 & 0 & 0.5069 & 0.1259 & 0 & 0.0571 & -0.1014 & 0.4880 & 0 & 0 & 0 & 0 \\
0 & 0 & 0 & 0 & 0.0255 & -0.1014 & 0.9663 & 0 & -0.0401 & -0.1395 & 0 & 0 \\
0 & 0 & 0 & 0 & -0.1226 & 0.4880 & 0 & -0.0357 & -0.1454 & -0.5057 & 0 & 0 \\
0 & 0 & 0 & 0 & 0 & 0 & -0.0401 & -0.1454 & -0.9381 & 0 & 0.3281 & 0 \\
0 & 0 & 0 & 0 & 0 & 0 & -0.1395 & -0.5057 & 0 & 0.1722 & -0.7642 & 0 \\
0 & 0 & 0 & 0 & 0 & 0 & 0 & 0 & 0.3281 & -0.7642 & -0.0006 & 1.0157 \\
0 & 0 & 0 & 0 & 0 & 0 & 0 & 0 & 0 & 0 & 1.0157 & 0
\end{bmatrix}$$

Figure 6.32: Coupling matrix of filter 7 (10-4-0).

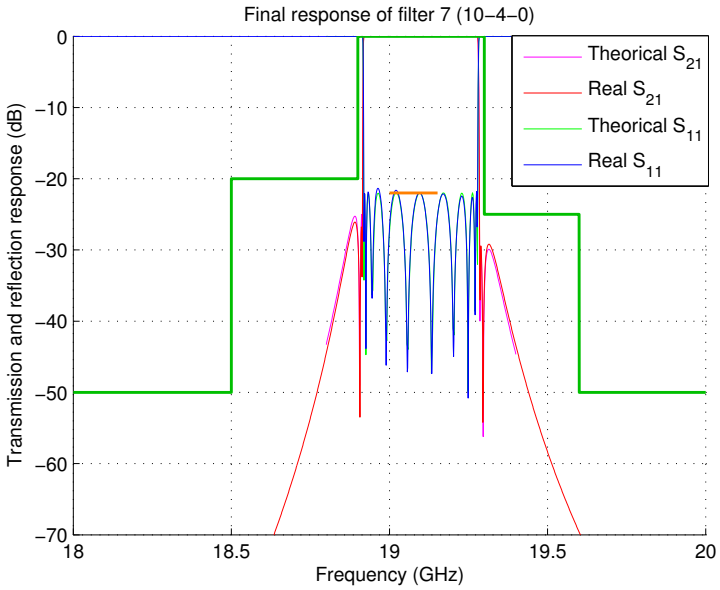

Figure 6.33: Response of filter 7 (10-4-0).

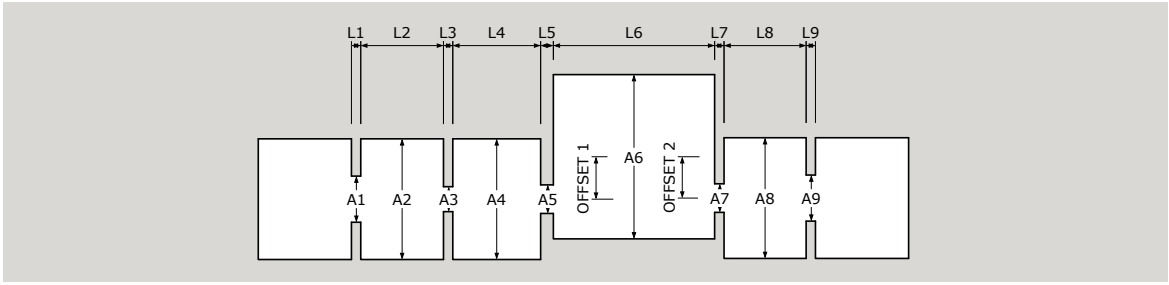

(a) Filter 1 (5-1-0).

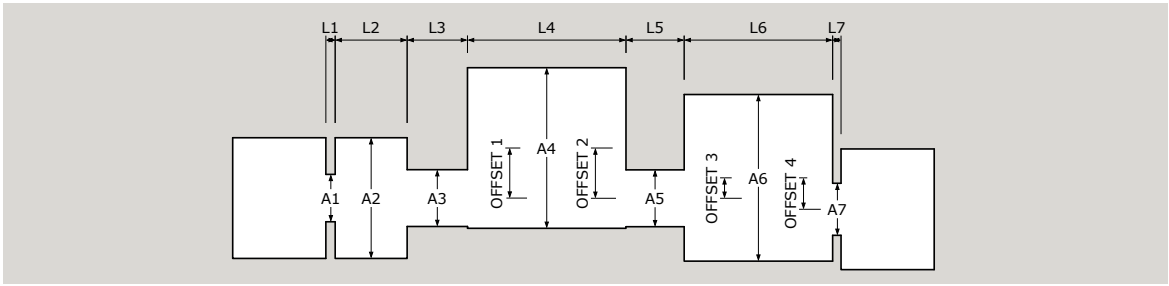

(b) Filter 2 (5-2-0).

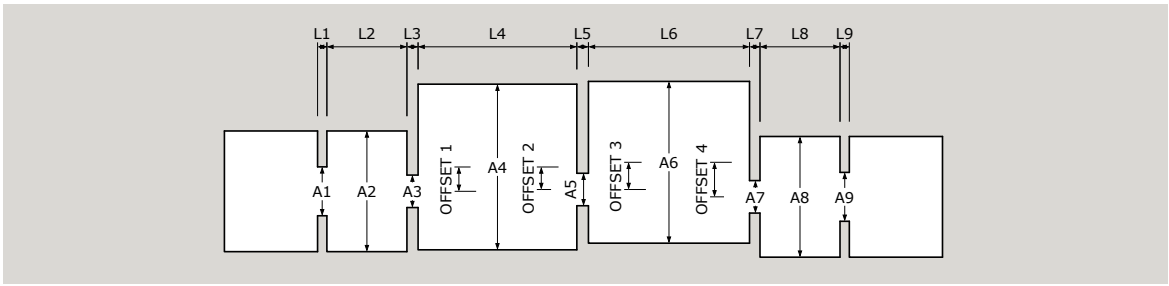

(c) Filter 3 (6-2-0).

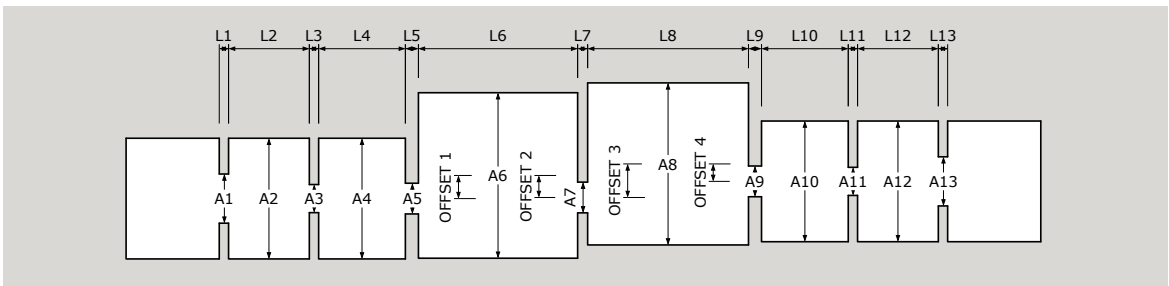

(d) Filter 4 (8-2-0).

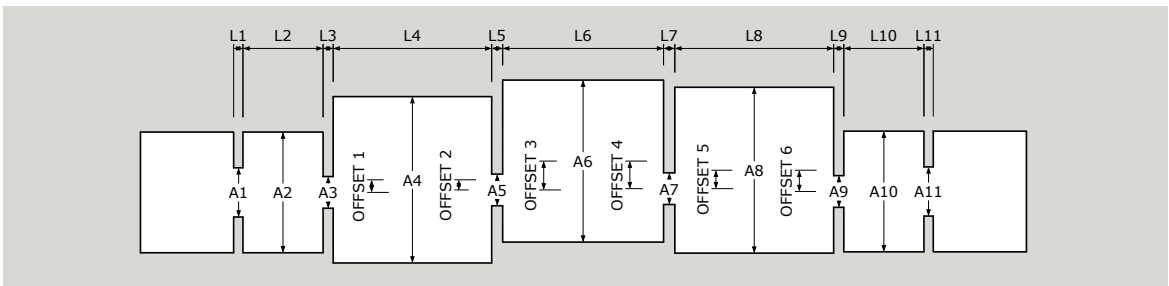

(e) Filter 5 (8-3-0).

Figure 6.34: Structure and parameters of each filter.

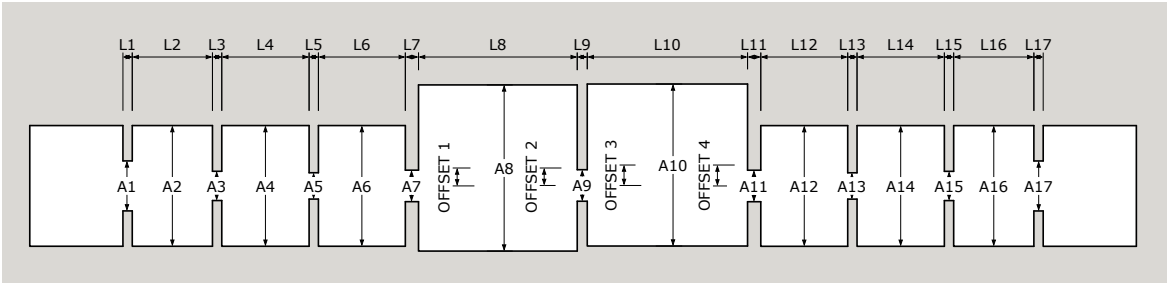

(f) Filter 6 (10-2-0).

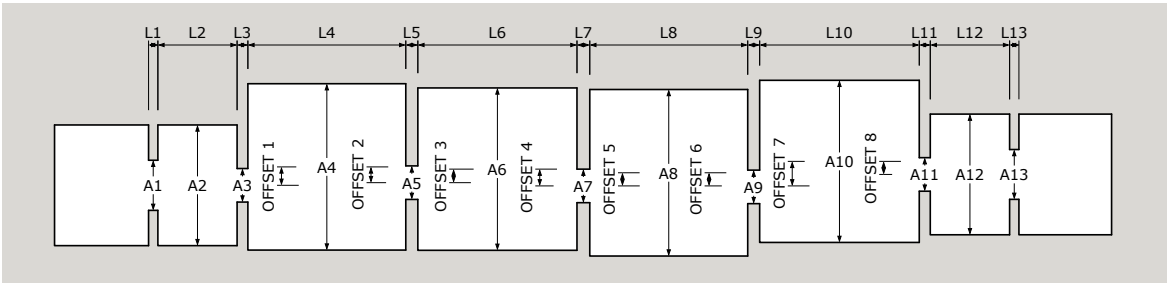

(g) Filter 7 (10-4-0).

Figure 6.34: Structure and parameters of each filter (continuation).

Parameter	Value (mm)	Parameter	Value (mm)	Parameter	Value (mm)
A1	4.9538	L1	1	OFFSET 1	-4.5544
A2	12.954	L2	8.8790	OFFSET 2	4.3774
A3	2.6785	L3	1		
A4	12.954	L4	9.4299		
A5	3.067	L5	1.3646		
A6	17.6306	L6	17.3108		
A7	3.067	L7	1.0097		
A8	12.954	L8	8.8123		
A9	4.9453	L9	1		

(a) Filter 1 (5-1-0).

Parameter	Value (mm)	Parameter	Value (mm)	Parameter	Value (mm)
A1	5.0877	L1	1	OFFSET 1	-5.3742
A2	12.954	L2	7.7241	OFFSET 2	5.3961
A3	6.0956	L3	6.4779	OFFSET 3	-2.1956
A4	17.2360	L4	17.0134	OFFSET 4	3.3771
A5	6.1014	L5	6.2447		
A6	17.8839	L6	15.9380		
A7	5.5865	L7	0.9		

(b) Filter 2 (5-2-0).

Parameter	Value (mm)	Parameter	Value (mm)	Parameter	Value (mm)
A1	5.2381	L1	1	OFFSET 1	-2.6257
A2	12.954	L2	8.5970	OFFSET 2	2.4369
A3	3.486	L3	1.2042	OFFSET 3	-2.9264
A4	17.7781	L4	17.0447	OFFSET 4	3.7026
A5	3.486	L5	1.2474		
A6	17.3634	L6	17.2921		
A7	3.486	L7	1.1335		
A8	12.954	L8	8.5971		
A9	5.2381	L9	1		

(c) Filter 3 (6-2-0).

Table 6.10: Physical dimensions of all filters designed in this section.

Parameter	Value (mm)	Parameter	Value (mm)	Parameter	Value (mm)
A1	5.2764	L1	1	OFFSET 1	-2.4817
A2	12.954	L2	8.6686	OFFSET 2	2.3635
A3	3.0167	L3	1	OFFSET 3	-3.6029
A4	12.954	L4	9.3088	OFFSET 4	1.8728
A5	3.3	L5	1.4022		
A6	17.7629	L6	17.0884		
A7	3.3	L7	1.0744		
A8	17.3943	L8	17.2648		
A9	3.3	L9	1.3993		
A10	12.954	L10	9.3088		
A11	3.0167	L12	1		
A12	12.954	L12	8.6686		
A13	5.2764	L13	1		

(d) Filter 4 (8-2-0).

Parameter	Value (mm)	Parameter	Value (mm)	Parameter	Value (mm)
A1	5.2827	L1	1	OFFSET 1	-1.3525
A2	12.954	L2	8.5993	OFFSET 2	1.0881
A3	3.4	L3	1.0862	OFFSET 3	-3.0973
A4	17.8571	L4	17.0130	OFFSET 4	2.9598
A5	3.4	L5	1.1806	OFFSET 5	-1.9798
A6	17.3883	L6	17.2676	OFFSET 6	2.2834
A7	3.4	L7	1.2116		
A8	17.8020	L8	17.0469		
A9	3.4	L9	1.0904		
A10	12.954	L10	8.6018		
A11	5.2758	L11	1		

(e) Filter 5 (8-3-0).

Parameter	Value (mm)	Parameter	Value (mm)	Parameter	Value (mm)
A1	5.3655	L1	1	OFFSET 1	-1.9226
A2	12.954	L2	8.6090	OFFSET 2	1.8756
A3	3.1394	L3	1	OFFSET 3	-2.1948
A4	12.954	L4	9.3732	OFFSET 4	2.2473
A5	2.8256	L5	1		
A6	12.954	L6	9.3296		
A7	3.3825	L7	1.4156		
A8	17.8356	L8	17.0351		
A9	3.3825	L9	1.0762		
A10	17.3893	L10	17.2063		
A11	3.3825	L11	1.4218		
A12	12.954	L12	9.3296		
A13	2.8256	L13	1		
A14	12.954	L14	9.3732		
A15	3.1394	L15	1		
A16	12.954	L16	8.6090		
A17	5.3655	L17	1		

(f) Filter 6 (10-2-0).

Parameter	Value (mm)	Parameter	Value (mm)	Parameter	Value (mm)
A1	5.3797	L1	1	OFFSET 1	-1.9752
A2	12.954	L2	8.5028	OFFSET 2	1.6921
A3	3.6	L3	1.1574	OFFSET 3	-1.4534
A4	17.8566	L4	16.9504	OFFSET 4	1.8012
A5	3.6	L5	1.2936	OFFSET 5	-1.4103
A6	17.4283	L6	17.0813	OFFSET 6	1.5156
A7	3.6	L7	1.3735	OFFSET 7	-2.7389
A8	17.8742	L8	16.9536	OFFSET 8	1.4028
A9	3.6	L9	1.2826		
A10	17.4017	L10	17.1307		
A11	3.6	L11	1.1815		
A12	12.954	L12	8.5157		
A13	5.3479	L13	1		

(g) Filter 7 (10-4-0).

Table 6.10: Physical dimensions of all filters designed in this section (continuation).

6.5 Design for manufacturing

All filters designed in this chapter are intended to fulfill the specifications of a satellite application. However these structures are not adequate to be manufactured yet without performing a list of changes and testing. Among the presented options for this applications, the fifth filter (8-3-0) was selected for manufacturing, thus it is necessary to redesign this filter taking into account the requirements of the manufacturing process.

Firstly, the filter will be implemented with a body-cover configuration. This means that the filter will be cut by the H-plane and two pieces will be manufactured namely the open-top filter structure and the cover plate. Due to this configuration, it is necessary to assure a quite good contact when both pieces of the filter are assembled. Thus it is necessary a large amount of mounting screws to provide such contact, specially in the coupling windows where a perfect contact is crucial in order to obtain the right coupling level. Moreover the irises thickness have to be increased in order to place tuning screws along the coupling windows, between each cavity. In this way the contact between the body and the cover in the area of the coupling windows is improved.

Secondly, due to the extremely high sensitivity of the filter response to small changes in the structure, this kind of filters can not be manufactured with the required precision. This filter require a precision up to 1 μm while the precision achievable throw the drilling process is about ± 10 μm. Thus the manufacturing error will deteriorate the filter response. To overcome this drawback it is necessary to add tuning screws to the top of each resonant cavity. The tuning screws will load the resonant mode within each cavity causing a reduction of the resonant frequency of each mode. If this frequency shifting is compensated for by decreasing the dimensions of the resonant cavities, then when the filter is build, it will be possible to adjust the resonant frequency of each mode by acting on the tuning screws.

Finally, since the filter structure is cut in the H-plane, the edges in the E-plane has to be rounded at least to the radius of the drill that will be used in the manufacturing process. This modification will not have a significant effect in the resonant frequency of each mode but may have strong impact in the in the coupling level provided by each coupling window. However it is possible to retrieve the original response by a slight adjustment of the coupling windows.

6.5.1 Thickness of the coupling windows

Since it is necessary to assure a good contact between the body and the cover, a set of mounting screws is placed around the filter and between the resonant cavities. The mounting screws will have a diameter of 2 mm ($M2$). Thus the thickness of the couplings windows must be increased in order to place the mounting screws between the resonant cavities what is crucial to obtain a proper contact in the couplings windows.

Figure 6.35 shows the structure of the coupling windows with thicker irises.

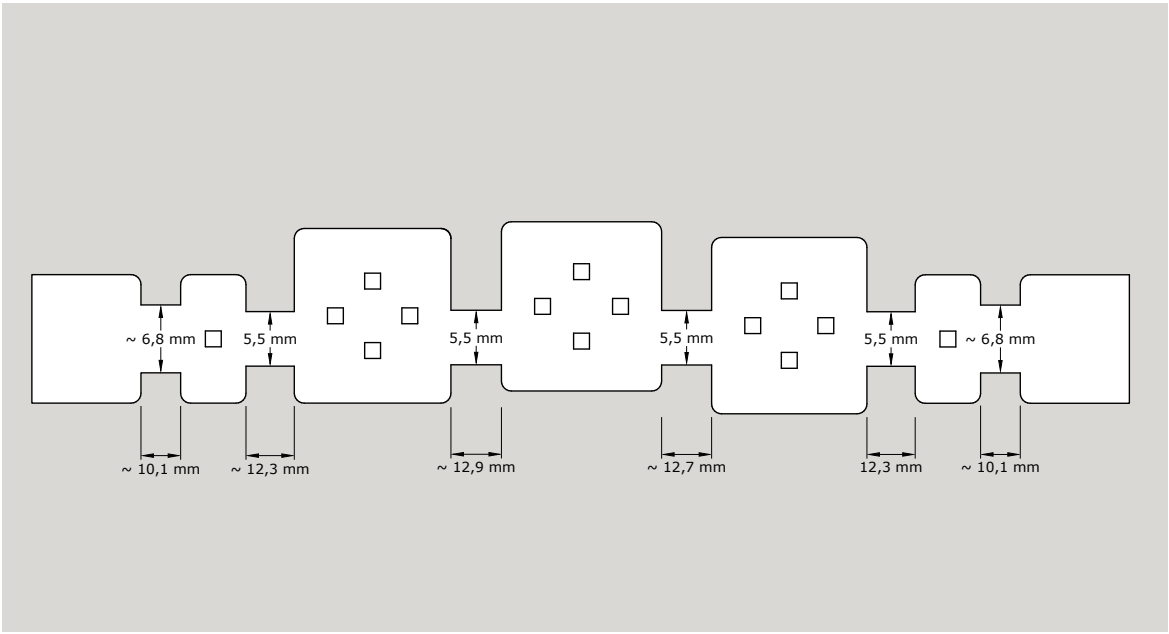

Figure 6.35: Filter structure with thicker irises and tuning screws in the resonators..

As the diameter of the mounting screws is 2 mm, the minimum thickness of the irises is set to 4 mm. As a result, the irises of the single-mode cavities will keep a thickness of 4 mm meanwhile the iris width of the

dual-mode cavities is set to 5.5 mm what provides some margin above 4 mm since in the dual-mode cavities it is necessary to adjust the iris thickness.

6.5.2 Rounded edges

Next, since a drill with a diameter of 2 *mm* will be used in the manufacturing process, the edges in the $E-plane$ must be rounded with at least 1 *mm* of radius. This is done by the component "Step with rounded corners", provided by the electromagnetic software FEST3D (see appendix B) used in this work, which implements a constant height 2D structure. Figure 6.36 shows the rounded filter edges with a radius of 1 *mm*. It should be noted that only the concave corners need to be rounded as the convex edges can be perfectly implemented with any drill.

As a result of the rounded edges, the coupling level provided by the coupling windows will be slightly lowered. Thus it will be necessary to reoptimize each coupling windows to retrieve the original response.

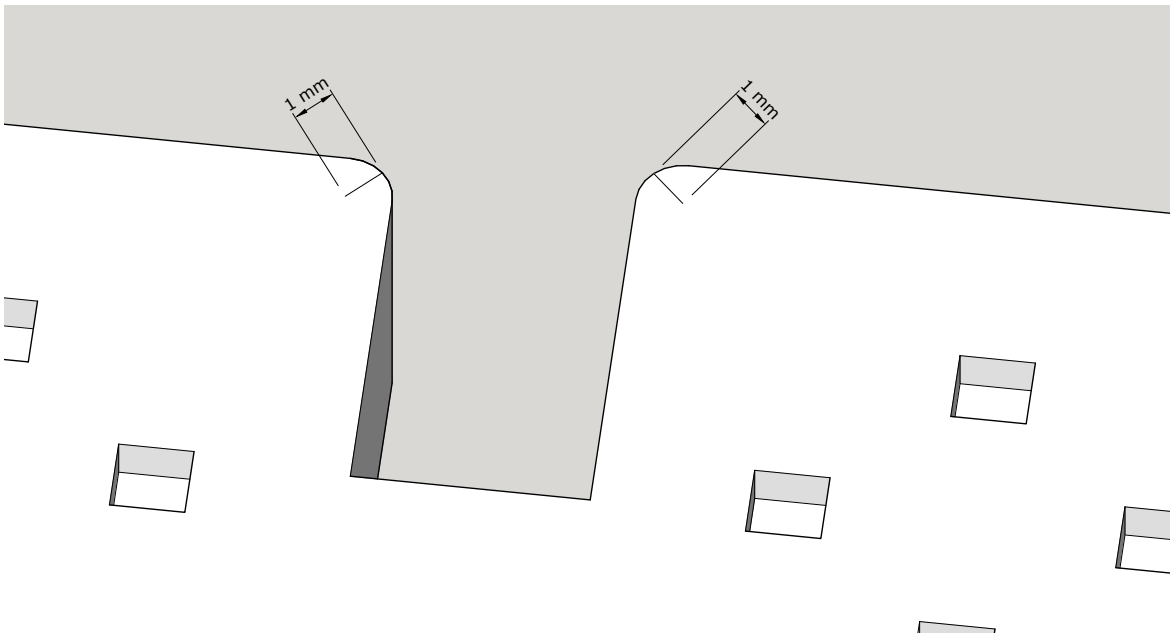

Figure 6.36: Details of the rounded edges close to a coupling window.

6.5.3 Tuning screws

Finally, due to the high sensitivity of the filter structure, tuning screws are necessary in order to compensate for the errors on the filter dimensions that will be introduced through the manufacturing process. The tuning screws used in this design are precisions screws with a diameter of 1.8 *mm*.

These tuning screws introduce a load effect to the resonant modes within the cavities. Then, the resonant frequency of all the modes is lowered. However this effect can be compensated for if the dimensions of the cavities are reduced, what will shift back the resonant frequencies to their original value. This decrement of the filter dimensions is the maximum error in the manufacturing process that can be compensated for by removing or introducing the tuning screws.

Moreover, the number and position of the tuning screws is important since the magnitude of the effect introduced by each screw will depend on the position of the tuning screw with respect to the maximum of the electric field. The screws will introduce the largest effect when they are placed at the point with the maximum electric field. In addition the effect will be greater if the number of screws increases. Similarly, the effect also increases when the size of the screws enlarges. Furthermore, it is important to assure that the screws placed in a dual-mode cavity affect exclusively to one single resonant mode with a negligible effect on the other mode within the dual-mode cavity.

In this example, the screws of the single-mode cavities have been placed in the middle of the cavity. In the dual-mode cavities the tuning screws are located where the electric field of one resonant mode is maximum and the field of the other mode is zero. In addition, the electric field of each resonant mode in a dual-mode cavity has two maximums. Thus two screws have been used for each mode, one in each maximum, in order not to disturb too much far the cavity symmetry. According to this, two tuning screws have been placed in

each cavity for each mode where the electric field of the other mode is negligible as it can be seen in Figure 6.35. This strategy has been previously described by other authors, for instance in [Guglielmi et al., 2001].

The screws are modeled in FEST3D as square screws (instead of modeling rounded screws) by introducing a ridge waveguide. In this way the computational cost of the simulation is actually reduced without compromising the accuracy of the filter response. The square screws have 1.6 mm side what provide the same area as the rounded screws with diameter of 1.8 mm that will be used in the manufacturing process. These tuning screws are seen in detail in Figure 6.37. Due to these screws the dimensions of the resonant cavities have been reduced in the range of 100 to 300 microns what offers enough margin in order to compensate for the manufacturing precision (about ± 10 μm).

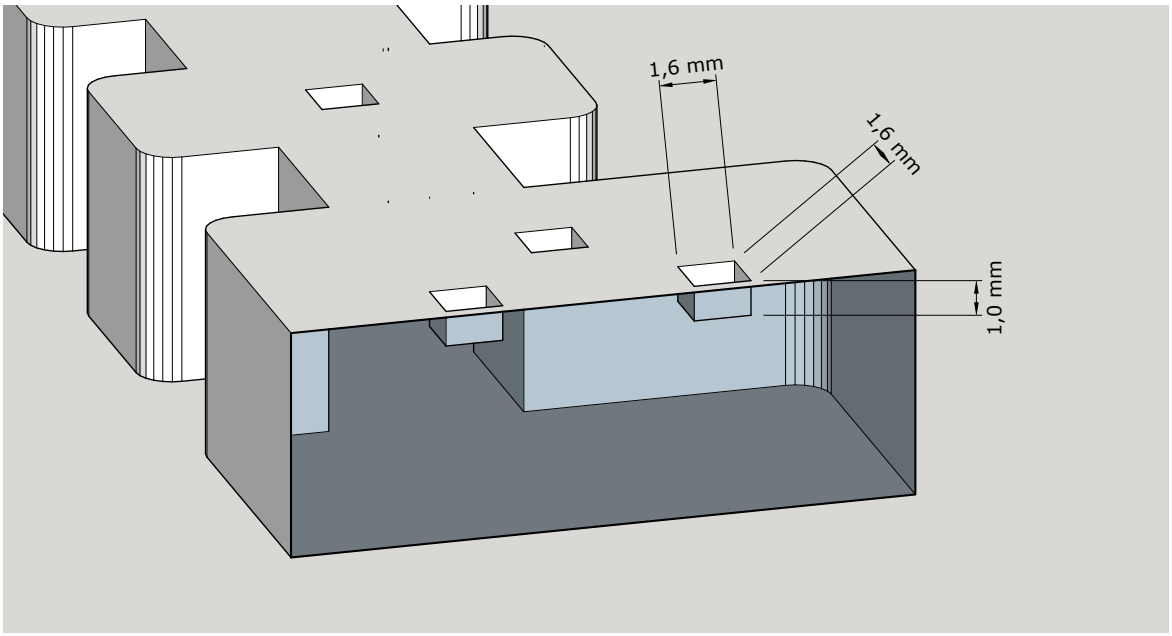

Figure 6.37: Tuning screws modeled as squared screws of 1.6 mm side.

6.5.4 Structure for manufacturing

After concluding this redesign process, the filter structure is adequate for manufacturing. Nevertheless, it is still necessary to perform a set of testing such as a losses analysis or a new tolerance analysis. The filter structure obtained at this point is shown in Figure 6.38 and the response provided after adjusting the filter dimensions when all tuning screws are 1 *mm* depth is shows in Figure 6.39.

6.6 Conclusions

In this chapter the topology composed of only dual mode cavities has been expanded by adding single-mode cavities in the filter input and output by the developed segmentation technique [Guglielmi and Melcon, 1993, Guglielmi, 1994]. In this way it is possible to overcome the drawbacks of the structures proposed in chapter 4. With this topology, the strong input/output coupling due to de filter bandwidth is no longer a problem. Thus the design range of bandwidth and the zeros positions is expanded. Moreover, the thicker irises are no longer necessary. As a result the designed filters have a considerable reduction in terms of footprint and volume what leads also in a lower mass of the manufactures prototypes (all of them important factors in space applications).

Next, in order to fulfill the filter specifications of a real satellite application, some examples are designed in collaboration with the *European Space Agency*. These examples are implemented with the topology proposed in this chapter and cover a wide range of specifications namely from fifth to tenth-order and a bandwidth from 180 MHz to 360 MHz.

Finally, one of these examples has been designed for manufacturing at *ESTEC* by the *European Space Agency* while taking into account the requirements and limitations of the manufacturing process.

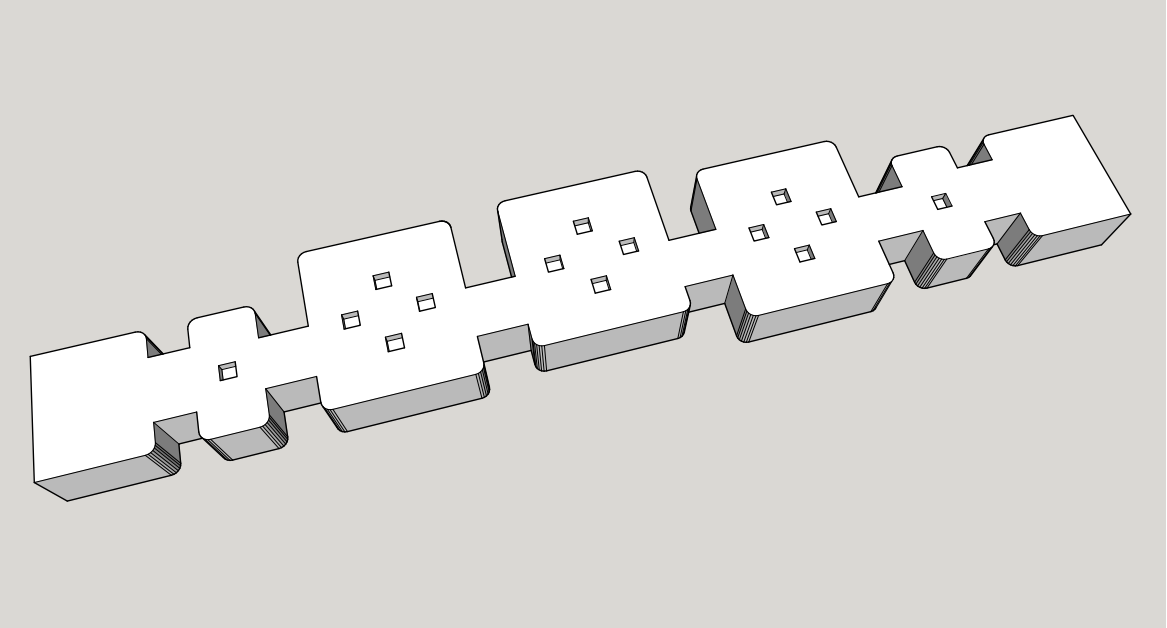

Figure 6.38: Final filter structure ready for manufacturing.

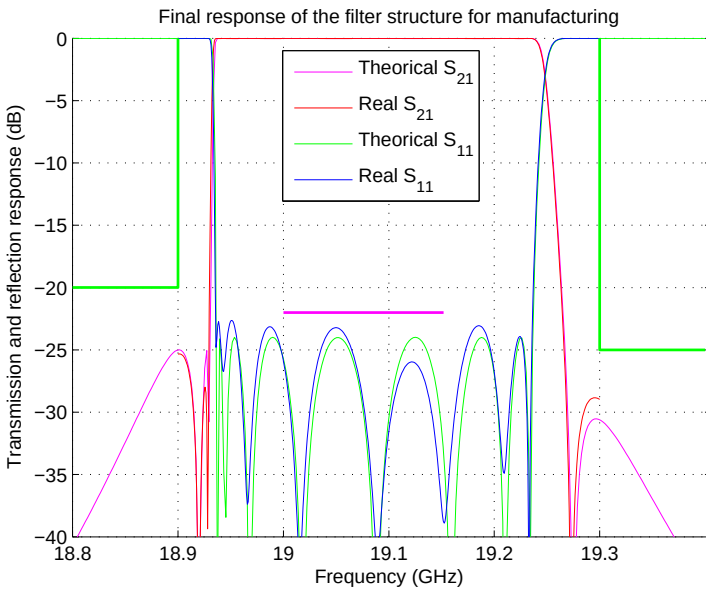

Figure 6.39: Filter response of the structure ready for manufacturing.

7 CONCLUSIONS

Through this work the theory of the coupling matrix has been reviewed in order to use it in combination with the segmentation technique presented in [Guglielmi and Melcon, 1993, Guglielmi, 1994]. This technique has allowed us to obtain the required internal responses of the filter structure by scaling the coupling matrix of the filter.

Firstly it has been necessary to scale the coupling matrix with the appropriate lumped elements of the lowpass prototype. The lumped elements values are calculated by using information of the real resonators that will be used during the physical implementation of the filter. Then the coupling matrix can be segmented and each segment will provide the same response as the correspondent segment of the physical filter structure.

In this way, we have performed a generalization of the design technique introduced in [Guglielmi and Melcon, 1993] by segmenting both the filter structure and the coupling matrix in a step-by-step fashion. Thus the filters design possibilities are expanded, since the mentioned approach could be applied not only for the design of in-line filters, but also for other more complex coupling topologies represented by the coupling matrix.

In order to validate the discussed approach, it has been used in the design of some in-line filters. In this context the obtained results have shown the effectiveness of this technique by providing efficiently the desired filter response even with a fractional bandwidth up to 25 % in spite of the non-linear mechanisms that exits in the waveguide technology, such as the dispersive behavior or the variation of the rejection in the stopband due to the presence of the spurious bands.

Moreover, the generalized step-by-step procedure has been applied to the design of alternative filter topologies beyond the in-line topology. It should be noted that if the topology is too much complex, the segmentation of the structure can not be chosen arbitrarily but it is necessary to cut the structure by the points where the target partial responses can be obtained by segmenting the coupling matrix. As an example, some dual-mode filters have been designed by extending the all-inductive dual-mode topology presented in [Guglielmi et al., 2001]. Nevertheless, in spite of the given advantages such as the reduction in volume and mass or the higher Q and lower insertion loss, this topology with only dual-mode cavities presents still some important drawbacks. For instance, the thicker inner irises and the limitation on the maximum bandwidth and the maximum distance from the passband of the transmission zeros. Furthermore, these limitations get worse when the filter order increases as the maximum bandwidth and distance of the transmission zeros decreases meanwhile the inner coupling windows gets even thicker compromising the compact-size of the structure.

To overcome the said drawbacks a new dual-mode topology has been proposed and presented by adding single-mode cavities in the filter input and output. With this topology, the design range of bandwidth and the zeros positions is expanded. In addition, the thicker irises are no longer necessary. Thus the designed filters achieve even a more compact-size than the filters originally proposed in [Guglielmi et al., 2001]. This means that both footprint and volume are reduced as well as the mass of the manufactured prototypes.

Following, a group of dual-mode filters with this novel topology has been designed in collaboration with the European Space Agency to fulfill the requirement of a real satellite application with a wide range of specifications, namely from fifth to tenth order and a bandwidth from 180 MHz to 360 MHz.

Finally, an eight order filter with a bandwidth of 300 MHz and three transmission zeros has been selected for manufacturing at the European Space Agency as an alternative to the well known in-line filters with extracted poles [Rhodes and Cameron, 1980, Montejo-Garai et al., 2005b, Mohottige et al., 2013].

8 FUTURE WORK

8.1 Introduction

This work opens the possibility to numerous lines of future work and research. In each of the topics addressed within this work, it is possible to develop new concepts that could improve both the accuracy and quality of the results as well as the way that they are achieved. Below some of these lines are shown with examples of the proposed ideas.

8.2 Corrections of the coupling matrix scaling for wideband filters

As it has been discussed in section 3.4, the slope parameter of a waveguide resonator can no be fitted properly in a wideband filter by an equivalent circuit with lumped elements. This fact is due to both the dispersive behavior of the waveguide and the presence of spurious bands at higher frequencies. Figure 8.1a shows the the impedance of a waveguide resonator and a LC resonator. Indeed it can be seen that the same impedance is obtained within a small bandwidth. However if we consider a larger wideband (Figure 8.1b) the impedance of both resonators is only fitted at some discrete frequencies. The dispersive behavior is responsible for a

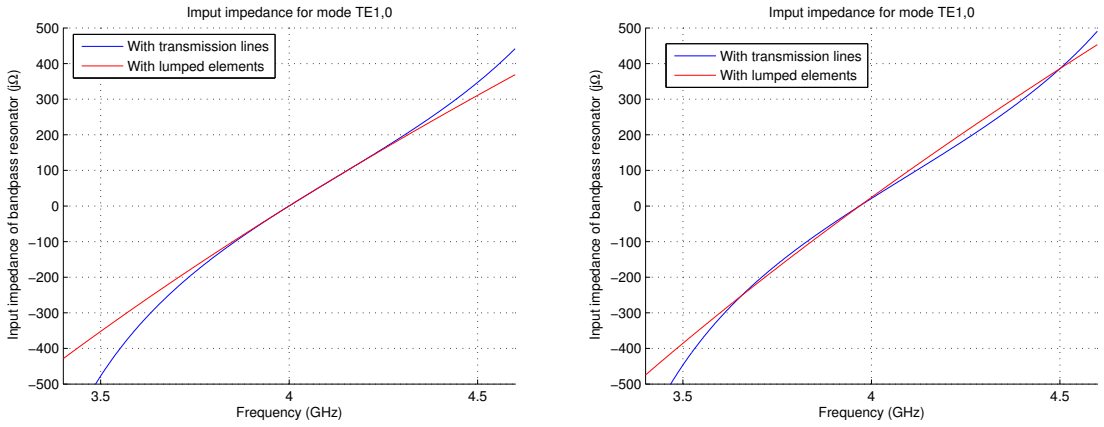

(a) Bandwidth of 100 MHz ($\Delta = 2.5\%$).

(b) Bandwidth of 1 GHz ($\Delta = 25\%$).

Figure 8.1: Comparison between input impedance of both circuits in Figure 2.13 with different fractional bandwidth (Δ).

small error in the level of the target transmission and reflection coefficients. Since the electrical sizes of the coupling apertures in the waveguide structure are frequency dependent, the scaling of the coupling matrix is right only at the central frequency of the passband and gets worse at the passband edges. This effect is negligible within a small bandwidth, however it gets more noticeable when the bandwidth increases and it makes the target partial responses to be deteriorated.

With regard to the presence of spurious bands, they affect the rejection in the stop-band. As a result, the rejection in the stop-band increases at frequencies below the passband meanwhile the rejection level above

the passband decreases. This leads to a frequency shifting of the reflection zeros to lower frequencies and make incorrect the ripple in the passband of the target responses.

To overcome this drawback, it would be necessary a transformation of the frequency axis that shifts the reflection zeros to lower frequencies, as well as a non-linear correction for the levels of the target transmission and reflection responses. In this context, some authors have presented corrections of the slope parameters that can improve the overall accuracy of the wideband filters design [Vanin et al., 2004].

Another possibility for this level correction could be to make the coupling matrix scaling frequency-dependent. In the current work, the coupling matrix is scaled with the lumped elements of the filter prototype which equates the slope parameter of each resonator in the filter prototype with the slope parameter of each waveguide resonator at the central frequency. This concept is shown in figure 8.1a. Nevertheless, it is not possible to fit both slope parameters within a large bandwidth as shown in figure 8.1b. Thus if it is desired to fit the slope parameter of a waveguide resonator at each frequency, a different lumped-elements resonator has to be used and the scaled coupling matrix would be frequency-dependent.

In this way, by using a different scaled coupling matrix for each frequency, the target partial responses would be improved, however it would still be necessary a non-linear transformation of the frequency axis in order to take into account the shifting of the reflection zeros.

8.3 Spurious suppression in in-line filters by using dual-mode cavities

It was advanced in chapter 4 that the dual-mode cavities can be used in spurious suppression techniques. Indeed, the transmission zeros provided by these cavities could cancel the spurious band if the dual-mode cavities are introduced in an in-line filter. By computing the width and height of the dual-mode cavities through the expressions (4.26) and (4.27) it is possible to place in the filter bandpass the first resonance of the dual-mode cavity meanwhile the second resonance together with the transmission zero will be in the spurious band.

Some authors used this technique in the past and designed in-line filters with dual mode cavities. In these designs, only the first resonance of the dual-mode cavities form part of the filter passband meanwhile the second resonance of each dual-mode cavity is used to implement a stop-band at the frequency where the spurious band is located [Guglielmi et al., 1995]. Furthermore, alternative spurious suppression techniques exist. In [Escudero et al., 2013] the spurious suppression is achieved by using different thickness in the filter coupling windows, which affects to the spurious frequencies of the filter. However the variation on the spurious frequency is different for each coupling of the filter. Thereby it is possible to avoid a constructive interference in the spurious band. Figure 8.2a shows the filter structure obtained with the technique of using different irises thickness. The response provided by this structure is shown in figure 8.2b where although the response in the spurious band is quite good there are still some frequencies with a too small rejection.

By introducing a dual-mode cavity in the structure shown in Figure 8.2a it is possible to cancel the remaining spurious frequencies in Figure 8.2b. To give an example, dual-mode cavities with the modes TE_{102} and TE_{301} are used since in this way it is not necessary to introduce offset in the structure. Equations (4.26) and (4.27) are used in order to obtain the dimensions of the dual-mode cavity required to make the mode TE_{102} to resonate in the filter passband and the mode TE_{301} at the spurious frequency. Obviously, these theoretical dimensions have to be adjusted to recover the filter response in the passband or even to improve the rejection in the spurious band.

Firstly, two dual-mode cavities are introduced in the structure shown in Figure 8.2a instead of the second and fourth single-mode cavities. The structure with dual mode cavities in the second and fourth place is shown in Figure 8.3a. The spurious suppression can be achieved if the width of these cavities is obtained by the equation (4.26). Then by adjusting the length of the dual-mode cavity, the original response in the passband is retrieved. In this way, it is possible to achieve the response shown in Figure 8.3b where the spurious rejection has been improved.

Secondly, if the first and last single-mode cavities are replaced by dual-mode cavities instead of the second and fourth ones, a better behavior in the spurious band is achieved. It can be demonstrated that in order to have a better spurious band, the dual-mode cavities should be placed as isolated as possible from the rest of the filter. In this way by placing the dual mode cavities at the beginning and at the end of the filter between thicker irises it is possible to obtain more advantages in terms of the spurious behavior. The structure where the first and last cavities are changed by dual-mode cavities is shown in Figure 8.4a and the response provided by this structure in Figure 8.4b.

Thus, the advantage of the dual-mode cavities in spurious suppression techniques has been proved. By conducting a deeper study on this technique, it would be possible to find different topologies with dual-mode cavities that could provide an in-line filter with a stopband in the spurious frequencies.

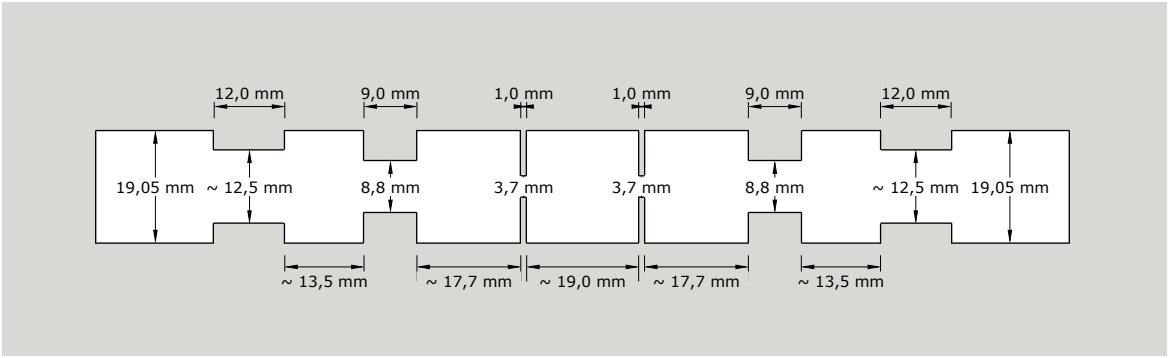

(a) Filter structure.

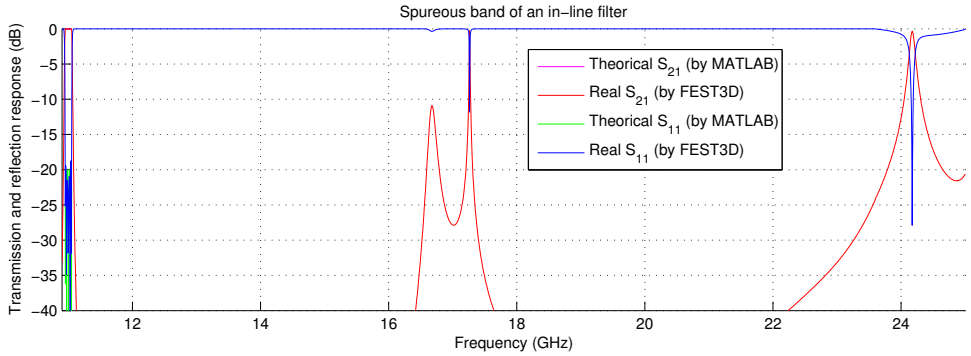

(b) Spurious band.

Figure 8.2: In-line filter with spurious suppression.

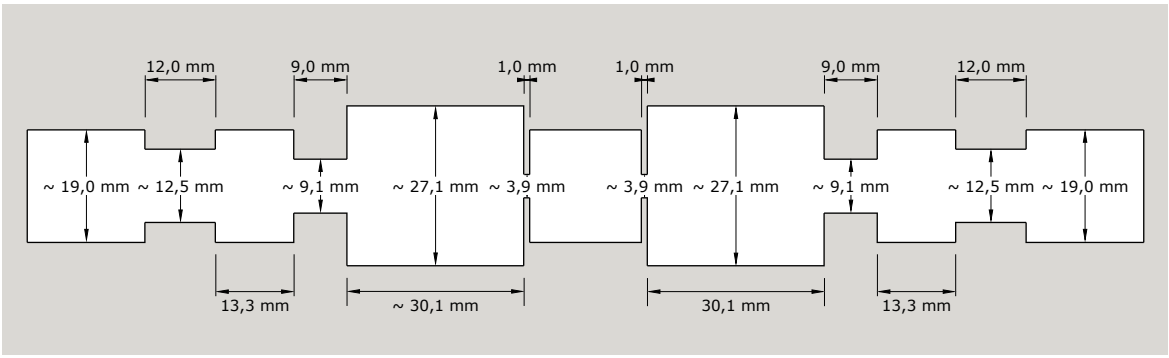

(a) Filter structure.

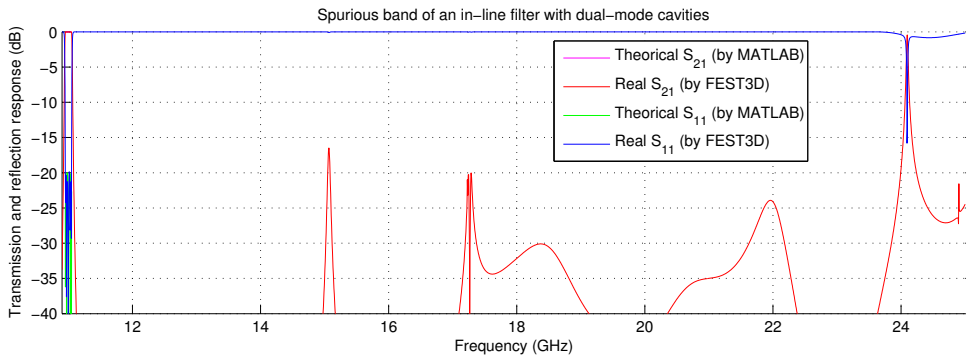

(b) Spurious band.

Figure 8.3: In-line filter with wider second and fourth cavities.

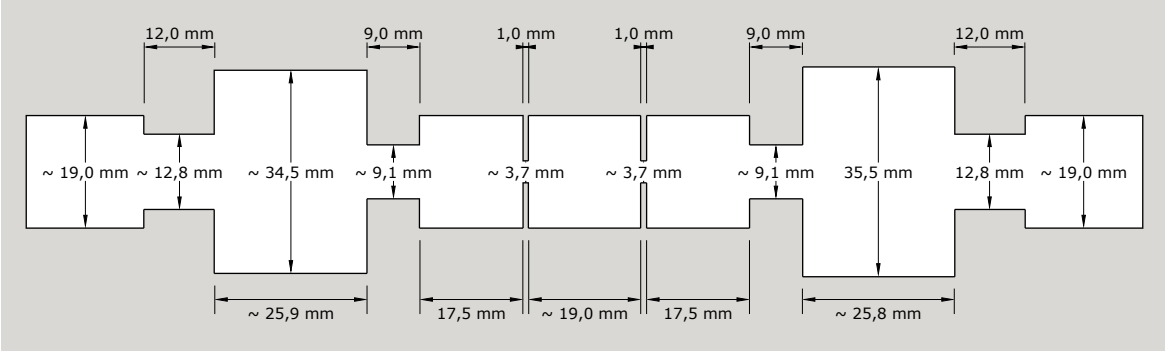

(a) Filter structure.

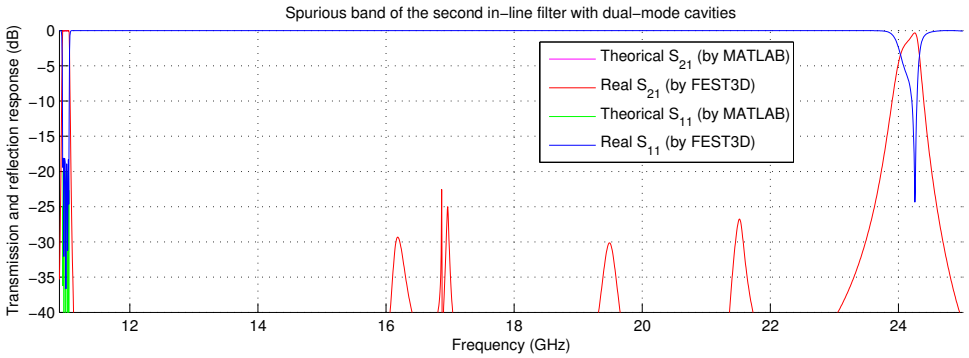

(b) Spurious band.

Figure 8.4: In-line filter with wider first and last cavities.

8.4 Dual-mode filter design with elements that favor the coupling to the TE_{201} mode and lower the coupling to the TE_{102} mode.

As it has been discussed in chapters 4 and 6, the main drawback of the design of dual mode cavities with offset is the maximum level of coupling that can be obtained to the mode TE_{201} while keeping the coupling to the mode TE_{102}. This problem limited the position of the transmission zero, specially when there is not single-mode cavities in the filter input and output or with an extremely high bandwidth.

In this context, it would be desirable to obtain a coupling structure with a stronger coupling to the mode TE_{201} at the expense of the coupling to the mode TE_{102}. In this way, if the coupling to the mode TE_{201} gets higher as compared to the mode TE_{102}, a lower offset will be required and it will be possible to place further from the passband the transmission zero (for a given bandwidth).

For instance, if a dielectric strip is placed inside the dual-mode cavity from the input to the output (where the electric field of the mode TE_{201} is negligible), the electric field of the mode TE_{102} would confine in the middle of the cavity. Then, the coupling to the mode TE_{102} would decrease. Thus if the coupling to the mode TE_{102} is decreased while keeping the coupling to the mode TE_{201}, the relation between the coupling to the second mode and the first one would increase and less offset would be necessary.

Figure 8.5a shows the field pattern in an empty dual-mode cavity. Moreover the hypothetical situation of a cavity with a dielectric strip is shown in Figure 8.5b. In this figure the field of the mode TE_{102} is confined inside the dielectric strip. Thus the coupling to the mode TE_{102} would be penalized. The coupling topology of the structures in both Figures 8.5a and 8.5b corresponds to the coupling diagram shown in figure 4.6. Another possibility would be to implement a topology in which the first excited mode is the mode TE_{201}. In this way it could be also possible to achieve a higher coupling to the mode TE_{201} and lower to the mode TE_{102}. For instance, if a double iris configuration is used [Cameron et al., 2007] it may be possible to get coupling mainly to the mode TE_{201}. In the topology shown in figure 8.6, the mode TE_{201} resonate within the single-mode cavities. This mode provides the right phase to excite the mode TE_{201} inside the dual-mode cavity. Thus, the coupling to this mode would be higher. Nevertheless, single-mode cavities are needed in the filter input and output what reduces the interest of this topology.

Finally, this topology could be combined with the idea of placing a dielectric strip in the middle of the dual-mode cavity in order to achieve the largest coupling to the mode TE_{201} as compared to the coupling to the mode TE_{102}.

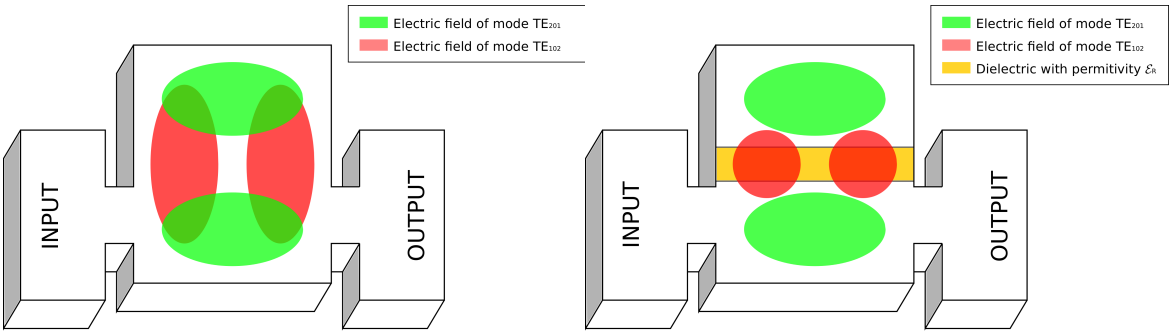

(a) Without dielectric. (b) With a dielectric strip.

Figure 8.5: Dual-mode cavity with vacuum and with a dielectric strip.

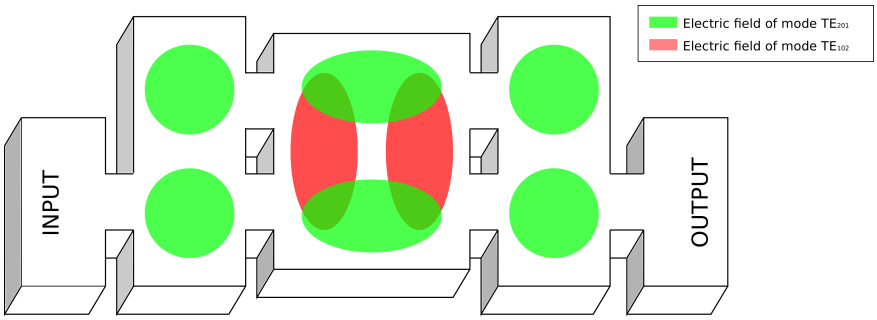

Figure 8.6: Dual-mode cavity with double iris configuration.

8.5 Self-equalized dual-mode filters with complex transmission zeros

In the present work, all waveguide filters have been designed while taking into account the module of the transmission parameter. However it is equally important the phase of the filter response, especially the group delay (τ) that considers the phase shift suffered by each frequency component as a result of the path from the filter input to the output. The aim is to get a constant group delay within the passband which is defined as the negative derivative of the phase with respect to the complex variable (s)[1] [Matthaei and Yones, 1980, Cameron et al., 2007].

$$\tau = -\frac{\partial \phi(S_{21})}{\partial s} \tag{8.1}$$

Thus the group delay is singular in the points where there is a discontinuity in the phase of the filter response, specifically in the poles and zeros of the filter transfer function. If these poles are close to the frequency axis ($s = j\omega$), then the phase and therefore the group delay at real frequencies is affected.

By introducing a pair of complex transmission zeros it is possible to move the poles of the transfer function away from the passband. As a result, a flatter group delay is obtained at real frequencies within the passband as it is briefly discussed in appendix A.

The filtering functions used in this work have transmission zeros only in the frequency axis ($s = j\omega$) what does not allow to modify the group delay of a given filter response. Nevertheless, here are some examples of self-equalization by introducing a pair of paraconjugate[2] zeros in the complex plane [Cameron et al., 2007].

In all the cases, only a complex pair of zeros have been placed in the real axis ($s = \pm\sigma + j \cdot 0$) since that is enough to achieve a flat group delay within a considerable range in the passband. If it is desired to achieve a extended range with constant group delay, then more pairs of paraconjugate zeros must be introduced in the complex plane with both real and imaginary parts ($s = \sigma + j\omega$).

Figures from 8.7 to 8.12 show the normalized filter responses of the filters designed in the chapter 6 and the group delay. It can be noticed the difference between the group delay without complex transmission zeros and by introducing a pair of paraconjugate zeros in the axis $\omega = 0$.

[1] In this work, s refers to the Laplace complex variable $s = \sigma + j\omega$ where $\omega = 2\pi f$ is the real frequency in rad/s.

[2] The term "paraconjugate pairs" refers to a pair of zeros that are mirror-image about the imaginary axis. The paraconjugate of a complex function F(s) can be defined as $\tilde{F}(s) \triangleq F^*(-s)$. Thus the paraconjugate of $s = \sigma + j\omega$ is $\tilde{s} = -\sigma + j\omega$

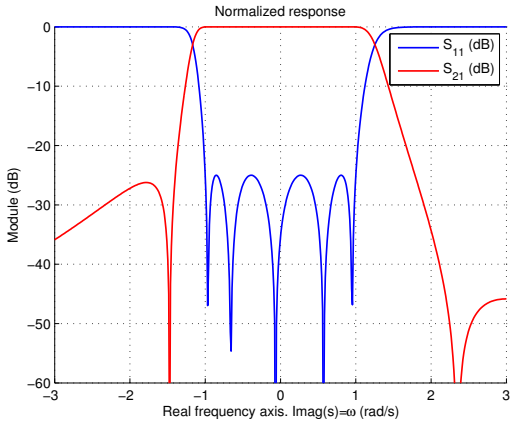

(a) Module response.

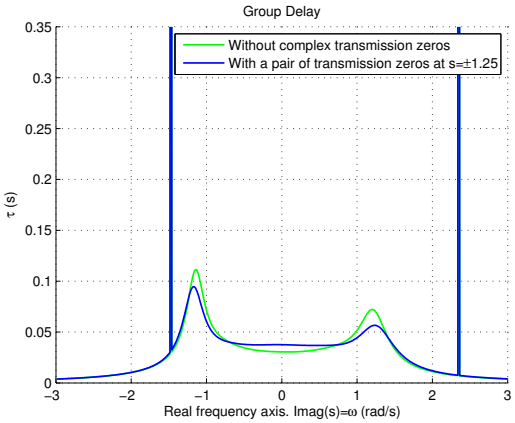

(b) Group delay.

Figure 8.7: Fifth order self-equalized filter with two transmission zeros in the real axis ($s = \pm\sigma + j \cdot 0$) and another two in the complex axis ($s = j\omega$).

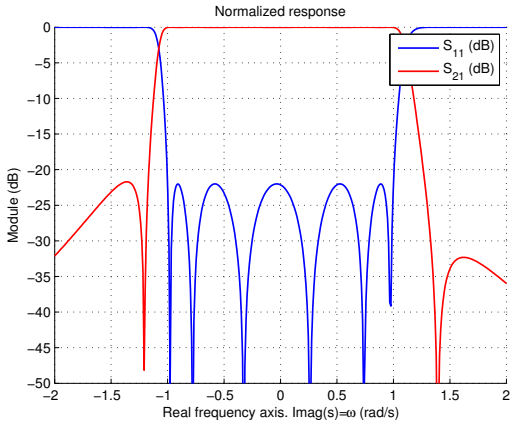

(a) Module response.

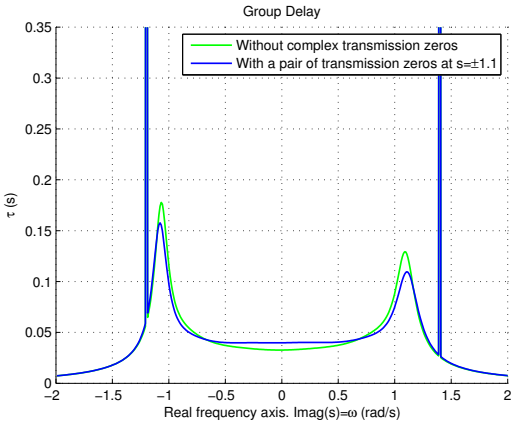

(b) Group delay.

Figure 8.8: Sixth order self-equalized filter with two transmission zeros in the real axis ($s = \pm\sigma + j \cdot 0$) and another two in the complex axis ($s = j\omega$).

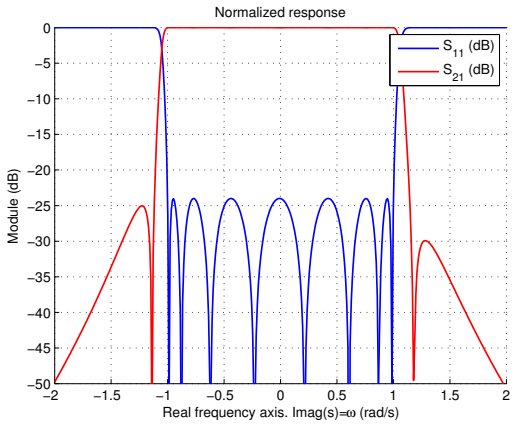

(a) Module response.

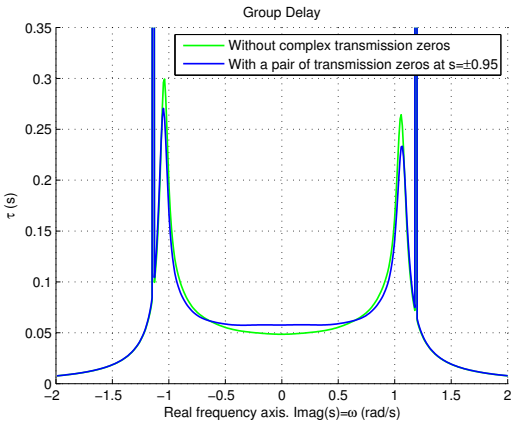

(b) Group delay.

Figure 8.9: Eight order self-equalized filter with two transmission zeros in the real axis ($s = \pm\sigma + j \cdot 0$) and another ones in the complex axis ($s = j\omega$).

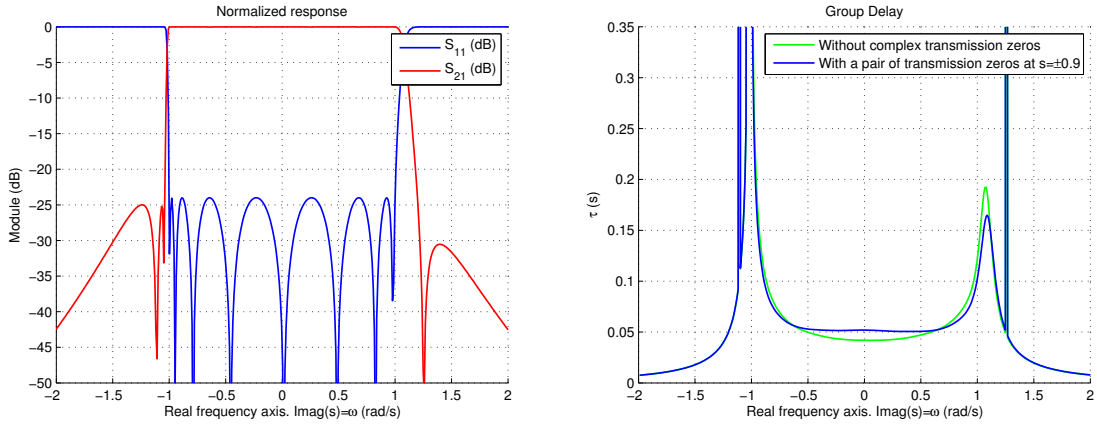

(a) Module response. (b) Group delay.

Figure 8.10: Eight order self equalized filter with two transmission zeros in the real axis ($s = \pm\sigma + j\cdot 0$) and three in the complex axis ($s = j\omega$).

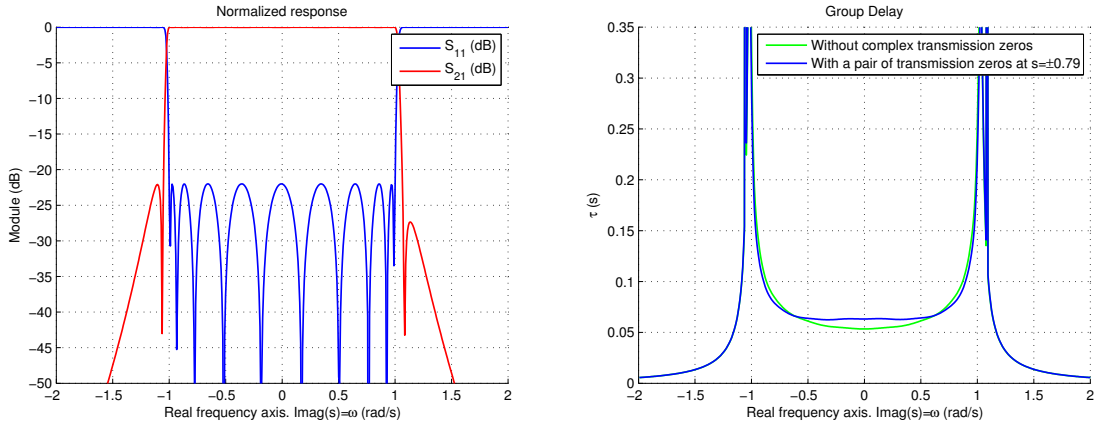

(a) Module response. (b) Group delay.

Figure 8.11: Tenth order self-equalized filter with two transmission zeros in the real axis ($s = \pm\sigma + j\cdot 0$) and another two in the complex axis ($s = j\omega$).

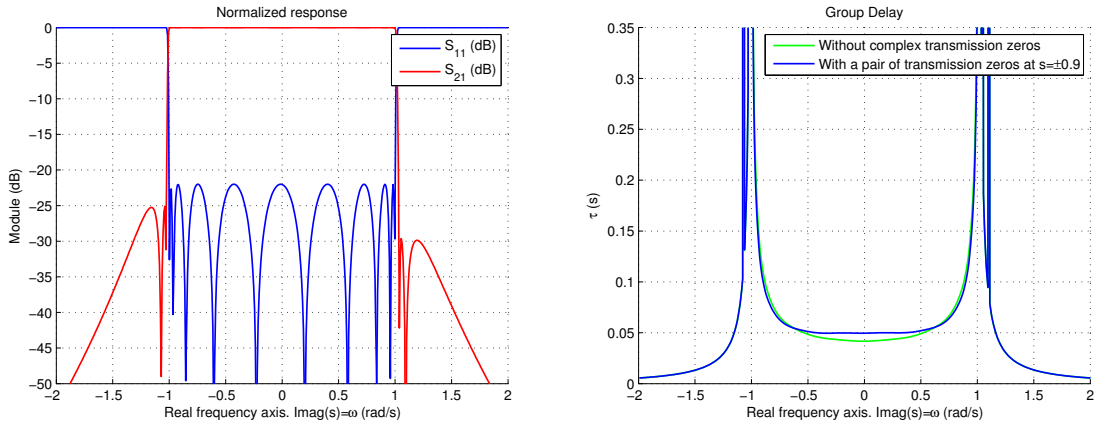

(a) Module response. (b) Group delay.

Figure 8.12: Tenth order self-equalized filter with two transmission zeros in the real axis ($s = \pm\sigma + j\cdot 0$) and four in the complex axis ($s = j\omega$).

8.6 Dual-mode filters with input and output single-mode cavities and extracted poles.

Usually, the design of waveguide filters with transmission zeros is performed by using extracted poles techniques. These approaches introduce finite transmission zeros that are realized by additional resonators added at each end of the filter. In order to achieve a good spurious behavior, these resonators are usually coupled in a given structure to the first and last resonators where the mode TE_{102} is excited [Rhodes and Cameron, 1980, Montejo-Garai et al., 2005b, Mohottige et al., 2013].

In this work, the presence of transmission zeros is achieved by a novel filter topology with all-inductive dual-mode cavities and a pair of single-mode cavities at the filter input and output. Whit the proposed topology the maximum number of transmission zeros that can be placed at finite frequencies is given by the following expressions:

$$\text{TZ (dual-mode with input/output single-mode cavities)} = \frac{N}{2} - 1 \quad \text{N even} \tag{8.2}$$

$$\text{TZ (dual-mode with input/output single-mode cavities)} = \frac{N-1}{2} - 1 \quad \text{N odd} \tag{8.3}$$

Since this topology have two single-mode cavities at the filter input and output, if the mode TE_{102} is excited in these cavities, then it is possible to a extracted pole to each single-mode cavity without compromising too much the compact-size of the structure. As a result, two more transmission zeros can be placed at finite frequencies. Then the maximum number of finite transmission zeros is given by the expressions (8.4) and (8.5).

$$\text{TZ (dual-mode with input/output single-mode cavities and extracted poles)} = \frac{N}{2} + 1 \quad \text{N even} \tag{8.4}$$

$$\text{TZ (dual-mode with input/output single-mode cavities and extracted poles)} = \frac{N-1}{2} + 1 \quad \text{N odd} \tag{8.5}$$

These two extra transmission zeros can be used, for instance to obtain an equalized group delay as it is explained in the previous section. Figure 8.13 shows the hypothetical structure of a filter with dual-mode cavities and input/output single-mode cavities where a pair of extracted poles has been added.

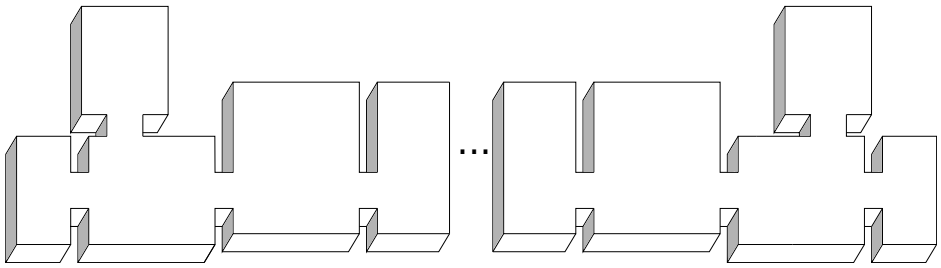

Figure 8.13: Topology with input/output single-mode cavities and extracted poles.

8.7 Adapting the designed dual-mode filters with input and output single-mode cavities to manifold multiplexers

With regard to the design of multiplexers, some diplexers and a triplexer have been designed in chapter 5. However, since all of them were star multiplexer, some drawbacks appear when the number of channels is further increased. This fact is due to the large size of the junction necessary to couple a big number of channels. Here, the main drawback is the presence of higher order modes that resonate within the diplexer junction and could deteriorate the filters responses.

To overcome this drawback it could be possible to implement these multiplexers with manifold configuration instead of star multiplexers. Moreover, by using the filters designed in chapter 6 it would be possible to avoid the problem of the input coupling that was faced in chapter 5. In conclusion, if a multiplexer is built with manifold configuration and by using the dual-mode filters designed in chapter 6 there would not be any limitation on the number of channels and the input coupling would not be a problem since the coupling is performed through a single-mode cavity.

As an example, Figure 8.14 shows a manifold triplexer designed in [Abenza, 2014] by a systematic optimization procedure [Brumos et al., 2014]. The final response provided by this triplexer is shown in Figure 8.15.

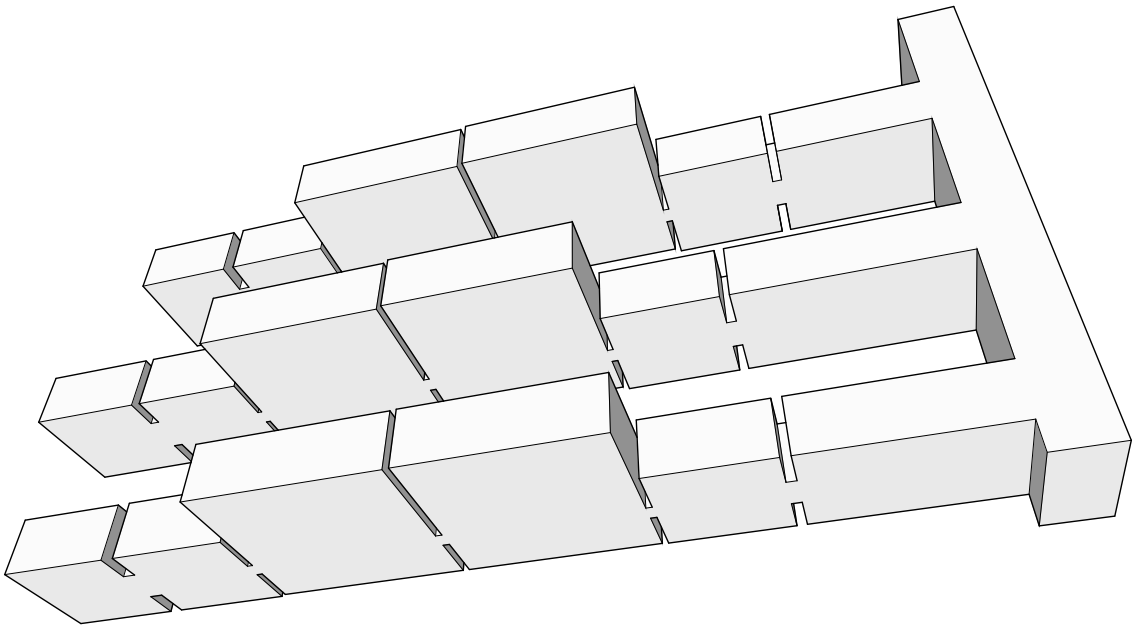

Figure 8.14: Manifold multiplexer with the presented dual-mode filters with input/output single-mode cavities.

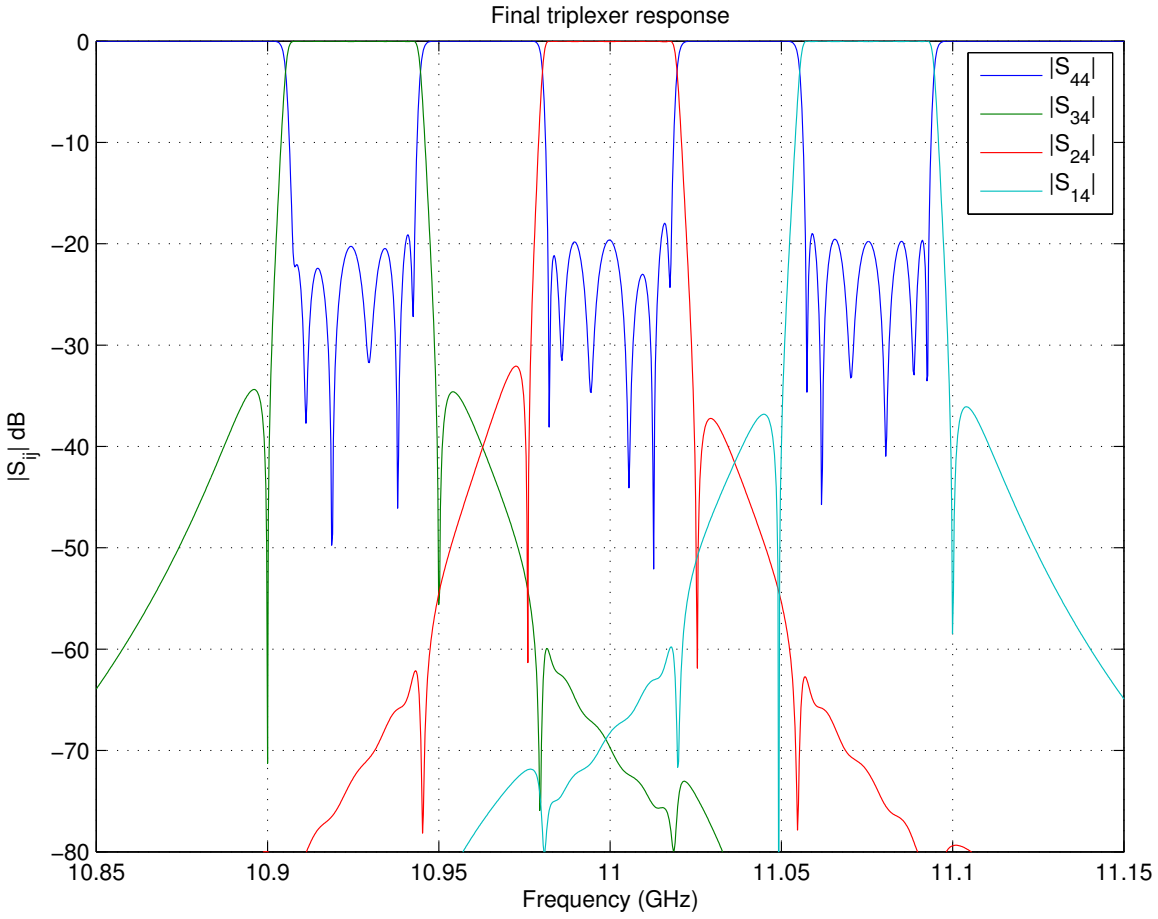

Figure 8.15: Final response of the manifold multiplexer presented in Figure 8.14.

8.8 Dual-mode filters with input and output dual-mode cavities that implements "Chained responses"

In this work a new topology of dual-mode filters has been introduced by extending the all-inductive dual-mode filters proposed by Guglielmi [Guglielmi et al., 2001] and by adding single-mode cavities to the filter input and output. In this way it is possible to deal with the strong couplings required at the filter input and output.

Moreover, the adaptation of the design technique shown in [Guglielmi and Melcon, 1993, Guglielmi, 1994] to the context of the coupling matrix allows to design these new dual-mode filters with an arbitrary order and number of transmission zeros. However, if it is desired to have at least one transmission zero in each side of the passband by using this new topology with input/output single-mode cavities, then the smallest filter possible is a sixth-order filter with two transmission zeros. This fact is a limitation on the minimum filter order that can be implemented with this topology.

This limitation may become a drawback if a given application does not require such a high order filter. For instance, if the desired filter specifications can be satisfied with a fourth-order filter with two transmission zeros, by using our concept it would be necessary to implement a sixth-order one, since at least two dual-mode cavities are required in order to provide the two transmission zeros and also two single-mode cavities at the filter input and output. As a result, the sixth-order filter will have a greater size and a larger sensibility to manufacturing errors than the forth-order filter that fulfills the filter specifications as well.

One possibility to overcome this drawback could be to implement "Chained transfer functions" [Guglielmi and Connor, 1997, Chrisostomidis and Lucyszyn, 2005] instead of the "Chebyshev functions" shown in the appendix A. By implementing a chained function it is possible to achieve a structure with lower sensibility to manufacturing errors at the expense of some selectivity degradation. In appendix A the generalized Chebyshev filtering function was introduced ($C_N(s)$) in order to obtain a Chebyshev transfer function.

$$C_N(s) = \cosh\left[\sum_{n=1}^{N} \operatorname{arccosh}\left(x_n(s)\right)\right] \tag{8.6}$$

$$x_n(s) = \frac{s - 1/s_n}{1 - 1/s_n} \tag{8.7}$$

Chained synthesis uses a generating function $C_M(s)$ obtained as the product of a given number (k) of sub-functions called "seed functions".

$$C_M(s) = \prod_{i=1}^{k} C'_{N_i}(s) \tag{8.8}$$

These seed functions C'_{N_i} may be or not Chebyshev functions with any order and specifications as long as they are realizable in order to assure that the obtained chained function $C_M(s)$ will be realizable as well. With these chained functions, it will be possible to obtain a filter response with reflection zeros of multiple order and a decreased rejection in the stopband. This decreased rejection will be similar to the rejection obtained with a filter of lower order. Then it will be possible to implement, for instance a filter response similar to a (4-2-0) response with the structure composed of two dual-mode cavities and two single-mode cavities. As a result, due to the presence of higher multiplicity reflection zeros, the sensitivity to manufacturing errors will be decreased since several parts of the filter structure will contribute to the same frequency range of the filter response.

Below some examples of chained function are presented by using generalized Chebyshev seed functions. Here, when all the seed function are Chebyshev functions, it is possible to distinguish between two different cases.

- All the seed functions are the same Chebyshev function of Nth-order.

  $$C'_{N_i} = C_N \tag{8.9}$$

  Then the resulting chained function will be of Mth-order ($M = k \cdot N$) where k is the number of seed functions. This function will have a constant ripple level with N reflection zeros of multiplicity k.

- The seed functions are Chebyshev functions of different order or number of transmission zeros. In this case the resulting chained function will no longer be equiripple. In addition, the number of reflection zeros will be at least the maximum order of the seed functions, some of them with higher multiplicity depending on the number and order of the seed functions.

  $$TZ \geq \max(N_i) \tag{8.10}$$

  where N_i refers to the order of the ith seed function.

Next we present several possibilities to implement chained functions by the structure with two dual-mode cavities and two single-mode cavities (6-2-0) since this is the minimum structure that can be built with input and output single-mode cavities that implements at least one transmission zero in each side of the passband.

The possibilities to implement a sixth-order response with a chained function are shown in table 8.1[3]. It should be noted that the characteristics shown in table 8.1 in terms of ripple level and number of reflection zeros are correct only for seed functions with the same number of transmission zeros. However, the chained functions presented below have two transmission zeros provided by the first seed function. As a result the reflection zeros of the first seed are shifted to the edges of the passband. Thus the reflection zeros provided by each seed function are not perfectly combined into zeros of higher multiplicity. Figure 8.16 shows this effect with a (2+2) chain function where the first seed function introduce two transmission zeros. It can be seen that since the transmission zeros are not too close to the passband, the mentioned frequency shifting in the reflection zeros of the first seed is only noticeable below -50 dB. Thus the reflection zeros will still be considered as zeros of second order.

Chained function	**Equiripple**	**Reflection zeros**
(1+1+1+1+1+1)	Yes	1 of 6th order
(2+1+1+1+1)	No	2 of 1st order and 1 of 4th order
(3+1+1+1)	No	2 of 1st order and 1 of 4th order
(4+1+1)	No	4 of 1st order and 1 of 2nd order
(5+1)	No	4 of 1st order and 1 of 2nd order
(2+1+3)	No	4 of 1st order and 1 of 2nd order
(2+4)	No	2 of 1st order and 2 of 2nd order
(2+2+1+1)	No	2 of 1st order and 2 of 2nd order
(2+2+2)	Yes	2 of 3rd order
(3+3)	Yes	3 of 2nd order

Table 8.1: Different possibilities to implement a 6th-order response by a chained function.

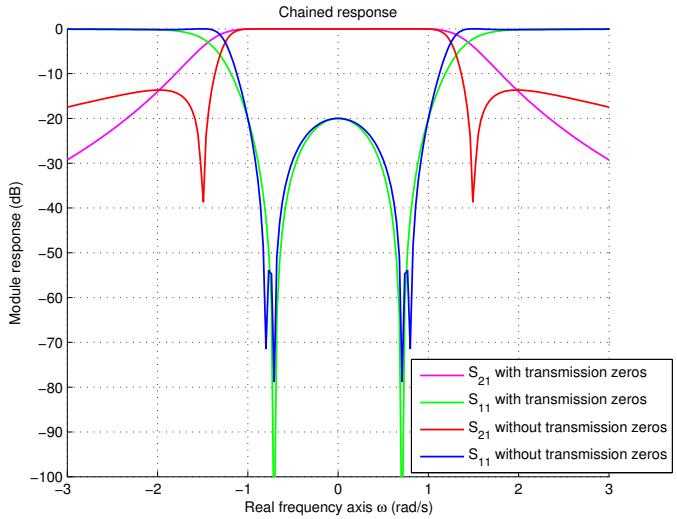

Figure 8.16: Comparison between a chained (2+2) function without transmission zeros and with two transmission zeros provided by the first seed.

Figure 8.17 shows the different possibilities listed in table 8.1 in order to implement a (6-2-0) response by a chained function. All these chained functions are compared with a (5-2-0) Chebyshev function. If it is desired to obtain with a chained function the same slope in the bandpass edges as with the fifth order Chebyshev response, then it can be seen that either a (2+4) chained response (figure 8.17f) or a (3+3) response (figure 8.17i) are equally good options. On the contrary, if the aim is to obtain the same ripple level in the stop-band, the best options are the chained (2+1+3) (figure 8.17e) or the chained (4+1+1) (figure 8.17c) responses.

Similarly, in Figure 8.18 the chained responses listed in table 8.1 are compared with a (4-2-0) Chebyshev response. Here, the chained responses (3+1+1+1) (figure 8.18b) and (2+2+1+1) (figure 8.18g) are the best options to fit the slope in the bandpass edges meanwhile with the chained function (2+1+1+1+1) (figure 8.18a) it is possible to obtain the same ripple level in the stopband as with a (4-2-0) Chebyshev response.

[3]In table 8.1, the nomenclature $(N_1 + N_2 + \cdots + N_k)$ refers to the order of each seed function where k is the number

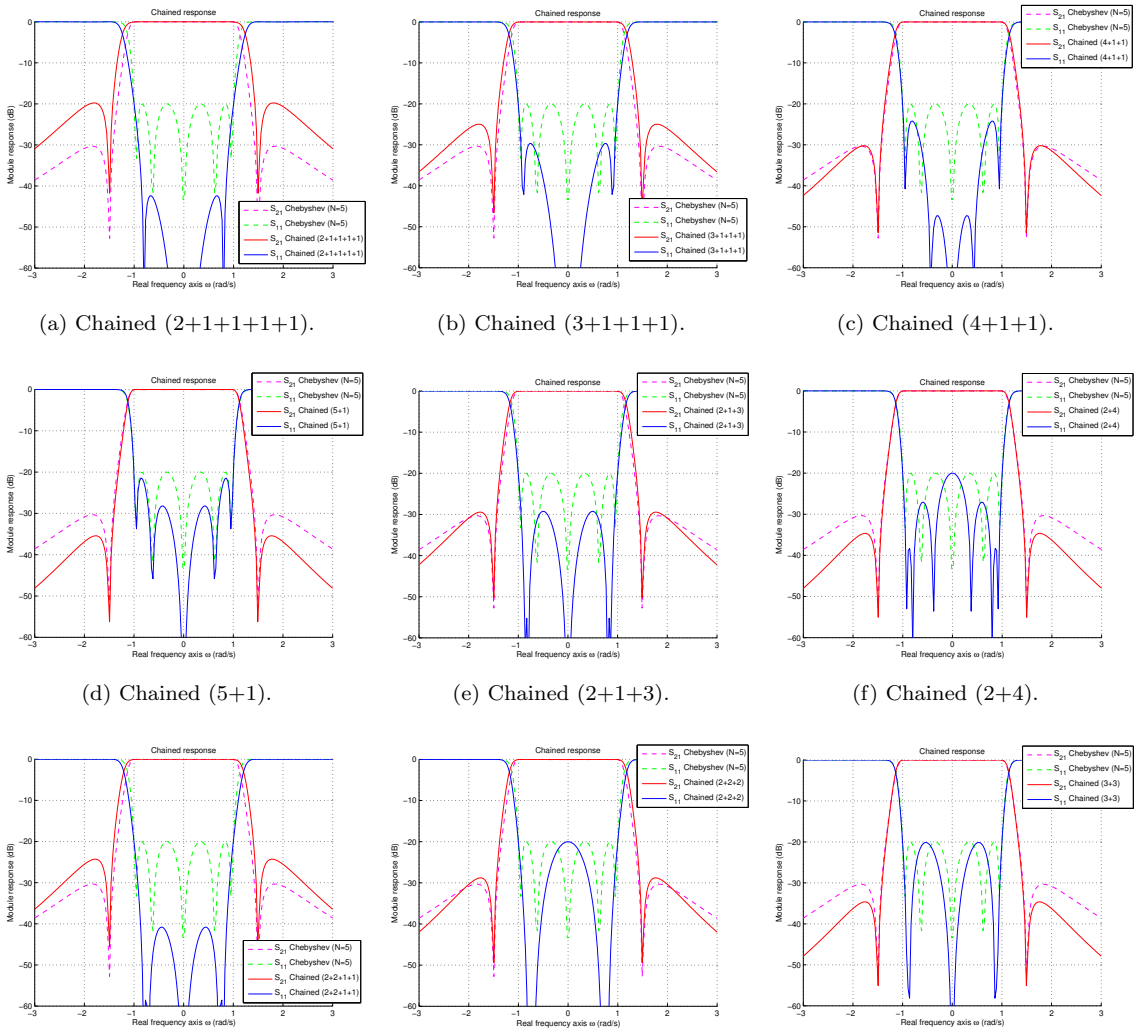

(a) Chained (2+1+1+1+1). (b) Chained (3+1+1+1). (c) Chained (4+1+1).

(d) Chained (5+1). (e) Chained (2+1+3). (f) Chained (2+4).

(g) Chained (2+2+1+1). (h) Chained (2+2+2). (i) Chained (3+3).

Figure 8.17: Comparison between (6-2-0) chained functions and a (5-2-0) Chebyshev function.

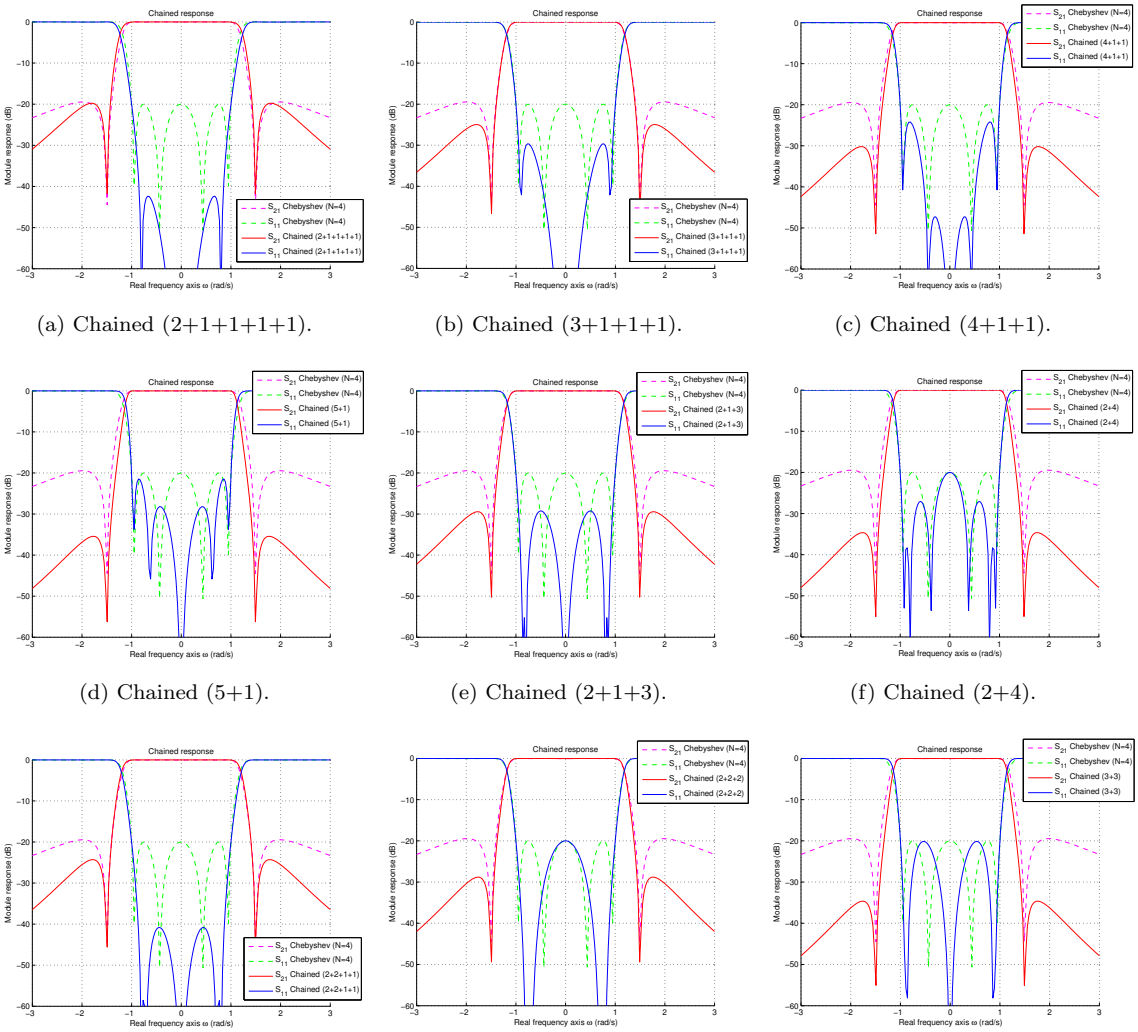

(a) Chained (2+1+1+1+1). (b) Chained (3+1+1+1). (c) Chained (4+1+1).

(d) Chained (5+1). (e) Chained (2+1+3). (f) Chained (2+4).

(g) Chained (2+2+1+1). (h) Chained (2+2+2). (i) Chained (3+3).

Figure 8.18: Comparison between (6-2-0) chained functions and a (4-2-0) Chebyshev function.

8.9 Transversal waveguide filters with triple-mode cavities

The last line of future work proposed is the extension of the design procedure presented in chapter 4 to implement cavities with three resonant modes within them. Some authors have actually presented transversal triple-mode filters design with integrated technology [Shen et al., 2010]. Moreover, in waveguide technology some triple-mode filters exist with other topologies. In [Mattes et al., 2000] a triple-mode cavity was presented. This cavity implemented an in-line topology where the coupling between each resonance and the next one was achieved by adding cut edges to the cavity. Furthermore, a triple-mode cavity that provides three transmission poles and two transmission zeros was designed in [Amari et al., 2004]. In this cavity, the modes TM_{110} and TE_{101} were excited by introducing offset in the YZ plane to the input iris. In addition, by rotating 90° the output waveguide and introducing offset in the XZ plane, it was possible to get coupling to the modes TM_{110} and TE_{011}. Nevertheless, this structure does not implemented a fully transversal topology either.

With regard to transversal triple-mode filters in waveguide technology it is necessary to increase the height of the resonant cavity in order to adjust the resonant frequencies of each mode with the three parameters: width, length and height. In this section, some examples of triple-mode cavities with the modes TE_{101}, TM_{110} and TE_{011} are presented. With these modes, it is possible to implement a transversal topology if the filter input is coupled to the three modes in the cavity at the same time, and all of them are coupled to the output. This topology is shown in Figure 8.19. With this topology, it is possible to implement a filter with three transmission poles and two zeros[4] and place them below or above the filter passband as desired.

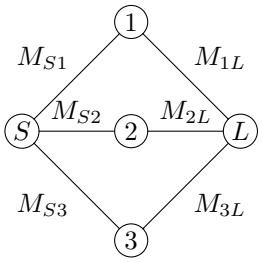

Figure 8.19: Coupling-routing diagram of a third order fully transversal filter.

As a first example, a third order filter with two transmission zeros (3-2-0) is designed. In this example the filter is centered at 3.29 GHz with 15 MHz bandwidth and a reflection level of -20 dB. The coupling matrix which implements this topology is shown in Figure 8.20. At is has been already discussed, in order to excite three resonant modes within the cavity, it is imperative to take into account the offset of the coupling windows. In a cavity with a centered aperture, only the resonant modes TE_{MN} or TM_{MN} are excited where M has to be a odd index and N an even index. If it is desired to excite the modes TE/TM_{QN} with Q even, then it is necessary to introduce some asymmetry in the XZ plane. Similarly, in order to excite the modes TE/TM_{MP} with P odd an asymmetry in the YZ plane is required. Thus to excite the modes TE_{101}, TM_{110} and TE_{011}, some asymmetries in both XZ and YZ planes are necessary.

$$M = \begin{bmatrix} 0 & 0.2950 & 0.2936 & -0.7522 & 0 \\ 0.2950 & 1.1109 & 0 & 0 & 0.2950 \\ 0.2936 & 0 & -1.1104 & 0 & 0.2936 \\ -0.7522 & 0 & 0 & -0.0026 & 0.7522 \\ 0 & 0.2950 & 0.2936 & 0.7522 & 0 \end{bmatrix}$$

Figure 8.20: Transversal matrix with a reflection level of -12.5 dB.

If a cubic cavity is built, it is possible to show these resonant modes by drawing the field pattern at the proper frequencies. Figure 8.21a shows the mode TE_{101} in the triple mode cavity. This is the fundamental mode in the waveguide and it is not necessary any asymmetry to excite it. Thus if the triple mode cavity is segmented with no offset in the coupling windows, only this mode is excited and it is possible to get the required coupling level to this mode by adjusting the aperture of the window.

of seed functions.

[4] As it is known, the number of transmission zeros in a transversal topology of Nth-order is given by $TZ_{\text{Transversal topology}} = N - 1$.

If an offset in the plane YZ is introduced, the mode TM_{110} shown in Figure 8.21b is excited. This is clearly a transversal magnetic mode since TE modes can not have a zero index in the longitudinal component. This mode is not affected by the longitudinal dimension of the cavity since the field components are constant in the Z axis. As a result, the cut-off frequency and the resonant frequency are the same for this mode, thus the coupling to the TM_{110} mode could be slightly difficult to adjust. To overcome this drawback it is necessary to lower the cut-off frequency of the mode TM_{110}. This can be done by increasing the dimensions width and height of the cavity or with an external element such as a screw. Once the right coupling to each mode is achieved, the triple-mode cavity can be set back to its original state, by restoring its dimensions or removing the screws.

Finally, if an offset is introduced in both planes XZ and YZ the mode TE_{011} shown in Figure 8.21c is excited. Similarly to the previous case, this mode can not be a TM mode as TM modes can not have a zero in a transversal index.

Whit regard to the resonant frequency of each mode, it can be adjusted by modifying the dimensions of the triple-mode cavity: width, height and length. In this case, each dimension controls the resonant frequency of two modes within the resonant cavity. Thus the adjustment may be a bit complex. As it can be noticed from Figure 8.21, the height of the cavity has no effect on the mode TE_{101} but it controls the resonant frequency of the modes TM_{110} and TE_{011}. In the same way, the cavity width affects to the modes TE_{101} and TM_{110} meanwhile by modifying the length of the triple-mode cavity it is possible to change the resonant frequency of the modes TE_{101} and TE_{011}.

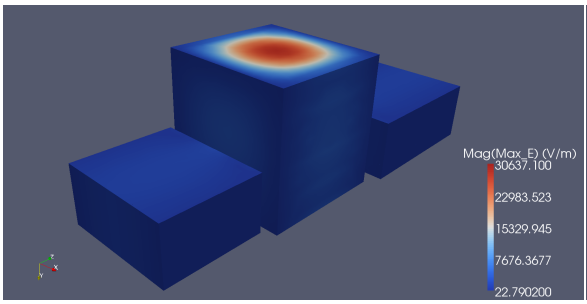

(a) Mode TE_{101}.

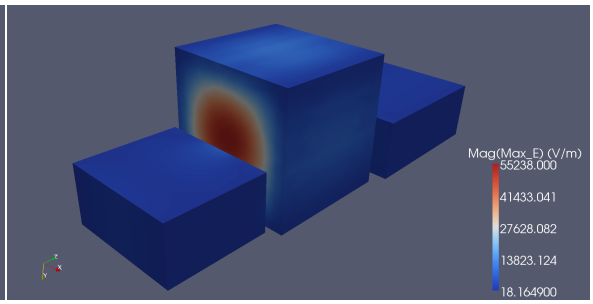

(b) Mode TM_{110}.

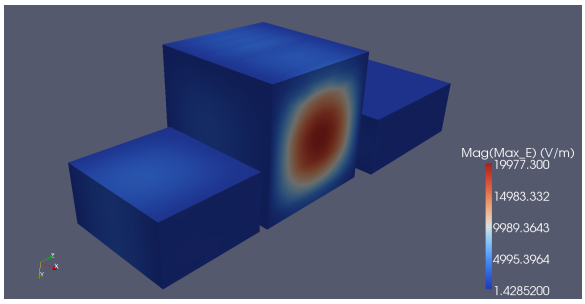

(c) Mode TE_{011}.

Figure 8.21: Field pattern of each resonant mode in the triple-mode cavity.

By performing the design with the matrix shown in Figure 8.20 and by the segmentation strategy outlined before, the response in Figure 8.23a is obtained. This is a third order response with two transmission zeros and it is provided by a one single resonant cavity that has a footprint similar to a single-mode cavity. Thus it is obtained an extremely compact-size structure with the corresponding reductions of volume and mass. Nevertheless, some disadvantages are present that limit the usefulness of the presented structured. Firstly, as it was already known the filter structure in Figure 8.24 can no longer be implemented with all-inductive technology as it is necessary to increase the height of the cavity as well as to introduce offset in both planes. Secondly the spurious-free band is reduced as it can be seen in Figure 8.23b. The natural spurious band of this filter should be at about 5 GHz meanwhile when a triple mode cavity is used, a spurious band appears at the frequency of 4 GHz. Finally, the design range in terms of bandwidth and the maximum distance from the passband of the transmission zeros is reduced when comparing with dual-mode filters.

Table 8.2 lists the dimensions of the structure in Figure 8.24. It should be noted that the structure is symmetric in the YZ plane and antisymmetric in the plane XZ. This antisymmetry is necessary in order to get implement the right sign of the couplings specified by the coupling matrix as the three resonant modes

in the cavity only present one variation in the respective dimensions.

$$M = \begin{bmatrix} 0 & 0.4392 & 0.4379 & -0.8613 & 0 \\ 0.4392 & 1.3884 & 0 & 0 & 0.4392 \\ 0.4379 & 0 & -1.3872 & 0 & 0.4379 \\ -0.8613 & 0 & 0 & -0.0026 & 0.8613 \\ 0 & 0.4392 & 0.4379 & 0.8613 & 0 \end{bmatrix}$$

Figure 8.22: Transversal matrix that provides the target response for the triple-mode filter.

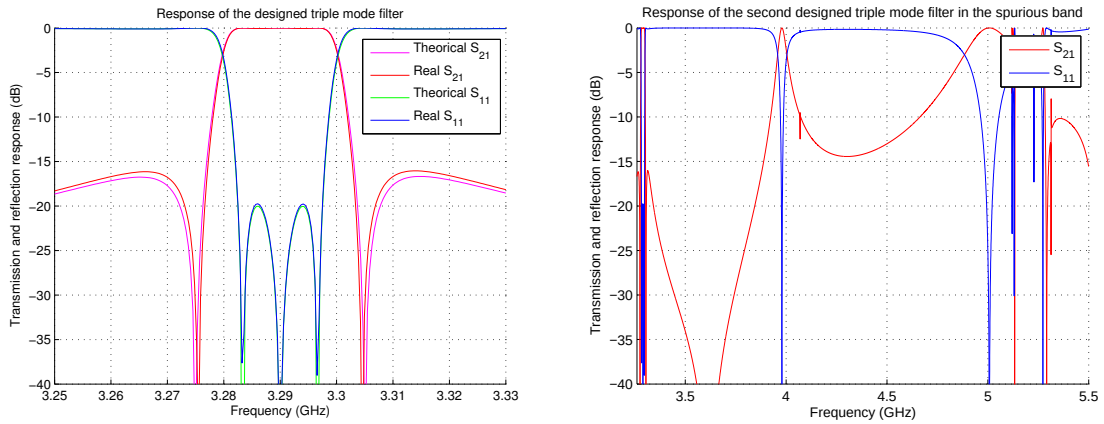

(a) Response in the passband.

(b) Response in the stopband.

Figure 8.23: Response of the designed triple mode filter.

Parameter	Value (mm)	Parameter	Value (mm)	Parameter	Value (mm)	Parameter	Value (mm)
AWG	58.17	BWG	29.083	LWG	50	OFFSET X1	-9.7241
A1	23.5148	B1	21.0332	L1	0.5	OFFSET Y1	-19.5165
A2	62.9887	B2	64.8046	L2	63.1607	OFFSET X2	-9.7241
A3	23.5148	B3	21.0332	L3	0.5	OFFSET Y2	19.5165

Table 8.2: Dimensions of the triple-mode filter.

In this structure the offset in the YZ plane has almost reached its maximum value, thus the bandwidth of the filters with this topology can not be further increased. This is the same drawback as it was faced in chapter 4. The filter bandwidth is limited since in order to have a larger bandwidth it is necessary to increase the aperture of the input and output windows of the filter and then, the offset in this windows is limited. To overcome this drawback, it may be a good idea to implement a topology similar to the one introduced in chapter 6. In this way, the greater input and output couplings can be easily achieved with a single mode cavity meanwhile the inner couplings are much smaller and are easily implemented with the coupling windows of the triple-mode cavity.

8.9.1 Triple-mode filter with input/output single-mode cavities

In this section, a triple-mode filter with input and output single-mode cavities is implemented in order to overcome the limitation on the maximum bandwidth previously discussed. The proposed topology is shown in the Figure 8.25. With this topology a triple-mode filter is implemented. The filter specification are similar to the specifications of the previous example, thus both topologies can be easily compared. This filter is centered at 3.295 GHz and has a bandwidth of 15 MHz and a reflection level of -20 dB. The coupling matrix with this topology that satisfies these specifications is shown in Figure 8.26.

By following the approach presented in chapter 4 it is possible to achieve the fifth-order response shown in Figure 8.27a. It can be noted that this response fits perfectly the specifications of bandwidth and reflection level. In the last design, the advantages of size, mass and reduced footprint were commented. This topology keeps the previous advantages and in addition to that, a good spurious suppression is obtained as it can be seen in Figure 8.27b. Since the triple-mode cavity provide a spurious component at a lower frequency than the single mode cavities, they both are mutually canceled. It should be noted from Figure 8.27b that both

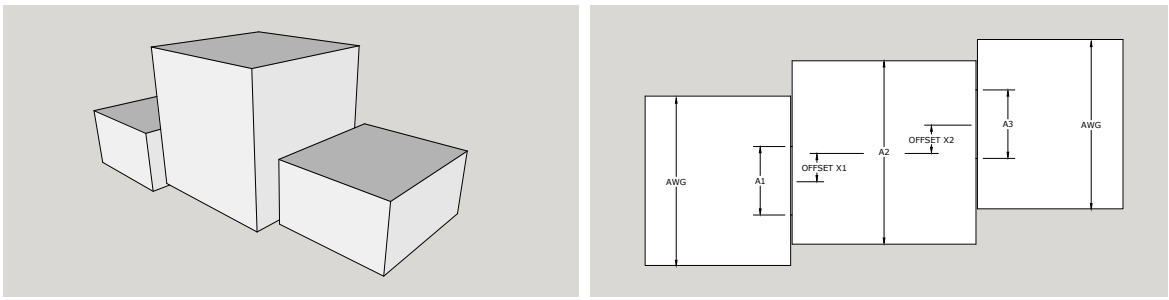

(a) 3D view.

(b) Top view.

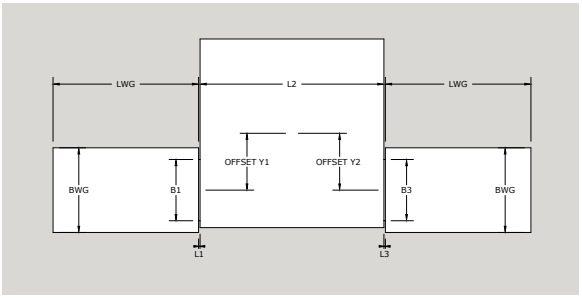

(c) Side view.

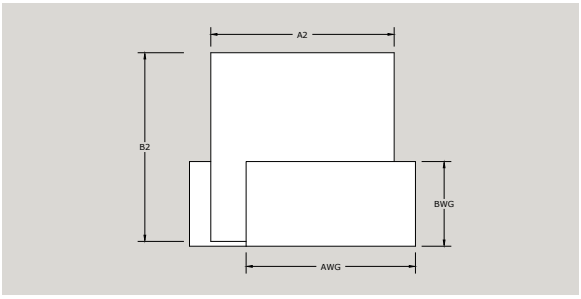

(d) Front view.

Figure 8.24: Structure of the triple mode filter.

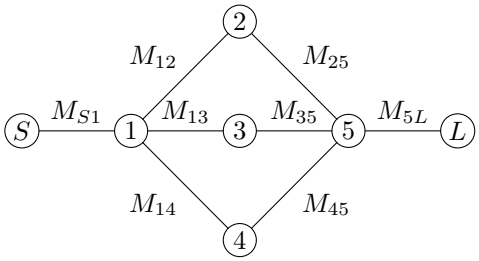

Figure 8.25: Coupling-routing diagram of a fifth order triple-mode filter with input/output single-mode cavities.

$$M = \begin{bmatrix} 0 & 1.0030 & 0 & 0 & 0 & 0 & 0 \\ 1.0030 & -0.0002 & -0.3653 & 0.3649 & 0.6682 & 0 & 0 \\ 0 & -0.3653 & 0.9531 & 0 & 0 & -0.3647 & 0 \\ 0 & 0.3649 & 0 & -0.9531 & 0 & 0.3651 & 0 \\ 0 & 0.6682 & 0 & 0 & 0 & -0.6687 & 0 \\ 0 & 0 & -0.3647 & 0.3651 & -0.6687 & 0.0002 & -1.0030 \\ 0 & 0 & 0 & 0 & 0 & -1.0030 & 0 \end{bmatrix}$$

Figure 8.26: Triple mode matrix with the topology shown in Figure 8.25.

spurious components have a rejection level above 20 dB, the one due to the triple-mode cavity about 4 GHz as well as the common spurious band of the single-mode cavities around 5 GHz. The obtained structure is shown in Figure 8.28 while its dimensions are listed in table 8.3.

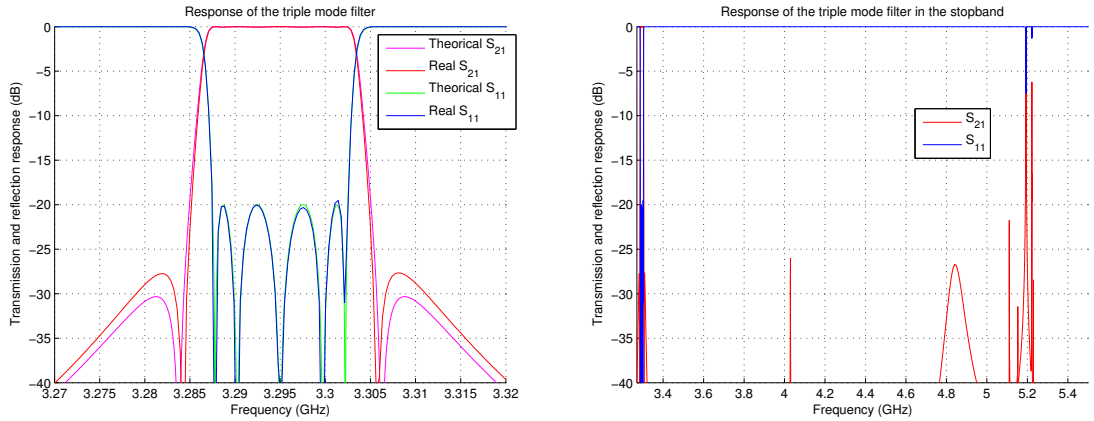

(a) Response in the passband.

(b) Response in the stopband.

Figure 8.27: Response of a triple-mode filter with input/output single-mode cavities.

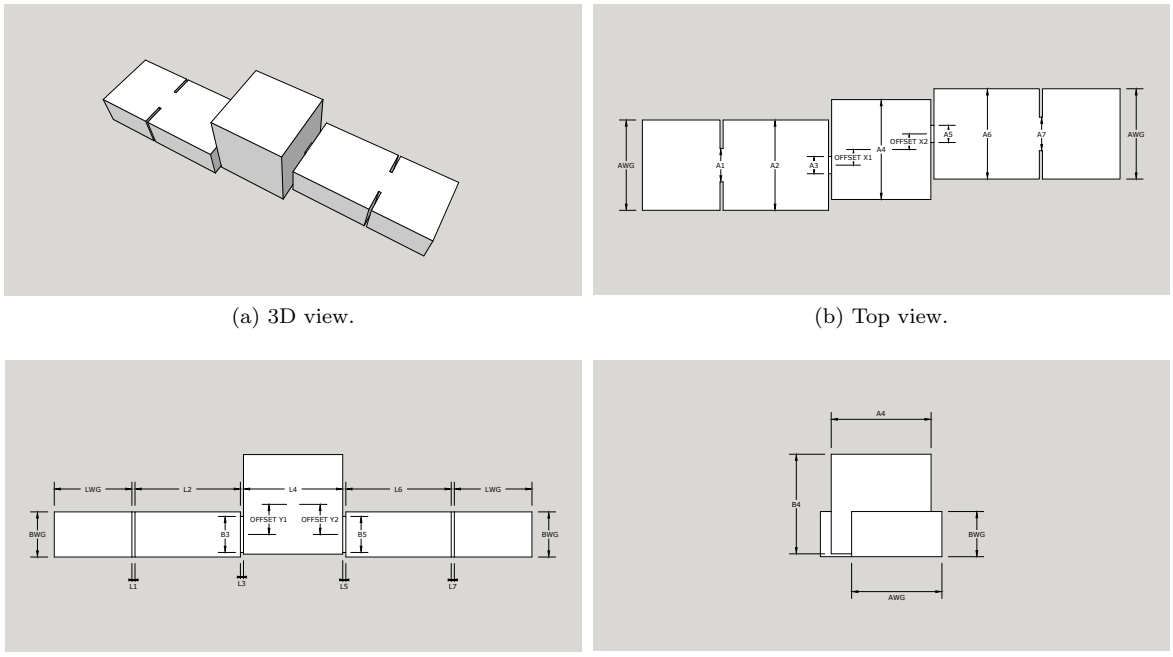

(a) 3D view.

(b) Top view.

(c) Side view.

(d) Front view.

Figure 8.28: Structure of the triple mode filter with input/output single-mode cavities.

Therefore, with this topology it has been possible to obtain a narrow-band filter (about 0.5% of fractional bandwidth) with a good rejection in the stopband using a triple-mode cavity. However it is known that when the filter bandwidth increases, the spurious band gets wider too. Thus, it would be desirable to build a wider bandwidth filter in order to study the behavior of the spurious band. In this context another filter is implemented centered at 3.9 GHz with a bandwidth of 100 MHz and a reflection level in the passband of -20 dB. Thus the fractional bandwidth has been increased from 0.5% to 2.5%. These bandwidth specifications are the same that were used in the filter built in chapter 4. In this way it is possible to show that the same bandwidth can be implemented with both topologies.

This filter is designed as it has been already explained and the resulting response is presented in Figure 8.29a and 8.29b. It can be seen in Figure 8.29a that in this case the specification of bandwidth and reflection level are properly fulfilled but not so the position of the transmission zeros. This is due to the offset limitation.

Parameter	Value (mm)	Parameter	Value (mm)	Parameter	Value (mm)	Parameter	Value (mm)
AWG	58.17	BWG	29.083	LWG	50	OFFSET X1	-10.0584
A1	22.6516	B1	29.083	L1	2	OFFSET Y1	-19.3799
A2	58.17	B2	29.083	L2	68.5960	OFFSET X2	-10.0584
A3	11.0654	B3	23.1937	L3	2	OFFSET Y2	19.3799
A4	64.3260	B4	64.1484	L4	63.9125		
A5	11.0654	B5	23.1937	L5	2		
A6	58.17	B6	29.083	L6	68.5960		
A7	22.6516	B7	29.083	L7	2		

Table 8.3: Dimensions of the triple-mode filter with input/output single-mode cavities.

The structure of this filter is presented in Figure 8.30 and Table 8.4. In this structure almost the maximum offset in both planes XZ and YZ has been applied to the coupling windows of the triple-mode cavity. Thus, this filter with a bandwidth of 100 MHz (2.5% of fractional bandwidth) has about the maximum bandwidth that is implementable with this topology. It can also be noted from the filter structure that the thickness of the coupling windows has been fixed to the minimum manufacturable value namely about $1-2$ mm. In the previous example the coupling windows were 0.5 mm thick. This fact gives an idea of the limitations of these structures.

Finally, with regard to the spurious-free band, when the bandwidth increases, the spurious components are not totally canceled as they were in the previous example. Now the spurious band due to the single-mode cavity appears still at about 6 GHz. Thus the spurious-free band has not been increased in comparison to an in-line filter. Moreover the spurious components due to the triple-mode cavity are not totally suppressed. It can be observed in Figure 8.29b that two peaks appear between 4.5 GHz and 5 GHz.

In summary, it would be desirable to find new coupling structures that provides stronger couplings to the modes within the triple-mode cavity. In this way the aperture of the coupling windows would be decreased and more offset range would be available. Furthermore, it could be necessary to overcome the drawback of the spurious-free band. For instance, by adding some elements to the cavity structure to modify the frequency of the spurious component it would be possible to use the transmission zeros in the spurious bands to cancel the spurious frequencies. This is the same idea that was used in in-line filters in order to cancel the spurious components by using the transmission zeros of the dual-mode cavities.

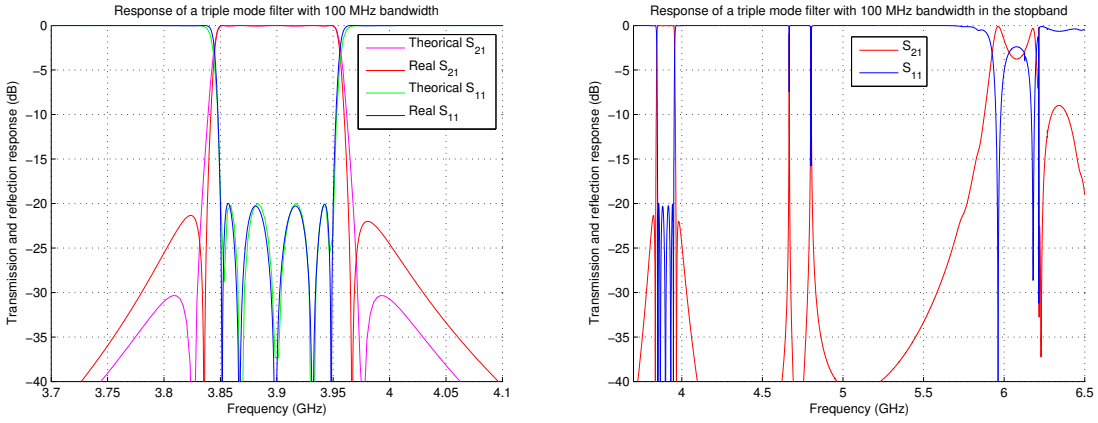

(a) Response in the passband.

(b) Response in the stopband.

Figure 8.29: Response of a triple-mode filter with 100 MHz bandwidth.

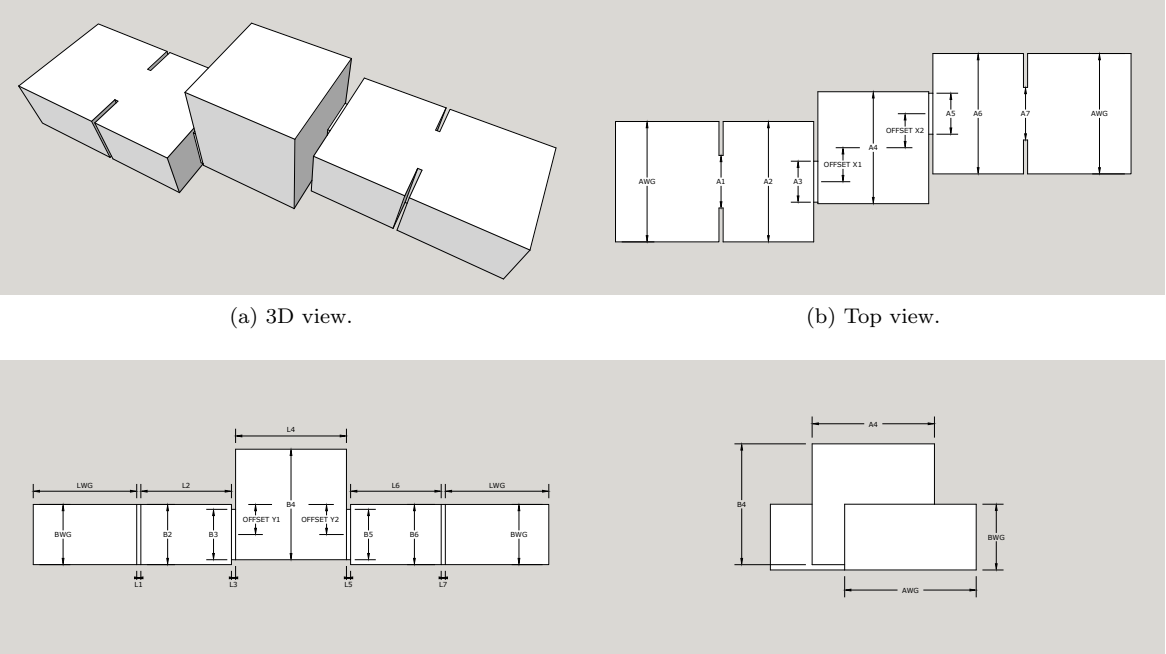

(a) 3D view.

(b) Top view.

(c) Side view.

(d) Front view.

Figure 8.30: Structure of the triple mode filter with 100 MHz bandwidth.

Parameter	Value (mm)	Parameter	Value (mm)	Parameter	Value (mm)	Parameter	Value (mm)
AWG	58.17	BWG	29.083	LWG	50	OFFSET X1	-16.4255
A1	25.4069	B1	29.083	L1	2	OFFSET Y1	-14.5205
A2	58.17	B2	29.083	L2	43.7790	OFFSET X2	-16.4255
A3	19.8113	B3	24.3380	L3	2	OFFSET Y2	14.5205
A4	54.0939	B4	53.4283	L4	53.5744		
A5	19.8113	B5	24.3380	L5	2		
A6	58.17	B6	29.083	L6	43.7790		
A7	25.4069	B7	29.083	L7	2		

Table 8.4: Dimensions of the triple-mode filter with 100 MHz bandwidth.

Appendix

A

SYNTHESIS OF THE CHEBYSHEV FILTER FUNCTION

Here is a brief review of the transmission and reflection polynomials of a Chebyshev response. Moreover, it is discussed how to obtain these polynomials from the desired specifications of the LPP namely the filter bandwidth, the reflection level in the passband and the position of the transmission and reflection zeros [Cameron et al., 2007, Mendoza, 2006].

The reflection and transmission coefficients can be expressed as a polynomial ratio.

$$S_{11} = \frac{F(s)}{\epsilon_R E(s)} \tag{A.1}$$

$$S_{21} = \frac{P(s)}{\epsilon E(s)} \tag{A.2}$$

where $s = \sigma + j\omega$ is the Laplace complex variable composed by both real and imaginary parts. This imaginary part $\omega = 2\pi f$ is the real normalized frequency in rad/s used with the lowpass filter prototype (LPP).

In these expressions (A.1) and (A.2):

- The polynomial $P(s)/\epsilon$ defines the transmission zeros at finite frequencies (n_{fz}) while the polynomial $E(s)$ defines the filter order (N). It can be demonstrated that:

  1. The numerator of $S_{21}(s)$ ($P(s)$) must have zeros that are purely imaginary or paraconjugate pairs[1].
  2. The maximum number of finite transmission zeros (n_{fz}) in a coupling structure is given by the total number of resonators (N) minus the minimum number of resonator between the input and the output of the coupling network.

- Finally, the constants ϵ_R and ϵ are used to normalize the polynomials $P(s)$ and $F(s)$ in order to obtain a constant ripple level in the edges of the passband.

$$S_{21}(s)|_{s=\pm j} = \sqrt{(10^{-RL/10}) - 1} \tag{A.3}$$

Next, the computation of these polynomials is reviewed more in detail.

A.1 Determination of P(s)

The numerator polynomial of S_{21} ($P(s)$) is given by the desired positions of the finite transmission zeros in the complex plane.

$$P(s) = \prod_{n=1}^{n_{fz}} (s - s_n)\, s_n \tag{A.4}$$

[1] The term "paraconjugate pairs" refers to a pair of zeros that are mirror-image about the imaginary axis. The paraconjugate of a complex function F(s) can be defined as $\tilde{F}(s) \triangleq F^*(-s)$. Thus the paraconjugate of $s = \sigma + j\omega$ is $\tilde{s} = -\sigma + j\omega$

A.2 Determination of F(s)

From equations (A.1) and (A.2):

$$S_{21}^2 = \frac{P^2(s)}{\epsilon^2 E^2(s)} = \frac{P^2(s)}{\epsilon^2 \left(\frac{F^2(s)}{\epsilon_R^2 S_{11}^2}\right)} = \frac{P^2(s)}{\epsilon^2 \left(\frac{F^2(s)}{\epsilon_R^2 (1-S_{21}^2)}\right)} \tag{A.5}$$

$$S_{21}^2(s)\left(1 + \frac{\epsilon_R^2 P^2(s)}{\epsilon^2 F^2(s)}\right) = \frac{\epsilon_R^2 P^2(s)}{\epsilon^2 F^2(s)} \tag{A.6}$$

$$S_{21}^2(s) = \left(1 + \frac{\epsilon^2 F^2(s)}{\epsilon_R^2 P^2(s)}\right)^{-1} \tag{A.7}$$

At this point it is possible to introduce the Chebyshev filtering function of Nth-degree namely $C_N(s)$.

$$k \cdot C_N(s) = \frac{F(s)}{P(s)} = \cosh\left[\sum_{n=1}^{N} \operatorname{arccosh}\left(x_n(s)\right)\right] \tag{A.8}$$

$$x_n(s) = \frac{s - 1/s_n}{1 - 1/s_n} \tag{A.9}$$

where k is a constant used to normalize the highest degree coefficient of $C_N(s)$ to 1.

Figure A.1 shows the Chebyshev function with three transmission zeros at $s = j\infty$. In this case with all transmission zeros at infinity, the pure Chebyshev function is obtained. It can be seen that the pure Chebyshev function satisfies the condition $|C_N(s)| \leq 1$ in the imaginary axis between $s = -j$ and $s = j$.

$$C_N(s)\|_{s\to\infty} = \cosh\left[N \cdot \operatorname{arccosh}(s)\right] \tag{A.10}$$

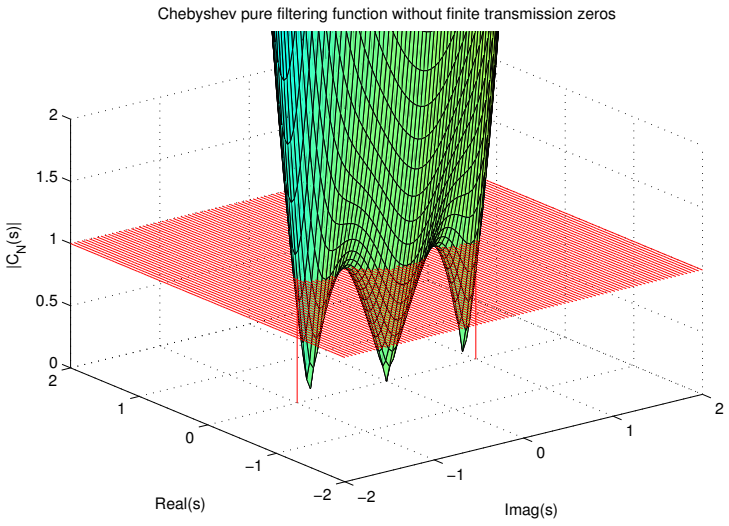

Figure A.1: Chebyshev function with 3 transmission zeros at $s = j\infty$.

Similarly, the generalized Chebyshev filtering function can be computed with finite transmission zeros. Here, it is important to consider the above introduced conditions related to the number and position of the finite transmission zeros.

1. $n_{fz} = N$ – "Minimum number of resonators between the input and the output in the filter network"
2. All zeros must be purely imaginary or mirror-image pairs about the imaginary axis.

Figure A.2 shows the generalized Chebyshev filtering function when a pair of complex transmission zeros is considered. In this example there are four transmission zeros, two of them at $s = \pm j\infty$ and a pair of complex mirror-image zeros at $s = \pm 2$. It can be noted from Figure A.2 that the above said condition $(|C_N(s)| \leq 1\|_{s\in[-j\omega,+j\omega])}$ is not satisfied in the whole bandpass due to the effect of having transmission zeros quite close to the passband.

Since $C_N(s) = \frac{F(s)}{P(s)}$, the poles of $C_N(s)$ are the roots of $P(s)$ meanwhile the zeros of $C_N(s)$ are the roots of $F(s)$. Thus, in order to get the expression of the polynomial $F(s)$ it is necessary to obtain the roots of the numerator of $C_N(s)$.

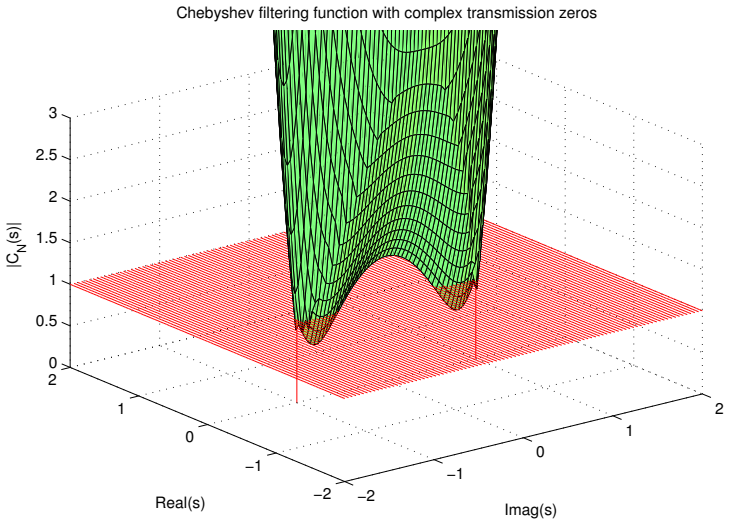

Figure A.2: Chebyshev function with 4 transmission zeros at $s = j\infty$, $s = -j\infty$, $s = 2$ and $s = -2$.

Firstly, it is possible to consider the next definition of the *arccosh* function.

$$\operatorname{arccosh}(x) = \ln\left(x + \sqrt{x^2 - 1}\right) \tag{A.11}$$

Then $C_N(s)$ can be expressed in the following form:

$$C_N(s) = \cosh\left[\sum_{n=1}^{N} \ln(a_n + b_n)\right] \tag{A.12}$$

where

$$a_n = x_n(s) = \frac{s - 1/s_n}{1 - s/s_n} \tag{A.13}$$

$$b_n = \sqrt{x_n^2(s) - 1} = \frac{\sqrt{(s - 1/s_n)^2 - (1 - s/s_n)^2}}{1 - s/s_n} = \frac{\sqrt{(s^2 - 1)(1 - 1/s^2)}}{1 - s/s_n^2} \tag{A.14}$$

If the transformed frequency variable $s' = \sqrt{s^2 - 1}$ is defined, the expression for b_n remains:

$$b_n = \frac{s'\sqrt{1 - 1/s^2}}{1 - s/s_n} \tag{A.15}$$

Then, introducing the definition of the function cosh:

$$C_N(s) = \frac{1}{2}\left[e^{\sum \ln(a_n + b_n)} + e^{-\sum \ln(a_n + b_n)}\right] = \frac{1}{2}\left[\prod_{n=1}^{N}(a_n + b_n) + \frac{1}{\prod_{n=1}^{N}(a_n + b_n)}\right] \tag{A.16}$$

By multiplying the second term top and bottom by $\prod_{n=1}^{N}(a_n - b_n)$ and introducing the expressions for a_n and b_n we obtain:

$$C_N(s) = \frac{1}{2}\left[\prod_{n=1}^{N}\left(x_n(s) + \sqrt{x_n^2(s) - 1}\right) + \prod_{n=1}^{N}\left(x_n(s) - \sqrt{x_n^2(s) - 1}\right)\right] \tag{A.17}$$

$$C_N(s) = \frac{1}{2}\left[\frac{\prod_{n=1}^{N}\left((s - 1/s_n) + s'\sqrt{1 - 1/s_n^2}\right) + \prod_{n=1}^{N}\left((s - 1/s_n) - s'\sqrt{1 - 1/s_n^2}\right)}{\prod_{n=1}^{N}(1 - s/s_n)}\right] \tag{A.18}$$

Finally, it is possible to obtain the equation (A.21) by defining two new expressions namely c_n and d_n.

$$c_n = (s - 1/s_n) \tag{A.19}$$

$$d_n = s'\sqrt{1 - 1/s_n^2} \tag{A.20}$$

Then

$$C_N(s) = \frac{F(s)}{P(s)} = \frac{1}{2}\left[\frac{\prod_{n=1}^{N}(c_n + d_n) + \prod_{n=1}^{N}(c_n - d_n)}{\prod_{n=1}^{N}(1 - s/s_n)}\right] \tag{A.21}$$

With the expression of $C_N(s)$ in the form (A.21) it is easy to be noted that the denominator of $C_N(s)$ is the polynomial $P(s)$. Thus, to obtain the expression for $F(s)$ it is necessary to find the roots of the numerator of $C_N(s)$.

The numerator of $C_N(s)$ is composed of two terms namely:

$$Num\left[C_N(s)\right] = \frac{1}{2}\left[G_N(s) + G'_N(s)\right] \tag{A.22}$$

$$G_N(s) = \prod_{n=1}^{N}(c_n + d_n) \tag{A.23}$$

$$G'_N(s) = \prod_{n=1}^{N}(c_n - d_n) \tag{A.24}$$

From $G_N(s)$ and $G'_N(s)$ it is possible to obtain the roots of the numerator of $C_N(s)$ by using a recursive technique starting from the transmission zero s_1 and by proceeding as described in (A.25) and (A.26). Each of these polynomials can be rewrite in terms of other two subpolynomials $U(s)$ and $V(s,s')$ where $U(s)$ is a function of the s variable meanwhile $V(s,s')$ contains the variable s' as well.

$$G_N(s,s') = U_N(s) + V_N(s,s') \tag{A.25}$$

$$G'_N(s,s') = U'_N(s) + V'_N(s,s') \tag{A.26}$$

Then, by grouping the terms with only the variable s in the polynomials $U_N(s)$ and $U'_N(s)$ and the terms with the variable s' in $V_N(s,s')$ and $V'_N(s,s')$, the following polynomials are obtained [2]:

$$U_N(s) = u_0 + u_1 s + u_2 s^2 + \cdots + u_N s^N \tag{A.27}$$

$$V_N(s,s') = s'\left(v_0 + v_1 s + v_2 s^2 + \cdots + v_N s^N\right) \tag{A.28}$$

$$U'_N(s) = u'_0 + u'_1 s + u'_2 s^2 + \cdots + u'_N s^N \tag{A.29}$$

$$V'_N(s,s') = -s'\left(v'_0 + v'_1 s + v'_2 s^2 + \cdots + v'_N s^N\right) \tag{A.30}$$

Consequently, $U_N(s) = U'_N(s)$ and $V_N(s,s') = -V'_N(s,s')$. Thus, the terms $V_N(s,s')$ and $V'_N(s,s')$ which contain the variable s' will be canceled.

$$Num\left[C_N(s)\right] = \frac{1}{2}\left[G_N(s) + G'_N(s)\right] = \frac{1}{2}\left[\left(U_N(s) + U'_N(s)\right) + \left(V_N(s,s') + V'_N(s,s')\right)\right] = U_N(s) \tag{A.31}$$

As a result, the polynomial $F(s)$ can be developed from the equation (A.22) by considering the terms related to $U_N(s)$.

$$F(s) = U(s) \tag{A.32}$$

A.3 Determination of the constants ϵ and ϵ_R

The constants ϵ and ϵ_R shown in Figures A.2 and A.1 are used to normalized the transmission and reflection coefficients respectively. At a result, it is possible to obtain the desired equiripple level within the passband. In this stage it is necessary to distinguish between two different cases.

On the one hand, in fully canonical networks, where all the transmission zeros are located at finite frequencies ($nfz = N$), it is possible to apply the energy conservation condition at $s = j\infty$.

$$|S_{11}|^2 + |S_{21}|^2 = 1 \tag{A.33}$$

$$S_{11}(j\infty)S_{11}(j\infty)^* + S_{21}(j\infty)S_{21}(j\infty)^* = 1 \tag{A.34}$$

$$\frac{F(j\infty)F(j\infty)^*}{\epsilon_R^2 E(j\infty)E(j\infty)^*} + \frac{P(j\infty)P(j\infty)^*}{\epsilon^2 E(j\infty)E(j\infty)^*} = 1 \tag{A.35}$$

Considering that all $E(s)$, $F(s)$ and $P(s)$ are $Nth-degree$ polynomials with the highest-power coefficients equal to unity, the following relations between ϵ and ϵ_R are obtained.

$$\frac{1}{\epsilon_R^2} + \frac{1}{\epsilon^2} = 1 \tag{A.36}$$

$$\epsilon_R = \frac{\epsilon}{\sqrt{\epsilon^2 - 1}} \tag{A.37}$$

[2] It should be noted that $s' \cdot V'_N(s,s') = (s^2 - 1)\cdot\left(v_0 + v_1 s + v_2 s^2 + \cdots + v_N s^N\right)$ only depends on the variable s. Thus it will belong to the polynomial $U(s)$

where ϵ_R and ϵ correspond to the return losses and the transmission losses respectively at infinity.

$$S_{21}(j\infty) = \frac{1}{\epsilon} = 20\log_{10}\epsilon \ dB \tag{A.38}$$

$$S_{11}(j\infty) = \frac{1}{\epsilon_R} = 20\log_{10}\epsilon_R \ dB \tag{A.39}$$

On the other hand, if $n_{fz} < N$ then there is at least one transmission zero at infinity ($s = j\infty$). In this case $|S_{21}(j\infty)| = 0$ and $|S_{11}(j\infty)| = 1$. Thus, ϵ_R must be equal to 1.

$$|S_{11}(j\infty)|^2 = \frac{1}{\epsilon_R^2} \cdot \left|\frac{F(j\infty)}{E(j\infty)}\right|^2 = 1 \tag{A.40}$$

$$\epsilon_R = 1 \tag{A.41}$$

Given the above expressions for ϵ_R, the constant ϵ can be obtained by setting the insertion losses to the ripple level in the edges of the passband ($s = \pm j$).

$$\left|\frac{S_{21}(s)}{S_{11}(s)}\right|^2_{s=\pm j} = \left|\frac{\epsilon_R P(s)}{\epsilon F(s)}\right|^2_{s=\pm j} = \sqrt{10^{RL/10} - 1} \tag{A.42}$$

$$\epsilon = \frac{1}{\sqrt{10^{RL/10} - 1}} \cdot \left|\frac{\epsilon_R P(s)}{F(s)}\right|_{s=\pm j} \tag{A.43}$$

A.4 Determination of E(s)

Once the polynomials $P(s)$ and $F(s)$ are known, the polynomial $E(s)$ can be obtained by the alternating singularity principle. Starting from the energy conservation equation and introducing the expressions (A.1) and (A.2) it is possible to obtain the expression of $E(s) \cdot E(s)^*$.

$$|S_{11}|^2 + |S_{21}|^2 = 1 \tag{A.44}$$

$$S_{11} \cdot S_{11}^* + S_{21} \cdot S_{21}^* = 1 \tag{A.45}$$

$$\left(\frac{F(s)}{\epsilon_R E(s)}\right) \cdot \left(\frac{F(s)}{\epsilon_R E(s)}\right)^* + \left(\frac{P(s)}{\epsilon E(s)}\right) \cdot \left(\frac{P(s)}{\epsilon E(s)}\right)^* = 1 \tag{A.46}$$

$$\frac{1}{\epsilon_R^2}\left(F(s) \cdot F(s)^*\right) + \frac{1}{\epsilon^2}\left(P(s) \cdot P(s)^*\right) = E(s) \cdot E(s)^* \tag{A.47}$$

This polynomial $E(s)$ will be the denominator of both the transmission coefficient (S_{21}) and the reflection coefficient (S_{11}) and its roots mush satisfy the Hurwitz condition [Matthaei and Yones, 1980]. This means that the roots of $E(s)$ must be in the semiplane of s with $\sigma < 0$ in order for the network to be stable. Since the result of $E(s) \cdot E(s)^*$ must be a scalar, the roots of $E(s) \cdot E(s)^*$ must form paraconjugate pairs, this means symmetrically arranged about the imaginary axis. Thus the solutions in the semiplane $\sigma < 0$ will be the roots of $E(s)$ meanwhile the roots in the semiplane $\sigma > 0$ will belong to $E(s)^*$.

The presented method to obtain the polynomial $E(s)$ is completely generic. However it involves working with a polynomial of degree twice the degree of $E(s)$ since the expression of $E(S) \cdot E(s)^*$ is computed. This fact leads to a low precision as the roots of $E(S) \cdot E(s)^*$ will be closer to $\pm j$. To overcome this drawback another method exist due to "Rhodes & Alseyab" that determines the roots of $E(s)$ by alternative transformations without having to deal with polynomials of $2\cot N$ degree. In this way the obtained roots are a little further from $\pm j$ and a higher precision is achieved. This technique can be reviewed in [Cameron et al., 2007, Mendoza, 2006].

A.5 Examples

Here are some examples of filter prototype responses obtained by the Chebyshev synthesis. All responses have four transmission poles and a reflection level of $-30\ dB$. However the first example shown in Figure A.3 have no transmission zeros, the response in Figure A.4 have a single transmission zero at $s = 1.5j$. Similarly, the response shown in Figure A.5 have a complex pair of transmission zeros at $s = \pm 2$. Finally, in the response from the Figure A.6 a pair of transmission zeros with both real and imaginary parts have been considered at $s = -0.5 + 1.5j$ and $s = 0.5 + 1.5j$. The interest of having complex transmission zeros comes from the possibility of obtain a equalized group delay in the passband at the expense of a lower rejection in the stopband. This issue can be achieved by placing complex pairs of transmission zeros within the passband (with a complex part $-1 < \omega < 1$) as it has been done in Figure A.4.

Figures A.3a, A.4a, A.5a and A.6a show the module of the filter response (S_{21}) in the complex plane measured in dB meanwhile a detailed view of these responses in the semiplane $\sigma < 0$ is shown in Figures

A.3b, A.4b, A.5b and A.6b. Figures A.3c, A.4c, A.5c and A.6b show the phase response of each filter in the semiplane $\sigma < 0$. The plots in Figures A.3d, A.3d, A.4d, A.5d and A.6d represent the group delay of the correspondent filter in the complex plane. The group delay has been obtained in the complex plane by differentiating the phase response with respect to the s variable in the direction $\overrightarrow{s} = j$. The 2D-cut in the complex axis ($s = j\omega$) of the group delay surface is shown in Figures A.3f, A.4f, A.5f and A.6f. Finally Figures A.3e, A.4e, A.5e and A.6e correspond to the "zero-pole" diagram in each case.

These examples show the position of the transmission and reflection zeros in the complex plane. Moreover it is possible to notice how the poles of both functions (the roots of the polynomial $E(s)$) are located in the semiplane with ($\sigma = Real(s) < 0$) to satisfy the Hurwitz condition. Due to the presence of these poles, in the semiplane with $\sigma > 0$ the filter parameters S_{21} and S_{11} are below 0 dB whereas in the semiplane with $\sigma < 0$ the filter parameter are greater than 0 dB. In addition, the position of the poles is directly related with the quality factor Q of the filter. The presented examples have been obtained by taking $Q_u = \infty$. However, in a filter response with a finite Q_u the poles of the transfer function that appear in the semiplane with $Real(s) < 0$ would be shifted to greater values of σ. At this point it is important to assure that the poles of the transfer function remain in the semiplane with a real part of s lower than zero in order to satisfy the Hurwitz condition.

Another interesting effect is the fact that the poles of both functions and the reflection zeros are affected by the transmission zeros. This effect can be observed in the "zero-polo" diagrams presented. In Figures A.4e and A.6e the poles near the transmission zero have been shifted closer to the passband whereas the poles in the other side of the passband get further from the transmission zero and from the passband as well. As a result the filter selectivity is increased in the side of the passband where the transmission zeros are closer to while on the opposite side of the passband the selectivity is lowered. In Figure A.5e, the transmission zeros are complex zeros in the middle of the passband ($s = \pm 2$) (it should be noted that this position is more distant from the passband than the natural position of the poles). Thus the poles in the middle of the passband get closer to the complex axis (to greater values of σ) meanwhile the poles near to the edges of the bandpass go away from the complex axis ($s = j\omega$). As a result the selectivity is decreased in both edges of the passband.

However this fact can be used to obtain a plain group delay within the passband. The issue is that the group delay is singular in the poles of the transfer function and in the transmission zeros. As it is shown in Figure A.3e, the first and last poles are closer to the axis $s = j\omega$. Then the group delay varies too fast due to the proximity of this poles. It can be noticed the maximum values of the group delay shape in Figure A.3f at the frequencies where the zeros in Figure A.3e are located closer to the passband. If we introduce a pair of complex transmission zeros in the middle of the passband, these poles are shifted further from the axis $s = j\omega$ and then the group delay is less affected by these poles. In addition, the poles near the transmission zero (the second and third pole in Figure A.3e) get closer to the complex axis ($s = j\omega$). Thus the central part of the group delay shape is affected and a flat group delay is obtained within a considerable range in the passband as it is shown in Figure A.4f.

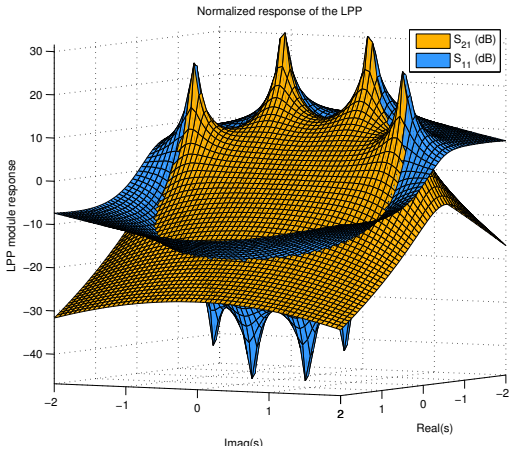

(a) Module (global view).

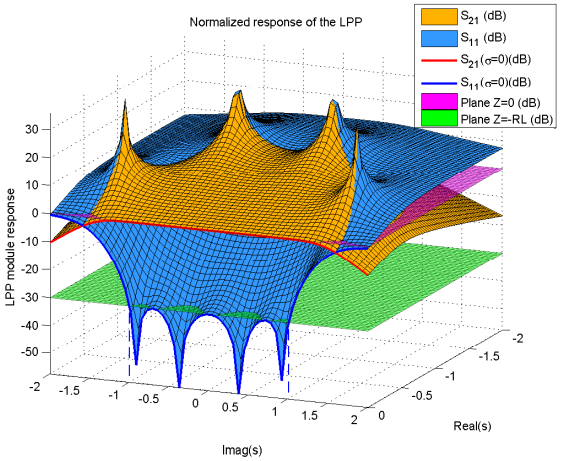

(b) Module (view of the semiplane $\sigma < 0.$).

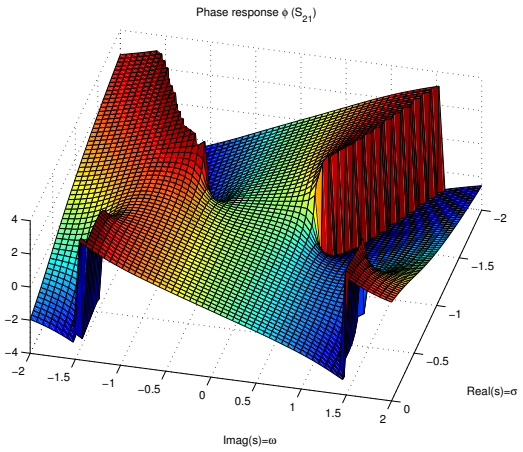

(c) Phase response.

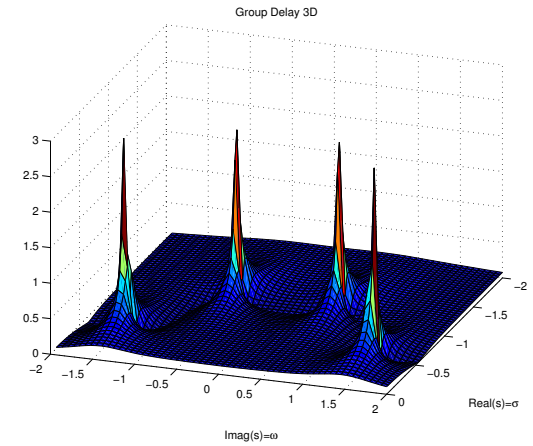

(d) Group delay.

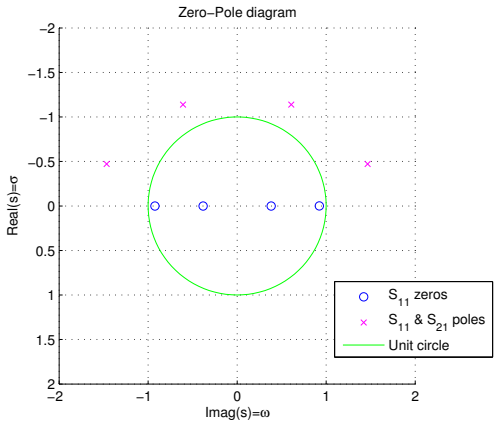

(e) Zero-pole diagram.

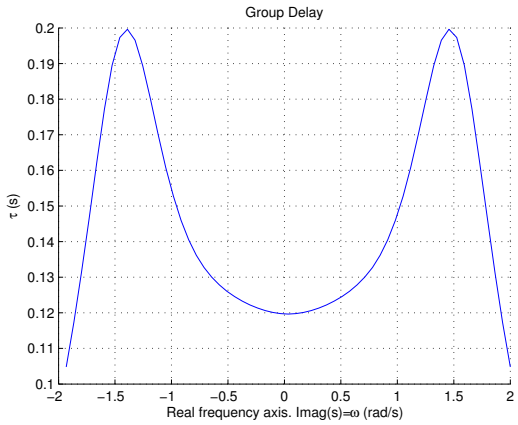

(f) Group delay.

Figure A.3: LPP fourth-orden response without transmission zeros.

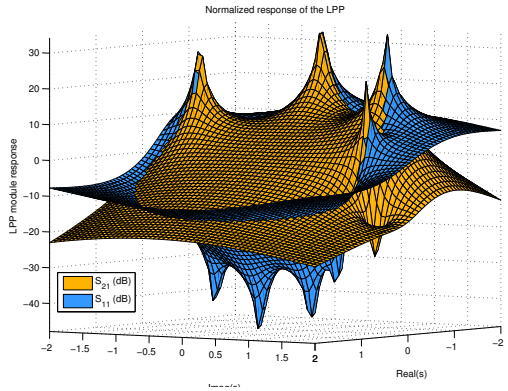

(a) Module (global view).

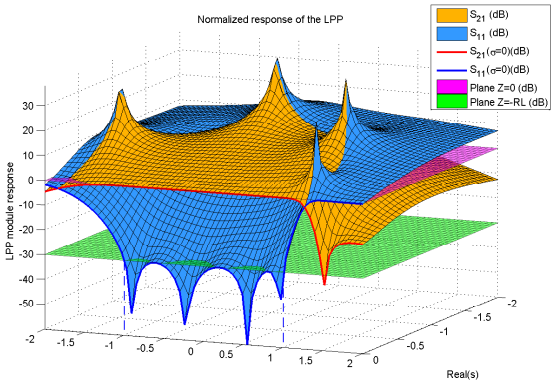

(b) Module (view of the semiplane $\sigma < 0$.).

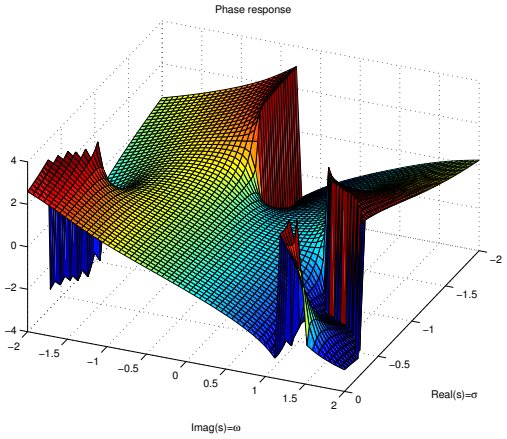

(c) Phase response.

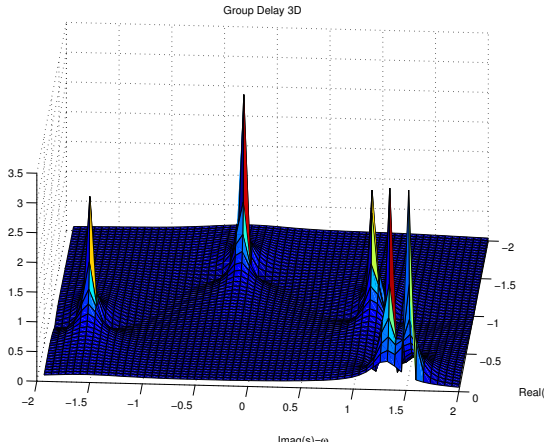

(d) Group delay.

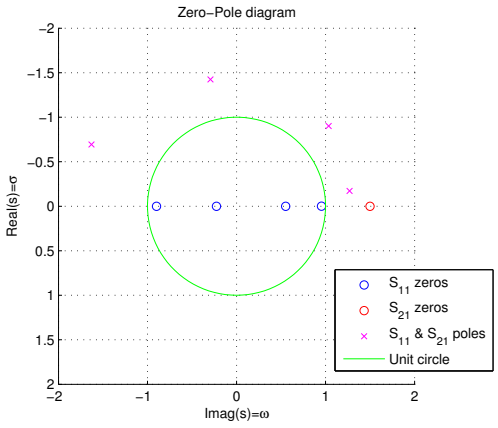

(e) Zero-pole diagram.

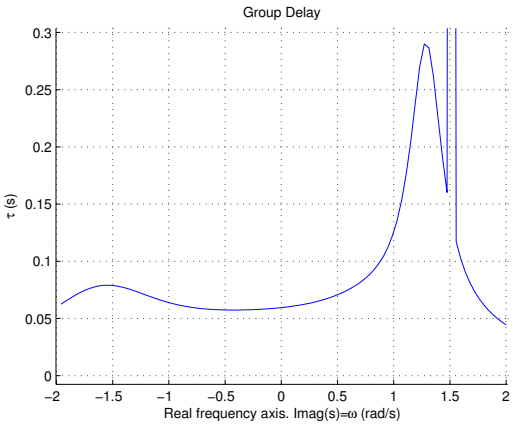

(f) Group delay.

Figure A.4: LPP fourth-orden response with a transmission zero at $s = 1.5j$.

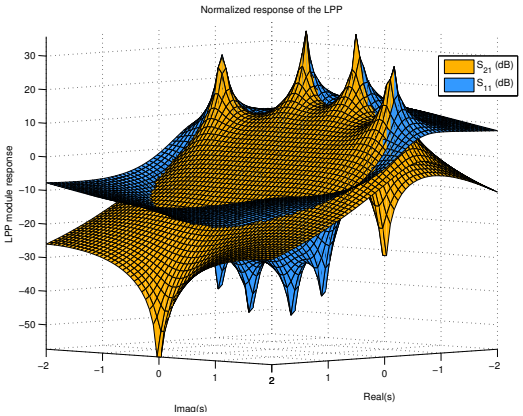

(a) Global view.

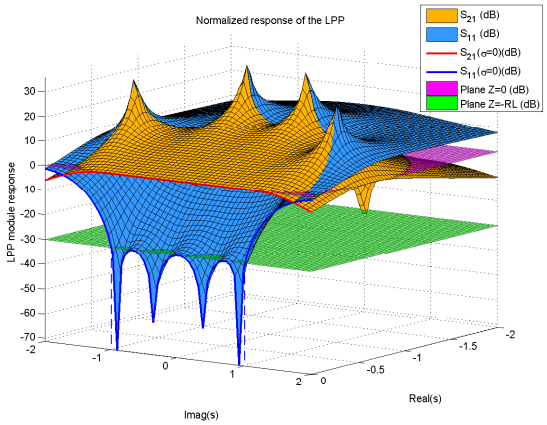

(b) View of the semiplane $\sigma < 0$.

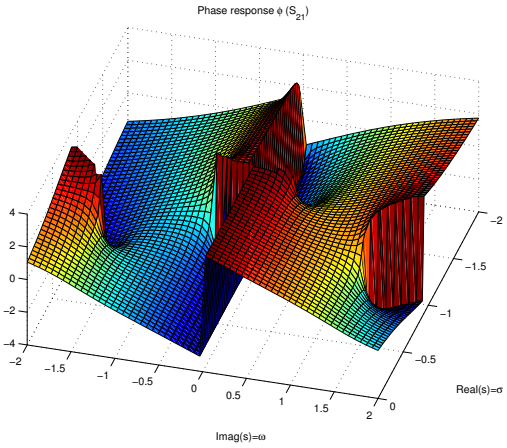

(c) Phase response.

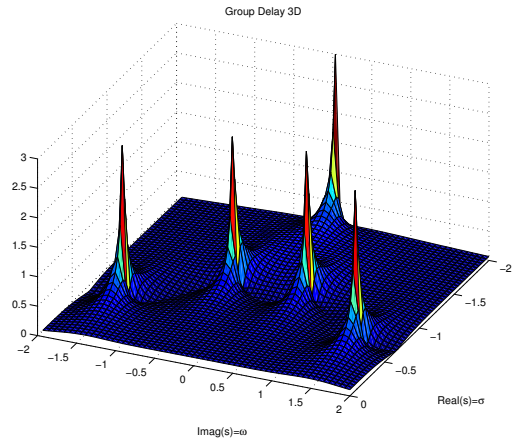

(d) Group delay.

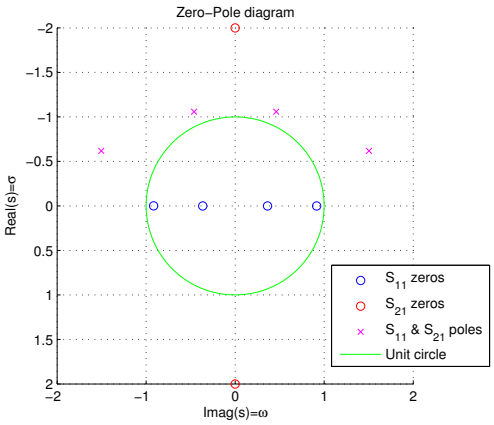

(e) Zero-pole diagram.

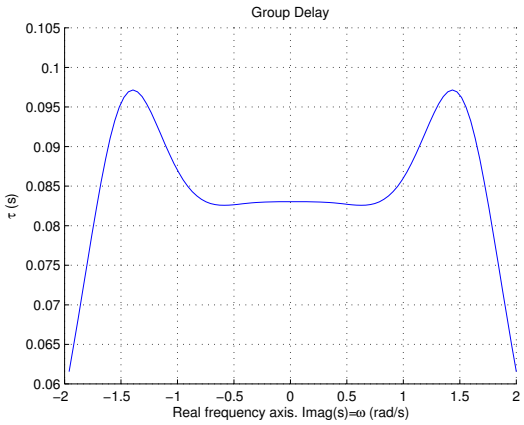

(f) Group delay.

Figure A.5: LPP fourth-orden self-equalized response with two transmission zeros at $s = \pm 2$.

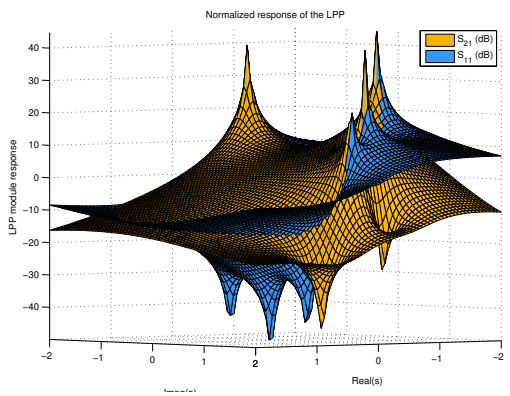

(a) Global view.

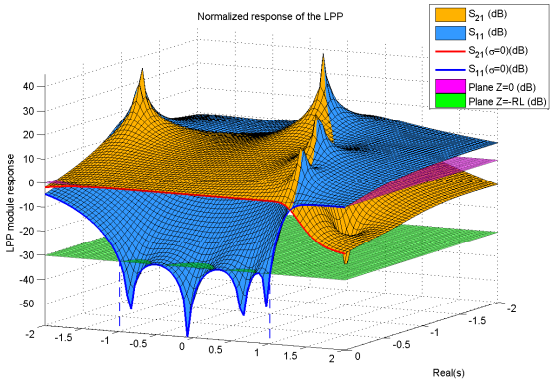

(b) View of the semiplane $\sigma < 0$.

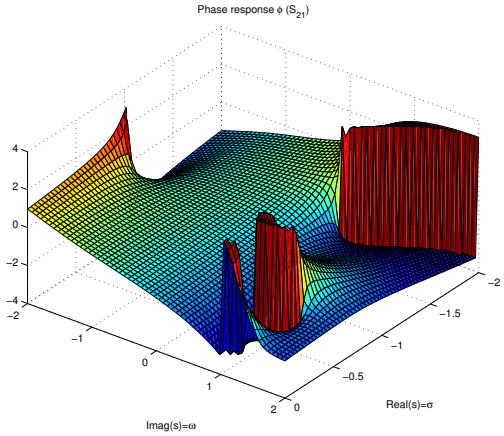

(c) Phase response.

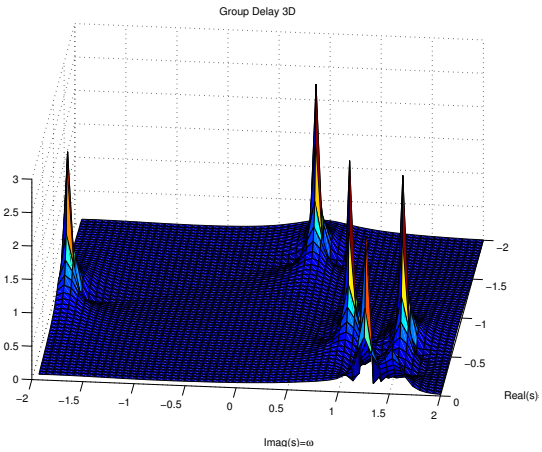

(d) Group delay.

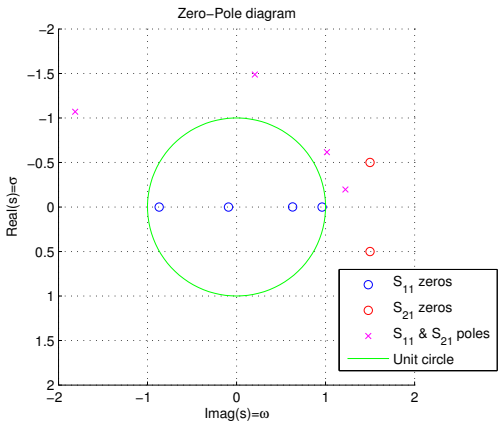

(e) Zero-pole diagram.

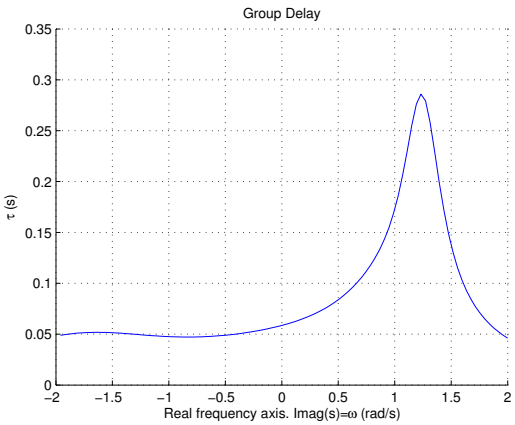

(f) Group delay.

Figure A.6: LPP fourth-orden response with two transmission zero at $s = \pm 0.5 + 1.5j$.

B

ELECTROMAGNETIC SIMULATION SOFTWARE

All simulations and optimizations in this work have been performed by using the electromagnetic simulation software FEST3D whose interface is shown in Figure B.1. The simulation algorithm of this software is based on an integral equation technique combined with the method of moments.

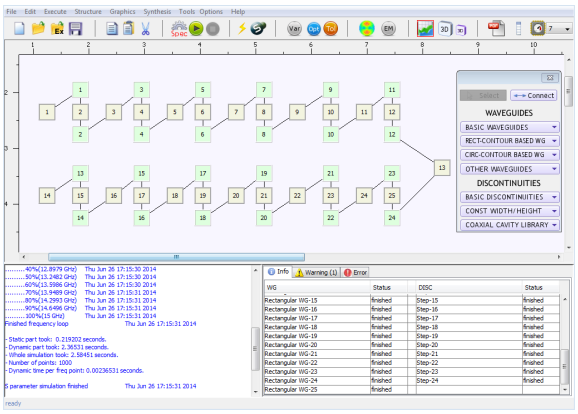

(a) Design interface.

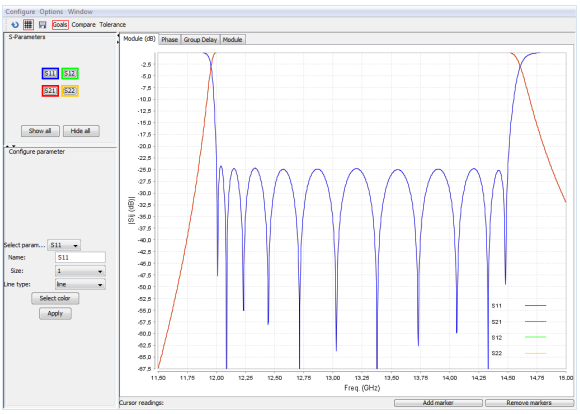

(b) S-parameters view.

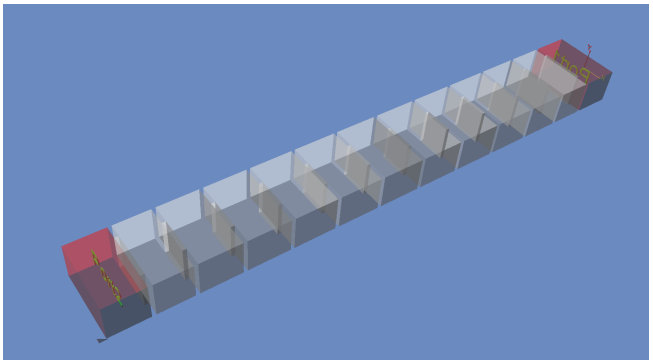

(c) Integrated 3D view.

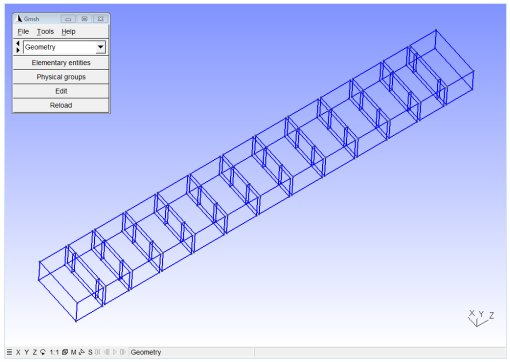

(d) 3D view with Gmsh.

Figure B.1: Interface of FEST3D software used in this work.

By using integral equation techniques, this software is able to analyze complex microwave devices based on predefined component such as rectangular waveguide quite faster than softwares based on mode-matching techniques.

Due to the above advantage and also since all devices designed in this work are formed by rectangular waveguides, an important decrease of the time spent as well as of the cpu and memory required for the filter designs is achieved through this software.

B.1 Optimization with the electromagnetic analysis software FEST3D

Regarding to the optimization procedure, FEST3D gives us several optimization algorithms. These algorithms are a simplex algorithm, a gradient algorithm, genetic algorithms or any other user-defined algorithm.

In this work the simplex algorithm and the gradient algorithm have been used due to its fastness. Both of it can achieve a good solution in the performed optimization within seconds depending on the structure complexity. However these algorithm can easily get stuck in a local minimum specially if the number of parameters to optimize increases. Thus, in order to get the right solution a good initial point is necessary which is close to the global minimum of the optimization. Due to this, sometimes in initial steps of the design procedure where there are only a couple of parameters to optimize and the response is quite simple a manual adjustment is performed.

Finally, although both algorithm are fast, the simplex algorithm is faster but the gradient algorithm is more reliable. The gradient algorithm is able to reach the right solution in times when the simplex algorithm gets stuck. Thus, the gradient algorithm will be used when the initial response is far from the target and the simplex one in any other case in where there is a good initial point.

Moreover, simplex algorithm requires at least two parameters to optimize. Thus when initial iris width of a filter is dimensioned, simplex algorithm can not be used and it is necessary to use gradient algorithm.

The following Table summarizes the cases when each algorithm has been used.

Algorithm	**Usage**
Simplex	In simulations with two or more parameters and with a good initial point, close to the target.
Gradient	Optimization of first iris aperture.
	Optimization of first step when there is no previous simulations to be taken as a initial point and after optimizing the structure manually.

Table B.1: Usage of FEST3D algorithms throughout this work.

Both algorithms listed in Table B.1 admits three input parameters, the maximum number of iterations, the target error and the initial step size. The number of iterations and the target error affect to the end of the optimization process meanwhile the step size controls the order of magnitude of the parameters variation. This parameter must be properly chosen since a too large initial step will cause that the algorithm diverges and reaches an incorrect solution. On the contrary, if the initial step size is much smaller than the required variation of the parameters, the convergence of the optimization process will be too slow and the algorithm may be stuck in a local minimum. Thus it is important to know the size of the parameters variation that could lead to the desired response. In this context, it is easy to realize that in dual-mode filters, a variation of tens of microns in the filter dimensions may produce a significant variation of the filter response depending on the frequency range while in in-line filters the sensitivity of the filter response to variations of the filter structure is much lower.

Figure B.2 shows the look of the optimization window of fest3d. Here it is possible to select the target S-parameters and to define constants formulas. Through these formulas the optimization parameters can be equated to a given expression or a function of other parameters. These parameters will be fixed to the given formula and will not be optimized.

Finally, it is important to establish the appropriate constraints to perform the optimization efficiently. For instance, usually in the structure of a dual-mode filter, the offset parameter between two waveguides can not be greater than the semi-subtraction of the width or height of both waveguides. This condition is shown in Figure B.3. However these conditions are not really a restriction in the optimization and should be avoid if it is possible. This condition will introduce an extra error in the optimization weighted by the weight parameters in Figure B.3 if the constraint is not satisfied. It could happen if the error introduced by the constraint is lower that the error in any other case. Thus in order to avoid this constraints it is advisable to adjust manually the filter structure first and then to use a proper initial point in the optimization with a small initial step size.

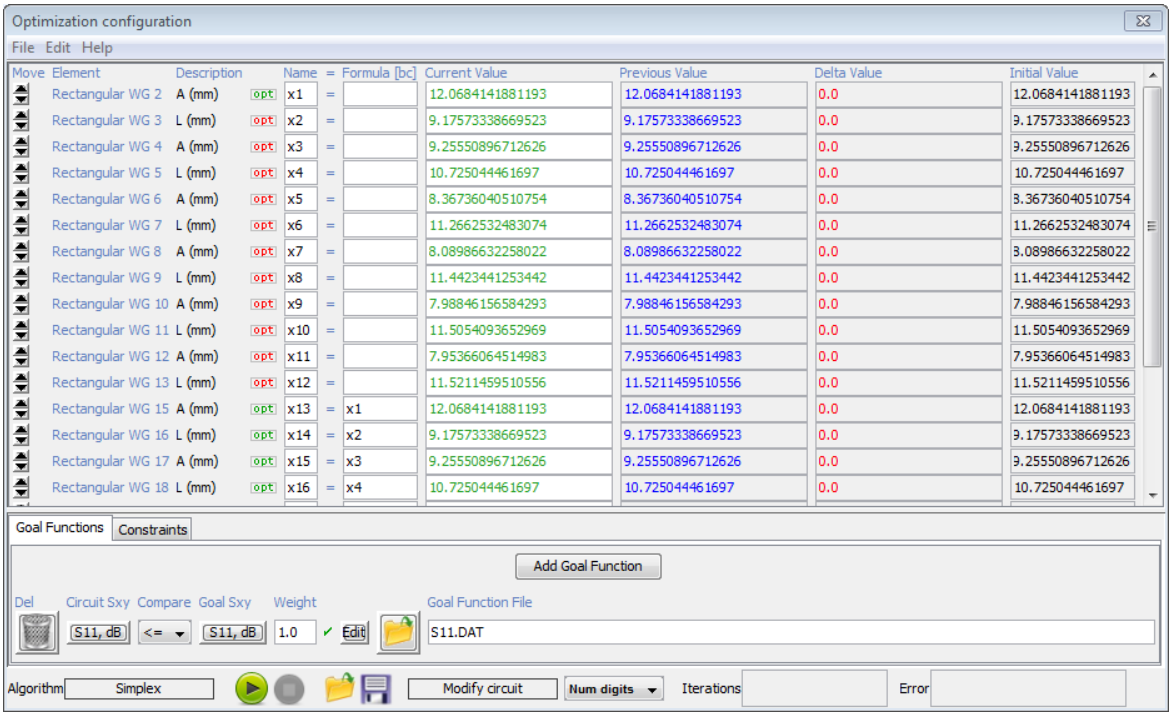

Figure B.2: Optimization window of fest3d.

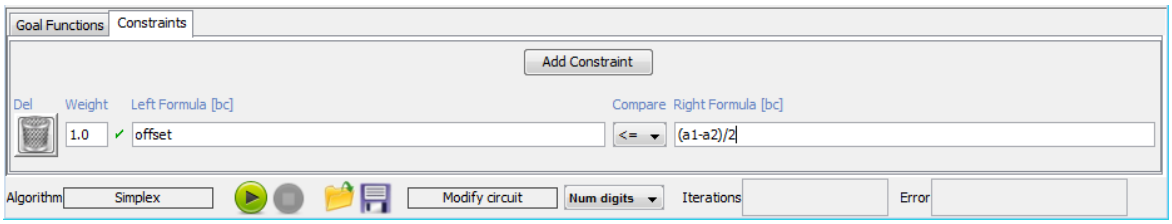

Figure B.3: Constraint in the optimization windows of fest3d.

C

CONVERGENCE STUDY

In the full-wave simulation process, the accuracy parameters of the integral equation technique must be properly chosen in order to assure the validity of the obtained response. The accuracy parameters are the number of accessible modes, the number of MoM basis functions and the number of Green function terms and must be adjusted in the following order[1]:

1. **Number of accessible modes.** It should be increased (in steps of 5 to 10 additional modes) starting from a small value until the change of the filter response is negligible.
2. **Number of MoM basis functions.** The initial value of these parameters must be set to the previously obtained number of accessible modes plus 1, with a minimum of 20. It has to be increased in steps of 10 to 20 until the filter response does not suffer significant changes.
3. **Number of Green Function terms.** Starting from a high value, it has to be decreased in steps of 100 to 200 until the filter response starts to change. The optimum value will be the value used before the filter response changed.
4. **Number of reference box modes.** This parameters will be decreased from a high value in the same way as the Number of basis functions while we see the variation of the S-parameters. The optimum value will be the one used before the filter response changed significantly.

The initial values of these parameters before starting the convergence study is shown in Figure C.1. It can also be seen that the box "All-Inductive" is selected. This is an important matter as most of the filters designed in this work are implemented in "All-Inductive" technology. By checking this box, the simulation software will only take into account the relevant modes within an inductive structure. As a result the convergent result will be achieved with a lower number of modes and therefore, in a shorter time.

Figure C.2 shows two results obtained with the same filter and with the same modes. In the first case the check-box "All inductive" has been checked and a convergent result is obtained meanwhile in the second one the result is not convergent as the box "All inductive" is not checked. In the first case, only the modes actually excited are taken into account, however when the box "All inductive" is not checked, the simulation software computing the same number of modes, but taking into account all modes within the structure regardless of the filter symmetry. Thus the number of modes that are actually excited is lower.

In order to guarantee that the simulation provides a truly convergent result, the filter response with the optimum parameters already obtained must be the same as the filter response when a extremely high value for each parameter is employed. However in practice it is necessary to find a trade off between the computational speed and the result accuracy.

In the theoretical design made in this work, we have perform a convergence study that favors the computing time at expense of a lower accuracy. Thus some of the presented structures could not provide precisely the same responses as they are shown. However, this is not a drawback since if it is desired a filter structure more accuracy, a new convergence study can be perform and the filter dimensions refined in order to achieve a more precise response. This approach was done in chapter 6 when the dual-mode filter was designed for manufacturing. In this case, after the filter design was completed, a new convergence study was performed to assure a high accuracy of the filter response. Finally the structure was readjusted to fit the target response with the new convergence parameters.

[1] As initial values to start the convergence study we have to take a small value for the Number of accessible modes and a big value for the other parameters. For instance, a possible values for an arbitrary rectangular waveguide is: 5 accessible modes; 200 basis functions; 1000 Green function terms and 3000 reference box modes.

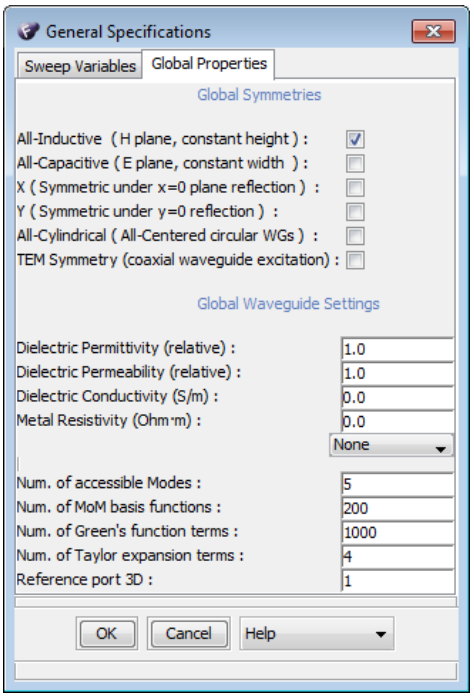

Figure C.1: General specifications window.

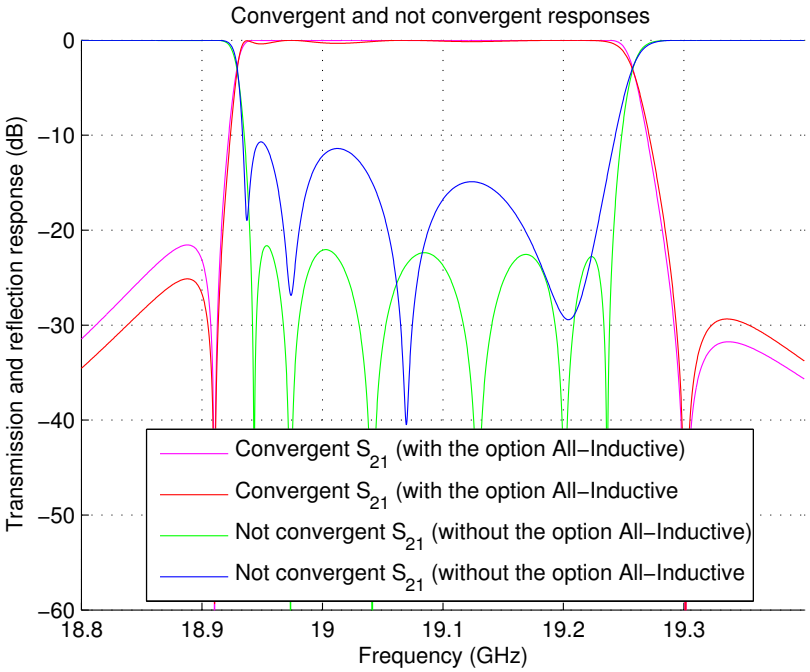

Figure C.2: Comparison between a convergent and a not convergent result by checking the "All-Inductive" box.

D

SIMULATION AND OPTIMIZATION OF SEVERAL RESONANT MODES SIMULTANEOUSLY WITH THE ELECTROMAGNETIC SOFTWARE FEST3D

In numerous occasions throughout this work, the coupling to two or even more modes in the output port is simulated and optimized. Nevertheless, it should be taken into account that the software fest3d does not allow to get the filter response by coupling to different output modes simultaneously. This is not a problem when the aim is to get the filter response with both output modes since both responses can be obtained alternately. However it is an important drawback if it is necessary to optimize the structure dimensions in order to get the right coupling to each output mode. Moreover, when trying to get the right coupling to each output mode, it is not possible to apply an iterative procedure by optimizing each mode through consecutive iterations since this approach diverges.

To overcome this drawback, a dual structure has been built. This structure is composed of two identical filters, each one with several modes propagating in the output port. Both filter are joined by the filters input through a slim and long waveguide. This junction must provides a coupling level between both filters of about $-200\ dB$ to $-500\ dB$, thus both filters are virtually isolated. Furthermore, the structure dimensions of the second filter are fixed to the dimensions of the first one both when simulating and when optimizing. As a result, both filters are actually the same filter as both have the same dimensions. Finally, the first output mode is selected in the first filter meanwhile in the second one the second mode is selected. Thus, if the first filter has the ports numbers "1" and "2" and the second one the ports numbers "3" and "4", then the S_{21} parameter will represent the transmission parameter when the output is taken with the output mode 1 while the parameter S_{43} represents the transmission parameters with the output mode 2.

Figure D.1 shows the dual structure used to optimize two modes simultaneously.

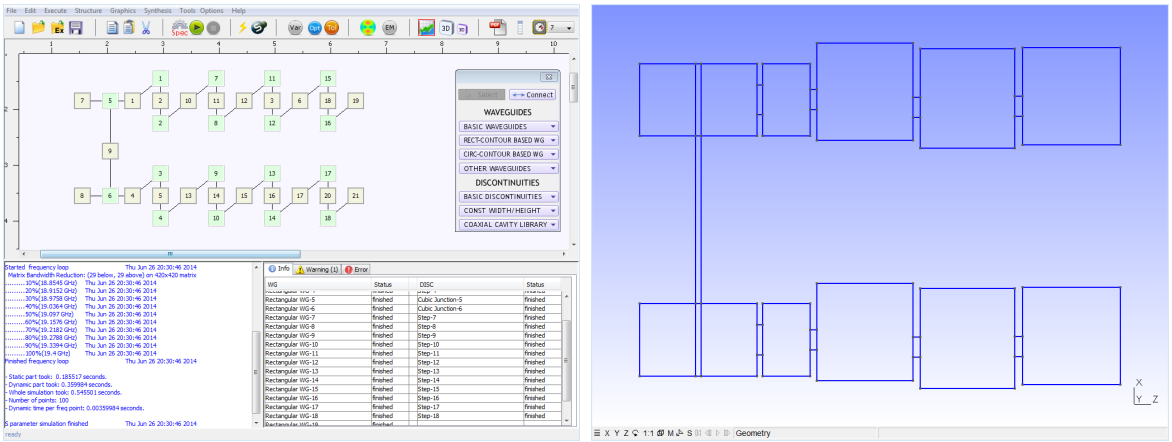

(a) Dual structure in the design window.

(b) View of the dual structure.

Figure D.1: Dual structure used to optimize the coupling to two resonant modes simultaneously.

E

MATLAB DESIGNED GUI

When a filter is designed by the coupling matrix and the step-by-step approach introduced in this work, it is necessary to obtain the required partial responses from the coupling matrix before the design of the filter structure starts. With the aim of obtaining these partial responses quickly and automatically a graphical interface has been designed. The said graphical interface is shown in Figure E.1 and it is composed of a panel to introduce the input parameters of the filter, two "pop-up menus" where it is possible to select each step of the filter design and the desired mode in the output waveguide and finally, a plot to show the selected target response as well as the options to save the results as a ".dat" file.

Below each of these fields is discussed:

1. **File and View menu.** These menus contain the options to view the slope parameter of each resonator and to save and load from a ".dat" file the filter parameters as well as the coupling matrix. Moreover it is possible to compare the input impedance of the bandpass resonator with the scaled lumped elements with the input impedance of a transmission line resonator.
2. **"Input Parameters" panel.** Intended to introduce the filter parameters.
   - **Waveguide Width.** In this field you must enter a vector with the theoretical widths of each waveguide, including the input and output waveguide of the filter.
   - **Waveguide Height.** A vector with the height of each waveguide like the previous parameter. If only one value is introduce in this field, the software will assume that the filter is implemented with "all-inductive" technology and that all elements have the same height.
   - **Frequency f1 and f2.** The lower and upper cut-off frequency of the filter. The filter bandwidth will be defined as: $BW = f2 - f1$, and the central frequency: $f_0 = \sqrt{f2 \cdot f1}$.
   - **Return Losses.** The reflection level in the passband. This value will be only used to obtain the in-line matrix of a filter with the given specifications in case that the coupling matrix is not provided.
   - **F. min and F. max.** These parameter together with the frequency points define the frequency vector that will be used to computing the filter response. The filter response will be obtain from "F. min" to "F. max".
   - **Frequency points.** The number of points of the frequency vector already commented
   - Coupling matrix. This field shows the coupling matrix currently load and give the possibility to reload this matrix or a different one.
3. **Calculate matrix.** This button obtain the coupling matrix of a transversal filter with the given specifications and then, transform this matrix into a coupling matrix with in-line topology [Cameron et al., 2007]. Thus, if it is desired to implement an in-line filter, it is not necessary to provide the in-line coupling matrix since this software can obtain it.
4. **Results for selected step.** Shows a list with each step of the filter design obtained from the number of elements in the widths vector. When a specific step is selected, the target response for this step is plotted in the embedded axes.
5. **TE mode.** In this field it is possible to select the desired mode in the output waveguide in case that the output port is a dual mode cavity. Otherwise only the mode TE_10 will be available.
6. **M-Matrix.** Shows the coupling matrix loaded that will be used to computing the partial responses of the filter.
7. **"Save options" panel.** It is useful to formatting the result in the ".dat" file.

- **Ports to format output.** This field is necessary when obtaining the target response for a multi-port structure such as a diplexer. Here you have to introduce the number of port of the desired structure, including the input port. If it is not required it must be left to 2.
- **Save goal to port.** Following with the previous field, if the target response is required for a multi-port structure, this field must contain the port number for which the target response is being calculated. The port number should be between 2 and the number of "Ports to format output". If it is not required it must be left to 2.
- **Min. and Max frequency.** This values defines the range of the target response that will be saved into the ".dat" file. If the box "Bandwidth" is selected, only the passband of the filter will be saved.
- **Save As button.** This button saves in different ".dat" files the target response in each step and for each output mode with the format that will be accepted by the software fest3d.

All these options are shown in Figure E.1 where the interface of the designed software is presented.

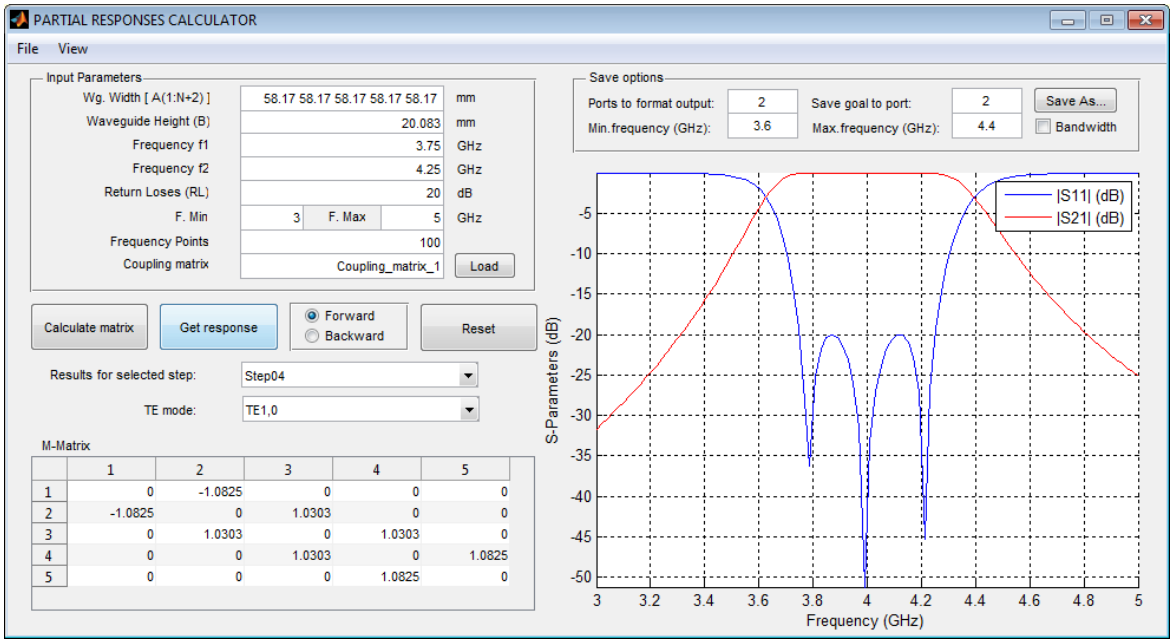

Figure E.1: Matlab designed GUI.

Bibliography

[Abenza, 2014] Abenza, A. P. (2014). Diseño de multiplexores en configuración manifold para aplicaciones por satélite (Manifold multiplexers for satellite communications). Master thesis, Universidad Politécnica de Cartagena (UPCT). 138

[Accatino and Mongiardo, 2002] Accatino, L. and Mongiardo, M. (2002). Hybrid circuit-full-wave computer-aided design of a manifold multiplexers without tuning elements. *IEEE Transactions on Microwave Theory and Techniques*, 50(9):2044–2047. 79

[Amari et al., 2004] Amari, S., Rosenberg, U., and Bornemann, J. (2004). A novel approach to dual and triple-mode pseudo-elliptic filter design. In *EuMC, European Microwave Conference*, pages 993–996, Amsterdam. 144

[Brumos et al., 2014] Brumos, M., Cogollos, S., Mendoza, M. M., Soto, P., Boria, V. E., and Guglielmi, M. (2014). Design of waveguide manifold multiplexers with dual-mode filters using distributed models. In *IEEE International Microwave Symposium Digest*, Tampa Bay, Florida. 138

[Cameron et al., 2007] Cameron, R. J., Kudsia, C. M., and Mansour, R. R. (2007). *Microwave Filters for Communication Systems*, pages 379–386. Wiley. ISBN: 978-0-471-45022-1. 1, 2, 5, 6, 7, 8, 19, 41, 43, 49, 52, 76, 77, 78, 79, 80, 134, 135, 153, 157, 171

[Cameron and Rhodes, 1981] Cameron, R. J. and Rhodes, J. D. (1981). Asymmetric realizations for dual-mode bandpass filters. *IEEE Transactions on Microwave Theory and Techniques*, 29(1):51–58. 41

[Cassivi et al., 2002] Cassivi, Y., Perregrini, L., Arcioni, P., Bressan, M., Wu, K., and Conciauro, G. (2002). Dispersion characteristics of substrate integrated rectangular waveguide. *IEEE Microwave and Wireless Components Letters*, 12(9):333–335. 43

[Cheng et al., 2013] Cheng, F., Lin, X., Song, K., Jiang, Y., , and Fan, Y. (2013). Compact diplexer with high isolation using the dual-mode substrate integrated waveguide resonator. *IEEE Microwave and Wireless Components Letters*, 23(9):459–461. 80, 90

[Chrisostomidis and Lucyszyn, 2005] Chrisostomidis, C. E. and Lucyszyn, S. (2005). On the theory of chained-function filters. *IEEE Transactions on Microwave Theory and Techniques*, 53(10):3142–3151. 140

[Cogollos et al., 2010] Cogollos, S., Brumos, M., Boria, V., Vicente, C., B.Gimeno, and M.Guglielmi (2010). New distributed model for synthesis of classical dual mode filters. In *IEEE*, pages 437–440, Anaheim, CA. Microwave Symposium Digest (MTT). Digital Object Identifier: 10.1109/MWSYM.2010.5517399. 2, 42

[Cogollos et al., 2012] Cogollos, S., Brumos, M., Boria, V. E., Vicente, C., Gil, J., Gimeno, B., and Guglielmi, M. (2012). A systematic design procedure of classical dual-mode circular waveguide filters using an equivalent distributed model. *IEEE Transactions on Microwave Theory and Techniques*, 60(4):1006–1016. 42

[Escudero et al., 2013] Escudero, J. M. P., Melcón, A. A., Acosta, J. A. L., and Guglielmi, M. (2013). Técnica para la reducción de espúreos basada en el control del espesor de las ventanas de acoplo. In *URSI 2013*, Santiago de Compostela, Spain. XXVIII Simposium Nacional de la Unión Científica Internacional de Radio. 132

[Ezzeddine et al., 2012] Ezzeddine, H., Mazet, P., Bila, S., and Verdeyme, S. (2012). Design of a compact dual-band diplexer with dual-mode cavities. In *EuMC, European Microwave Conference*, volume 42, pages 455–458, Amsterdam, The Netherlands. EuMC. 80, 90

[Fiedziuszko, 1982] Fiedziuszko, S. J. (1982). Dual-mode dielectric resonator loaded cavity filters. *IEEE Transactions on Microwave Theory and Techniques*, 30(9):1311–1316. 41

[Gál et al., 2013] Gál, T., Ladvánszky, J., and Lénárt, F. (2013). Improvement of waveguide diplexer components. In *Asia Pacific Microwave Conference*, pages 28–30, Seoul. Digital Object Identifier: 10.1109/APMC.2013.6695180. 80

[Guglielmi, 1994] Guglielmi, M. (1994). A simple cad procedure for microwave filters and multiplexers. *IEEE Transactions on Microwave Theory and Techniques*, 42(7):1347–1352. 1, 3, 9, 13, 14, 19, 31, 38, 48, 76, 80, 90, 99, 127, 129, 140

[Guglielmi and Connor, 1997] Guglielmi, M. and Connor, G. (1997). Chained function filters. *IEEE Microwave and Guided Wave Letters*, 7(12):390–392. 140

[Guglielmi et al., 1991] Guglielmi, M., Gheri, G., and Melcon, A. A. (1991). CAD of tunnning-less band-pass filters. Estec Working Paper 1624, European Space Agency, ESA-ESTEC, Noordwijk, The Netherlands. 9, 51

[Guglielmi et al., 2001] Guglielmi, M., Jarry, P., Kerherve, E., Roquebrun, O., and Schmitt, D. (2001). A new family of all-inductive dual-mode filters. *IEEE Transactions on Microwave Theory and Techniques*, 49(10):1764–1769. 2, 3, 43, 52, 76, 99, 127, 129, 140

[Guglielmi and Melcon, 1993] Guglielmi, M. and Melcon, A. A. (1993). Novel design procedure for microwave filters. In *Proc. 23th European Microwave Conference*, pages 212–213, Madrid, Spain. EuMC. 1, 2, 3, 13, 14, 19, 31, 38, 48, 76, 80, 90, 99, 127, 129, 140

[Guglielmi et al., 1995] Guglielmi, M., Montauti, F., Pellegrini, L., and Arcion, P. (1995). Implementing transmission zeros in inductive-window bandpass filters. *IEEE Transactions on Microwave Theory and Techniques*, 43(8):1911–1915. 132

[Hu and Wu, 2013] Hu, H. and Wu, K.-L. (2013). A deterministic em design technique for general waveguide dual-mode bandpass filters. *IEEE Transactions on Microwave Theory and Techniques*, 61(2):800–807. 42

[Hu et al., 2013] Hu, H., Wu, K.-L., and Cameron, R. J. (2013). Stepped circular waveguide dual-mode filters for broadband contiguous multiplexers. *IEEE Transactions on Microwave Theory and Techniques*, 61(1):139–145. 2, 79

[Li et al., 2013] Li, J., Huang, H., Zhang, Z., Song, W., Shao, H., Chen, C., , and Huang, W. (2013). A novel x-band diplexer based on overmoded circular waveguides for high-power microwaves. *IEEE Transactions on plasma science*, 41(10):2724–2728. 80

[Liang et al., 1992] Liang, X.-P., Zaki, K. A., and Atia, A. E. (1992). Dual mode coupling by square corner cut in resonators and filters. *IEEE Transactions on Microwave Theory and Techniques*, 40(12):2294–2302. 42

[Macchiarella, 2011] Macchiarella, G. (2011). Synthesis of star-junction multiplexers. *IEEE Microwave Magazine*, 12(6):101–109. Digital Object Identifier: 10.1109/MMM.2011.942011. 2, 80

[Macchiarella and Tamiazzo, 2006] Macchiarella, G. and Tamiazzo, S. (2006). Novel approach to the synthesis of microwave diplexers. *IEEE MTT-S International Microwave Symposium Digest*, 54(12):4281–4290. 80

[Macchiarella and Tamiazzo, 2010] Macchiarella, G. and Tamiazzo, S. (2010). Synthesis of star-junction multiplexers. *IEEE Transactions on Microwave Theory and Techniques*, 58(12):3732 – 3741. Digital Object Identifier: 10.1109/TMTT.2010.2086570. 2, 80

[Macchiarella and Tamiazzo, 2011] Macchiarella, G. and Tamiazzo, S. (2011). Polynomial design of manifold multiplexers. In *IEEE International Microwave Symposium Digest*, pages 1–4, Baltimore, MD. Digital Object Identifier: 10.1109/MWSYM.2011.5972610. 79

[Martínez et al., 2013] Martínez, D. M., Melcón, A. A., Pereira, F. Q., and Guglielmi, M. (2013). Segmentación de la matriz de acoplos para el diseño de filtros pasobanda. In *URSI 2013*, Santiago de Compostela, Spain. XXVIII Simposium Nacional de la Unión Científica Internacional de Radio. 3, 7, 15, 19, 99

[Mattes et al., 2000] Mattes, M., Mosig, J., and Guglielmit, M. (2000). Six-pole triple mode filters in rectangular waveguide. In *IEEE International Microwave Symposium Digest*, pages 1775 – 1778, Boston, MA, USA. Digital Object Identifier: 10.1109/MWSYM.2000.862323. 144

[Matthaei and Yones, 1980] Matthaei, G. and Yones, E. (1980). *Microwave Filters, Impedance Matching Networks, and Coupling Structures*. Artech House, Boston, Massachusetts, USA. 10, 11, 13, 14, 16, 49, 135, 157

[Mendoza, 2006] Mendoza, M. M. (2006). Síntesis de filtros usando el método de la matriz de acoplos, y aplicación al diseño de filtros transversales multicapa. Master thesis, Universidad Politécnica de Cartagena (UPCT). 19, 153, 157

[Mendoza et al., 2014] Mendoza, M. M., Martínez, D. M., Rebenaque, D. C., , and Melcón, A. A. (2014). Enhanced topologies for the design of dual-mode filters using inductive waveguide structures. Manuscript submitted for publication. 48, 53

[Mohottige et al., 2013] Mohottige, N., Glubokov, O., and Budimir, D. (2013). Ultra compact inline -plane waveguide extracted pole bandpass filters. *IEEE Microwave and Wireless Components Letters*, 23(8):409–411. 3, 129, 138

[Montejo-Garai et al., 2005a] Montejo-Garai, J. R., Ruiz-Cruz, J. A., and Rebollar, J. M. (2005a). Full-wave design of h-plane contiguous manifold output multiplexers using the fictitious reactive load concept. *IEEE Transactions on Microwave Theory and Techniques*, 53(8):2625–2632. 79

[Montejo-Garai et al., 2005b] Montejo-Garai, J. R., Ruiz-Cruz, J. A., Rebollar, J. M., Padilla-Cruz, M. J., noro Navarro, A. O., and Hidalgo-Carpintero, I. (2005b). Synthesis and design of in-line n-order filters with n real transmission zeros by means of extracted poles implemented in low-cost rectangular h-plane waveguide. *IEEE Transactions on Microwave Theory and Techniques*, 53(5):1636–1642. 3, 129, 138

[Morini et al., 1997] Morini, A., Rozzi, T., and Morelli, M. (1997). New formulae for the initial design in the optimization of t-junction manifold multiplexers. In *IEEE International Microwave Symposium Digest*, pages 1025–1028, Denver, CO, USA. Digital Object Identifier: 10.1109/MWSYM.1997.602976. 79

[Neubauer et al., 2002] Neubauer, V., Mayer, M., and Magerl, G. (2002). A novel low loss microwave multiplexer design based on directional filters. In *RAWCON, Radio and Wireless Conference*, pages 257–260, Vienna, Austria. Digital Object Identifier: 10.1109/RAWCON.2002.1030166. 79

[Rhodes and Cameron, 1980] Rhodes, J. D. and Cameron, R. J. (1980). General extracted pole synthesis technique with applications to low-loss TE011 mode filters. *IEEE Transactions on Microwave Theory and Techniques*, 28(9):1018–1028. 3, 129, 138

[Shen et al., 2010] Shen, W., Yin, W.-Y., Sun, X.-W., , and Mao, J.-F. (2010). Compact substrate integrated waveguide (siw) transversal filter with triple-mode microstrip resonator. In *Asia Pacific Microwave Conference*, pages 1875 – 1878, Yokohama. 144

[Soto et al., 2010] Soto, P., Tarin, E., Boria, V. E., Vicente, C., Gil, J., and Gimeno, B. (2010). Accurate synthesis and design of wideband and inhomogeneous inductive waveguide filters. *IEEE Transactions on Microwave Theory and Techniques*, 58(8):2220–2230. 1, 31

[Uhm et al., 2005] Uhm, M. S., Lee, J., Park, J. H., and Kim, J. P. (2005). An efficient optimization design of a manifold multiplexer using an accurate equivalent circuit model of coupling irises of channel filters. In *IEEE International Microwave Symposium Digest*, pages 1263–1266. Digital Object Identifier: 10.1109/MWSYM.2005.1516907. 79

[Vanin et al., 2004] Vanin, F. M., Schmitt, D., and Levy, R. (2004). Dimensional synthesis for wide-band waveguide filters and diplexers. *IEEE Transactions on Microwave Theory and Techniques*, 56(11):2488–2495. 1, 31, 32, 37, 38, 132

[Wanselow, 1975] Wanselow, R. D. (1975). Prototype characteristics for a class of dual-mode filters. *IEEE Transactions on Microwave Theory and Techniques*, 23(8):708–711. 41